

# Urban ground-based thermography

William Morrison

Department of Meteorology

Submitted for the degree of Doctor of Philosophy

June 2019



## Abstract

Urban climates are driven by micro-meteorological processes associated with the complex urban form, materials, and land cover patterns. Given its close link to the surface energy balance, surface temperature observations are key to the improvement and evaluation of models. This work contributes to the application of ground-based thermography in urban settings as an observational method to further our understanding of urban climate processes.

In this thesis, ground-based thermography observations are collected and interpreted in a unique way so that they are relatable to scales used by urban climate models and earth observation (EO) satellites. At two measurement sites (simplified outdoor scale model and complex central urban setting), variations in surface temperature are quantitatively linked to micro-scale features such as shadow patterns and material characteristics at unprecedented levels of detail. Previous studies with low level of detail have inferred these properties. The detected upwelling longwave radiation is corrected to surface temperature ( $T_s$ ) using a novel, high-resolution three-dimensional (3D) radiative transfer (RT) approach. From multi-day observational evaluation, the atmospheric correction has 0.39 K mean absolute error.

Ground-based observations are combined with a comprehensive 3D radiative transfer model, enabling detailed simulation of EO land surface temperature ( $T_s^{\text{EO}}$ ). For a mainly clear-sky summer day,  $T_s^{\text{EO}}$  at night underestimates the unbiased “complete” surface temperature ( $T_c$ ) by 0.5 – 1 K, is similar to  $T_c$  during morning and evening, and for other times varies significantly with view angle (up to 5.1 K). Generally, view angle variation is smaller than prior studies as they typically use simpler geometry and temperature descriptions, and lack vegetation. Here, the observational basis and high-resolution modelling in a real central urban setting serves as a benchmark for future improvements of simplified model parameterisations.

## Declaration of original authorship

I confirm that this is my own work and the use of all material from other sources has been properly and fully acknowledged. This work contains three publications, presented as:

**Chapter 2:** Morrison W, Kotthaus S, Grimmond CSB, Inagaki A, Yin T, Gastellu-Etchegorry J-P, Kanda M, Merchant CJ 2018: A novel method to obtain three-dimensional urban surface temperature from ground-based thermography. *Remote Sensing of Environment*, 215(May), 268–283. <https://doi.org/10.1016/j.rse.2018.05.004>.

Morrison performed all modelling and data analysis and wrote the manuscript; Kotthaus, Inagaki and Kanda conducted the ground-based observational campaign; Morrison, Kotthaus and Grimmond designed the manuscript structure; Yin developed the sensor view modelling in the Discrete Anisotropic Radiative Transfer (DART) model; Yin and Gastellu-Etchegorry developed DART and provided support and advice; all co-authors read and provided feedback on the manuscript.

**Chapter 3:** Morrison W, Yin T, Lauret N, Guilleux J, Kotthaus S, Gastellu-Etchegorry J-P, Norford L, Grimmond CSB 2019: Atmospheric and emissivity corrections for ground-based thermography using 3D radiative transfer modelling. *Remote Sensing of Environment*, *In Press*, <https://doi.org/10.1016/j.rse.2019.111524>.

Morrison conducted the ground-based observational campaign, performed all modelling and data analysis and wrote the manuscript (Yin assisting with Section 3.3.2.2); Morrison, Kotthaus and Grimmond designed the manuscript structure; Lauret developed the DART sensor view model; Yin, Lauret, Guilleux and Gastellu-Etchegorry developed DART and provided support and advice; all co-authors read and provided feedback on the manuscript.

**Chapter 4:** Morrison W, Kotthaus S, & Grimmond CSB (2019): Urban satellite view uncertainty assessed with ground-based thermography. *In preparation*.

Morrison planned and carried out the ground-based observational campaign, performed all modelling and data analysis, made all figures and wrote the manuscript; Morrison, Kotthaus and Grimmond designed the manuscript structure; all co-authors read and provided feedback on the manuscripts.

William Morrison

## Acknowledgements

I thank my supervisor Sue Grimmond for giving me the opportunity to conduct this research. Throughout the PhD Sue and my second supervisor Simone Kotthaus have supported me in a way that has provided constant inspiration and motivation due to their insights and dedication. I also thank my third supervisor Christopher Merchant particularly for his interest and valuable comments during early discussions on the PhD planning and direction which built a strong foundation for the overall thesis.

I am thankful to all my co-authors who have given time and offered their expertise to help enhance this thesis and its associated publications. I have learnt a lot from them. For the DART developer co-authors, I am grateful for your assistance with the model and my queries and also your provision of many model enhancements that have helped shaped this PhD. In particular I thank Jean-Philippe Gastellu-Etchegorry, who leads the model development, and also Tiangang Yin who made a large part of the observational corrections possible in DART and engaged in vital discussions on the overall correction procedure.

For the observational campaign, the advice and support from Kjell Zum Berge as the London urban micrometeorological observatory (LUMO) research group technician was invaluable. Ben Crawford, Andy Gabey, Bethany Saunders, Bryam Orihuela and Agnieszka Walenkiewicz from LUMO also helped with fieldwork and some tricky programming tasks. Without the help of Esther Lamontagne and others at Islington Council, and also Prof Sir Paul Curran, Dean Beeden and others at City University of London, the London observations would not have been possible, so I am forever thankful. All others within LUMO have also helped in some way to make the observations possible. More broadly, PhD peers and also friends and family have shown unwavering support throughout and I am grateful for this.

# Contents

<b>Abstract</b> .....	<b>iii</b>
<b>Declaration of original authorship</b> .....	<b>iv</b>
<b>Acknowledgements</b> .....	<b>v</b>
<b>Contents</b> .....	<b>vi</b>
<b>List of Figures</b> .....	<b>ix</b>
<b>List of Tables</b> .....	<b>xv</b>
<b>Chapter 1 Introduction</b> .....	<b>1</b>
1.1 Motivation .....	1
1.2 Objectives .....	5
1.3 Thesis structure .....	5
<b>Chapter 2 A novel method to obtain three-dimensional urban surface temperature from ground-based thermography</b> .....	<b>7</b>
Abstract .....	7
2.1 Introduction .....	7
2.2 Methods .....	10
2.2.1 Real world site .....	11
2.2.2 Real world instrumentation .....	12
2.2.3 Model world site .....	13
2.2.3.1 Surface creation .....	16
2.2.3.2 Surface classification .....	16
2.2.4 Model world instrumentation .....	17
2.2.4.1 Estimation of camera internal parameters .....	18
2.2.4.2 Reprojection error .....	19
2.2.4.3 Classification of camera images .....	22
2.3 Longwave radiation flux extrapolated to 3D distribution .....	23
2.4 Results and discussion .....	24
2.4.1 Image classification .....	24
2.4.2 Inter-camera comparison .....	26
2.4.3 Classified brightness temperature observations .....	27
2.4.4 Extrapolated longwave radiation flux .....	28
2.4.5 Normalised effective anisotropy .....	32
2.5 Conclusions .....	33
List of symbols and acronyms [units] .....	36
Acknowledgements .....	37
<b>Chapter 3 Atmospheric and emissivity corrections for ground-based thermography using 3D radiative transfer modelling</b> .....	<b>38</b>
Abstract .....	38
3.1 Introduction .....	39

3.2	Theoretical background to the corrections .....	41
3.3	Methods.....	42
3.3.1	DART radiative transfer and sensor view model .....	43
3.3.2	Atmospheric correction procedure .....	45
3.3.2.1	DART simulation.....	45
3.3.2.2	Post-processing of DART simulation .....	45
3.3.3	Emissivity correction procedure.....	46
3.3.3.1	Surface temperature and optical properties .....	47
3.3.3.2	Simulation and emissivity correction.....	47
3.4	Application of Methods.....	49
3.4.1	Study area and observation sites .....	49
3.4.2	Instrumentation and observations.....	51
3.4.3	Model setup.....	53
3.4.3.1	Atmospheric correction.....	54
3.4.3.2	Emissivity correction .....	54
3.5	Results.....	55
3.5.1	Atmospheric correction.....	55
3.5.2	Emissivity correction .....	62
3.5.2.1	Temporally resolved surface temperatures and incoming LWIR radiation .....	62
3.5.2.2	Spatially resolved longwave irradiance and emissivity correction .....	64
3.5.2.3	Uncertainty analysis .....	65
3.6	Discussion .....	68
3.6.1	Flexibility in the correction framework .....	68
3.6.2	Future application of corrected ground-based observations.....	69
3.7	Conclusions .....	70
	List of symbols and acronyms [units].....	72
	Acknowledgements.....	73
<b>Chapter 4</b>	<b>Urban satellite view uncertainty assessed with ground-based thermography...</b>	<b>74</b>
	Abstract.....	74
4.1	Introduction .....	74
4.2	Methods.....	76
4.2.1	Real world study area and observations.....	77
4.2.2	Model world.....	79
4.2.2.1	Surface-sun geometry.....	82
4.2.2.2	Shadow history.....	83
4.2.2.3	Instrumentation and image classification.....	83
4.2.3	Upscaling classified surface temperature across model world.....	86
4.2.3.1	Gap-filling per-class surface temperatures.....	88
4.2.3.2	Extrapolating observations to 3D and complete surface temperature .....	88

4.2.4	Simulation of satellite surface temperature .....	89
4.3	Results .....	90
4.3.1	Assessment of the morphometric and land cover characteristics of the MW area ...	90
4.3.1.1	Observational source area and image classification .....	92
4.3.2	Drivers of observed surface temperature variability.....	94
4.3.2.1	Variability from surface orientation and material at the building scale .....	94
4.3.2.2	Variability from shortwave irradiance.....	96
4.3.2.3	Variability from shadow history .....	98
4.3.3	Crossing scales between satellite and ground-based observations .....	100
4.3.3.1	Spatially resolved thermal anisotropy .....	100
4.3.3.2	Time series of thermal anisotropy .....	103
4.4	Conclusions .....	109
	List of symbols and acronyms [units] .....	112
	Acknowledgements .....	113
<b>Chapter 5</b>	<b>Conclusions .....</b>	<b>114</b>
5.1	Main contributions and conclusions .....	114
5.1.1	Application and interpretation of ground-based thermography.....	114
5.1.2	Retrieval of surface temperature.....	115
5.1.3	Urban effective thermal anisotropy .....	116
5.2	Recommendations for future work .....	118
<b>Appendix A</b>	<b>: Thermal camera lens distortion correction .....</b>	<b>122</b>
<b>Appendix B</b>	<b>: Longwave infrared camera meta data .....</b>	<b>125</b>
<b>Appendix C</b>	<b>: Camera image emissivity maps from the DART model .....</b>	<b>126</b>
<b>Appendix D</b>	<b>: Creation and classification of complex 3D surface and vegetation models .....</b>	<b>127</b>
<b>Appendix E</b>	<b>: Thermal camera enclosures .....</b>	<b>133</b>
<b>Appendix F</b>	<b>: Camera spectral response function .....</b>	<b>137</b>
<b>Appendix G</b>	<b>: Siting of camera for observational evaluation of atmospheric correction .....</b>	<b>138</b>
<b>Appendix H</b>	<b>: Time series images of atmospheric and emissivity correction.....</b>	<b>139</b>
<b>Appendix I</b>	<b>: Statistics for atmospheric correction.....</b>	<b>145</b>
<b>Appendix J</b>	<b>: Three-dimensional bidirectional reflectance factor from DART.....</b>	<b>151</b>
<b>Appendix K</b>	<b>: Details of DART longwave infrared simulation.....</b>	<b>153</b>
<b>Appendix L</b>	<b>: Meteorological conditions for 26<sup>th</sup> – 27<sup>th</sup> August 2017.....</b>	<b>154</b>
<b>Appendix M</b>	<b>: Time series and per-pixel classification of observations.....</b>	<b>155</b>
<b>Appendix N</b>	<b>: Surface temperature variability by shortwave irradiance – extended .....</b>	<b>156</b>
<b>References</b>	<b>.....</b>	<b>157</b>

## List of Figures

- Figure 2-1. Flow chart of procedures to estimate and evaluate exitant broadband longwave radiation prescribed across an urban canopy ( $M_{LW}^{3D}$ ) using ground-based longwave infrared (LWIR) imagery coupled with camera view and 3D modelling techniques. See list of symbols and acronyms for all other definitions. .... 11
- Figure 2-2. COSMO test site and longwave infrared (LWIR) camera observational setup: (a) test site domain (plan view) with focus area (green box); (b) focus area with LWIR camera ( $C^{\text{south}}$ ,  $C^{\text{north}}$ ) locations and approximate orientations (blue) and source areas (red) for camera field of view; (c) north-west facing oblique visible image taken near the  $C^{\text{north}}$  camera location and perspective (d) vertical cross section of building array (grey squares) showing instrument tower and camera geometry..... 12
- Figure 2-3. Surface representation and interaction in the “model world” (MW) is defined by triangle face ( $S$ ) and voxel ( $Vx$ ) elements, with camera view modelling to simulate camera image plane (IP). See table and text for symbol and acronym definitions and Figure 4-2 for further details..... 15
- Figure 2-4. Coordinate and transformation definitions for “model world” elements.  $(X, Y, Z) \rightarrow (x_c, y_c, z_c)$  is the rigid transformation from the three-dimensional coordinate frame with origin  $O$ , to the three-dimensional camera coordinate frame with origin  $O_c$  using camera extrinsic parameters of rotation  $R$  and translation  $t$ .  $(x_c, y_c, z_c) \rightarrow (x, y)$  is the projective transformation from camera coordinate frame to two-dimensional camera image plane (IP) frame (yellow).  $R$  represents a series of Euler angles  $\beta$ ,  $\varphi$  and  $\omega$  that define a sequence of rotations: first around the  $x_c$ -axis ( $\beta$ ), then around the  $y_c$ -axis ( $\varphi'$ ) that has already been rotated by  $\beta$ , and finally around the  $z_c$ -axis ( $\omega''$ ) that has already been twice rotated firstly by  $\beta$  and then  $\varphi'$  (Heikkila and Silven, 2002).  $t$  is a vector that describes the translation between the model world coordinate origin ( $O$ ) and camera coordinate origin ( $O_c$ ). Intrinsic parameters of focal length  $F$ , pixel scale factor (Eqn. 2.4) and principle point offset are used for the final projection of 3D points onto the 2D camera IP as  $(x_c, y_c, z_c) \rightarrow (x, y)$ . These parameters are determined by physical camera features including pixel size and the relative position of the IP to  $O_c$ . The point at which the principle axis ( $z_c$ ) intersects with the IP is the principle point  $P$  (Hartley and Zisserman, 2004). For a pinhole camera,  $P$  intersects at the centre of the IP. For real world cameras, the principle point offset describes the offset between  $P$  and the centre of the IP which may arise from imperfections in the lens-FPA assembly. This results in a misalignment of the lens with the FPA (Clarke, Wang and Fryer, 1998) and hence needs to be accounted for..... 18
- Figure 2-5. Observations, classification and extrapolation of results for Optris PI longwave infrared (LWIR) camera (a – d)  $C^{\text{south}}$  and (e – h)  $C^{\text{north}}$  at COSMO test site (Figure 2-2, 2<sup>nd</sup> August 2014 10:00 local standard time). (a, e) “Real world” (RW) brightness temperature ( $T_b$ ) images; (b, f) classification of per-pixel surface orientation using Blender “model world” (MW) camera view of the digital surface model (DSM) containing surface orientation information. Surface information is coded as per-class RGB textures projected onto a Blender camera for per-pixel identification of surface orientation. RGB values in the image not associated with an RGB texture class see more than one class and are classified as mixed pixels (black); (c, g) classification of per-pixel surface shadowing derived by DART shortwave scattering simulation and camera view model shown as shortwave bidirectional reflectance factor (BRF; Schaepman-Strub *et al.*, 2006), dark pixels (BRF = 0) indicate no first order scattering from surface to camera; (d, h) simulated  $T_b$  thermographs:  $T_b$  observations extrapolated to a MW three-dimensional distribution based on surface classes (shown in b, c, f, g) reprojected onto a MW camera image plane simulated in DART, simulating RW camera observations (a, e). The hollow cubes have more material around block edges, and increased heat storage, potentially explaining warm edges in (a, e)..... 21
- Figure 2-6. Images of COSMO test site taken at 15:25 local standard time on 26<sup>th</sup> September 2014 with approximate  $C^{\text{north}}$  perspective (Figure 2-2) from (a) a “real world” (RW) digital camera and (b) simulated by a “model world” (MW) camera in the shortwave using the Discrete Anisotropic Radiative Transfer (DART) model to compare the performance of DART when 1) simulating RW camera perspectives 2) resolving shadow patterns at high spatial resolution (0.04 m) across a canopy

surface. Greyscale intensity (b) is used for qualitative indication of shaded (black) and sunlit (grey → white) surfaces. Comparison (c) shown as RW – MW greyscale intensity difference..... 23

Figure 2-7. Per-voxel brightness temperature ( $V_{X_{Tb}^S}$ ) extrapolated from observations for one time-step (2<sup>nd</sup> August 2014 10:00 local time, (same as Figure 2-5) for an arbitrary 8 m x 8 m subset of the “model world” (MW) domain visualized as a three-dimensional point cloud, with each point at the centroid of a voxel.  $V_{X_{Tb}^S}(\Delta X, \Delta Y, \Delta Z)$  resolved at  $\Delta X = \Delta Y = \Delta Z = 0.04$  m spatial resolution. .... 24

Figure 2-8. Fraction  $f$  of all pixels in a camera image assigned to surface class  $i$  for cameras C<sub>south</sub> and C<sub>north</sub> for day of year 214 at local standard time. Resolution of classified images is 1 min. Short periods of daytime shadow due to overcast periods determined from [ESW,dir↓ (COSMO)] observations (Figure 2-9a). Mixed pixels (Section 2.2.4.3) contain more than one surface class around building edges or are isolated pixels for oblique sun angles. .... 25

Figure 2-9. Inter-camera comparison of the mean broadband longwave radiation derived from roof pixels within the FOV of both cameras shown as (a) brightness temperatures ( $T_{b_{roof}^{cam}}$ ) for C<sub>south</sub> (black) and C<sub>north</sub> (red) surfaces with observations at 1 min resolution. Direct incoming shortwave radiation  $E_{SW,dir\downarrow}$  (COSMO) measured on site using MS-56 Pyrheliometer (EKO Instruments) at 1 min resolution. Japan Meteorological Agency (JMA) air temperature measurements [ $T_a$  (JMA)] measured at Kumagaya AMeDAS (Automated Meteorological Data Acquisition System) station at 1 min resolution. (b) Relation between  $T_{b_{roof}^{cam}}$  (C<sub>south</sub>) and  $T_{b_{roof}^{cam}}$  (C<sub>north</sub>) with linear regression slope (m) and intercept (b) coefficients, used to correct the observations used throughout all results. In this figure observations are shown uncorrected. .... 27

Figure 2-10. Intra-class variability of camera brightness temperatures ( $T_b^{cam}$ ) on 2<sup>nd</sup> August 2014. Each boxplot is all pixels assigned to a class (colour) from both cameras (images 1 min samples) during 1 h, with 5<sup>th</sup> and 95<sup>th</sup> percentiles (whiskers), interquartile range (box) and median (horizontal line) for pixels classified by: (a) all, (b) surface insolation status, (c) surface orientation, and (d) orientation and insolation status. .... 29

Figure 2-11. Brightness temperature ( $T_b$ ) differences between LWIR camera observations from “real world” (RW) [ $T_b^{cam}(RW)$ ] and “model world” (MW) for six times (see labels on sub-plots) on 2<sup>nd</sup> August 2014, for camera (a – f) C<sub>south</sub> and (g – l) C<sub>north</sub>.  $T_b^{cam}(MW)$  is simulated by DART camera view modelling using predetermined 3D distribution of longwave flux ( $M_{LW}^{3D}$ ). (a – f) Radiometer boom masked (grey) from results. Boxplot (inside legend) for all non-masked pixels within all timesteps throughout the day (15 min resolution) with 1<sup>st</sup> and 99<sup>th</sup> percentiles (whiskers), interquartile range (box) and median (vertical line). .... 30

Figure 2-12. Comparison of “real world” (RW) and “model world” (MW) aggregated at-sensor broadband longwave radiation observations (as brightness temperatures) for cameras C<sub>south</sub> (black) and C<sub>north</sub> (red) 2<sup>nd</sup> August 2014 local standard time. MW observations simulated by DART camera view modelling using predetermined 3D distribution of longwave flux ( $M_{LW}^{3D}$ ) at the COSMO test site.  $M_{LW}^{3D}$  prescribed using shadowing and orientation classes (solid lines) and orientation classes only (dashed lines)..... 31

Figure 2-13. Simulated brightness temperatures for 375 discrete directions using predetermined 3D distribution of longwave flux ( $M_{LW}^{3D}$ ) for the COSMO test site for 6 times on 2<sup>nd</sup> August 2014. Results normalized by the simulated brightness temperature at nadir ( $\phi = 0^\circ$ , given in sub-headings) and shown with 1 K contours. Data and sun angle (yellow dot) are oriented with true north ( $\theta = 0^\circ$ ), with COSMO building orientation displayed (centre grey square, 06:00). .... 33

Figure 3-1. Procedure to correct LWIR camera observations for atmospheric and emissivity effects to obtain surface temperature ( $T_s$ ) for pixels. See list of symbols and acronyms for definitions. .... 44

Figure 3-2. Study area characteristics: plan view of (a) above sea level raster digital surface model ( $r^{DSM}$ ) of all surfaces with (black lines) a reference building footprint model from Evans, Hudson-Smith and Batty (2006), (b) orthorectified raster RGB ( $r^{RGB}$ ) image from a mosaic of Google Earth (Google, 2019a) images (Appendix D.1) with (symbols) locations of the study sites, (c) “model world” (MW) surface geometry with surface orientation and material properties ( $\Sigma$ ), (d) impervious

and grass surfaces (white) and vegetation canopy elements (VCEs, light green) seen by the LWIR cameras within the observation network (Table 3-1). Camera locations (numbers) shown as pink dots (white text) with approximate azimuthal facing (pink arrow). Dark colours are surfaces not seen by cameras. MW surface geometry rendered using Blender (Blender, 2018) for: (e) camera C2 perspective and (f) oblique orthogonal view of scene. Coordinates for (a – d) are Coordinate Reference System WGS84 UTM grid zone 31N for study area extent of 420 m x 420 m. .... 50

Figure 3-3. Digital camera images of: (a) cameras C5 and C6 taken at WCT site on 25<sup>th</sup> October 2017 looking southwest, with C6 enclosure shown open for maintenance, (b) southeast view from IMU site taken next to C4 on 21<sup>st</sup> July, (c) C1 enclosure taken at IMU site on 12<sup>th</sup> July looking east with WCT (C5, C6) site in background, and (d) northeast view from IMU site taken next to C2 and C3 on 30<sup>th</sup> May, with a portion of the roof at CUB site sampled by C7 (Appendix G) annotated. .... 51

Figure 3-4. (a) Undistorted brightness temperature images ( $T_b^{cam}$ ) from Optris PI longwave infrared (LWIR) cameras at 11:30 on 27<sup>th</sup> August 2017 and (b) surface orientation and material property ( $\Sigma$ ) projected onto the image plane (IP) of each “model world” (MW) camera classified for each image pixel using the perspective projection (Chapter 2) of a similarly classified DSM (Appendix D.2). 53

Figure 3-5. Atmospheric correction evaluation using the C2 and C7 cameras (Table 3-1, Figure 3-2, Figure 3-3) and meteorological variables (Section 3.4.2) observed at BCT and IMU sites (Figure 3-2): (a, red) uncorrected ( $T_b^{cam}$ ) minus corrected ( $T_b^{surf}$ ) surface brightness temperature for 155 m “far” path length from C2, (a, blue) uncorrected “far” minus reference ~15 m “near” path length from C7 and (a, black) corrected “far” minus “near”, (b)  $T_b^{cam}(C2)$ , (c) air temperature ( $T_a$ ) and absolute humidity ( $\rho_v$ ) and (d) incoming shortwave ( $E_{sw}^{sky}$ ) and longwave ( $E_{LW}^{sky}$ ) radiation, and timing of rainfall (blue)..... 57

Figure 3-6. Comparison of surface brightness temperature corrected for atmospheric effects of a flat felt roof sampled with path length ~155 m [ $T_b^{surf}(C2)$ ] and surface brightness temperature of the same surface sampled with path length ~15 m [ $T_b^{surf}(C7)$ ] with negligible atmospheric effects. .... 58

Figure 3-7. Atmospheric correction of longwave infrared (LWIR) camera observations for six timesteps on 24<sup>th</sup> September 2017, using pixels within  $\pm 10$  m of five path lengths ( $z^{path}$ ) with (white cells) meteorological input variables (coloured cells) median[IQR] values of: (a) difference between uncorrected camera brightness temperature ( $T_b^{cam}$ ) and corrected surface brightness temperature ( $T_b^{surf}$ ), (b) surface-camera path contribution of the at-sensor band integrated atmosphere radiance ( $L^{atm}$ ), and (c) surface-camera path contribution of band integrated atmospheric transmissivity ( $\Gamma^{atm}$ ). See list of symbols and acronyms for all definitions and Appendix I for other days..... 59

Figure 3-8. Per-pixel atmospheric correction of all longwave infrared (LWIR) camera observations at 5 min resolution on 24<sup>th</sup> September 2017, with density of pixels (coloured shading; grey < 1000 pixels) against surface-camera path length ( $z^{path}$ ) and (a) difference between uncorrected camera brightness temperature ( $T_b^{cam}$ ) and corrected surface brightness temperature ( $T_b^{surf}$ ), (b) surface-camera path contribution of the at-sensor band integrated atmosphere radiance ( $L^{atm}$ ), and (c) surface-camera path contribution of band integrated atmospheric transmissivity ( $\Gamma^{atm}$ ). .... 60

Figure 3-9. Atmospheric correction variables for each camera (Table 3-1) at 12:00 (24<sup>th</sup> September 2017): (a) Surface – sensor path length ( $z^{path}$ , m), (b) band integrated longwave emission from the atmosphere [ $L^{atm}(x, y) = 7\mu m 14\mu m d\lambda \cdot R_\lambda(x, y) \cdot L_\lambda^{atm}(x, y)$ ] with  $d\lambda = 0.2$  and  $R_\lambda(x, y)$  the sensor spectral response function, (c) band average atmospheric transmissivity. DART calculated  $\Gamma_\lambda^{atm}(x, y)$  and  $L_\lambda^{atm}(x, y)$ , and (d) final difference between uncorrected ( $T_b^{cam}$ ) and corrected ( $T_b^{surf}$ ) brightness temperature observations. C3 shows more foreground roof than in Figure 3-4 (pixels excluded from all other results) from an altered view angle between the observation dates. .... 61

Figure 3-10. Observed and modelled data for 27<sup>th</sup> August 2017 stratified by surface orientation and material type ( $\Sigma$ ) (colours) with (a) median per-pixel surface brightness temperatures [ $T_b^{surf}(x, y)$ ]. For spatial pattern of emissivity correction (11:30, dashed lined) see Figure 3-11. (b) BCT observations of air temperature, relative humidity, Kipp & Zonen CNR1 net radiometer broadband incoming shortwave ( $E_{sw}^{sky}$ ) and longwave ( $E_{LW}^{sky}$ ) radiation. (c) Broadband LWIR irradiance ( $E_{LW}$ ) onto surfaces within the camera field of view, with  $E_{LW}^{sky}$  for comparison. (d) Difference between

emissivity (0.93) corrected surface temperature [ $T_s(\epsilon_{0.93})$ ] for non-vegetative surfaces and surface brightness temperature. Boxplots: based on pixels from all camera images (5 min resolution, for 2 h: 07:00 – 08:55 i.e. 08:00 is between 07:00 and 09:00 vertical lines) with 5<sup>th</sup> and 95<sup>th</sup> percentiles (whiskers), interquartile range (box), and median (horizontal line).  $E_{LW}^{sky}$  boxplot uses 15 min resolution observations and min and max values (whiskers). ..... 63

Figure 3-11. Observed and modelled results (27<sup>th</sup> August 2017 at 11:30) of (a) longwave irradiance ( $E_{LW}$ ) from broadband hemispherical radiometer (sky component) and 3D distribution of surface brightness temperatures from the network of longwave infrared cameras (canopy component) prescribed to DART to simulate the emission, irradiance and multiple scattering processes of LWIR radiation for correction of surface brightness temperature ( $T_b^{surf}$ ) to emissivity (0.93) corrected surface temperature [ $T_s(\epsilon_{0.93})$ ], (b)  $T_s - T_b^{surf}$  difference. .... 65

Figure 3-12. Per-pixel emissivity corrected surface temperature  $T_s$  differences (median = black lines, inter-quartile range = shaded) from LWIR camera observations (27<sup>th</sup> August 2017, 60 min resolution) using different spectral library (Kotthaus *et al.*, 2014) broadband emissivity values: mean ( $\epsilon_{0.93}$ ), minimum ( $\epsilon_{0.89}$ , orange) and maximum ( $\epsilon_{0.97}$ , aqua) for non-vegetative surfaces (walls E, N, S, W; ground, roof) simulated using DART. .... 66

Figure 3-13. Difference in surface temperature  $T_s$  (60 min resolution, 27<sup>th</sup> August 2017) derived from LWIR camera observations based on emissivity ( $\epsilon$ ) corrections with a heterogeneous ( $T_b^{3D}$ ) and isothermal ( $T_b^{iso}$ ) assumption, respectively, using a range of  $\epsilon$  values (non-vegetative surfaces) according to dark impervious materials in the Kotthaus *et al.* (2014) spectral library. As observations are not areally weighted, the lower and upper extent of the distributions can still represent large fractions of the surface seen by the LWIR cameras. .... 68

Figure 4-1. Plan view of study area with: (a) height of all surfaces above sea level (asl) with building footprints (black lines, from Evans *et al.*, 2011), (b) orthorectified RGB image from a mosaic of Google Earth (Google, 2019a) images with locations (symbols) of the study sites, (c) a render of the “model world” (MW) digital surface model (DSM) and vegetation canopy element (VCE) geometry with DSM (white) and VCEs (green) seen by the cameras located (pink dots) around the observation sites with different view directions (pink arrows) and unique camera identification (white) numbers (Table 4-1 gives details), (d) Digital camera image looking southeast and next to camera number 4 (C4) on 25<sup>th</sup> Oct 2017. (a – c) use Coordinate Reference System WGS84 UTM grid zone 31N. ... 77

Figure 4-2. Surface representation and interaction in the “model world” (MW) that is used to interpret the “real world” (RW) urban area and observations, with radiative processes and triangle-voxel intersection managed by the DART model. The pinhole camera can also be below the bottom of atmosphere (BOA) layer. See list of symbols and acronyms for definitions. .... 80

Figure 4-3. Digital surface model (DSM) and vegetation canopy elements (VCE) for the study area created from Google Earth (Google, 2019a) imagery (Appendix D) with (colours) orientation and material surface properties ( $\Sigma$ ), rendered in Blender (Blender, 2018) for off-nadir view directions facing: (a) north, (b) east, (c) south, (d) west and (e) northeast with focus on the study sites and surface geometry, rendered without  $\Sigma$ . The VCE product covers slightly larger area than the DSM. .... 81

Figure 4-4. Surface geometry of the “model world” (MW) with bi-directional reflectance factor (BRF) (bins) from direct incoming solar radiation simulated using DART for 27<sup>th</sup> August 2017 11:00 and stored as a 3D array of voxels. See Figure 4-1b for (pink symbols) observation sites. .... 82

Figure 4-5. (a) Optris PI longwave infrared (LWIR) camera observations for 27<sup>th</sup> August 2017 12:00 UTC and (b – d) simulated surface properties projected onto the image plane (IP) of “model world” (MW) cameras that simulate the perspective of (a). Surface properties are: (b) orientation and material ( $\Sigma$ ), (c) shortwave bidirectional reflectance factor (BRF) assuming Lambertian reflecting surfaces, and (d) time surfaces have spent in shade ( $t_{shd}$ , white → blue) or sun (white → red). The cameras (Table 4-2) are indicated to the left of each image. .... 85

Figure 4-6. All C3 camera (Table 4-2) roof-viewing pixels shaded from  $t = 0$  and  $t = 90$  (min) (10:00 and 11:30 on 27<sup>th</sup> August 2017): (a) all samples (grey lines) and one (random, black) cooling event with the background surface temperature (blue) line (b) an exponential fit (red, Eqn. 4.4) to one (black line from a) to one cooling event. .... 87

Figure 4-7. Variability of surface characteristics in central London (49 areas of 420 m x 420 m) oriented to grid north (WGS84 UTM grid zone 31N) around the study area (red) and MODIS M\*D11A1 pixel (orange) with (upper) maps and (lower) histograms with  $n^{\text{th}}$  percentiles ( $P_n$ ) of (dashed lines)  $P_{25} \rightarrow P_{75}$ , (solid line)  $P_{50}$  for the study area. (a) Land cover (4 m) central London with (white dashed box) extent of maps in b – 1 and (red) the study area (Figure 4-1). Surface characteristics: (b) plan area fraction of tall vegetation ( $> 2$  m) (c) plan area fraction of grass (d) plan area fraction of buildings (i.e. plan area index), (e – h) building height, (i – l) sky view factor (Dozier and Frew, 2002) calculated in R (R Core Team, 2017) with the “horizon” package (Doninck, 2018), and (g, l) standard deviation of the respective parameter. .... 91

Figure 4-8. Area of surface ( $\text{m}^2$ ) across ( $A_{\text{TOTAL}}$ ) the total three-dimensional study area and ( $A_{\text{CAM}}$ ) seen by the LWIR cameras (Table 4-2) for (colours) different surface and orientation properties. 92

Figure 4-9. Frequency of pixels by surface orientations within the instantaneous field of view of each camera (excluding VCE but including “mixed” and “masked” pixels) for (a) azimuth facing (zenith angle  $< 135^\circ$ ), and (b) zenith angles of pixels. Azimuth angle of  $0^\circ$  ( $180^\circ$ ) is north (south) for WGS84 UTM grid zone 31N. Pixels with a zenith angle of  $90^\circ$  ( $180^\circ$ ) face vertically (horizontally). .... 94

Figure 4-10. Variability of LWIR camera derived surface temperature ( $T_s$ ) for 27<sup>th</sup> August with observations classified as (a) all classes (white) (except VCE and “masked” and “mixed” (grey) pixels, (b) roofs, (c) walls, and (d) ground. Boxplot are from all camera images (5 min samples) by group (colour) during 1 h (e.g. first hour is 00:00  $\rightarrow$  00:55 for Time (HH) “01” between vertical lines) with interquartile range (box), median (horizontal line) and 5 and 95 percentiles (whiskers) of pixel values. .... 96

Figure 4-11. Observed daytime surface temperature ( $T_s$ ) for 27<sup>th</sup> August for (top) pixels viewing surfaces with bidirectional reflectance factor (BRF, Schaepman-Strub *et al.*, 2006) equivalent to solar irradiance for a flat surface ( $\text{BRF} \approx 1$ ) and (bottom) BRF for any given daytime sun angle and binned values of BRF ( $\text{BRF}$ , bin width 0.25) across all observed sun-surface geometries (shown as difference to  $\text{BRF} \approx 1$  i.e. top). BRF calculated using DART assuming Lambertian surfaces. .... 97

Figure 4-12. Surface temperature ( $T_s$ ) cooling rates observed (x axis) and estimated (using Eqn. 4.4) for each pixel with colours indicating number of pixels ( $n_{\text{pixel}}$ ) with (row 1) fitted time constant  $\tau$  per pixel [ $\tau(x, y, \Sigma)$ ] and (row 2) modelled time constant as median  $\tau(x, y, t, \Sigma)$  per surface type [ $\tau(\Sigma)$ ] for (column 1) ground (grass and impervious), (column 2) roof (light and dark) and (column 3) walls (N, E, S, W). Statistical metrics: coefficient of determination ( $r^2$ ), mean absolute error (MAE).. 100

Figure 4-13. Surface-leaving radiance across the study area as brightness temperatures ( $T_b$ ) simulated using observationally derived and three-dimensional (3D) surface temperature and the DART model for 27<sup>th</sup> August at (left) 10:00 and (right) 14:00 for (top) nadir and (middle – bottom) off-nadir zenith ( $\phi$ ) angles and (triangles) IMU and CUB sites (Figure 4-1b). Images projected onto the bottom of atmosphere horizontal plane (Figure 4-2) with (grey labels) surface  $\rightarrow$  sky directions, with  $\theta = 0^\circ$  grid north and e.g.  $\theta = 90^\circ$  grid east (WGS84 UTM grid zone 31N) and  $\phi = 0^\circ$  ( $\phi = 90^\circ$ ) perpendicular (horizontal) to the surface. Rotating images view angle by ( $\theta, \phi$ ) gives orthographic projections. 102

Figure 4-14. Polar plots with difference in surface temperature [ $T_s(\theta, \phi, \Omega)$ ] from nadir temperature [ $(T_s(\theta, \phi = 0, \Omega) - T_s(\theta, \phi, \Omega))$ ] for upward directions with zenith angle ( $\phi$ )  $\leq 50^\circ$  simulated using observationally derived, three-dimensional (3D)  $T_s$  across the study area (Figure 4-1). DART is used to simulate surface-leaving radiance for (black crosses) discrete directions. Directions and (yellow dot) the sun position are oriented with a surface  $\rightarrow$  sky perspective, with  $\theta = 0^\circ$  grid north,  $\theta = 90^\circ$  grid east, etc (WGS84 UTM grid zone 31N) and  $\phi = 0^\circ$  ( $\phi = 90^\circ$ ) perpendicular (horizontal) to the surface. Grey lines have (radial)  $\Delta\phi = 10^\circ$  (straight)  $\Delta\theta = 30^\circ$ . The maximum absolute difference  $\Delta$  and nadir temperatures are given at each timestep. .... 104

Figure 4-15. Temperatures for 27<sup>th</sup> August 2017 with: (grey line) complete surface temperature ( $T_c$ ) from median ( $P_{25}$  and  $P_{75}$ , shading) of intra-class observations and extrapolated as a three-dimensional (3D)  $T_s$  and then areally weighted across the complete surface of the study area, ( $T_s^{EO}(\theta, \phi, \Omega)$ , black) directional surface temperature simulated using 3D  $T_s$  (median of intra-class observations) and the DART simulation (triangles, centre point in Figure 4-14 polar plots) for  $T_s^{EO}$  at (upward triangles) nadir view and (vertical lines) minimum and maximum range for  $0^\circ \rightarrow 50^\circ$  off-nadir view directions, (black dots) MODIS collection 6 LST with (dashed lines) error from quality assurance data flags and (blue line) air temperature ( $T_a$ ) from nearby weather station. .... 107

Figure 4-16. Temporal and angular variation (on 27<sup>th</sup> August 2017 06:00 to 14:00) in the fractional contribution of different surface types (colours) to upwelling radiance, with median (dots) 5<sup>th</sup> – 95<sup>th</sup> percentile (shading) of all azimuth angle variations for the given zenith angle ( $\phi$ ). .... 108

## List of Tables

Table 2-1. Field of view of undistorted pinhole camera equivalent LWIR cameras used in the study. See text for methods. See Figure 2-2 for camera locations.....	19
Table 3-1. Siting properties of the ground-based longwave infrared (LWIR) cameras installed on high-rise residential towers (IMU, WCT) and London City University Building roof (CUB) within the study area. Study area, sites and position of instrumentation shown in Figure 3-2 and Figure 3-3. Further camera meta data shown in Appendix B. See list of symbols and acronyms for all other definitions.....	52
Table 3-2. General model parameters set for the Discrete Anisotropic Radiative Transfer (DART) model atmospheric and emissivity correction routines.....	54
Table 4-1. Measurement and corrections used to determine surface temperature ( $T_s$ ) from LWIR cameras.....	78
Table 4-2. Siting properties of the ground-based longwave infrared (LWIR) cameras installed on two high-rise residential towers (IMU, WCT) within the study area (Figure 4-1). .....	78
Table 4-3. Surface properties of orientation and material ( $\Sigma$ ), bidirectional reflectance factor (BRF) and shadow history ( $t_{shd}$ ) assigned to each surface element (Figure 4-2) of the “model world” (MW) at $\Delta X = \Delta Y = \Delta Z = 1$ m spatial and 5 min temporal resolution. A surface element has three surface properties: $i(\Sigma, BRF, t_{shd})$ .....	80
Table 4-4. Surface temperature sub-classes used to determine exponential cooling (Eqn. 4.4). See text and list of symbols and acronyms for definitions. ....	86
Table 4-5. Study area (Figure 4-1) land cover fractions in the MW (from raster data) and variability of morphometric parameters indicated by percentiles ( $P$ ). .....	90
Table 4-6. MODIS collection M*D11A1 land surface temperature and emissivity for the grid cell intersecting the study area. Products obtained using MODIS <sub>Stp</sub> package (Busetto and Ranghetti, 2016). .....	105



# Chapter 1 Introduction

## 1.1 Motivation

Already more than half the global population live in cities and this is expected to increase to 68 % by 2050 (United Nations, 2018) along with increasingly urbanised areas. The structure, material and land cover of urban areas affect the local and regional climate (Oke, 1987; Roth, 2000) caused by changes to the surface energy balance (SEB) with implications for human comfort (Thorsson, Lindqvist and Lindqvist, 2004) and health (Barata *et al.*, 2011). The most frequently studied climatological effect of urbanisation is the urban heat island of cities relative to more open rural surroundings which results from the urban-induced SEB changes (Oke, 1982).

Assuming zero net horizontal advection of energy, the SEB for a three-dimensional (3D) urban volume can be written (Oke *et al.*, 2017):

$$Q^* + Q_F = Q_H + Q_E + \Delta Q_S \quad [\text{W m}^{-2}] \quad \text{Eqn. 1.1}$$

with  $Q^*$  the net all-wave radiation,  $Q_F$  the anthropogenic heat flux,  $Q_H$  and  $Q_E$  the turbulent fluxes of sensible and latent heat and  $\Delta Q_S$  the net uptake or release of stored energy. The  $Q_F$  term is associated with human activity in cities, with energy released by transport, buildings (e.g. industry, heating, air conditioning) and people's metabolism (Chrysoulakis *et al.*, 2018; Gabey, Grimmond and Capel-Timms, 2019). Often rural areas have more vegetation cover whereas cities have a large area of impervious materials such as concrete, asphalt, metal and glass. As a result,  $Q_E$  (or evaporation) is reduced, causing enhanced  $Q_H$ , air temperatures, boundary layer depth (Kotthaus and Grimmond, 2018), and dispersion of pollutants (Nadeau *et al.*, 2009). The convoluted nature of the surfaces cast shadows and enhance radiative trapping, altering  $Q^*$ . The large vertical extent of the surface, along with the low albedo and high heat capacity of materials enhances the  $\Delta Q_S$  energy flux into the urban surface during the day which provides a source of heat that is released slowly at night (Meyn and Oke, 2009).

Observations are fundamental to an improved understanding of urban SEB components (Grimmond, 2006). They are critical for evaluating and improving urban land surface schemes that are used in meso- and global-scale models with increasing resolution (Grimmond *et al.*, 2010). Accurate representation of urban processes in models is critical for forecasting high impact weather and future climates (i.e. hours to decades). Results inform a wide range of integrated urban climate services (Baklanov *et al.*, 2018), including urban planning (Rosenzweig *et al.*, 2018).

There are many methods to observe urban climate processes. Ground-based sensors can measure variables such as air temperature and humidity. Historically, such observations were critical to the foundations of urban climate study (Howard, 1833).  $Q_H$  and  $Q_E$  can be measured using eddy covariance (Kotthaus and Grimmond, 2014) or scintillometry sensors (Ward, 2017), providing

valuable insights into the relation between surface characteristics and the exchanges of energy (Crawford *et al.*, 2017). The storage term is challenging to directly observe (Offerle, Grimmond and Fortuniak, 2005). It can be determined as the residual of Eqn. 1.1 if all other terms are estimated.  $Q^*$  consists of incoming ( $\downarrow$ ) and outgoing ( $\uparrow$ ) shortwave ( $E_{SW}$ ) and longwave ( $E_{LW}$ ) irradiances:

$$Q^* = (E_{SW} \downarrow - E_{SW} \uparrow) + (E_{LW} \downarrow - E_{LW} \uparrow). \quad \text{Eqn. 1.2}$$

Warmer urban profiles can increase  $E_{LW} \downarrow$  (Oke and Fuggle, 1972; Suckling, 1981) whereas polluted air will decrease  $E_{SW} \downarrow$  (Jacovides, Steven and Asimakopoulos, 2000). The albedo (ratio of  $E_{SW} \uparrow$  to  $E_{SW} \downarrow$ ) is dependent on materials and the 3D canopy structure. Urban heat island mitigation strategies have involved modifying surface properties of roofs (Costanzo, Evola and Marletta, 2016) and pavements (Santamouris, 2013).  $E_{LW} \uparrow$  varies with the kinetic temperature of the urban surface ( $T_s$ , K) and the surface emissivity.

Components of  $Q^*$  can be measured with instruments sensitive to ultraviolet  $\rightarrow$  visible  $\rightarrow$  near infrared and midwave  $\rightarrow$  longwave infrared (LWIR) regions of the electromagnetic spectrum, respectively. LWIR sensors can remotely (i.e. non-contact) determine  $T_s$  using Planck's radiation law. Across entire cities, earth observation (EO) satellites can resolve  $T_s$  ( $T_s^{\text{EO}}$ ) at local-scales ( $O(1 \text{ km})$ ).  $T_s^{\text{EO}}$  provides information on the surface urban heat island (e.g. Roth, Oke and Emery, 1989; Kandel, Melesse and Whitman, 2016), changes of land use (e.g. Dousset and Gourmelon, 2003; Weng and Lu, 2008) and SEB components of  $Q_H$  (e.g. Voogt and Grimmond, 2000; Xu, Wooster and Grimmond, 2008; Crawford *et al.*, 2018) and  $\Delta Q_s$  (e.g. Kato and Yamaguchi, 2007; Chrysoulakis *et al.*, 2018). As  $T_s$  appears in the equations of three SEB fluxes (i.e.  $Q^*$ ,  $Q_H$ ,  $\Delta Q_s$ ), it is frequently determined in urban land surface models, meaning  $T_s^{\text{EO}}$  is a valuable measurement for both model evaluation and data assimilation (e.g. Ghent *et al.*, 2010; Li and Bou-Zeid, 2014).

With large demand for quality  $T_s$  observations of cities, urban surfaces have received increasing attention by EO. While the atmosphere is often accounted for, there is no operational procedure for view angle corrections. The effect is often ignored (e.g. Peng *et al.*, 2018), assumed to average out across multiple observations (Peng *et al.*, 2012) or oblique view angles are rejected (e.g. Chrysoulakis *et al.*, 2018). Simple correction procedures are required to determine effects of anisotropy based on view angle and solar position and more research is required to inform such simplified relations. At the micro-scale ( $O(1 - 100 \text{ m})$ ) the urban area has a complex 3D "surface" canopy that can be challenging to define (Norman and Becker, 1995; Voogt and Oke, 2003). The urban morphology (i.e. form) created by the buildings, streets, vegetation, etc., has an uneven exposure to the sky, with differential solar irradiance and radiative cooling. The variability of materials and their thermal properties adds another layer of complexity resulting in a  $T_s$  that is highly variable over short distances (Hénon *et al.*, 2012). Combined, these characteristics cause directional variability or "effective thermal anisotropy" (Krayenhoff and Voogt, 2016) of longwave radiation leaving the surface towards the sky. This proves challenging when monitoring the urban surface

using remote sensing (RS) instruments that inherently have a directional and limited view of the complete surface (Voogt and Oke, 2003). For example, a satellite with a near-perpendicular angle (nadir) is biased to viewing the surface-leaving radiation towards this direction (Roth, Oke and Emery, 1989). In urban areas this is mainly from the roofs, ground (Hu and Wendel, 2019) and the top of vegetation (Dyce and Voogt, 2018). As the sensor view angle changes, so does the relative contribution of surface-leaving radiation from different surface components. Repeated measurements of the same area from different orbits and view angles can therefore account for different parts of the surface which confounds any time series analysis (Hu *et al.*, 2016). With greater spatial and angular resolution, airborne observations (e.g. using helicopters) have estimated the magnitude of effective thermal anisotropy to be greater than 10 K (Lagouarde *et al.*, 2004, 2010). This uncertainty is an order of magnitude greater than for many land surface temperature products over more homogeneous (e.g. grassland, desert) surfaces (Duan *et al.*, 2019). However, studies of urban thermal anisotropy are so far limited to very short time periods with few repeat observations.

Although ground-based sensing may only cover small spatial extents, high spatial and temporal resolutions permit investigation of the micro-scale processes that contribute to uncertainties in  $T_s^{\text{EO}}$ .  $T_s$  from ground-based platforms can use *in-situ* or RS observation techniques. *In-situ* probes are affixed to the surface (e.g. Offerle *et al.*, 2007) whereas RS instruments can measure spatially resolved (e.g. thermal cameras) or integrated (e.g. pyrgeometer radiometers) surface-leaving radiation across larger areas. Unlike satellite-based RS with narrow and downward view angles, ground-based RS can concurrently sample the horizontal and vertical components of the urban surface. For pyrgeometers, the view angle can be large (near-hemispherical) with source areas typically assumed to represent  $E_{\text{LW}}\uparrow$  at the local scale (Christen and Vogt, 2004). A LWIR camera has a narrower field of view (FOV) capable of resolving facet or sub-building scale surface components from the thermal imagery (thermography). A single ground-based LWIR camera has a relatively narrow FOV allowing the temporal variability of urban  $T_s$  to be explored for impervious (e.g. Christen, Meier and Scherer, 2012) and pervious (e.g. Meier and Scherer, 2012) urban surfaces, non-destructive assessment of building envelope energy losses (Balaras and Argiriou, 2002), and street-level pedestrian comfort (Lee *et al.*, 2018). Concurrent and multi-directional sampling permits local-scale urban areas to be observed and linked to the satellite scale. Sampling of this type includes transect data from vehicle mounted radiometers combined with airborne imagery (Voogt and Oke, 1997) and a single LWIR camera rotated on a mast (Adderley, Christen and Voogt, 2015). These have been used to assess urban surface temperature variability at local-scales and to determine view angle uncertainties of  $T_s^{\text{EO}}$ .

The scale-dependence of urban surface temperature variations poses challenges to ground-truthing urban EO. If ground-based observations are confined to small (micro-scale) areas it can be difficult to make the link to the local-scale  $T_s^{\text{EO}}$ . It is therefore critical to understand the representation of

ground-based observations across a satellite pixel observation (Duan *et al.*, 2019). This can be achieved by determining which surface facets (e.g. walls, roofs, ground) are “seen” (i.e. sampled) by the ground-based sensor and the satellite, respectively. As thermography provides spatially resolved images, it is easier to determine visually which surfaces are sampled compared to a pyrgometry’s spatially integrated  $E_{LW\uparrow}$ . Typically, prior ground-based thermography studies have used manual inspection of images to determine the different facets viewed by pixels (e.g. Christen, Meier and Scherer, 2012), or relate contrasting distributions of observed values to different surface characteristics (Voogt and Oke, 1997). These methods can be time consuming, qualitative, and have not been shown to reliably classify many complex micro-scale features associated with e.g. surface materials and vegetation. Having confidence in the surface observed otherwise involves sampling it from close proximity (e.g. Rotach *et al.*, 2005; Pigeon *et al.*, 2008) which reduces the spatial extent further. Although ground-based RS is promising, there is not an established method to reliably quantify what surfaces are “seen” at the micro-scale or to assess how representative these are of the local-scale view angle effects on  $T_s^{EO}$ . Previously idealised descriptions of “real-world” geometry (e.g. TUF-3D, Krayenhoff and Voogt, 2007; GUTA, Wang, Chen and Zhan, 2018) have been used for effective thermal anisotropy modelling involving combinations of observed and modelled  $T_s$ . Furthermore, the evaluation of these models with real-world observations is very limited. Challenges have even been reported over relatively homogeneous terrain for ground-truthing EO land surface temperature, particularly during daytime with more micro-scale variation in temperatures across small changes in topography (e.g. Wan, 2014; Duan *et al.*, 2019).

To adequately study thermal conditions of the urban surface, the kinetic surface temperature  $T_s$  needs to be retrieved from the at-sensor radiance observed by the ground-based LWIR RS. Radiation detected by LWIR cameras includes both the emitted and reflected components from the target surface plus the contribution from the atmosphere between the surface and the instrument. By removing the atmosphere effect (atmospheric correction) and reflected radiation from non-BB surfaces (referred to here as the emissivity correction, following Adderley, Christen and Voogt, 2015), only the radiation emitted by the surface remains and is related to  $T_s$  by Planck’s radiation law. Atmospheric corrections of LWIR RS (Sobrino, Coll and Caselles, 1991) have considered urban areas from airborne (Sugawara and Takamura, 2006) and ground-based (Meier *et al.*, 2011) platforms but these do not include an emissivity correction. At the micro-scale, the complex nature of LW radiation exchanges within the urban canopy (Arnfield, 1982; Harman, Best and Belcher, 2004) combined with the spatial variability of surface emissivity (Kotthaus *et al.*, 2014) determines the emissivity correction effect. A detailed emissivity correction therefore requires the process of radiation exchanges within the canopy to be resolved at a similar resolution as the observations. As this has not yet been achieved in previous studies using ground-based thermography, the observed surfaces have been assumed to be perfect emitters of radiation (black bodies) which leads to an

approximate uncertainty of 0.5 – 5.0 K (Meier *et al.*, 2011) with generally unknown spatial and temporal variability.

## 1.2 Objectives

This research uses ground-based thermography in urban areas to explore the effective thermal anisotropy that gives rise to uncertainties in LWIR RS from EO satellites. As ground-based thermography in urban climate study is still rare, significant contributions of this work arise from advancing the observational technique.

The objectives of this PhD are:

- 1) To develop an automated and objective method to classify what is “seen” by each pixel in ground-based thermography observations in urban settings with any 3D geometry.
- 2) To develop a methodology to correct both atmospheric and emissivity effects on observations at the spatial resolutions of ground-based thermal cameras (< 1 m) to enable realistic surface temperature retrieval. Improvements compared to prior studies in terms of reduced uncertainty are to be quantified through sensitivity analyses of the corrections.
- 3) To analyse thermal camera observations, that are capable of viewing surfaces at very high resolution across small areas, at scales representative of satellite pixels. To develop techniques to facilitate crossing of scales from micro (thermal camera) to local (satellite pixel), that use both classified observations (objective 1) (to retain high spatial and temporal resolution information) and multiple cameras (to increase the observational source area).
- 4) To assess the effective thermal anisotropy in urban areas using the upscaled observations and provide a new high level of detail benchmark.

## 1.3 Thesis structure

A framework to classify ground-based observations in urban areas is developed and tested using a hardware scale (1.5 m tall buildings) urban model (Chapter 2<sup>a</sup>). This simplified urban surface removes many “real world” complexities. As the model has repeating geometry and material cf. “real” cities, two cameras positioned above the urban canopy can view all surface orientations. The simple scale model geometry allows for an uncertainty analysis of satellite thermal remote sensing to be performed via simulations of effective thermal anisotropy, here using broadband flux approximations and the Discrete Anisotropic Radiative Transfer (DART) model (Gastellu-Etchegorry, Grau and Lauret, 2012).

---

<sup>a</sup> Morrison W, Kotthaus S, Grimmond CSB, Inagaki A, Yin T, Gastellu-Etchegorry J-P, Kanda M, Merchant CJ (2018). A novel method to obtain three-dimensional urban surface temperature from ground-based thermography. *Remote Sensing of Environment*, 215(May), 268–283.

Building on Chapter 2, a novel correction framework is presented (Chapter 3<sup>b</sup>) to retrieve surface temperature from ground-based LWIR RS observations using DART with finite spectral bands (cf. broadband in Chapter 2) to account for spectral variation in atmospheric optical properties. The correction is applied to a network of seven LWIR cameras installed in a “real world” (cf. scale model, Chapter 2) central London (UK) site, which enable an evaluation of the correction framework and a detailed uncertainty analysis to be performed. The latter for the first time, uses a detailed multi-path and multi-camera atmospheric and emissivity correction. Chapter 3 demonstrates cameras mounted among buildings (cf. above buildings, Chapter 2). Prior to this, this had not been tested or demonstrated using DART. Additionally, new camera housing techniques (cf. Chapter 2) are developed to further improve calibration stability.

Chapter 4<sup>c</sup> uses the classified and corrected central London observations from Chapter 3, with further developments in the parameterisation of observed brightness temperatures such as shadow histories first identified in Chapter 2, to explore the micro-scale surface temperature variability in unprecedented detail. These observations are extrapolated across a local-scale description of the surface geometry. Based on the upscaled surface temperature time series, effective thermal anisotropy is simulated using DART to evaluate the uncertainties in  $T_s^{EO}$ .

Chapter 5 summarises the novel contributions, scientific conclusions and recommendations for future work.

---

<sup>b</sup> Morrison W, Yin T, Lauret N, Guilleux J, Kotthaus S, Gastellu-Etchegorry J-P, Norford L, Grimmond CSB (2019). Atmospheric and emissivity correction for ground-based thermography using 3D radiative transfer modelling. *Remote Sensing of Environment, In Press*.

<sup>c</sup> Morrison W, Kotthaus S, Grimmond CSB (2019). Urban satellite view uncertainty assessed with ground-based thermography. *In preparation*.

## Chapter 2 A novel method to obtain three-dimensional urban surface temperature from ground-based thermography

### Abstract

Urban geometry and materials combine to create complex spatial, temporal and directional patterns of longwave infrared (LWIR) radiation. Effective anisotropy (or directional variability) of thermal radiance causes remote sensing (RS) derived urban surface temperatures to vary with RS view angles. Here a new and novel method to resolve effective thermal anisotropy processes from LWIR camera observations is demonstrated at the Comprehensive Outdoor Scale MOdel (COSMO) test site. Pixel-level differences of brightness temperatures reach 18.4 K within one hour of a 24-h study period with median hourly changes up to 5.5 K (day, 07:00 – 08:00) and 1.8 K (night, 20:00 – 21:00). To understand this variability, the orientation and shadowing of surfaces is explored using the Discrete Anisotropic Radiative Transfer (DART) model and Blender three-dimensional (3D) rendering software. Observed pixels and the entire canopy surface are classified in terms of surface orientation and illumination. To assess the variability of exitant longwave radiation ( $M_{LW}$ ) from the 3D COSMO surface ( $M_{LW}^{3D}$ ), the observations are prescribed based on class. The parameterisation is tested by simulating thermal images using a camera view model to determine camera perspectives of  $M_{LW}^{3D}$  fluxes. The mean brightness temperature differences per image (simulated and observed) are within 0.65 K throughout a 24-h period. Pixel-level comparisons are possible with the high spatial resolution of  $M_{LW}^{3D}$  and DART camera view simulations. At this spatial scale ( $< 0.10$  m), shadow hysteresis, surface sky view factor and building edge effects are not completely resolved by  $M_{LW}^{3D}$ . By simulating apparent brightness temperatures from multiple view directions, effective thermal anisotropy of  $M_{LW}^{3D}$  is shown to be up to 6.18 K across directions up to  $60^\circ$  off-nadir. The developed methods can be extended to resolve some of the identified sources of sub-facet variability in realistic urban settings. The extension of DART to the interpretation of ground-based RS is shown to be promising for the development of ground-based thermography campaigns.

### 2.1 Introduction

Urban surface temperature ( $T_s$ ) plays a significant role in the urban surface energy balance as it is central to longwave radiation (LW), turbulent sensible heat and storage heat fluxes. Remote sensing (RS) methods have the potential to provide  $T_s$  at large spatial scales for understanding exchanges of sensible heat (e.g. Voogt and Grimmond, 2000; Xu, Wooster and Grimmond, 2008), the thermal comfort of city dwellers (Thorsson, Lindqvist and Lindqvist, 2004), and the urban surface heat island phenomenon (Roth, Oke and Emery, 1989; Kato and Yamaguchi, 2005; Huang *et al.*, 2016). Two major challenges of urban thermal RS observations relate to the complex three-dimensional (3D) urban surface form and material heterogeneity, both causing large spatiotemporal variability of  $T_s$ .

(Voogt and Oke, 2003). Spatiotemporal variability of  $T_s$  is influenced by the relative orientation of surfaces to the sun during the day, and sky at night (Voogt and Oke, 2003). The diversity of thermal and radiative properties of surface materials causes additional variability (Voogt, 2008). What results is a directional variability, or an effective thermal anisotropy (Krayenhoff and Voogt, 2016), of broadband longwave radiation ( $M_{LW}$ ,  $\text{W m}^{-2}$ ) from the urban canopy surface. The anisotropic behaviour of urban canopies is defined as “effective” to differentiate from thermal anisotropy exhibited by individual surface components (Voogt and Oke, 1998a). Effective thermal anisotropy clearly affects satellite measured radiance, which is indicative of satellite derived longwave radiation flux ( $M_{LW}^{RS}$ ). As a result, the apparent  $T_s$  can vary depending on view direction.  $M_{LW}^{RS}$  can be described by:

$$M_{LW}^{RS} = \sum_i^n M_{LW,i} f_i \quad \text{Eqn. 2.1}$$

where  $M_{LW,i}$  is the exitant broadband longwave radiation from a given canopy surface element  $i$  that comprises fraction  $f$  of the instrument field of view (FOV). Out of the total number of canopy surface elements  $n$ ,  $M_{LW,i}$  may differ to other canopy surface elements due to the highly variable radiative properties associated with its surface temperature, emissivity ( $\epsilon$ ) and contributions from longwave reflections.  $M_{LW}^{RS}$  is also sensitive to urban canopy geometry and to the specific view angle within each image swath. These factors combine to form a view angle specific  $f_i$  which translates to a view angle specific value of  $M_{LW}^{RS}$ . For example,  $f_i$  for roof and tree tops is generally overemphasised within  $M_{LW}^{RS}$  for urban areas (Roth, Oke and Emery, 1989). Corrections of effective thermal anisotropy are critical when retrieving high-quality  $T_s$  products for urban environments at large spatial scales from satellite-derived  $M_{LW}^{RS}$ .

The impact of effective thermal anisotropy on  $M_{LW}^{RS}$  has been studied using various observation and modelling techniques. Observations from airborne platforms (Voogt and Oke, 1998a; Lagouarde *et al.*, 2004; Sugawara and Takamura, 2006) allow highly variable view angles at scales representative of satellite pixel resolutions (100 m – 1 km). However, cost and air traffic restrictions usually limit these to short-term research campaigns. As obtaining different view angles requires multiple flyovers (i.e. difficult to conduct simultaneously), sequential flyovers with one aircraft may temporally confound results. Thus, the directional variability of  $M_{LW}^{RS}$  at a micrometeorological timeframe (sub-hourly) for energy exchange processes (Christen, Meier and Scherer, 2012) may be unresolved. Ground-based RS observations are interesting in that  $M_{LW}$  can be resolved at high temporal resolutions (e.g. Christen, Meier and Scherer, 2012) while resolving the individual facet (e.g. roof, wall) and sub-facet scale classes of  $M_{LW,i}$  that constitute the structural and radiative characteristics of the urban canopy. For ground-based RS, a challenge is to sample enough facets representative of the complete 3D urban canopy at any one time. A single ground-based measurement provides a

highly directional sample at high spatial resolution. Several ground-based sensors are required to sample facets of all orientations, unless a single ground-based sensor is operated on a rotating (Adderley, Christen and Voogt, 2015) or mobile (e.g. Voogt and Oke, 1997) platform. As satellite-based RS has a bias directional view of canopy surfaces, it is important to be able to understand the nature of this bias.

Modelling can further help resolve the contribution of sub-facet scale variability of  $M_{LW}$  on effective thermal anisotropy. The nature of effective thermal anisotropy and  $M_{LW}^{RS}$  can be understood under constrained conditions at high temporal and spatial resolutions. Therefore, modelling is considered key to progress (Voogt and Oke, 2003; Voogt, 2008). Approaches typically involve a parameterisation of surface geometry, an energy balance model prescription of surface temperature and sensor view modelling of  $M_{LW}^{RS}$  to resolve  $M_{LW,i}$  and  $f_i$  (Eqn. 2.1) for a given surface-sensor viewing geometry. Surface temperatures can be prescribed from 2D (Kusaka *et al.*, 2001; Sugawara and Takamura, 2006; Voogt, 2008), 2.5D infinite street canyon (Lagouarde *et al.*, 2010) and 3D (Soux, Voogt and Oke, 2004; Krayenhoff and Voogt, 2007, 2016) energy balance simulations to estimate  $M_{LW,i}$  (Eqn. 2.1) at facet (e.g. surface orientation, roof, ground) or sub-facet (e.g. insolation, material) scales.

Few sensor-view modelling studies exist that prescribe  $M_{LW,i}$  from observations at facet and sub-facet scale, despite this complementing and constraining energy balance simulations. Classifying surfaces within ground-based RS source areas poses challenges because of the potentially diverse viewing geometries, complex 3D urban canopy structure, and low resolution of longwave infrared (LWIR) camera imagery. Previously, the spatial frequency distributions of  $M_{LW}$  determined by ground-based LWIR imagery were used to infer canopy surface classes (e.g. Voogt and Grimmond, 2000) or surface classes were manually identified and extracted (e.g. Voogt, 2008). Manual approaches based on broadband thermal imagery are limited when the temperature contrast between facets is low (because of orientation or material properties). Information at multiple wavelengths can be valuable to improve classification. With maturing of sensor view modelling, it is becoming a powerful tool to objectively classify surface elements captured by RS imagery. Previous studies interpreting ground-based LWIR imagery have determined per-pixel path lengths for atmospheric correction of observations from on top of a high-rise building in Berlin (Meier *et al.*, 2011). The SUM surface-sensor-sun model (Soux, Voogt and Oke, 2004) enables sensor view modelling of  $M_{LW,i}$  prescribed from observations, limited to urban surface geometry resolved as regular arrays of rectangular shaped buildings. Studies using SUM have prescribed temperatures intermittently (e.g. Voogt, 2008) from ground-based and airborne platforms observations. 3D rendering and editing software and a 3D vector model have facilitated the classification of ground-based LWIR imagery in a suburban area in Vancouver (Adderley, Christen and Voogt, 2015). As the camera views a subset of the total surface, classified temperature “textures” are gap-filled to enable extrapolation across the

3D vector model as a complete brightness temperature product for sensor view modelling of hemispherical radiometer measurements using a single LWIR camera on a rotating mast.

In the current study, a flexible observational and modelling approach is developed to prescribe  $M_{LW}$  from broadband longwave radiation fluxes derived from static ground-based LWIR camera observations. A 3D distribution of exitant broadband longwave radiation ( $M_{LW}^{3D}$ ,  $W m^{-2}$ ) is constructed from observations. The approach involves a novel method to classify each camera image. Pixels within each image are associated with a specific surface class prior to observations being extrapolated to all urban canopy surface elements in 3D. A “model world” (MW) is used to process and interpret observations which enables “real world” (RW) surfaces to be related to each camera image by camera view modelling. It provides a robust and quantitative method to interpret observations. Surface class  $i$  is determined in 3D space [i.e.  $i(X, Y, Z)$ ] and is then accurately mapped to the 2D  $(x, y)$  coordinates of a camera image plane (IP) [i.e.  $i(x, y)$ ].

Unique here is the camera view modelling used to interpret observations, as surface classes are determined at high temporal and spatial resolution using surface geometry and shortwave (SW) radiative characteristics for each time step. This is designed to ensure all canopy surfaces are always accounted for when allocating observed temperatures across areas of the surface not directly observed (hereafter “extrapolated” over the 3D urban surface). A potential constraint of highly directional ground-based measurements is turned to an advantage by positioning two cameras at opposing view angles. This permits a combined observational source area representative of all surface classes that constitute the 3D urban surface. Extrapolated observations are compared with original camera imagery. This is done by projecting the extrapolated observations through the perspective of simulated cameras, with modelled perspectives matching those seen by the original camera imagery. This approach is unique in that the modelled perspectives are shown to reproduce the perspectives of the original imagery at pixel level and to a high degree of accuracy. Extrapolated observations have potential as a tool for further sensor view modelling to explore the impact of effective thermal anisotropy on directionally variable  $M_{LW}^{RS}$  products for any given surface-sensor configuration.

The observational setup (Section 2.2.1, Section 2.2.2), the classification methods (Section 2.2.3, Section 2.2.4) and extrapolation (Section 2.3) of observations are introduced. Results (Section 2.4) include evaluation of proposed methods and demonstrate their benefits for application in urban RS. It is concluded (Section 2.5) that the detailed modelling approach provides a valuable tool for future studies in real city settings.

## 2.2 Methods

LWIR camera observations are interpreted and estimated as  $M_{LW}^{3D}$  in a MW environment (Figure 2-1). Two LWIR cameras (Section 2.2.2) were installed on ground-based platforms above an urban test



weathering effects (Figure 2-2c) are likely to affect the radiative characteristics, but the apparently random patterns are too small a spatial scale to be accounted for in this study.

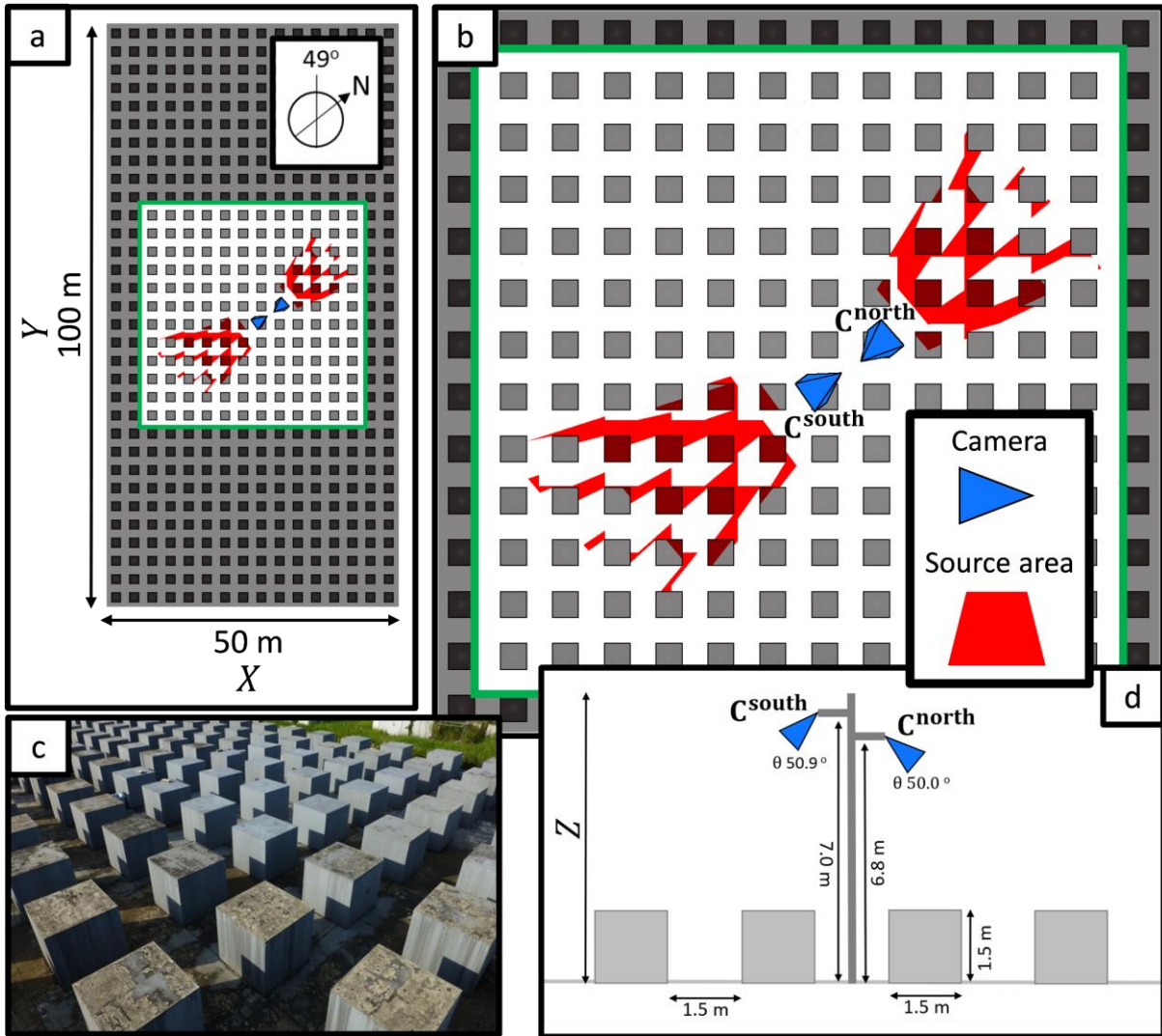


Figure 2-2. COSMO test site and longwave infrared (LWIR) camera observational setup: (a) test site domain (plan view) with focus area (green box); (b) focus area with LWIR camera ( $C^{south}$ ,  $C^{north}$ ) locations and approximate orientations (blue) and source areas (red) for camera field of view; (c) north-west facing oblique visible image taken near the  $C^{north}$  camera location and perspective (d) vertical cross section of building array (grey squares) showing instrument tower and camera geometry.

## 2.2.2 Real world instrumentation

Two Optris PI-160 LWIR cameras (Optris GmbH, 2018) were installed on an aluminium lattice tower at 6.8 m and 7.0 m above ground level (Figure 2-2d) at opposing azimuth angles with oblique views of ground, roof and all cardinal facing surfaces. Cameras are defined as ( $C^{north}$ ,  $C^{south}$ ) based on their azimuthal view angle (Figure 2-2b, camera meta data in Appendix B). The horizontal and vertical pixel resolution of the cameras ranges from approximately 0.030 m x 0.043 m to 0.079 m x 0.111 m. The small, lightweight industrial grade cameras use uncooled microbolometer technology,

with 25  $\mu\text{m}$  x 25  $\mu\text{m}$  bolometer elements arranged as a 160 x 120 focal plane array (FPA). With multiple cameras, multiple view angles and building facets (e.g. Figure 2-2b) can be sampled simultaneously in a static setup (cf., rotating one sensor, Adderley *et al.*, 2015; or vehicle traverses, Voogt and Oke, 1997). The instrument outputs digital number values for each microbolometer pixel. These values relate to at-sensor broadband 7 – 13  $\mu\text{m}$  radiance and are radiometrically calibrated by the manufacturer to brightness temperatures [ $T_b^{cam}(x, y)$ ] using black-body reference measurements. The per-pixel broadband longwave radiation flux [ $M_{LW}^{cam}(x, y)$ ] is related to  $T_b^{cam}(x, y)$  by Stefan-Boltzmann law:

$$M_{LW}^{cam}(x, y) = \sigma [T_b^{cam}(x, y)]^4 \quad \text{Eqn. 2.2}$$

with  $\sigma$  the Stefan-Boltzmann constant ( $5.67 \times 10^{-8} \text{ W m}^{-2} \text{ K}^{-4}$ ). The temperature resolution is 0.1 K and the manufacturer's specified accuracy is 2 °C at ambient temperatures  $23 \pm 5$  °C (Optris GmbH, 2018). Although images can be captured at 120 Hz, for this study images recorded every 60 s are used to reduce data overhead but capture temporal variability of  $M_{LW}^{cam}$  caused by transient surface shadowing. The manufacturer specified camera horizontal and vertical FOV is 41° x 31°. Observations were taken between 2014/06/16 and 2014/09/26. In this paper, the focus is on a predominantly clear-sky day (2014/08/02). Both cameras were connected to the same field laptop for data acquisition via USB using the Optris PI connect software.

Multiple internal processing steps need to be considered to achieve radiometrically calibrated measurements from LWIR cameras. Uncooled microbolometer calibration and measurement processes are reviewed by Budzier and Gerlach (2015). Here the quality control steps undertaken are presented.

After a camera is sited, the FPA requires a “warm up” period to allow the current induced self-heating of the sensor elements to stabilise (Vollmer and Möllmann, 2017) prior to measurements. As laboratory testing found up to 2 h warm up period is required depending on target and camera body temperature conditions (cf. manufacturer's recommended 10 mins), data prior to this are excluded. To correct for changes in the contribution of interior radiance incident on the FPA due to any change in the camera body temperature resulting from ambient air temperature variability, a shutter inside the camera with assumed black-body characteristics and of known temperature obscures the sensor before every measurement so that its emission is sampled. The cameras are fitted with aluminum covers (enclosure: 945 mm x 45 mm x 62 mm). These are designed to prevent lens exposure to precipitation and any rapid, directional heating of the sensor body due to direct sun exposure.

### 2.2.3 Model world site

To interpret  $M_{LW}^{cam}$  for subsequent parameterisation and evaluation of  $M_{LW}^{3D}$ , a MW is used. It has realistic surface-sensor geometry and processes contributing to variability in  $M_{LW}$  exitant across the RW (COSMO) site. For a given RW point at 3D coordinates ( $X, Y, Z$ ), the RW radiative processes

that determine  $M_{LW,i}$  from all canopy surfaces [ $M_{LW}^{3D}(X, Y, Z)$ ] are approximated by assuming Lambertian facets, first order scattering, isotropic sky thermal radiance, invariance of emissivity across a broadband of thermal wavelengths and invariance of emissivity with facet kinematic temperature, *viz*:

$$\begin{aligned}
M_{LW}^{3D}(X, Y, Z) = & \sigma [T_b^{3D}]^4(X, Y, Z) = [1 - \varepsilon(X, Y, Z)] \cdot \Psi^{sky}(X, Y, Z) \cdot E_{LW}^\downarrow \\
& + [1 - \varepsilon(X, Y, Z)] \cdot \Psi^{can}(X, Y, Z) \cdot M_{LW}^{can} \\
& + \varepsilon(X, Y, Z) \cdot \sigma [T_b^{3D}]^4(X, Y, Z)
\end{aligned} \tag{Eqn. 2.3}$$

where  $\Psi^{sky}$  and  $\Psi^{can}$  are sky and canopy view factors (Johnson and Watson, 1984) that influence the radiant flux incident on RW point  $(X, Y, Z)$ ;  $E_{LW}^\downarrow$  is broadband longwave irradiance from sky;  $M_{LW}^{can}$  is broadband longwave radiation emitted from surrounding canopy elements;  $T_b^{3D}(X, Y, Z)$  and  $T_s^{3D}(X, Y, Z)$  are the surface brightness and kinematic temperatures for the given point; and  $\varepsilon(X, Y, Z)$  the broadband surface emissivity for the given point. The COSMO test site (Figure 2-2) and observational period chosen enables Eqn. 2.3 to be simplified: 1) the homogeneous surface material allows  $\varepsilon(X, Y, Z)$  to be treated as constant and isotropic, and 2) the high material emissivity reduces any variability in reflection contributions from  $E_{LW}^\downarrow$  and  $M_{LW}^{can}$ .  $E_{LW}^\downarrow$  is assumed isotropic in Eqn. 2.3 as a simplification due to clear-sky conditions for the study date. The remaining factors determining COSMO  $M_{LW}^{3D}(X, Y, Z)$  in Eqn. 2.3 ( $T_s^{3D}$ ,  $\Psi^{sky}$  and  $\Psi^{can}$ ) are highly variable across the site. To parameterise the variability of  $M_{LW}^{3D}$  in this paper, facets are classified by their orientation using Blender (Blender Foundation, 2016) and sub-facet insolation status (or shadow patterns) using the DART 3D radiative transfer model (Gastellu-Etchegorry, Grau and Lauret, 2012) (Figure 2-1). Combining Blender (version 2.78) and DART (version 5.6.6, build v935) allows the 3D distribution of specific surfaces classes [ $i(X, Y, Z)$ ] to be determined across the site.  $i(X, Y, Z)$  is prescribed with similarly classified observations to formulate  $M_{LW}^{3D}$ .

Two spatial reference systems defined in the MW by DART and Blender facilitate the creation of  $i(X, Y, Z)$ :

- 1) In both DART and Blender, the RW surface geometry is represented by a vector-based digital surface model (DSM) of triangles in a 3D mesh. This resolves surface geometry at a high level of detail (Gastellu-Etchegorry, 2008) which is not limited to simple geometry (e.g. Soux *et al.*, 2004). A triangle face ( $S$ ) is the planar area between three vertices each with  $X, Y, Z$  coordinates (Figure 2-3) with attribute  $S_i$  a determinable facet-scale surface class.
- 2) In DART, the MW is discretised into voxels  $Vx$  of uniform size in a 3D raster format (see Figure 2-3;  $\Delta X, \Delta Y, \Delta Z$ ; Yin *et al.*, 2015). Surface voxels contain surface elements of the DSM  $Vx^S$  (Figure 2-3), whereas other voxels only contain atmosphere. Voxels enable radiative transfer processes to be calculated within DART at high (sub-facet scale;  $< S$ ) resolution. Surface voxels (Figure 2-3) are used to track radiation emitted and intercepted by

$S$  (Gastellu-Etchegorry, 2008), meaning MW geometry is resolved by the DSM during simulation. The prescribed surface temperature ( $Vx_{T_s}^S$ ) and sub-facet-scale surface class information [ $i(X, Y, Z)$ ] are stored by surface voxels. Therefore, a surface voxel that occupies an area  $\Delta X, \Delta Y, \Delta Z$  of the DSM stores surface class  $Vx_i^S(\Delta X, \Delta Y, \Delta Z)$  and temperature  $Vx_{T_s}^S(\Delta X, \Delta Y, \Delta Z)$  data. Simulated sources of emitted radiation can be from any combination of sun, upper atmosphere,  $Vx^S$  and atmosphere voxels. Here, sun angle and insolation are modelled by DART to determine  $Vx_i^S(\Delta X, \Delta Y, \Delta Z)$  for sunlit [ $Vx_{sunlit}^S(\Delta X, \Delta Y, \Delta Z)$ ] and shaded [ $Vx_{shaded}^S(\Delta X, \Delta Y, \Delta Z)$ ] elements of the MW surface at a spatial resolution of  $\Delta X, \Delta Y, \Delta Z = 0.04$  m which is representative of the RW observation spatial resolution (Section 2.2.2).

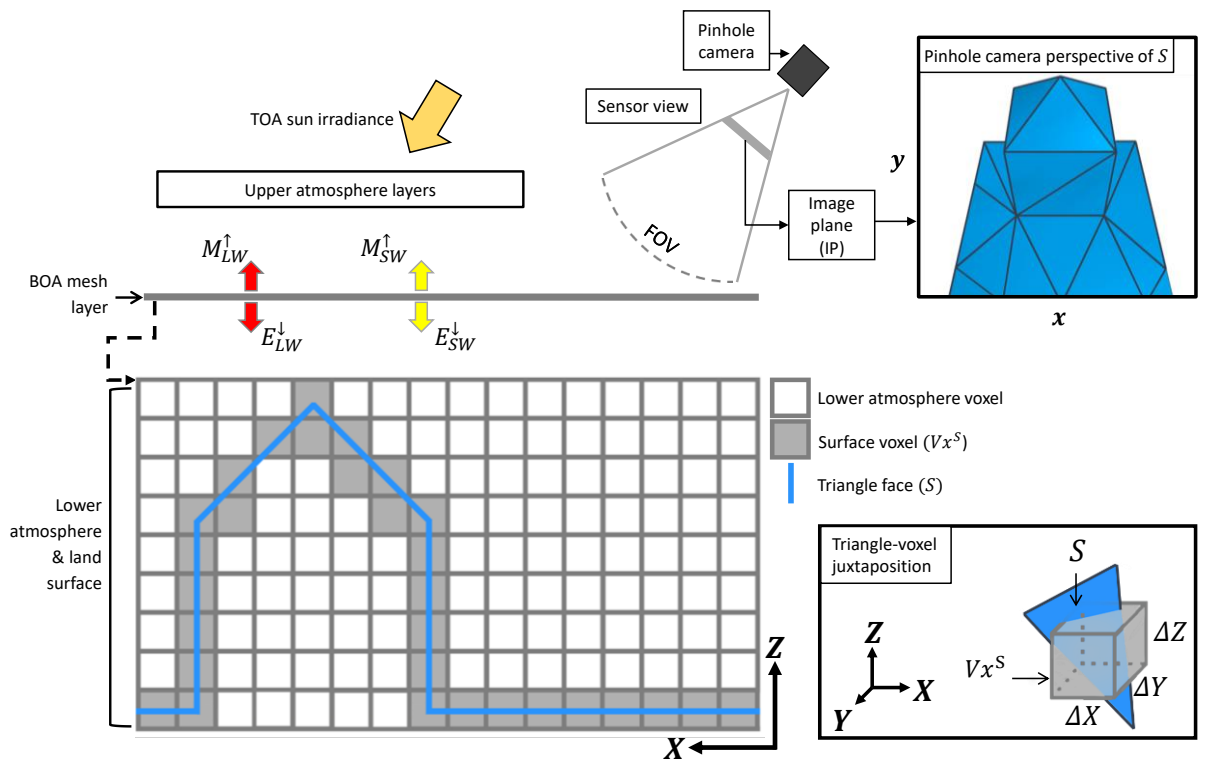


Figure 2-3. Surface representation and interaction in the “model world” (MW) is defined by triangle face ( $S$ ) and voxel ( $Vx$ ) elements, with camera view modelling to simulate camera image plane (IP). See table and text for symbol and acronym definitions and Figure 4-2 for further details.

DART can simulate radiative transfer processes in the visible to LWIR regions of the electromagnetic spectrum (Yin, Lauret and Gastellu-Etchegorry, 2015) in the atmosphere and any urban or natural landscape. Individual rays are tracked along discrete directions within angular cones (Yin *et al.*, 2013). Landscape, or “bottom of atmosphere” (BOA), illumination is due to direct and diffuse sun radiation ( $E_{SW}^{\downarrow}$ ) and  $E_{LW}^{\downarrow}$ . It is simulated as rays that flow from a horizontal BOA layer at the top of the landscape (Figure 2-3). The surface density of these illumination rays is  $1/D^2$ , with  $D$  the BOA

illumination grid resolution. To simulate RW camera images taken above the BOA layer (Figure 2-3), rays that reach the BOA mesh layer are projected onto a simulated camera IP (Yin, Lauret and Gastellu-Etchegorry, 2015). A comprehensive description of DART including further functionality beyond the scope of this paper is provided by Gastellu-Etchegorry *et al.* (2015). DART camera image simulation specifics are detailed in Yin *et al.* (2015).

### 2.2.3.1 Surface creation

The DSM was created using Blender, based on the known site geometry (Section 2.2.1) and stored as a DART compatible “\*.obj” wavefront data format. Here the metadata stored by this format for each triangle face includes facet orientation for the surface classification (Section 2.2.3.2). The DSM has the RW surface geometry (Figure 2-2) for the full site ( $X = 50$  m,  $Y = 100$  m,  $Z = 1.5$  m), discretised into surface voxels using the MW definition of DSM – voxel interaction (Figure 2-3) at a resolution of  $\Delta X = \Delta Y = \Delta Z = 0.04$  m. The  $X$  axis of the voxel array is aligned with the  $X$  axis of the DSM (Figure 2-2).

### 2.2.3.2 Surface classification

The spatial and temporal class characteristics (orientation, surface insolation state) allow a dynamic high spatial resolution 3D classification of the MW surface as  $i(X, Y, Z)$ .

DART stores local incident and intercepted radiation in two different ways. It stores the upward directional radiance per surface element of the landscape, for simulating RS measurements. Also, the landscape 3D radiative budget is stored: irradiance and exitance per voxel upper face; and the radiation that is intercepted, absorbed and emitted per voxel. Here, the DART simulated 3D radiative budget is used to determine the sunlit or shaded status of  $Vx_i^S(X, Y, Z)$  through time, where  $i = \text{sunlit}$  or  $i = \text{shaded}$ . The sunlit and shaded areas of the MW are resolved at the voxel size ( $\Delta X = \Delta Y = \Delta Z = 0.04$  m, Section 2.2.3.1). Direct downwelling SW radiation ( $E_{SW,dir}^\downarrow$ ) is simulated with solar angles calculated using NOAA solar calculator equations (NOAA, 2016). Here, DART tracks BOA rays (mesh cell size  $D = 0.02$  m) with radiant flux density  $E_{SW}(\Omega, \theta, \phi)$  ( $\text{W m}^{-2}$ ) along solid angle  $\Omega$  (sr) with direction  $(\theta, \phi)$  until incident on a DSM triangle. Hence, each triangle intercepted  $E_{SW}(\Omega, \theta, \phi)$  is stored for the voxel that occupies the 3D space of the triangle (Figure 2-3) which across the entire scene produces a 3D array of voxels with values of intercepted irradiance ( $\text{W m}^{-2}$ ). If a surface voxel has stored no direct solar irradiance (i.e. cloud, night or building obstruction) then the voxel is classified as shaded ( $Vx_{i=\text{shaded}}^S$ ), otherwise it is sunlit ( $Vx_{i=\text{sunlit}}^S$ ). If RW geometry were more complex, the classes could be split into discrete or binned values of irradiance intercepted by a MW surface.

The surface orientation attribute of each triangle face  $S$  (Section 2.2.3.1) is one of the four cardinal orientations relative to north (e.g.  $i = \text{east}$ ) or horizontal orientations (e.g.  $i = \text{roof}$ ). Blender is used

to determine the smallest angular difference between a triangle normal and the normal of each orientation. Once classified, the DSM is used to determine the orientation of sunlit or shaded voxels. Any sunlit or shaded surface voxel intersected by  $S_i$  is classified as a sunlit or shaded voxel with orientation class  $i$  [e.g.  $Vx_{i=roof,sunlit}^S(X, Y, Z)$ ].

#### 2.2.4 Model world instrumentation

MW “instrumentation” is used to classify each pixel of a RW camera observation by camera view modelling and to perform camera view modelling of  $M_{LW}^{3D}$  for a given RS view angle. Here, a MW “instrument” is defined as the simulation of a RW camera perspective using camera view modelling. The RW camera images are classified at pixel level as  $i(x, y)$  using basic pinhole cameras as the MW instruments. A basic pinhole camera has a rectilinear projection, meaning any straight lines in the MW domain are always projected as straight lines in the pinhole camera IP. A comprehensive description of this technique can be found in Hartley and Zisserman (2004). An overview of the steps taken to map a MW domain surface element with coordinates  $(X, Y, Z)$  onto an IP with pixel coordinates  $(x, y)$  is presented in Figure 2-4. Common discrepancies between a theoretical and RW camera are highlighted, with methods given for the calibration of the low-resolution RW LWIR cameras to perform as a pinhole camera (Section 2.2.4.1). Methods used to apply the MW camera with the classified DSM (Section 2.2.4.3) are given along with uncertainties associated with the alignment error between RW and MW camera perspectives (Section 2.2.4.2).

All cameras have *extrinsic* and *intrinsic* parameters that determine the  $(X, Y, Z) \rightarrow (x, y)$  coordinate transformation (Figure 2-4). Extrinsic parameters of rotation ( $R$ ) and translation ( $t$ ) describe the rigid transformation of a 3D coordinate frame to a 3D camera reference frame  $(X, Y, Z) \rightarrow (x_c, y_c, z_c)$  with new coordinate origin  $O_c$  (Heikkila and Silven, 2002; Hartley and Zisserman, 2004). RW cameras with physically small, wide-angle lenses exhibit radial distortion, meaning image points are displaced radially in the IP. This type of projection is not comparable to that of an ideal pinhole camera. Here, the camera intrinsics and lens distortion parameters are defined together as the camera internal parameters, which must be estimated (Section 2.2.4.1).

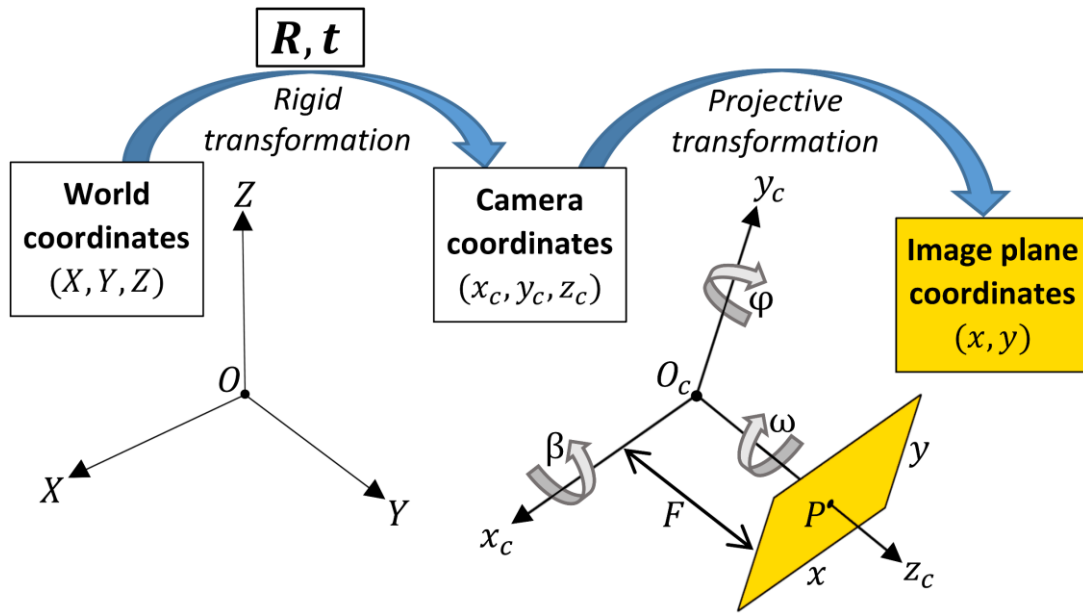


Figure 2-4. Coordinate and transformation definitions for “model world” elements.  $(X, Y, Z) \rightarrow (x_c, y_c, z_c)$  is the rigid transformation from the three-dimensional coordinate frame with origin  $O$ , to the three-dimensional camera coordinate frame with origin  $O_c$  using camera extrinsic parameters of rotation  $R$  and translation  $t$ .  $(x_c, y_c, z_c) \rightarrow (x, y)$  is the projective transformation from camera coordinate frame to two-dimensional camera image plane (IP) frame (yellow).  $R$  represents a series of Euler angles  $\beta$ ,  $\phi$  and  $\omega$  that define a sequence of rotations: first around the  $x_c$ -axis ( $\beta$ ), then around the  $y_c$ -axis ( $\phi'$ ) that has already been rotated by  $\beta$ , and finally around the  $z_c$ -axis ( $\omega''$ ) that has already been twice rotated firstly by  $\beta$  and then  $\phi'$  (Heikkila and Silven, 2002).  $t$  is a vector that describes the translation between the model world coordinate origin ( $O$ ) and camera coordinate origin ( $O_c$ ). Intrinsic parameters of focal length  $F$ , pixel scale factor (Eqn. 2.4) and principle point offset are used for the final projection of 3D points onto the 2D camera IP as  $(x_c, y_c, z_c) \rightarrow (x, y)$ . These parameters are determined by physical camera features including pixel size and the relative position of the IP to  $O_c$ . The point at which the principle axis ( $z_c$ ) intersects with the IP is the principle point  $P$  (Hartley and Zisserman, 2004). For a pinhole camera,  $P$  intersects at the centre of the IP. For real world cameras, the principle point offset describes the offset between  $P$  and the centre of the IP which may arise from imperfections in the lens-FPA assembly. This results in a misalignment of the lens with the FPA (Clarke, Wang and Fryer, 1998) and hence needs to be accounted for.

#### 2.2.4.1 Estimation of camera internal parameters

To formulate a MW camera, extrinsic and internal parameters must be known or estimated. Extrinsic parameters of RW camera location and orientation are determined by on-site measurements. Internal parameters are required to match the RW image projection to a MW pinhole camera. A method is presented to experimentally estimate the internal parameters of a RW LWIR camera for correction of raw images to a rectilinear pinhole projection. The method requires known parameters of physical

FPA size ( $d_{FPA}$ , mm) and image resolution ( $n_{px}$ , pixels) which are obtained from instrument specifications.

Camera internals are determined using a 0.5 m x 0.5 m polished steel plate ( $\epsilon \approx 0.02$ ) populated by squares of masking tape ( $\epsilon \approx 0.95$ ) to produce a planar calibration grid of 8 x 7 cells each 0.05 m x 0.05 m (Appendix A). This configuration allows a grid cell corner to be identified as  $(X_o, Y_o, Z_o)$  in camera  $(x, y)$  coordinates (Figure 2-4). When placed outside on a clear or totally overcast day, the grid pattern can be observed in the LWIR due to the emissivity contrast between steel and masking tape. Images are taken until the grid has been captured by all parts of the LWIR camera IP at different rotations ( $\sim 25$  images per camera). Captured images are processed with the Matlab *camera calibration toolbox* (Bouguet, 2008) to map each grid cell corner,  $(X_o, Y_o, Z_o)$  to  $(x, y)$  coordinates. Estimated camera extrinsic and internal parameters are used to transform the image using the Matlab toolbox. Grid corner points are again detected in this transformed image and compared to points projected onto the IP by the estimated extrinsic and internal parameters. This is an iterative process that stops when the error between detected and projected points is minimised in the least squares sense. The internal parameters applied to achieve this “best fit” between detected and projected points are assigned as the camera internal parameters enabling it to be treated as a pinhole camera.

The specified FOV (Section 2.2.2) decreases when images are transformed to pinhole projections (Table 2-1). The FOV is determined by obtaining the focal length ( $F$ ) from the calibrated pixel scaling factor ( $s$ ) and the known FPA size ( $d$ ) in the image  $x$  or  $y$  coordinate directions with known FPA resolution ( $n^{px}$ ) in the image  $x$  or  $y$  coordinate directions:

$$F = s(d_{FPA}/n^{px}) \quad \text{Eqn. 2.4}$$

which is related to the camera FOV (radians) in the image  $x$  or  $y$  coordinate direction by:

$$FOV = 2\arctan\left(\frac{d_{FPA}}{2F}\right) \quad \text{Eqn. 2.5}$$

The derived internal parameters are used to re-map each pixel from each RW image using the nearest neighbour technique.

Table 2-1. Field of view of undistorted pinhole camera equivalent LWIR cameras used in the study. See text for methods. See Figure 2-2 for camera locations.

Camera ID	Undistorted FOV	
	Horizontal (°)	Vertical (°)
<b>C<sup>north</sup></b>	41.4	31.6
<b>C<sup>south</sup></b>	40.5	30.9

#### 2.2.4.2 Reprojection error

Assuming internal parameters have been accurately accounted for (Section 2.2.4.1), any misalignment between RW and MW camera perspectives depends on the prescribed MW camera extrinsic parameters of  $(\beta, \phi, \omega)$  rotation ( $R$ ) and  $(X, Y, Z)$  translation ( $t$ ) shown in Figure 2-4. These

parameters can be determined from RW measurements. An uncertainty in these measurements translates as an error in the MW camera perspective. A misalignment error based on estimates of uncertainty associated with on-site measurement of camera extrinsic parameters is calculated in root mean square error (RMSE) terms. Firstly, the extrinsic parameters for camera  $C^{\text{south}}$  (Figure 2-2) measured on site are defined as “aligned” parameters. It is assumed that measurements of camera location (performed using a tape-measure) have an estimated measurement uncertainty of 0.1 m for each location axis.  $(\beta, \varphi)$  are estimated from azimuth and zenith angle measurements  $(\theta, \phi)$  taken using a compass and protractor, respectively. Cameras are installed with no intentional rotation around the camera axis  $(\omega)$ . Each rotation has an assumed uncertainty of  $1^\circ$ . To quantify the impact of this assumed  $R$  and  $t$  measurement uncertainty, all possible permutations of these rotations and translations are determined at resolution of  $\Delta^\circ = 0.5$  (e.g.  $[\beta - 1^\circ] \rightarrow [\beta + 1^\circ]$ ,  $\Delta^\circ = 0.5$ ) and  $\Delta\text{m} = 0.05$  (e.g.  $[X - 0.1 \text{ m}] \rightarrow [X + 0.1 \text{ m}]$ ,  $\Delta\text{m} = 0.05$ ). For each permutation, all roof vertices of the DSM  $(X, Y, Z)$  are updated with new MW coordinates  $(X', Y', Z')$  by rotating and translating each DSM roof vertex around the camera origin  $O_c$  (Figure 2-4) based on the permutation-specific  $(R, t)$  values. The Euclidean distance  $d$  between the original and updated vertices, where:

$$d = \sqrt{(X' - X)^2 + (Y' - Y)^2 + (Z' - Z)^2} \quad \text{Eqn. 2.6}$$

is used to quantify the misalignment RMSE. Only roof vertices are analysed as occluded surfaces cannot be tracked from the camera perspective. With this degree of uncertainty, the maximum RMSE between all roof vertices within the camera FOV is 0.43 m. A final adjustment of simulated  $(R, t)$  extrinsic parameters is needed as this error is significant. This is challenging given that  $(R, t)$  combine to give a high number of degrees of freedom. Adjustment is done using the experimentally derived  $(R, t)$  parameters applied to a Blender pinhole camera perspective of the DSM. A RW camera image corrected to pinhole camera projection (Section 2.2.4.1) is made semi-transparent and then draped over the Blender camera FOV. The camera is then moved interactively around the DSM allowing  $(R, t)$  to be manually adjusted as a supervised final alignment. A new alignment uncertainty when extrinsic parameters are manually adjusted is assumed  $< 0.1^\circ$  for each rotation and  $< 0.05 \text{ m}$  for each location parameter (RMSE  $< 0.06 \text{ m}$ ). This method yields good alignment results when comparing the projected geometry for RW (Figure 2-5a, e) and MW (e.g. Figure 2-5b, c) imagery, which is further evaluated using high resolution digital camera imagery (Figure 2-6).

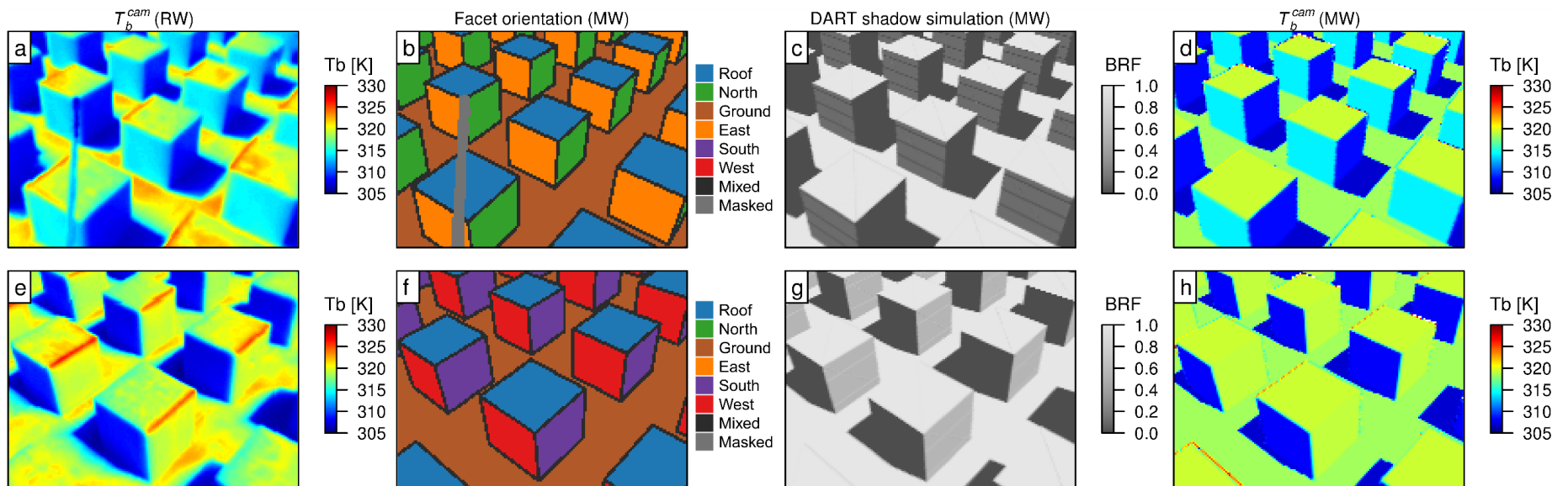


Figure 2-5. Observations, classification and extrapolation of results for Optris PI longwave infrared (LWIR) camera (a – d)  $C^{\text{south}}$  and (e – h)  $C^{\text{north}}$  at COSMO test site (Figure 2-2, 2<sup>nd</sup> August 2014 10:00 local standard time). (a, e) "Real world" (RW) brightness temperature ( $T_b$ ) images; (b, f) classification of per-pixel surface orientation using Blender "model world" (MW) camera view of the digital surface model (DSM) containing surface orientation information. Surface information is coded as per-class RGB textures projected onto a Blender camera for per-pixel identification of surface orientation. RGB values in the image not associated with an RGB texture class see more than one class and are classified as mixed pixels (black); (c, g) classification of per-pixel surface shadowing derived by DART shortwave scattering simulation and camera view model shown as shortwave bidirectional reflectance factor (BRF; Schaepman-Strub *et al.*, 2006), dark pixels (BRF = 0) indicate no first order scattering from surface to camera; (d, h) simulated  $T_b$  thermographs:  $T_b$  observations extrapolated to a MW three-dimensional distribution based on surface classes (shown in b, c, f, g) reprojected onto a MW camera image plane simulated in DART, simulating RW camera observations (a, e). The hollow cubes have more material around block edges, and increased heat storage, potentially explaining warm edges in (a, e).

### 2.2.4.3 Classification of camera images

The classified MW surface (Section 2.2.3.2) is projected onto a MW camera IP to facilitate RW image classification. MW cameras are created using Blender and DART to simulate the RW camera per-pixel perspective of orientation (e.g. Figure 2-5b) and shadowing (e.g. Figure 2-5c) attributes, respectively.

The 3D rendering capabilities of Blender are used to classify images by surface orientation. All triangle faces of the DSM within an orientation class  $i$  ( $S_i$ , Section 2.2.3.2) are assigned a colour with a specific RGB value. The DSM is then projected onto each MW camera IP to produce images with per-pixel RGB values related to each orientation class (Figure 2-5b, f) which enables per-pixel surface classification as  $i(x, y)$ . The instantaneous field of view (IFOV) of some pixels within these images contain more than one surface class. This effect translates as pixels without a RGB value associated with a single class. Pixels with this characteristic are classified as “mixed”. The radiometer boom within  $C^{\text{south}}$  observations (Figure 2-5a) is manually masked. Mixed and masked pixels are not included as part of any surface class.

Sunlit and shaded pixels for each RW image are classified using the 3D distribution of sunlit and shaded surfaces from the DART simulation of direct downwelling SW radiation (Section 2.2.3.2). DART camera view modelling enables the 3D distribution of sunlit and shaded surfaces to be projected onto the MW camera perspective (Figure 2-5c, g). First order scattering of  $E_{SW}(\Omega, \theta, \phi)$  from a surface is considered during the image classification, with DSM triangles being assigned as Lambertian reflectors in DART. Scattering from the surface occurs isotropically with exitance  $M_{SW}^{\uparrow}$  ( $\text{W m}^{-2}$ ):

$$M_{SW}^{\uparrow} = \int_{2\pi} E_{SW}(\Omega, \theta, \phi) \cdot \cos\theta \cdot d\Omega. \quad \text{Eqn. 2.7}$$

Due to first order scattering, any pixels of the DART MW camera with at-sensor radiance  $> 0 \text{ W m}^{-2} \text{ sr}^{-1}$  originates from a sunlit voxel ( $M_{SW}^{\uparrow} > 0 \text{ W m}^{-2}$ ) intersected by a sunlit portion of the DSM. The IFOV of pixel  $(x, y)$  with at-sensor radiance  $> 0 \text{ W m}^{-2} \text{ sr}^{-1}$  is therefore classified as observing a sunlit surface (e.g. Figure 2-5b). Isolated pixels (i.e. no adjacent pixels of the same class) are reclassified as “mixed” as it is assumed there is insufficient spatial representation of the surface class from one pixel. The DART modelling of shadow distributions is evaluated in the RW using a Panasonic DMC-TZ31 digital camera image taken during clear sky daytime conditions (Figure 2-6a). The digital camera is assumed to exhibit pinhole camera characteristics. Shadow distributions across the image are then classified using a DART MW camera using manufacturer derived internal camera parameters. The illuminated surface geometry and distribution of shadow patterns visible in the MW camera image (Figure 2-6b) agree with the digital camera image (Figure 2-6a).

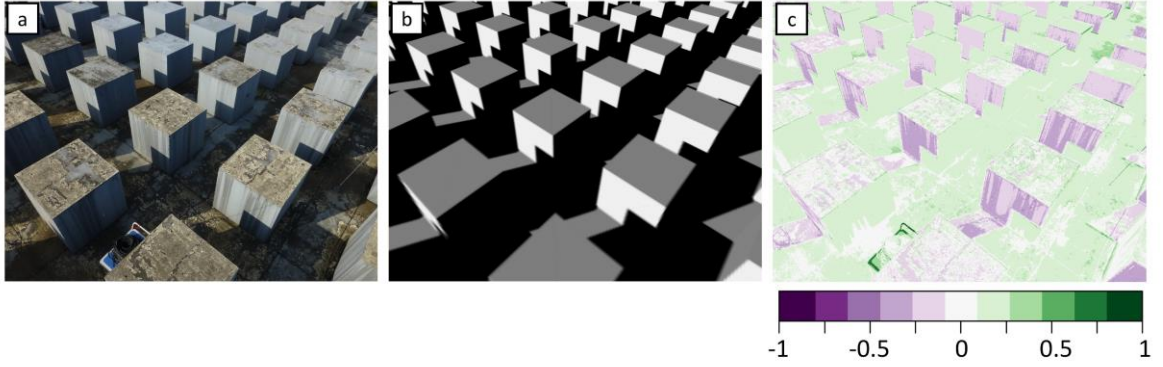


Figure 2-6. Images of COSMO test site taken at 15:25 local standard time on 26<sup>th</sup> September 2014 with approximate  $C^{\text{north}}$  perspective (Figure 2-2) from (a) a “real world” (RW) digital camera and (b) simulated by a “model world” (MW) camera in the shortwave using the Discrete Anisotropic Radiative Transfer (DART) model to compare the performance of DART when 1) simulating RW camera perspectives 2) resolving shadow patterns at high spatial resolution (0.04 m) across a canopy surface. Greyscale intensity (b) is used for qualitative indication of shaded (black) and sunlit (grey → white) surfaces. Comparison (c) shown as RW – MW greyscale intensity difference.

### 2.3 Longwave radiation flux extrapolated to 3D distribution

Data from classified images (Section 2.2.4.3) are used with the classified MW surface (Section 2.2.3.2) to produce  $M_{LW}^{3D}$  at high spatial resolution. Pixels classified as class  $i(x, y)$  within each MW camera image are associated with observations from the RW LWIR camera to obtain classified RW  $M_{LW}^{cam}(x, y)$  in the form  $M_{LW,i}^{cam}(x, y)$ . The mixed and masked pixels (Figure 2-5b, f) are not considered. All pixels for a given class from all cameras are aggregated to a mean value  $\tilde{M}_{LW,i}^{cam}$ . Voxels of class  $i$  are assigned  $M_{LW,i}^{cam}$  to resolve per-voxel  $M_{LW}$ , shown in Figure 2-7 as brightness temperatures. This product constitutes  $M_{LW}^{3D}$  for a given time step. A voxel may be intersected by two or more triangles with faces of different class, which can occur at the corner of a building (Figure 2-7). In this case, the mean of  $\tilde{M}_{LW,i}^{cam}$  for all classes involved is calculated for these voxels. This causes the unique brightness temperature values at intersecting facets with different orientation and temperature (Figure 2-7).

The view angle configuration of the RW cameras (Figure 2-2) and the nature of allocatable surface classes means the classes assigned in 3D space  $Vx_i^S(\Delta X, \Delta Y, \Delta Z)$  are always observed by a camera for any given time step. The spatial form of  $M_{LW}^{3D}$  is inherently linked to the DSM (Figure 2-3) meaning the methodology is applicable to complex geometry and limited only by the voxel resolution and DSM level of detail.

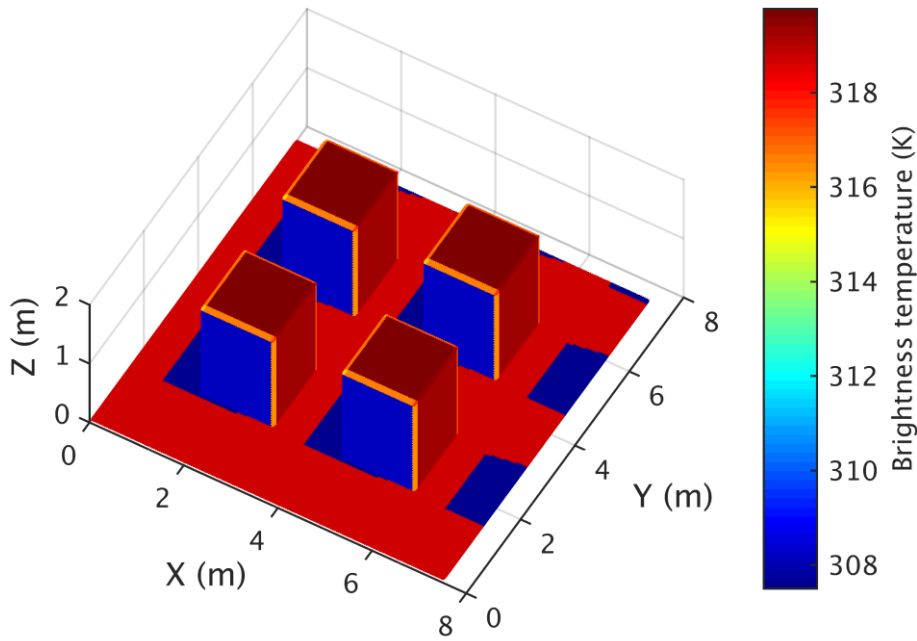


Figure 2-7. Per-voxel brightness temperature ( $V_{X_{Tb}}^S$ ) extrapolated from observations for one time-step (2<sup>nd</sup> August 2014 10:00 local time, (same as Figure 2-5) for an arbitrary 8 m x 8 m subset of the “model world” (MW) domain visualized as a three-dimensional point cloud, with each point at the centroid of a voxel.  $V_{X_{Tb}}^S(\Delta X, \Delta Y, \Delta Z)$  resolved at  $\Delta X = \Delta Y = \Delta Z = 0.04$  m spatial resolution.

## 2.4 Results and discussion

The methodology is applied using observations referenced at local time for 2<sup>nd</sup> August 2014 (day of year 214). This is a mostly cloud-free day following an extended dry period of cloudy and part-cloudy days. The short time period is chosen to ensure the high temporal resolution of observations is fully applied and resolved.

### 2.4.1 Image classification

The classification methodology enables quantitative identification of the surface types seen by each camera on a per-pixel level. Figure 2-8 summarises the fraction of pixels assigned to each class within each camera image constrained by the intrinsic viewing geometry of cameras and sun-surface geometry. Differences in the inter-camera pixel fractions assigned to each class can be explained by the location and orientation of each camera.  $C^{\text{south}}$  views north and east facing walls and  $C^{\text{north}}$  views south and west facing walls. Both cameras view roof and ground.  $C^{\text{north}}$  views the higher fraction of ground and roof surfaces (53.80%, 10327 pixels) due to the lower camera zenith angle (Figure 2-2). Camera  $C^{\text{south}}$  views a higher fraction of vertical surfaces (37.44%, 7190 pixels). Mixed pixels make up 29.12% ( $C^{\text{south}}$ ) and 20.11% ( $C^{\text{north}}$ ) of the images. Mixed pixels are identified during image classification of surface geometry (e.g. Figure 2-5b) and if any classified

pixels are isolated (Section 2.2.4.3).  $C^{\text{south}}$  imagery contains 528 (2.75%) masked radiometer boom pixels and more mixed pixels than  $C^{\text{north}}$ . This is explained by its higher zenith angle and therefore longer average path length. Surfaces further away from the camera are more likely to be mixed within each pixel IFOV.

When a vertical surface first becomes insolated, the incident radiation is low as the angle of incidence is near parallel with the surface. In the MW, this is associated with a low density of DART illumination rays (Section 2.2.3.2) incident on these surfaces which introduces erroneous patterns in surface insolation status. Until the density of rays is sufficient across the MW surface, some pixels may be isolated from other pixels of the same insolation class. This explains the observed temporal variability in mixed pixels that coincides with walls coming into, and out of, shade. It could be corrected by increasing the surface density of illumination rays in the DART SW simulations (Section 2.2.3.2) at the expense of computation time. With the given MW resolution, the effect occurs twice for both cameras around 10:00 and 13:00. Each period has a  $\sim 10$  min duration that increases mixed pixels across each image by up to 9% (Figure 2-8). Afternoon periods when all non-mixed pixels are intermittently classified as shaded are caused by short periods of overcast conditions based on direct incoming SW radiation (Figure 2-9a) measurements taken at the COSMO test site using a MS-56 Pyrheliometer (EKO Instruments).

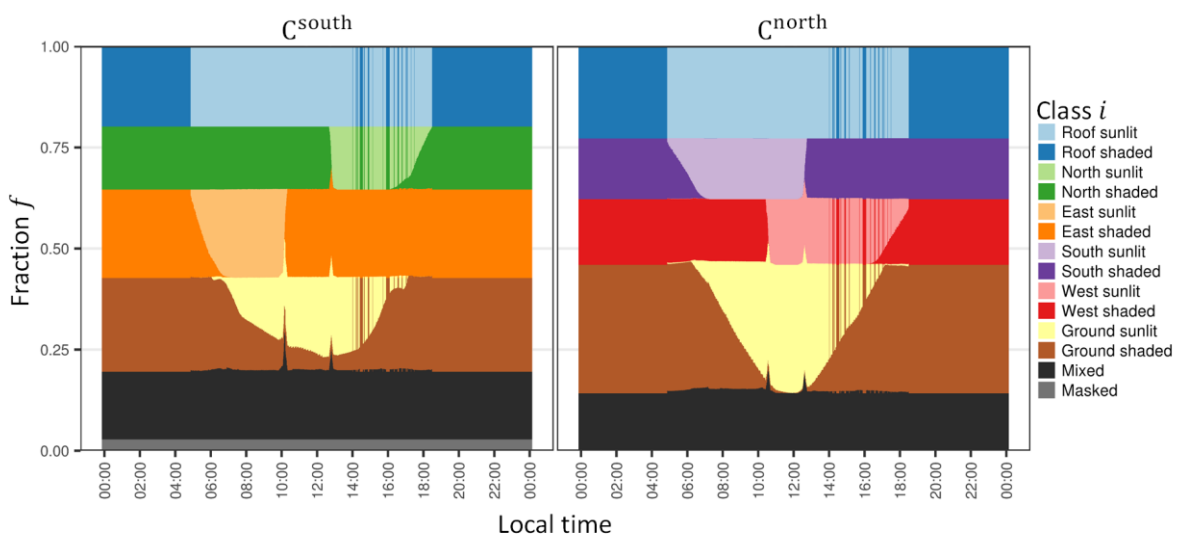


Figure 2-8. Fraction  $f$  of all pixels in a camera image assigned to surface class  $i$  for cameras  $C^{\text{south}}$  and  $C^{\text{north}}$  for day of year 214 at local standard time. Resolution of classified images is 1 min. Short periods of daytime shadow due to overcast periods determined from  $[ESW, dir \downarrow]$  (COSMO) observations (Figure 2-9a). Mixed pixels (Section 2.2.4.3) contain more than one surface class around building edges or are isolated pixels for oblique sun angles.

## 2.4.2 Inter-camera comparison

$M_{LW}^{cam}$  agreement between instruments using manufacturer derived calibration coefficients (Section 2.2.2) is evaluated using measurements taken during the study day. Given the camera fields of view did not overlap, contact thermocouples were installed to give reference measurements enabling comparison of the camera calibrations. Unfortunately, instrumentation issues resulted in complete data loss from the thermocouples. With the exception of variation in surface weathering effects (e.g. Figure 2-2c), roof facets have a highly uniform radiative environment across the whole COSMO test site and offer the best available comparison to evaluate camera agreement (Figure 2-9). Camera heights and zenith angles are similar (Section 2.2.1) with 19.86 % and 22.26 % of image pixels classified as roofs for  $C^{south}$  and  $C^{north}$ , respectively (Figure 2-8). Results show a systematic difference (slope 1.07, intercept -22.01 K) between observations of the roof pixels by the two cameras (Figure 2-9). The camera calibration sensitivity to camera body temperature in an outdoor setting is likely the primary contributor to the instrument uncertainty seen with the setup at COSMO (2 K). This translates into systematic differences in the observations and a hysteresis effect (Figure 2-9). Potentially rapid and uneven changes in temperature across each camera body cannot be fully accounted for by the camera calibration routine (Section 2.2.2). Other contributing factors, which cannot be easily quantified at this observational scale using the classification approach adopted, include differences in roof emissivity from surface weathering effects and anisotropy in surface emissivity (Nakayoshi, Kanda and de Dear, 2015). To reduce the impact of any systematic sensor disagreement on the extrapolated  $M_{LW}^{3D}$  product,  $C^{north}$  is corrected to  $C^{south}$  by linear regression using observations of the roof pixels from each camera (Figure 2-9). This approach is considered reasonable within the scope of the study as inter- and intra-facet variability is retained, and sensor specific biases are minimised.

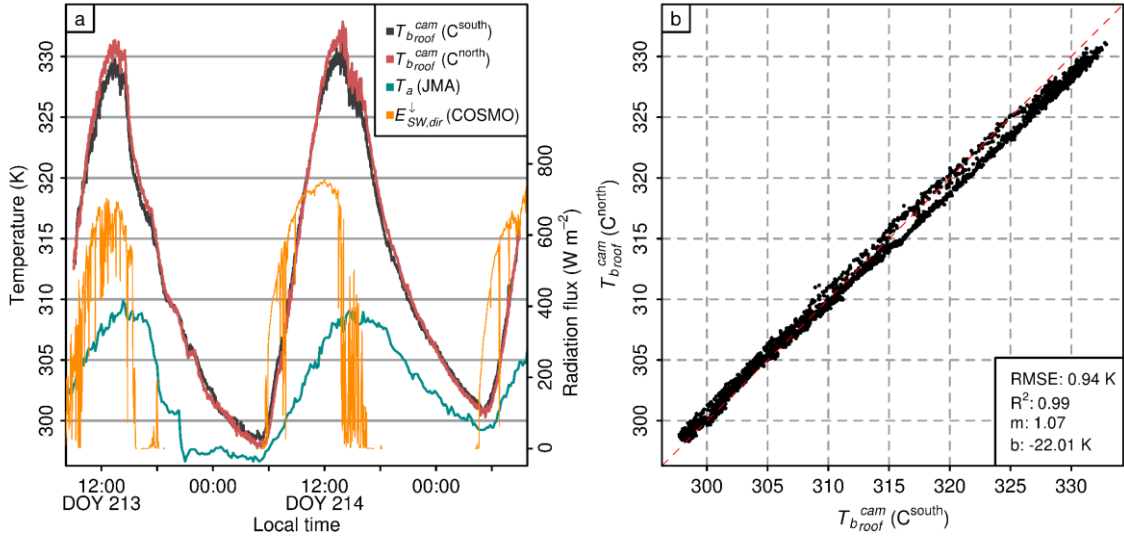


Figure 2-9. Inter-camera comparison of the mean broadband longwave radiation derived from roof pixels within the FOV of both cameras shown as (a) brightness temperatures ( $T_{b,roof}^{cam}$ ) for  $C^{south}$  (black) and  $C^{north}$  (red) surfaces with observations at 1 min resolution. Direct incoming shortwave radiation  $E_{SW,dir}^{\downarrow}$  (COSMO) measured on site using MS-56 Pyrheliometer (EKO Instruments) at 1 min resolution. Japan Meteorological Agency (JMA) air temperature measurements [ $T_a$  (JMA)] measured at Kumagaya AMeDAS (Automated Meteorological Data Acquisition System) station at 1 min resolution. (b) Relation between  $T_{b,roof}^{cam}$  ( $C^{south}$ ) and  $T_{b,roof}^{cam}$  ( $C^{north}$ ) with linear regression slope (m) and intercept (b) coefficients, used to correct the observations used throughout all results. In this figure observations are shown uncorrected.

### 2.4.3 Classified brightness temperature observations

Variability of inter-class and intra-class observations is shown in Figure 2-10 on a per-pixel level for all cameras throughout the study date (mixed and masked pixels are excluded). As expected, the variability of the pre-classified pixels for all cameras (Figure 2-10a) is greatest during the daytime, with hourly differences between the 5<sup>th</sup> and 95<sup>th</sup> percentiles of pixel distributions reaching 18.4 K between 12:00 – 13:00. With increasing level of spatial detail in pixel classification accounting for insolation status (Figure 2-10b), orientation (Figure 2-10c) and both combined (Figure 2-10d), the inter-class ranges of  $T_b^{cam}$  typically decrease. This suggests the class related differences are helpful in explaining some of the  $T_b^{cam}$  variability. Brightness temperatures are most variable for the ground pixels (Figure 2-10c), with shaded or sunlit ground surface pixel distributions (Figure 2-10d) both being large throughout daytime. Hourly differences between 5<sup>th</sup> and 95<sup>th</sup> percentiles reach 15.0 K (12.2 K) for all shaded (sunlit) ground surface pixels between 12:00 – 13:00 (11:00 – 12:00). The shadowing history is associated with this variability, with a thermal hysteresis effect due to the thermal inertia of concrete. For example, between 14:00 – 15:00, the 25<sup>th</sup> percentile of sunlit pixels have similar values to the 75<sup>th</sup> percentile of shaded pixels. The greater sky view factor of roofs compared to all other facets influences inter-class variability, with median brightness temperature of

roof pixels up to 2 K lower than all other classes between 00:00 – 05:00 (sunrise 04:55). Similarly, daytime roof brightness temperatures are highest (median = 330.8 K, 13:00 – 14:00, Figure 2-10c) and for this time interval 15 K greater than north wall facet temperatures. Sunlit pixels are cooler than shaded at sunrise (Figure 2-10b) and highlights a potential caveat when only using sunlit and shaded representations of data. Inclusion of the surface orientation reveals that these are mainly roof pixels which, being cooler throughout the night, take time in the morning to heat to temperatures above those of the within-canopy surfaces.

#### 2.4.4 Extrapolated longwave radiation flux

The parameterisation of  $M_{LW}^{3D}$  is evaluated by modelling its upwelling LWIR radiation projected onto the IP of MW cameras. The per-pixel MW camera perspective is  $M_{LW}^{cam}(MW, x, y)$  (i.e. Figure 2-5d, h).  $M_{LW}^{cam}(RW)$  is extrapolated to  $M_{LW}^{3D}$  (Section 2.3) with per-pixel differences calculated [ $M_{LW}^{cam}(RW, x, y) - M_{LW}^{cam}(MW, x, y)$ ] as an evaluation step. Figure 2-11 shows brightness temperature differences [i.e.  $T_b^{cam}(RW, x, y) - T_b^{cam}(MW, x, y)$ ] at six times during the case study day. Nighttime period per-pixel RW - MW brightness temperature differences never exceed  $\pm 1$  K (not shown) due to the low intra-class variability (Figure 2-10d). Daytime per-pixel RW - MW differences are evident and indicate some RW processes remain unresolved by  $M_{LW}^{3D}$ . Areas within the imagery where  $T_b^{cam}(MW)$  underestimates  $T_b^{cam}(RW)$  (red) or where  $T_b^{cam}(MW)$  overestimates  $T_b^{cam}(RW)$  (blue) include edges of building blocks, edges of shadows and locations across all ground surfaces.  $T_b^{cam}(MW)$  typically underestimates  $T_b^{cam}(RW)$  for top-of-wall pixels. Absolute maximum differences between  $T_b^{cam}(RW)$  and  $T_b^{cam}(MW)$  can reach 15 K for individual pixels within both  $C^{south}$  and  $C^{north}$  imagery, with 1<sup>st</sup> and 99<sup>th</sup> percentiles -4.34 K and 4.97 K, respectively. There are artefacts in MW camera imagery around all roof edges that face away from the cameras (e.g. Figure 2-5d, h). These are caused by the resolution of  $M_{LW}^{3D}$  and DART discretisation of LWIR surface exitance and explain some of the large absolute differences around roof edge pixels. The camera point spread function may impact how well the intersection between facets of contrasting temperatures are resolved but was not available from the manufacturer for further investigation. This effect coupled with any slight misalignment between RW and MW cameras (Section 2.2.4.2) may compound to explain high  $T_b^{cam}(RW) - T_b^{cam}(MW)$  differences near facet edges.

Surface energy exchange processes may further contribute to  $T_b^{cam}(RW) - T_b^{cam}(MW)$  differences near facet edges. The building blocks are hollow causing different thermal admittance at their edges. Further, the edges of buildings may be exposed to higher wind speeds which modify heat transfer and therefore surface temperature. In addition, roof edges on the sunlit side of buildings have distinctly high observed brightness temperatures (e.g. Figure 2-5a, e) associated with the different sky view factors. Maximum brightness temperatures for mixed pixels at these building edges are up to 7.4 K (13.3 K) higher than the median of intersecting roof (wall) facets at 13:35. This may be

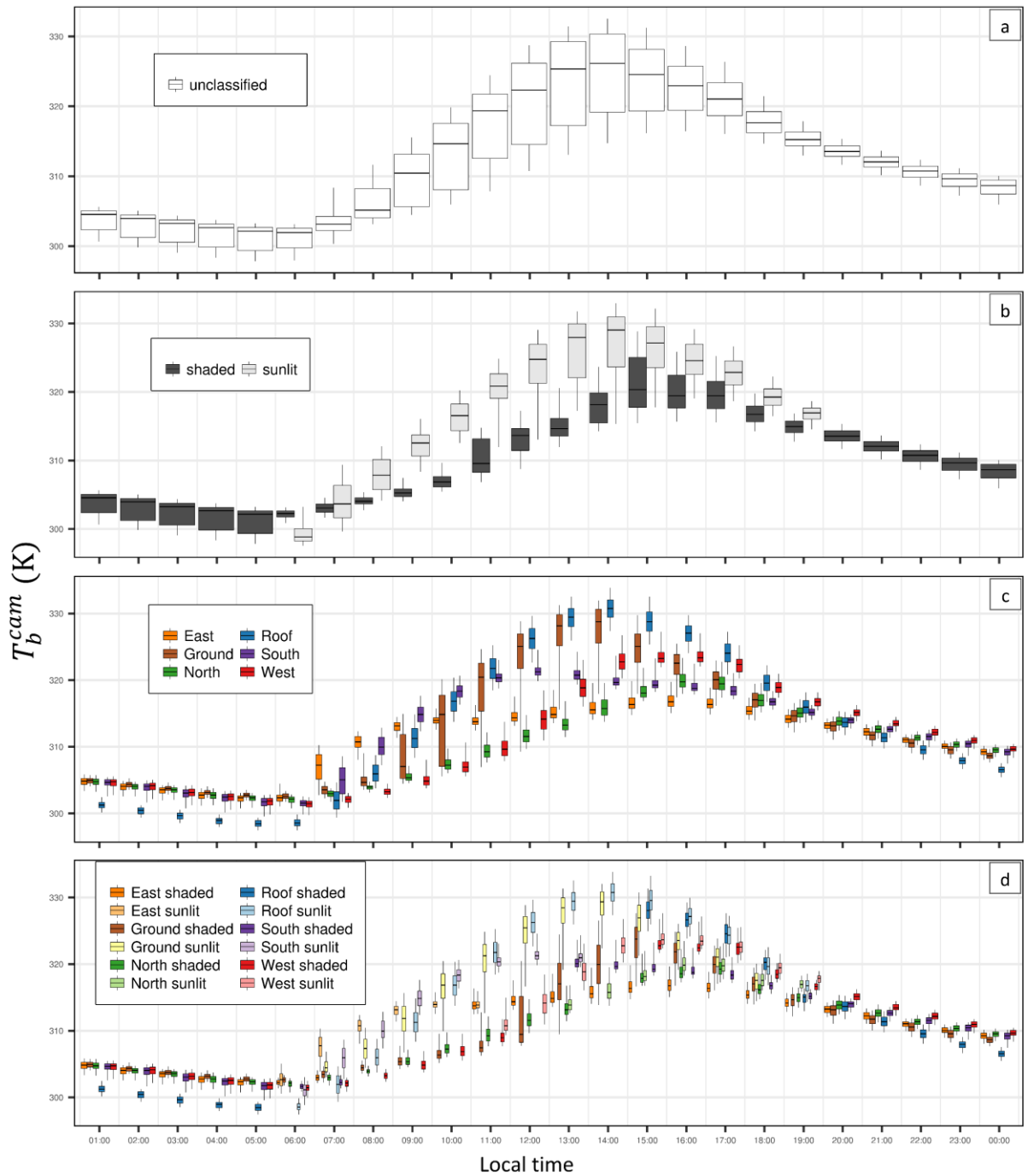


Figure 2-10. Intra-class variability of camera brightness temperatures ( $T_b^{cam}$ ) on 2<sup>nd</sup> August 2014. Each boxplot is all pixels assigned to a class (colour) from both cameras (images 1 min samples) during 1 h, with 5<sup>th</sup> and 95<sup>th</sup> percentiles (whiskers), interquartile range (box) and median (horizontal line) for pixels classified by: (a) all, (b) surface insolation status, (c) surface orientation, and (d) orientation and insolation status.

explained by high solar irradiance (high sky view factor) and absorption of these areas throughout the day.

Closer to the ground, wall view factors are larger and ground surface reflection captured by  $T_b^{cam}(RW)$  is more important. Surfaces in these regions receive radiation from regions with cooler

surface temperatures that have been in shade for prolonged periods (e.g. Figure 2-11e), and from regions with warmer surface temperatures that have been sunlit for prolonged periods (e.g. Figure 2-11i). The large distribution of brightness temperatures for observed ground pixels (Figure 2-10c, d) is not represented in  $M_{LW}^{3D}$  which only contains information on mean values of  $M_{LW,i}^{cam}$  (Section 2.3). The errors associated with this assumption are seen in Figure 2-11 mainly for shaded ground pixels and ground pixels at the edges of buildings. A shadow hysteresis is evident at multiple time steps (e.g. Figure 2-11d centre block, Figure 2-11i front centre block) as brightness temperatures of surfaces coming out of (into) shade are overestimated (underestimated) by  $M_{LW}^{3D}$ .

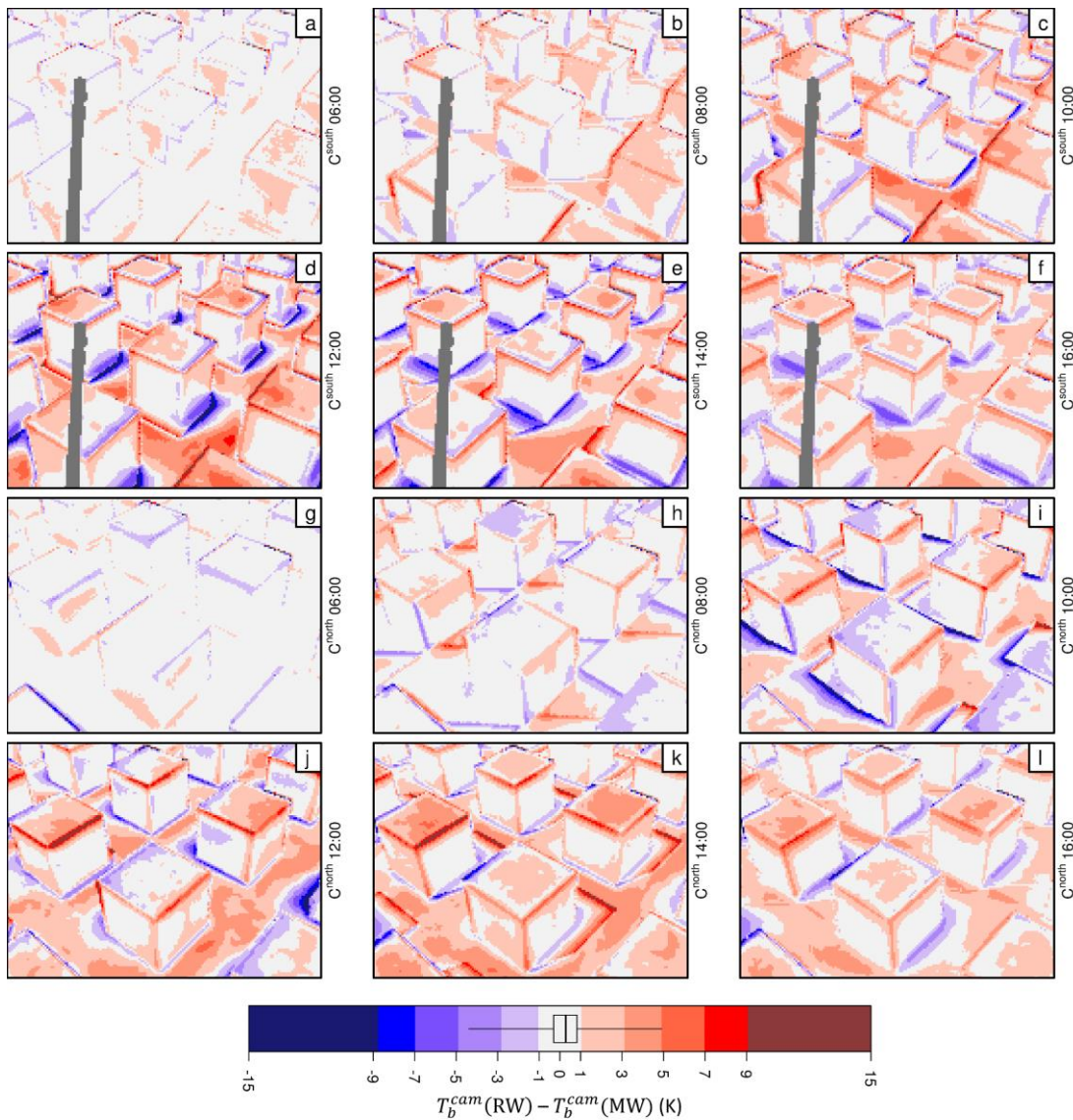


Figure 2-11. Brightness temperature ( $T_b$ ) differences between LWIR camera observations from “real world” (RW) [ $T_b^{cam}(RW)$ ] and “model world” (MW) for six times (see labels on sub-plots) on 2<sup>nd</sup> August 2014, for camera (a – f) C<sup>south</sup> and (g – l) C<sup>north</sup>.  $T_b^{cam}(MW)$  is simulated by DART camera view modelling using predetermined 3D distribution of longwave flux ( $M_{LW}^{3D}$ ). (a – f) Radiometer boom masked (grey) from results. Boxplot (inside legend) for all non-masked pixels within all timesteps throughout the day (15 min resolution) with 1<sup>st</sup> and 99<sup>th</sup> percentiles (whiskers), interquartile range (box) and median (vertical line).

The extent to which these unresolved sub-facet processes influence the directional brightness temperature aggregated across each IP of  $T_b^{cam}(MW)$  is subsequently investigated. The aggregated at-sensor brightness temperature ( $\tilde{T}_b^{cam}$ ) for  $T_b^{cam}(RW)$  and  $T_b^{cam}(MW)$  view is determined at 15 min resolution for the whole day (Figure 2-12).  $\tilde{T}_b^{cam}$  is the mean of all non-masked pixels in a camera IP. This analysis is similar to results demonstrated for existing sensor view modelling approaches (e.g. Soux, Voogt and Oke, 2004). In this paper,  $\tilde{T}_b^{cam}(RW) - \tilde{T}_b^{cam}(MW)$  differences show a diurnal pattern (Figure 2-12). When  $M_{LW}^{3D}$  is prescribed using insolation and orientation (solid lines, Figure 2-12), RW - MW differences reach  $\pm 0.65$  K during daytime at 12:45 for  $C^{north}$ , and are within 0.40 K during nighttime. Prescribing  $M_{LW}^{3D}$  based only on orientation (dashed lines, Figure 2-12; shown as inter-class distributions at pixel level in Figure 2-10c) leads to good agreement at night when inter-class variability is small and shadows do not occur. During daytime, however, not accounting for shadow patterns means  $\tilde{T}_b^{cam}(MW)$  is up to 0.90 K warmer (cooler) than  $\tilde{T}_b^{cam}(RW)$  for  $C^{south}$  ( $C^{north}$ ) at 12:45.

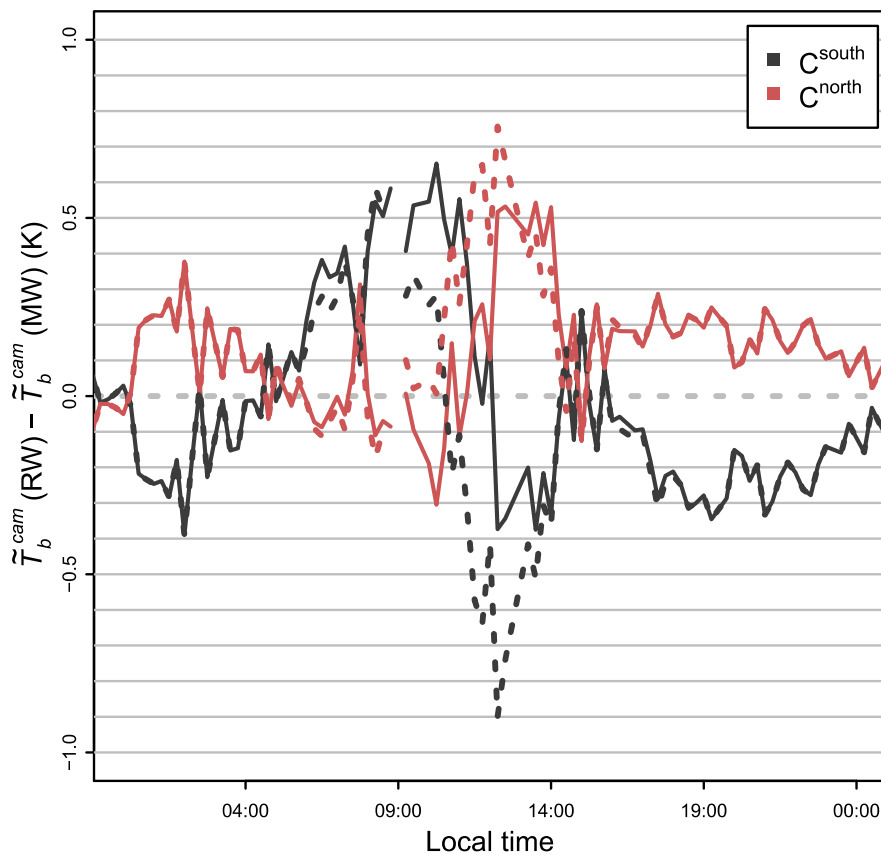


Figure 2-12. Comparison of “real world” (RW) and “model world” (MW) aggregated at-sensor broadband longwave radiation observations (as brightness temperatures) for cameras  $C^{south}$  (black) and  $C^{north}$  (red) 2<sup>nd</sup> August 2014 local standard time. MW observations simulated by DART camera view modelling using predetermined 3D distribution of longwave flux ( $M_{LW}^{3D}$ ) at the COSMO test site.  $M_{LW}^{3D}$  prescribed using shadowing and orientation classes (solid lines) and orientation classes only (dashed lines).

### 2.4.5 Normalised effective anisotropy

Apparent brightness temperatures viewed from the COSMO surface over multiple discrete directions (375 directions over the hemisphere) are simulated using DART and  $M_{LW}^{3D}$ . The apparent brightness temperature for a direction is the parallel projection of  $M_{LW}^{3D}$  onto a plane that is perpendicular to the view direction, aggregated to a single directional brightness temperature value. Here a 29.5 m x 29.5 m sample of  $M_{LW}^{3D}$  is analysed. The normalized effective anisotropy (Figure 2-13) is defined as the apparent brightness temperature from a nadir view minus the apparent brightness temperature at a given direction. Modelled values of normalised effective anisotropy range from -6.10 K (12:30) to 3.41 K (08:00) on the case study day, with a maximum difference between any direction of 6.18 K (13:00) and 3.55 K for view zenith angles up to 30° off-nadir (10:00). For zenith angles < 10° (i.e. representative of Landsat swath) the normalised anisotropy is typically within ±0.5 K. Lowest directional brightness temperatures occur at high zenith angles and at azimuth angles near the sun position. This is in agreement with prior results (Voogt, 2008). Around midday and early afternoon (e.g. 12:00, 14:00), view angles with high zenith angles ( $\phi > 40^\circ$ ) near each cardinal azimuth angle underestimate nadir view brightness temperature by up to 6 K. This is likely caused by the cooler walls occluding the warm ground surfaces at these view angles. A “hot spot” around the sun angle is prominent during morning periods (08:00, 10:00) where brightness temperature differences between currently insolated facets and shaded facets is greatest. Inter-facet temperature differences are lower during afternoon, reducing the magnitude of any hot spot (14:00, 16:00). These examples highlight a critical application of the modelling approach presented to any thermal RS study in a real urban setting.

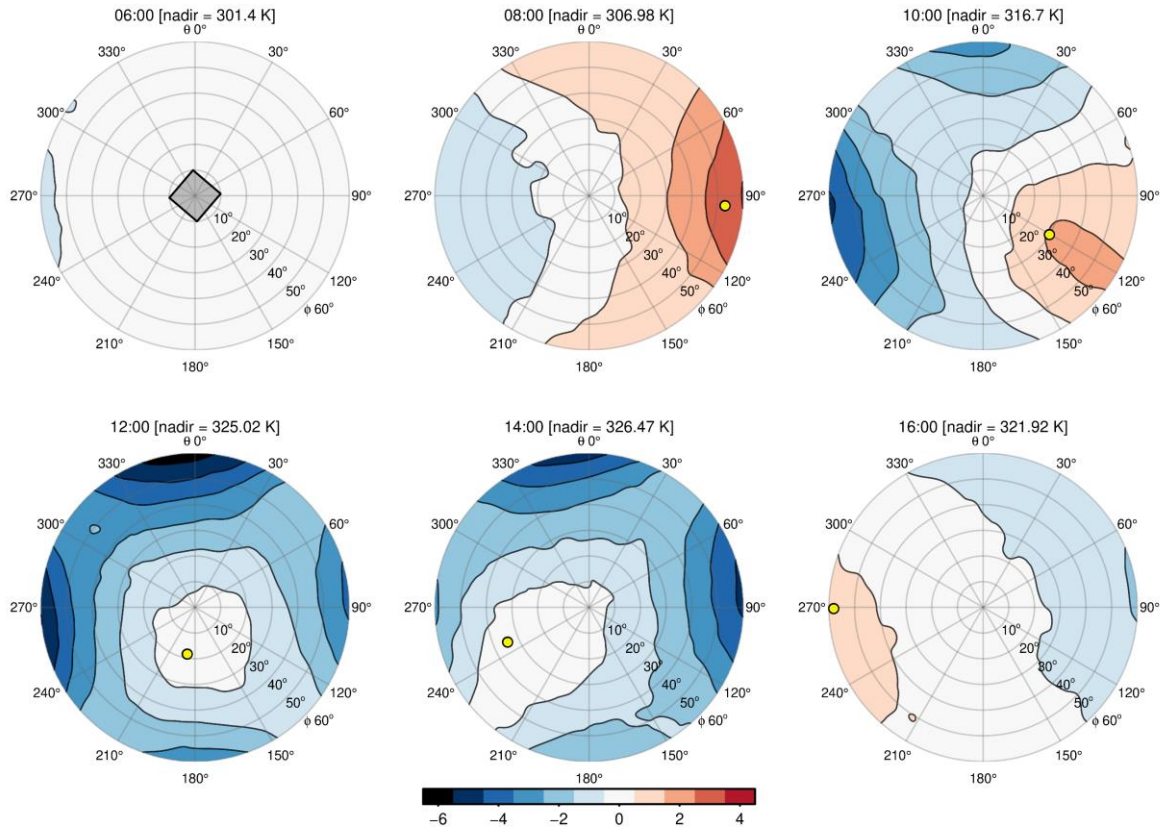


Figure 2-13. Simulated brightness temperatures for 375 discrete directions using predetermined 3D distribution of longwave flux ( $M_{LW}^{3D}$ ) for the COSMO test site for 6 times on 2<sup>nd</sup> August 2014. Results normalized by the simulated brightness temperature at nadir ( $\phi = 0^\circ$ , given in sub-headings) and shown with 1 K contours. Data and sun angle (yellow dot) are oriented with true north ( $\theta = 0^\circ$ ), with COSMO building orientation displayed (centre grey square, 06:00).

## 2.5 Conclusions

The exitant longwave radiation from a simplified urban surface (COSMO outdoor scale model) is studied based on ground-based LWIR camera observations with detailed radiative transfer and camera view modelling. Ground-based LWIR camera ( $M_{LW}^{cam}$ ) observations from the COSMO test site over 24 h illustrate spatial and temporal patterns in upwelling LWIR radiation.

Hourly per-pixel camera brightness temperatures are low at night but vary more widely during the day (5<sup>th</sup> – 95<sup>th</sup> percentile differences reach 313.05 – 331.45 K between 12:00 – 13:00). As shadows cast by buildings and facet orientations likely explain most of this observed variability, these are often used to parameterise kinematic and radiometric temperature variability across the complete urban surface. Here, radiative transfer and camera view modelling is undertaken to identify the sunlit/shaded dynamics of camera pixels. The nature of inter-class and intra-class  $M_{LW}^{cam}$  distributions derived from the modelling results suggest that manual digitization or frequency distribution analysis may be problematic, particularly during daytime when inter-class distributions frequently overlap. This effect is most prominent for distributions of sunlit and shaded ground pixels.

Despite the simple surface geometry of the study site, image classification by camera view modelling demands small margins of error for camera parameters such as image distortion (Section 2.2.4.1) and the physical positioning of cameras (Section 2.2.4.2) for the perspective of  $M_{LW}^{cam}$  to be modelled accurately. This finding can be attributed to the short surface-sensor path lengths of the observational setup. Furthermore, sun-surface geometry and the timekeeping of observations must be known to a high degree of accuracy. Previous studies have not demonstrated direct comparison of observed and simulated results in such detail.

Methods in this paper overcome sensor view modelling challenges by using the DART and Blender camera view models. A comparison between a captured and modelled high resolution digital camera image (Section 2.2.4.3) demonstrates the potential accuracy and resolution of the methods. Evaluating the ability of classified  $M_{LW}^{cam}$  observations to explain the variability of broadband longwave radiation exitant across the COSMO canopy surface uses the 3D distribution of exitant LWIR radiation ( $M_{LW}^{3D}$ ). It is concluded that  $M_{LW}^{3D}$  accurately resolves the surface geometry of the test site when the parameterisation is at high temporal (15 min) and spatial (0.04 m) resolution, where  $M_{LW}^{3D}$  is evaluated for a given time step by projecting prescribed values of exitant broadband longwave radiation onto simulated “model world” (MW) cameras with perspectives matching that of the “real world” (RW)  $M_{LW}^{cam}$ . Pixel level comparison between RW and MW camera imagery identifies areas where the prescribed  $M_{LW}^{3D}$  does not resolve  $M_{LW}^{cam}$  variability; *viz.*, building edges, sky view factor variability of vertical surfaces, and ground areas with a distinct shadow hysteresis. By aggregating all pixels in each image to a single brightness temperature for each MW and RW camera, these features average out to RW – MW differences within 0.65 K throughout a 24 h period (1<sup>st</sup> – 99<sup>th</sup> per-pixel differences of -4.34 – 4.97 K). Understanding unresolved sub-facet processes may be required for parameterisation of  $M_{LW}^{cam}$  in more complex urban environments. Further classes of absolute irradiance values and sky view factor have potential to be applied using DART.

$M_{LW}^{3D}$  coupled with DART is shown to be useful for assessment of urban thermal anisotropy (Section 2.4.5). Modelled anisotropy results for the study day show large differences between nadir and off-nadir apparent brightness temperatures which in general is in good agreement with prior studies. Modelled anisotropy is simplified in that it does not consider irregular building geometry and materials found in real cities. The regularity of the COSMO geometry may introduce an overestimation of modelled anisotropy compared to real world cities (Krayenhoff and Voogt, 2016).

It is concluded that shadow histories classes and further quantification of surface irradiance fluxes using DART radiative transfer functionality would be useful to address in future studies. Depending on the availability of spatial databases, building geometry and material properties can also be resolved at levels of detail representative of complex urban environments. Material properties may be challenging to obtain due to a general lack of urban materials spatial databases. If the surface form

is a predominant factor in effective thermal anisotropy, simplified assumptions of surface material may be sufficient when classifying  $M_{LW}^{cam}$  and parameterising  $M_{LW}^{3D}$  for complex urban environments.

Applying the methods presented in this paper to real cities may require a different approach to sensor siting. The current study uses a mast as a sensor platform that is  $\sim 4$  times the mean building height (Figure 2-2). This enables an observational source area that is representative of the domain and that resolves sub-facet processes. A similar source area could be achieved in urban areas with compact low-rise and open high-rise morphology, with cameras installed on top of the taller high-rise buildings.

Overall, this work provides a significant improvement to interpreting ground-based RS observations. Applied to real city settings, this has the potential to provide essential improvements to evaluating errors associated with operationally retrieved urban surface temperatures from satellite RS platforms and the parameterisation of longwave radiation exchanges in urban surface schemes.

## List of symbols and acronyms [units]

$\beta, \varphi, \omega$	Euler angles describing a sequence of rotations within the $(x_c, y_c, z_c)$ coordinate frame
BOA	Bottom of atmosphere
BRF	Bidirectional reflectance factor
C	Non-specific camera
COSMO	COMprehensive urban Scale MOdel
$d_{FPA}$	Camera focal plane array size [mm]
DART	Discrete Anisotropic Radiative Transfer model (Gastellu-Etchegorry, Grau and Laurent, 2012)
DSM	Digital surface model
$\varepsilon$	Emissivity
$E_{LW}^\downarrow$	Broadband longwave radiation flux (irradiance) downward from sky [ $\text{W m}^{-2}$ ]
$E_{SW}^\downarrow$	Broadband shortwave radiation flux (irradiance) downward from sky [ $\text{W m}^{-2}$ ]
$E_{SW,dir}^\downarrow$	Broadband direct shortwave radiation flux (irradiance) downward from sky [ $\text{W m}^{-2}$ ]
$F$	Camera focal length [mm]
$f$	Fraction
FOV	Field of view
FPA	Focal plane array
$i$	Nonspecific surface class
IFOV	Instantaneous field of view
IP	Image plane
$\lambda$	Wavelength [ $\mu\text{m}$ ]
LW	Longwave
LWIR	Longwave infrared
$M_{LW}$	Broadband longwave radiation flux (exitance) from a surface [ $\text{W m}^{-2}$ ]
$M_{LW}^{3D}$	Broadband longwave radiation flux (exitance) from discrete points of an urban surface, resolved in 3D [ $\text{W m}^{-2}$ ]
$M_{LW}^{cam}$	Camera derived broadband longwave radiation flux (exitance) [ $\text{W m}^{-2}$ ]
$M_{LW}^{can}$	Non-specific broadband longwave radiation flux (exitance) from urban canopy elements [ $\text{W m}^{-2}$ ]
$M_{LW}^\uparrow$	Broadband longwave radiation flux (exitance) upward from ground [ $\text{W m}^{-2}$ ]
$M_{LW}^{RS}$	Nonspecific (e.g. satellite) remote sensing derived broadband longwave radiation flux (exitance) [ $\text{W m}^{-2}$ ]
$M_{SW}^\uparrow$	Broadband upwelling shortwave radiation flux (exitance) upward from ground [ $\text{W m}^{-2}$ ]
$M_{SW}$	Shortwave radiant flux (exitance) from a MW surface element [ $\text{W m}^{-2}$ ]
MW	Model world
$O$	Origin of model world domain coordinate frame
$O_c$	Origin of camera intrinsic coordinate frame
$P$	Camera principle point
$\phi$	Zenith angle
$\psi^{sky}$	Sky view factor
$\psi^{can}$	Canopy view factor
$R$	Camera rotation parameters
RGB	Red, green, blue
RW	Real world
$s$	Camera pixel scaling factor
$S$	Triangle face of vector model
SW	Shortwave
$t$	Camera translation parameters
$\tau$	Transmissivity
$T_b$	Brightness temperature [K]
$T_b^{cam}$	Camera derived brightness temperature [K]
TOA	Top of atmosphere
$T_s$	Thermodynamic surface temperature [K]
$T_s^{3D}$	Thermodynamic surface temperature at discrete points of an urban surface, resolved in 3D [K]
$Vx$	Voxel (a volume element)
$Vx^S$	Voxel intersected by a digital surface model element (surface voxel)
$X, Y, Z$	Model world domain coordinate frame
$x, y$	Camera pixel coordinate frame
$x_c, y_c, z_c$	Camera intrinsic coordinate frame
$z_c$	Camera principle axis

## **Acknowledgements**

This study was funded by Newton Fund/Met Office Climate Science for Service Partnership China (CSSP China), EU H2020 UrbanFluxes, Japan Society for the Promotion of Science (JSPS), NERC ClearfLo, NERC/Belmont TRUC, EUf7 emBRACE and the National Research Foundation (NRF) Singapore through the Singapore-MIT Alliance for Research and Technology's Centre for Environmental Sensing and Modeling (SMART-CENSAM) interdisciplinary research program. We thank Nicholas Lauret and Lucas Landier of the DART team for ongoing DART model development and valuable support. We thank all students at Kanda lab who contributed to conducting the measurements.

## Chapter 3 Atmospheric and emissivity corrections for ground-based thermography using 3D radiative transfer modelling

### Abstract

Methods to retrieve urban surface temperature ( $T_s$ ) from remote sensing observations with sub-building scale resolution are developed using the Discrete Anisotropic Radiative Transfer (DART, Gastellu-Etchegorry, Grau and Lauret, 2012) model. Corrections account for the emission and absorption of radiation by air between the surface and instrument (atmospheric correction), and for the reflected radiation from non-black-body surfaces (emissivity correction) within a single modelling framework. The atmospheric correction can use horizontally and vertically variable distributions of atmosphere properties at high resolution ( $< 5$  m). Here it is applied with vertically extrapolated weather observations and MODTRAN atmosphere profiles. The emissivity correction resolves the reflection of longwave infrared radiation (LWIR) as a series of scattering events at high spatial ( $< 1$  m) and angular ( $\Delta\Omega \approx 0.02$  sr) resolution using a heterogeneous distribution of radiation leaving the urban surfaces. The method is applied to a novel network of seven ground-based cameras measuring LWIR radiation across a dense urban area (extent: 420 m x 420 m) where detailed three-dimensional representation of the surface and vegetation geometry is used. The multiple cameras have large variations in: path lengths (5<sup>th</sup> and 95<sup>th</sup> percentile of all pixel path lengths are 41.3 m and 220.1 m), view angles, brightness temperatures and observed surface geometry. Corrected brightness temperatures are up to 4.5 K warmer than the uncorrected. The detailed surface geometry is shown to accurately register the pixel path lengths even for complex urban features such as sloped roofs.

Simultaneous 20-days (4110 timesteps) of “near” ( $\sim 15$  m) and “far” ( $\sim 155$  m) path length observations are used to evaluate the atmospheric correction method. The mean absolute error is 0.39 K and the coefficient of determination is 0.998 between the “near” and corrected “far” data. The emissivity correction has clear diurnal variability, particularly when a cool and shaded surface (e.g. north facing) is irradiated by warmer (up to 17.0 K) surfaces (e.g. south facing). Uncertainty analysis of the emissivity correction for common dark building materials ( $\varepsilon = 0.89 \rightarrow 0.97$ ) translates to around 3 K (1.5 K) for roof (south facing) surfaces and during daytime is within 0.1 K for cooler north facing surfaces. Corrected observations assuming a homogeneous radiation distribution from surfaces (analogous to a sky view factor correction) differ from a heterogeneous distribution by up to 0.25 K. The proposed correction provides more accurate  $T_s$  observations with improved uncertainty estimates. Potential applications include ground-truthing air- or space-borne surface temperatures and evaluation of urban energy balance models.

### 3.1 Introduction

Development of sustainable cities, informed by weather and climate models, requires a clear understanding of how urban areas modify the surface energy balance (SEB). A key variable in the SEB is the surface temperature ( $T_s$ , Porson *et al.*, 2010), which is affected by surface morphology, material composition and human activities.  $T_s$  observations are hence valuable for the evaluation and improvement of urban SEB models (Grimmond *et al.*, 2010). While longwave infrared (LWIR) remote sensing (RS) from space provides surface temperature observations for this purpose at increasing resolutions (Chrysoulakis *et al.*, 2018), their biased view of the full 3D surface (Voogt and Oke, 2003) and low temporal resolution means the complex spatio-temporal variations of  $T_s$  related to components of the surface energy balance are not fully captured. Ground-based LWIR thermography, however, allows temporally continuous observations from individual facets (e.g. roof, wall) and sub-facets (e.g. material, shadowing) that make up the three dimensional (3D) urban form (Voogt and Oke, 1997; Chapter 2). These observations are crucial for understanding uncertainties of satellite derived  $T_s$  and have proven valuable as inputs to urban SEB models studies (e.g. Ghent *et al.*, 2010) and for model evaluation (e.g. Krayenhoff and Voogt, 2007; Pigeon *et al.*, 2008; Harshan *et al.*, 2018). To derive  $T_s$  from RS, a range of corrections are required. A LWIR camera may record a radiometrically calibrated brightness temperature ( $T_b^{\text{cam}}$ ) that differs from  $T_s$  because of radiation emitted or attenuated by the atmosphere between the surface and the sensor (atmospheric effects). Emissivity effects arise from LWIR radiation reflected at the observed surface if it is not a perfect emitter of black-body (BB) radiation. For ground-based LWIR RS in urban areas, there are unique challenges associated with these corrections. Procedures to retrieve  $T_s$  from satellite sensors (e.g. Wan, 2014) cannot be directly applied to ground-based observations as urban geometry, materials and radiative exchanges are resolved at sub-building scales rather than within a mixed satellite pixel. Depending on the viewing geometry and sensor resolution, a similar issue affects airborne observations (e.g. Voogt and Grimmond, 2000; Lagouarde *et al.*, 2010).

There are few studies with full  $T_s$  retrieval from observations at sub-building scales in complex urban areas. Ground-based cameras sensitive to LWIR in the atmosphere window ( $\sim 8 - 14 \mu\text{m}$ ) can underestimate atmospherically corrected  $T_s$  by more than 6 K for surface-camera path lengths ( $z^{\text{path}}$ ) of  $\sim 300$  m in an urban setting (Meier *et al.*, 2011). With oblique view angles in ground-based RS the  $z^{\text{path}}$ , and therefore atmospheric effects, can vary greatly. Previously,  $z^{\text{path}}$  has been treated as a constant (e.g. Yang and Li, 2009) or spatially variable (e.g. Meier *et al.*, 2011; Hammerle *et al.*, 2017).

While  $z^{\text{path}}$  is a primary influence on the atmospheric correction, for an emissivity correction the emissivities and reflected radiance across the observed surfaces are critical. Facet surface materials and emissivity can be highly variable (Kotthaus *et al.*, 2014). Although urban geometry is an important influence on reflected radiation from the sky and canopy elements that undergo complex

scattering events (Harman, Best and Belcher, 2004), space-borne or airborne RS emissivity corrections often only consider material effects (e.g. Mitraka *et al.*, 2012; Chrysoulakis *et al.*, 2018). To account for radiation trapping within street canyons, the emissivity correction has been parameterised using the sky view factor (SVF) characteristic for both urban earth observation (EO) (Yang *et al.*, 2015, 2016) and for ground-based LWIR RS at sub-building scale (Adderley, Christen and Voogt, 2015).

Limitations to the current methods to retrieve facet  $T_s$  include the following. Meier *et al.*'s (2011) correction procedure considers only the atmospheric effect and uses a lookup table based on the MODTRAN radiative transfer (RT) model. Adderley *et al.*'s (2015) emissivity correction simplifies the reflected radiation contribution by assuming isothermal radiation emission relative to the SVF of the target surface. No previous study has accounted for both the atmospheric and emissivity corrections within a single framework that explicitly resolves the related RT processes for both flexible instrument siting and number.

As LWIR radiation exchanges within the canopy are very complex, some anisotropic factors determining the irradiance across urban surfaces may be important for the description (and correction) of emissivity effects in RS observations. LWIR radiance of clear sky varies with zenith angle (Verseghy and Munro, 1989), material and shadow patterns cause variability in surface temperature (Voogt and Oke, 1997; Chapter 2), and materials may have anisotropic emissivity (Sobrino and Cuenca, 1999). Relatively little is known about the magnitude of the uncertainties associated with these effects. Beyond Adderley *et al.*'s (2015) emissivity correction procedure, ground-based studies that derive  $T_s$  use: (1) bulk approximations for surface emissivity and reflected radiation (Yang and Li, 2009); (2) nocturnal observations (e.g. Ghandehari, Emig and Aghamohamadnia, 2018) when radiation received from sky and buildings are more similar; or (3) *in-situ* measurements (e.g. thermocouples affixed to surfaces, e.g. Rotach *et al.*, 2005; Offerle *et al.*, 2007) with very limited spatial extent and portability. Given the complexity of within-canopy radiation scattering, many studies avoid obtaining  $T_s$  altogether by assuming black-body (BB) characteristics (Voogt and Oke, 1997; Christen, Meier and Scherer, 2012). However, the emissivity effect magnitude can be substantial (Jiménez-Muñoz and Sobrino, 2006; Chen *et al.*, 2016) with effects on spatial thermal variations (Chapter 2). Analysing brightness temperatures  $T_b$  (K) rather than  $T_s$  means energy balance characteristics may not be portrayed adequately.

Here the objective is to retrieve high-quality  $T_s$  at the sub-facet scale from ground-based LWIR RS by applying both atmospheric and emissivity corrections within a single modelling framework. The developed approach is flexible, uses RT, and is applicable for any high-resolution ground-based thermography. The 3D radiative transfer approach used here accounts for atmospheric and emissivity corrections using recent enhancements to the Discrete Anisotropic Radiative Transfer (DART, Gastellu-Etchegorry *et al.*, 2015) model. No other high resolution 3D sensor view and RT model

(e.g. LESS, Qi *et al.*, 2019) accounts for the atmosphere or LWIR surface emission and multiple scattering effects or describes temperature and optical properties of the surface and atmosphere at similar resolutions. This is the first study to exploit these high-resolution RT capabilities of DART. Through using these methods, new insights into LWIR radiation exchanges between surfaces at high spatial resolution ( $< 1$  m) are obtainable. Results are also expected to be valuable for the development of the increasingly detailed representations of urban processes in SEB model radiation schemes (Hogan, 2019).

After the theoretical background for the retrieval of  $T_s$  is introduced (Section 3.2), the methods developed using DART (Section 3.3.1) are outlined, separated into the atmospheric (Section 3.3.2) and emissivity (Section 3.3.3) corrections. The developed methods are applied for LWIR cameras in a dense urban canopy that is characterised at a uniquely high level of detail (LOD) (Section 3.4). The atmospheric correction is evaluated using observations (Section 3.5.1), while the emissivity correction results are analysed using a sensitivity analysis (Section 3.5.2). Alternative and future ways the method can be applied are discussed (Section 3.6).

### 3.2 Theoretical background to the corrections

Atmospheric correction of RS observations is undertaken to remove the effects from emission and absorption of radiation by the air between the sensor and target (Sobrino, Coll and Caselles, 1991). The spectrally dependent path radiance ( $L_\lambda^{\text{atm}}$ ) and transmittance of the atmosphere ( $\Gamma_\lambda^{\text{atm}}$ ) between a target surface and a RS instrument contribute to the at-sensor radiance. For pixel  $(x, y)$  of a LWIR camera, the at-camera band radiance ( $L^{\text{cam}}$ ,  $\text{W m}^{-2} \text{sr}^{-1}$ ) is (Meier *et al.*, 2011):

$$L^{\text{cam}}(x, y) = \int_{\lambda_1}^{\lambda_2} d\lambda [B_\lambda(T_s)(x, y) \cdot \Gamma_\lambda^{\text{atm}}(x, y) + L_\lambda^{\text{atm}}(x, y)] \cdot R_\lambda(x, y) \quad \text{Eqn. 3.1}$$

where  $R_\lambda$  is the normalised spectral response function and  $B_\lambda(T_s)$  is the contribution of the assumed BB Planck radiance ( $B_\lambda$ ,  $\text{W m}^{-2} \text{sr}^{-1} \mu\text{m}^{-1}$ ) of LW radiation exitant from the surface.

Eqn. 3.1 assumes the target surface is a perfect emitter of black-body radiation, whereas typically the spectral emissivity ( $\varepsilon_\lambda$ ) is less than unity with the radiance  $L_\lambda$  ( $\text{W m}^{-2} \text{sr}^{-1} \mu\text{m}^{-1}$ ) emitted by a body at temperature  $T$  less than the Planck BB radiance at the same temperature (Becker and Zhao-Liang Li, 1995):

$$\varepsilon_\lambda = \frac{L_\lambda(T)}{B_\lambda(T)} \quad \text{Eqn. 3.2}$$

The spectral radiance from an opaque, non-BB surface located on a horizontal plane detected by a theoretical LWIR camera pixel at wavelength  $\lambda$  ( $L_\lambda^{\text{cam}}(x, y)$ ,  $\text{W m}^{-2} \text{sr}^{-1} \mu\text{m}^{-1}$ ) is a combination of emitted and reflected radiation from the surface, after correction for any atmospheric effects. Assuming  $\varepsilon_\lambda$  is isotropic, the surface temperature can be related to  $L_\lambda^{\text{cam}}$  by:

$$L_{\lambda}^{\text{cam}}(x, y) = \varepsilon_{\lambda} B_{\lambda}(T_s) + (1 - \varepsilon_{\lambda}) \frac{1}{\pi} E_{\lambda} \quad \text{Eqn. 3.3}$$

with  $E_{\lambda}$  ( $\text{W m}^{-2} \mu\text{m}^{-1}$ ) the downwelling, isotropic spectral irradiance from the sky. Rearranging Eqn. 3.3 gives  $B_{\lambda}(T_s)$ :

$$B_{\lambda}(T_s) = \frac{L_{\lambda}^{\text{cam}}(x, y) - (1 - \varepsilon_{\lambda}) \frac{1}{\pi} E_{\lambda}}{\varepsilon_{\lambda}} \quad \text{Eqn. 3.4}$$

which is related to  $T_s$  using the inverse of the Planck function ( $B_{\lambda}^{-1}$ ) as:

$$T_s = B_{\lambda}^{-1}[B_{\lambda}(T_s)] = c_2 \left/ \left[ \lambda \cdot \ln \left( \frac{c_1}{\lambda^5 \frac{L_{\lambda}^{\text{cam}}(x, y) - (1 - \varepsilon_{\lambda}) \frac{1}{\pi} E_{\lambda}}{\varepsilon_{\lambda}}} + 1 \right) \right] \right. \quad \text{Eqn. 3.5}$$

with  $c_1 = 1.191042 \times 10^9$  ( $\text{W m}^{-2} \text{sr}^{-1} \mu\text{m}^{-1}$ ) and  $c_2 = 1.4387770 \times 10^4$  ( $\mu\text{m K}$ ) the first and second radiation constants.

In urban areas, the 3D surface structure gives rise to LW irradiance contributions from other surfaces and a reduction of sky irradiance. For a given point within the urban canopy, the spectral irradiance ( $E_{\lambda}$ ,  $\text{W m}^{-2}$ ) can be described as (Nunez, Eliasson and Lindgren, 2000):

$$E_{\lambda} = \int_{2\pi} L_{\lambda}^{\text{sky}}(\Omega_{\downarrow}) \cos\theta d\Omega + \int_{2\pi} L_{\lambda}^{\text{can}}(\Omega_{\downarrow}) \cos\theta d\Omega \quad \text{Eqn. 3.6}$$

with  $L_{\lambda}^{\text{sky}}(\Omega_{\downarrow})$  [ $L_{\lambda}^{\text{can}}(\Omega_{\downarrow})$ ] the spectral radiance ( $\text{W m}^{-2} \text{sr}^{-1} \mu\text{m}^{-1}$ ) that originates from the sky [canopy] after any multiple scattering received by the surface from solid angle  $d\Omega$  (sr), with  $\theta$  the angle of incidence to the surface normal.  $L_{\lambda}^{\text{can}}(\Omega_{\downarrow})$  varies with surface temperature and emissivity within the given solid angle. For wavelengths in the LWIR atmospheric window, where typically thermal RS instruments are sensitive to absorption, emission and scattering of LW radiation, the air within the canopy surfaces (i.e. between buildings) can be neglected if the path lengths are short (determined by canyon geometry).  $L_{\lambda}^{\text{sky}}(\Omega_{\downarrow})$  varies with wavelength, the depth of precipitable water within the atmosphere and the portion of the sky seen (Versegny and Munro, 1989). Critically, both  $L_{\lambda}^{\text{sky}}$  and  $L_{\lambda}^{\text{can}}$  change due to any prior scattering of both diffuse and specular radiation.

### 3.3 Methods

The correction of LWIR RS observations for atmospheric (Section 3.3.2) and emissivity (Section 3.3.3) effects are outlined and applied to a central urban area (Section 3.4). The methods are applicable to any ground-based or airborne sensor for atmospheric window (7 – 14  $\mu\text{m}$ ) radiation and are applied in the context of LWIR cameras.

### 3.3.1 DART radiative transfer and sensor view model

The Discrete Anisotropic Radiative Transfer (DART) model (Gastellu-Etchegorry, Grau and Lauret, 2012) is used to determine  $T_s$  from LWIR camera observations. This state-of-the-art 3D RT model has tools to generate and import surface and atmosphere properties of landscapes, as well as to simulate RT processes in the shortwave (e.g. Wu *et al.*, 2018) and longwave (e.g. Wang *et al.*, 2018) IR spectrum. DART has been evaluated for simple terrain (Sobrino *et al.*, 2011) with more recent updates (Grau and Gastellu-Etchegorry, 2013; Gastellu-Etchegorry *et al.*, 2017) where the atmosphere RT in DART has shown good agreement with MODTRAN simulations. Using a discrete ordinate (DO) ray tracing approach, DART simulates 3D RT processes in both natural and urban landscapes. Individual rays are tracked along discrete directions within angular cones (Yin *et al.*, 2013; Yin, Lauret and Gastellu-Etchegorry, 2015). DART's "forward-tracking" allows emitted radiation from any combination of surface, sun and atmosphere not available in other software (e.g. LESS, Qi *et al.*, 2019). DART is used for a simple urban landscape in Chapter 2. For a full description of the DART model see Gastellu-Etchegorry *et al.* (2015).

Unlike Meier *et al.*'s (2011) MODTRAN-based atmospheric correction approach that uses sensor-specific lookup tables (LUT) for each pixel distance, DART's DO and 3D ray-tracing is combined with its recently updated ability to describe both the atmosphere and any number of virtual sensors among the landscape elements. This atmosphere can describe optical and temperature properties of air between the surface and sensor at high horizontal and vertical resolution ( $< 5$  m). An updated sensor view model first shown here accepts hemispherical to narrow field of view (FOV) radiometers and frame cameras. The number of sensors used does not significantly alter the computation time. For the current work, the updated sensor view model can view the landscape from any location and direction with any sensor type rather than only downward directions with orthographic (Sobrino *et al.*, 2011) or frame camera (Yin, Lauret and Gastellu-Etchegorry, 2015; Chapter 2) perspectives. The virtual sensors can be set up to exactly reproduce "real-world" observations with any sensor view perspective, geometry and spectral response functions. Modelled output images for the perspective of these sensors include the atmospheric transmittance and emission and the surface exitance. Such a model-based setup allows for very fast adjustments of virtual camera settings without the need to create specific correction factors for a new viewing geometry.

Multiple scattering effects on emissivity corrections are simulated using DART at ground-based LWIR camera spatial resolutions ( $< 1$  m). The DO approach tracks individual rays within the model landscape in many directions to simulate multiple scattering affecting the radiation reflected from the urban canopy surfaces and then detected by the LWIR cameras.

To correct observations, DART uses a "model world" (MW) extending beyond the observed surface area, with the following components:

- 1) A vector-based 3D surface model (digital surface model, DSM) with a voxelated vegetation distribution (of e.g. trees and shrubs). The DSM consists of a mesh of triangles.
- 2) A spatial distribution of surface temperature and materials to apply across the DSM and vegetation geometry.
- 3) A spatial distribution of atmospheric properties to prescribe to the air within and above the canopy.
- 4) The position, view angle, resolution and focal length (if applicable) of the RS observations to be corrected.

DART populates the volume occupied by the MW surface with a 3D array of voxels with the selected horizontal ( $\Delta X = \Delta Y$ ) and vertical ( $\Delta Z$ ) resolution (Gastellu-Etchegorry, 2008). Each voxel manages the tracking of radiation for the media that occupies its space and stores optical properties (e.g. surface emissivity, extinction coefficient of air), temperatures (surface and air), and land cover properties (e.g. surface orientation and material). Here, effects of emission and absorption of radiation by the air along the surface-camera path (atmospheric correction, Section 3.3.2) and multiple scattering of LWIR radiation (emissivity correction, Section 3.3.3) are determined using DART and the MW (Figure 3-1). DART virtual sensors are chosen as frame (or “pinhole”) cameras (hereafter “MW cameras”) with any straight line of the MW surface projected as a straight line for the camera perspective (Hartley and Zisserman, 2004). The RT processes are for the perspective of these LWIR RS instruments to facilitate correction of atmospheric and emissivity effects on the observations.

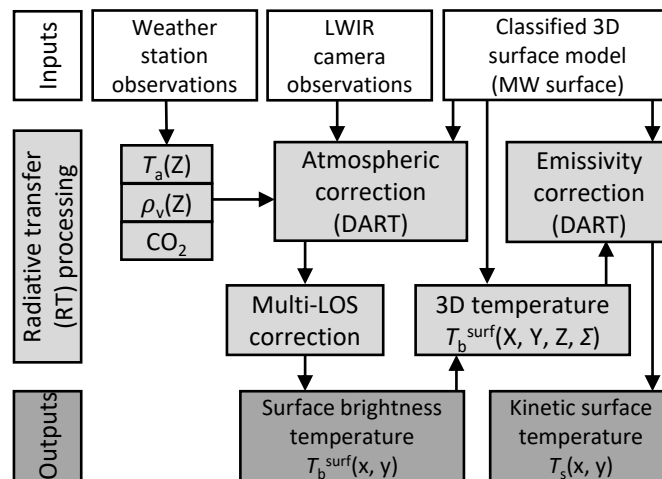


Figure 3-1. Procedure to correct LWIR camera observations for atmospheric and emissivity effects to obtain surface temperature ( $T_s$ ) for pixels. See list of symbols and acronyms for definitions.

### 3.3.2 Atmospheric correction procedure

#### 3.3.2.1 DART simulation

MW voxels that do not intersect any DSM geometry are “air voxels”. Each air voxel contains aerosols and gases, with a cross section, density, single scattering albedo and scattering regime (Rayleigh function for gases, double Henyey-Greenstein functions for aerosols), air temperature ( $T_a$ , K) and water vapor content. The vertical profile of gas and aerosol optical properties is provided by weather station observations. The choice of voxel spatial resolution needs to consider computational resources, MW surface complexity, sensor spatial resolution and surface-sensor path lengths. Following tests ( $z^{\text{path}} > 100$  m) with the applied setup (Section 3.4) we recommend a voxel resolution of  $< 10$  m. There are no other studies at this high resolution for reference.

To simulate the atmosphere RT process in DART, all MW surfaces are initially prescribed a homogeneous kinetic surface temperature. Emission of rays  $W$  from the surface ( $W^{\text{surf}}$ ) are used by DART to determine the path atmospheric transmittance. Rays that cross a DART camera pixel carry at-sensor spectral radiances for the atmosphere and surface components separately; i.e.,  $W^{\text{atm}}$  are at-sensor spectral radiance from the atmosphere only [ $L_\lambda^{\text{atm}}(x, y)$ ] and tracked  $W^{\text{surf}}$  rays with at-sensor radiance [ $L_\lambda^{\text{cam}}(x, y, W^{\text{surf}})$ ] have  $\Gamma_\lambda^{\text{atm}}(x, y)$  determined by DART using (derived from Eqn. 3.1):

$$\Gamma_\lambda^{\text{atm}}(x, y) = L_\lambda^{\text{cam}}(x, y, W^{\text{surf}}) / B_\lambda(x, y, W^{\text{surf}}). \quad \text{Eqn. 3.7}$$

#### 3.3.2.2 Post-processing of DART simulation

Although  $\Gamma_\lambda^{\text{atm}}(x, y)$  and  $L_\lambda^{\text{atm}}(x, y)$  can be used in the final atmospheric correction, with highly varying  $z^{\text{path}}$  across camera images we recommend a post-processing step for the following reasons. Atmospheric transmittance and thermal emission between two points depends on the characteristics (optical depth, single scattering albedo, temperature) of the gases and aerosols present along that path. In the LWIR the most important is water ( $\text{H}_2\text{O}$ ) vapour, and to a lesser extent, carbon dioxide and ozone. The optical depth describes the spatial integral of the product of particle density and cross section. The cross section of  $\text{H}_2\text{O}$  varies as a function of  $z^{\text{path}}$ , relative humidity (RH, %),  $T_a$ , pressure and wavelength. DART uses a single path length calculation for the atmosphere. This initial single line of sight (SLOS) path length ( $z^{\text{path, SLOS}}$ ) is used to determine a SLOS cross section of  $\text{H}_2\text{O}$  for the DART simulations and here is based on the average path length of the observations. The MW instrumentation and 3D surface is loaded into rendering software (e.g. Blender, 2018) to render images from the MW instruments as  $z^{\text{path}}(x, y)$  using the z-buffer image channel output. This method is recommended as it requires less configuration compared to determining  $z^{\text{path}}(x, y)$  by transforming 3D DSM geometry coordinates to the sensor view geometry (e.g. Meier *et al.*, 2011).

DART  $\Gamma_\lambda^{\text{atm}}$  and  $L_\lambda^{\text{atm}}$  products (Section 3.3.2.1) based on  $z^{\text{path,SLOS}}$  (defined here as  $\Gamma_\lambda^{\text{atm,SLOS}}$  and  $L_\lambda^{\text{atm,SLOS}}$ ) are corrected for the multi-line of sight (MLOS) nature of  $\Gamma_\lambda^{\text{atm}}$  and  $L_\lambda^{\text{atm}}$  by post-processing. A five-dimensional (5D) LUT for H<sub>2</sub>O built using MODTRAN and available within the DART database files and developed by the DART modelling team (Tiangang Yin, Jean-Philippe Gastellu-Etchegorry personal communication 2018) considers the self- and global-broadening of spectral lines and non-B Beer law behaviour of transmittance in spectral domains (i.e., where gas optical properties have strong spectral variations). The 5 dimensions are:  $z^{\text{path}}$ , RH,  $T_a$ , pressure and wavelength.

The optical depths ( $\tau$ ) of H<sub>2</sub>O ( $\tau_\lambda^{\text{H2O}}$ ) obtained from the 5D LUT for the SLOS [ $\tau_\lambda^{\text{H2O,SLOS}}(x, y)$ ] and MLOS [ $\tau_\lambda^{\text{H2O,MLOS}}(x, y)$ ] for each pixel are applied to convert  $\Gamma_\lambda^{\text{atm,SLOS}}$  to  $\Gamma_\lambda^{\text{atm,MLOS}}$  using:

$$\Gamma_\lambda^{\text{atm}}(x, y) = \exp \left[ \ln \left( \Gamma_\lambda^{\text{atm,SLOS}}(x, y) \right) + \tau_\lambda^{\text{H2O,SLOS}}(x, y) - \tau_\lambda^{\text{H2O,MLOS}}(x, y) \right]. \quad \text{Eqn. 3.8}$$

Initially, the equivalent emissivity for the SLOS path ( $\varepsilon_\lambda^{\text{SLOS}}$ ) is estimated:

$$\varepsilon_\lambda^{\text{SLOS}} = L_\lambda^{\text{atm,SLOS}} / B_\lambda(\bar{T}_a) \quad \text{Eqn. 3.9}$$

where  $\bar{T}_a$  (K) is the mean temperature of all air voxels in the MW area and  $B_\lambda(\bar{T}_a)$  the Planck radiance at  $\bar{T}_a$ . The equivalent emissivities for each pixel of the MLOS path [ $\varepsilon_\lambda^{\text{MLOS}}(x, y)$ ] are then estimated:

$$\varepsilon_\lambda^{\text{MLOS}}(x, y) = 1 - \exp \left[ \ln(1 - \varepsilon_\lambda^{\text{SLOS}}) + \tau_\lambda^{\text{SLOS}} - \tau_\lambda^{\text{MLOS}}(x, y) \right] \quad \text{Eqn. 3.10}$$

to calculate  $L_\lambda^{\text{atm}}$ :

$$L_\lambda^{\text{atm}}(x, y) = \varepsilon_\lambda^{\text{MLOS}}(x, y) \cdot B_\lambda(\bar{T}_a). \quad \text{Eqn. 3.11}$$

This very fast (e.g. < 1 min for six cameras each with 160 x 120 pixels) post-processing can be configured to automatically run after a DART simulation. The post-processed  $L_\lambda^{\text{atm}}(x, y)$  and  $\Gamma_\lambda^{\text{atm}}(x, y)$  are used to calculate the per-pixel and band integrated LW radiance from the observed surface [ $L^{\text{surf}}(x, y)$ , W m<sup>2</sup> sr<sup>-1</sup>] using Eqn. 3.1.  $L^{\text{surf}}$  is related to the surface brightness temperature ( $T_b^{\text{surf}}$ ) using a polynomial fit derived from a relation between band radiance and temperature, using band radiance calculated from:

$$L = \int_{7 \mu\text{m}}^{14 \mu\text{m}} d\lambda \cdot R_\lambda(\lambda) \cdot B_\lambda(T_b) \quad \text{Eqn. 3.12}$$

and fitted using a range of brightness temperatures (250 K → 350 K,  $\Delta K = 0.1$ ).

### 3.3.3 Emissivity correction procedure

LW emission and scattering processes from surface reflected radiation is determined for the at-sensor radiance using DART multiple scattering simulations of LWIR radiation across the MW surface.

### 3.3.3.1 Surface temperature and optical properties

Optical properties and LWIR radiation exiting the canopy surfaces are assigned. DART voxels that occupy DSM geometry space are surface voxels ( $Vx^S$ ) with a specified surface temperature and emissivity. Unlike other RT models with sub-facet resolution, variables are not limited to planar 3D voxels geometry (e.g. TUF, Krayenhoff and Voogt, 2007) or require the DSM triangles to be the smallest spatial unit (e.g. SOLENE, Hénon *et al.*, 2012; radiosity models, Ghandehari, Emig and Aghamohamadnia, 2018). The former prevents urban geometry such as pitched roofs and the latter is more challenging to adjust (i.e. the input DSM requires time consuming modification to adjust the model resolution). Thus, the DART combination of voxels and complex DSM geometry for RT models is both unique and highly flexible for prescribing and simulating surface properties for complex terrain. Here surface temperature and optical properties are assigned to voxels that occupy DSM surfaces classified by type (e.g. roofs, walls of different orientation, ground, grass).

Observed vegetation (e.g. trees or bushes) have leaves with optical properties as a turbid representation with a given angular distribution (Wang, Li and Su, 2007; Pisek, Ryu and Alikas, 2011). Given highly heterogeneous surface temperatures and materials, emissivity correction simulations are performed using a higher voxel resolution (i.e.  $< 2.5$  m) than the atmospheric correction.

### 3.3.3.2 Simulation and emissivity correction

DART tracked rays are emitted across the surface geometry varying with surface temperature and optical properties for the simulated wavelength(s) across a predetermined number of discrete directions ( $\Omega$ ) over the  $4\pi$  space. Each  $Vx^S$  face is split into multiple sub-faces to reduce the number of concurrent rays. Any rays tracked along the same discrete direction that cross the same sub-face are aggregated to a single ray.

A specified number of rays are emitted across the top layer of voxels in the MW (bottom of atmosphere (BOA) layer) and simulate the downwelling spectral radiance from the sky ( $L_{\lambda}^{\text{sky}}$ ) using a prescribed isotropic sky brightness temperature ( $T_b^{\text{sky}}$ ) where DART determines an isotropic  $L_{\lambda}^{\text{sky}}$  using the Planck function at the simulation wavelength.

After all rays are emitted and tracked to other surfaces or have crossed the BOA layer, some energy is scattered from the rays that intercept surface elements based on the surface reflectance ( $1 - \varepsilon_{\lambda,p}$ ) under a state of thermodynamic equilibrium. Scattered rays are re-intercepted by surfaces for a specified maximum number of scattering events. If consecutive iterations have less than a specified threshold for exitance differences or are below a specified intensity the simulation is halted. Rays exiting a MW vertical side re-enter on the opposite side with same direction but at a height that accounts for differences in topography between the exit and re-entry points.

Rays tracked across the MW camera pixels determine the at-sensor spectral radiance from the surfaces as  $L_\lambda^{\text{DART}}(x, y)$  ( $\text{W m}^{-2} \text{sr}^{-1} \mu\text{m}^{-1}$ ). At each timestep both a BB ( $\varepsilon_\lambda = 1$ ) and a non-BB ( $\varepsilon_\lambda < 1$ ) DART simulation are processed to separate the radiation received by the surfaces within each camera pixel IFOV (instantaneous FOV). Both simulation types use the same voxel resolution (Section 3.3.3.1) with a spatially variable, rather than an isothermal (e.g. Adderley, Christen and Voogt, 2015), surface temperature distribution to estimate the contribution of LWIR radiation from the urban canopy elements to the emissivity correction.

MW camera images for the non-BB simulation [ $L_\lambda^{\text{DART}}(x, y, \Omega_\uparrow, \varepsilon_\lambda < 1)$  ( $\text{W m}^{-2} \text{sr}^{-1} \mu\text{m}^{-1}$ )] have at-sensor radiance contributions from both emitted and reflected radiation leaving ( $\Omega_\uparrow$ ) the surfaces which is analogous to  $L_\lambda^{\text{cam}}$  (Eqn. 3.3). MW camera images for the BB simulation [ $L_\lambda^{\text{DART}}(x, y, \Omega_\uparrow, \varepsilon_\lambda = 1)$ ] have at-sensor radiance contributions from the emission only (analogous to  $B_\lambda(T_s)$ , Eqn. 3.3). The BB simulation is computationally cheap as only the rays from surfaces within the FOV of the MW camera(s) are tracked. Results from the DART simulations are used to separate the spectral radiance received ( $\Omega_\downarrow$ ) by the surfaces within the IFOV of each camera pixel [ $L_\lambda^{\text{DART}}(x, y, \Omega_\downarrow)$ ] ( $\text{W m}^{-2} \text{sr}^{-1} \mu\text{m}^{-1}$ ) by rearrangement of Eqn. 3.3:

$$L_\lambda^{\text{DART}}(x, y, \Omega_\downarrow) = \frac{L_\lambda^{\text{DART}}(x, y, \Omega_\uparrow, \varepsilon_\lambda < 1) - \varepsilon_\lambda(x, y)L_\lambda^{\text{DART}}(x, y, \Omega_\uparrow, \varepsilon_\lambda = 1)}{1 - \varepsilon_\lambda(x, y)} \quad \text{Eqn. 3.13}$$

with  $\varepsilon_\lambda(x, y)$  the per-pixel surface emissivity.

The required  $\varepsilon_\lambda(x, y)$  (Eqn. 3.13) can be created two ways. The optical properties across the MW surface have a simple or homogeneous distribution in the applied correction (Section 3.4) and have an isotropic scattering phase function, meaning here an image offset mask is created. For scenes with more complex emissivity distributions including anisotropic scattering phase functions, the view angle dependent emissivity across an image can be determined using DART (Appendix C).

The final conversion of  $T_b^{\text{surf}}(x, y)$  to surface temperature  $T_s(x, y)$  is performed using the inverse of the Planck function on the emissivity corrected spectral radiance:

$$T_s(x, y) = B^{-1} \left\{ \frac{B_\lambda[T_b^{\text{surf}}(x, y)] - [1 - \varepsilon_\lambda(x, y)]L_\lambda^{\text{DART}}(x, y, \Omega_\downarrow)}{\varepsilon_\lambda(x, y)} \right\}. \quad \text{Eqn. 3.14}$$

By simulation of RT processes at a narrow waveband, this approach assumes the surface and sky are grey bodies. Further, not explored in this study is the possibility of integrating over a broader range of wavelengths with spectral variance in surface emissivity.

## 3.4 Application of Methods

### 3.4.1 Study area and observation sites

The study area (Figure 3-2), in the Borough of Islington, London, UK (51°31'35" N, 0°06'19" W), has two primary observation sites on two high-rise residential tower blocks: IMU at 74 m agl (above ground level) and WCT at 36 m agl. A third rooftop (CUB, 26 m agl) is used for observational evaluation of the atmospheric correction. The area has an irregular arrangement of streets often lined with deciduous trees, with four- to six-storey residential and commercial buildings either as terraces or as large single units, parks with green space and asphalt, and three additional high-rise residential tower blocks (i.e. five high-rise buildings including IMU and WCT).

The MW is a 420 x 420 m horizontal area centred on the IMU site with a DSM and VCEs (Figure 3-2e, f) determined by Google Earth Pro (Google, 2019a) images and photogrammetry (Appendix D). The DSM (Figure 3-2e, f; grey) has ~750,000 triangles to capture all the Google Earth 3D surface elements except for vegetation. Vegetation canopy elements (VCE) are a 3D array of voxels ( $V_x^V$ ) at  $\Delta X = \Delta Y = 1$  m,  $\Delta Z = 0.1$  m (Figure 3-2e, f; green) that are either filled with VCE or empty.

As with vegetation canopies (Kuusk, 2017), a key issue in developing 3D RT models for urban canopies relates to how the canopy structure is described. Here a uniquely high level of detail (LOD) canopy description is created (Appendix D.1), with sub-facet structures such as sloped roofs and balconies, rather than the planar faces as used in other studies (e.g. Meier *et al.*, 2011; Ghandehari, Emig and Aghamohamadnia, 2018). Its triangles are classified by orientation and material properties ( $\Sigma$ ) including their cardinal facing direction, roofs, ground and vegetation (Figure 3-2c, Appendix D.2).

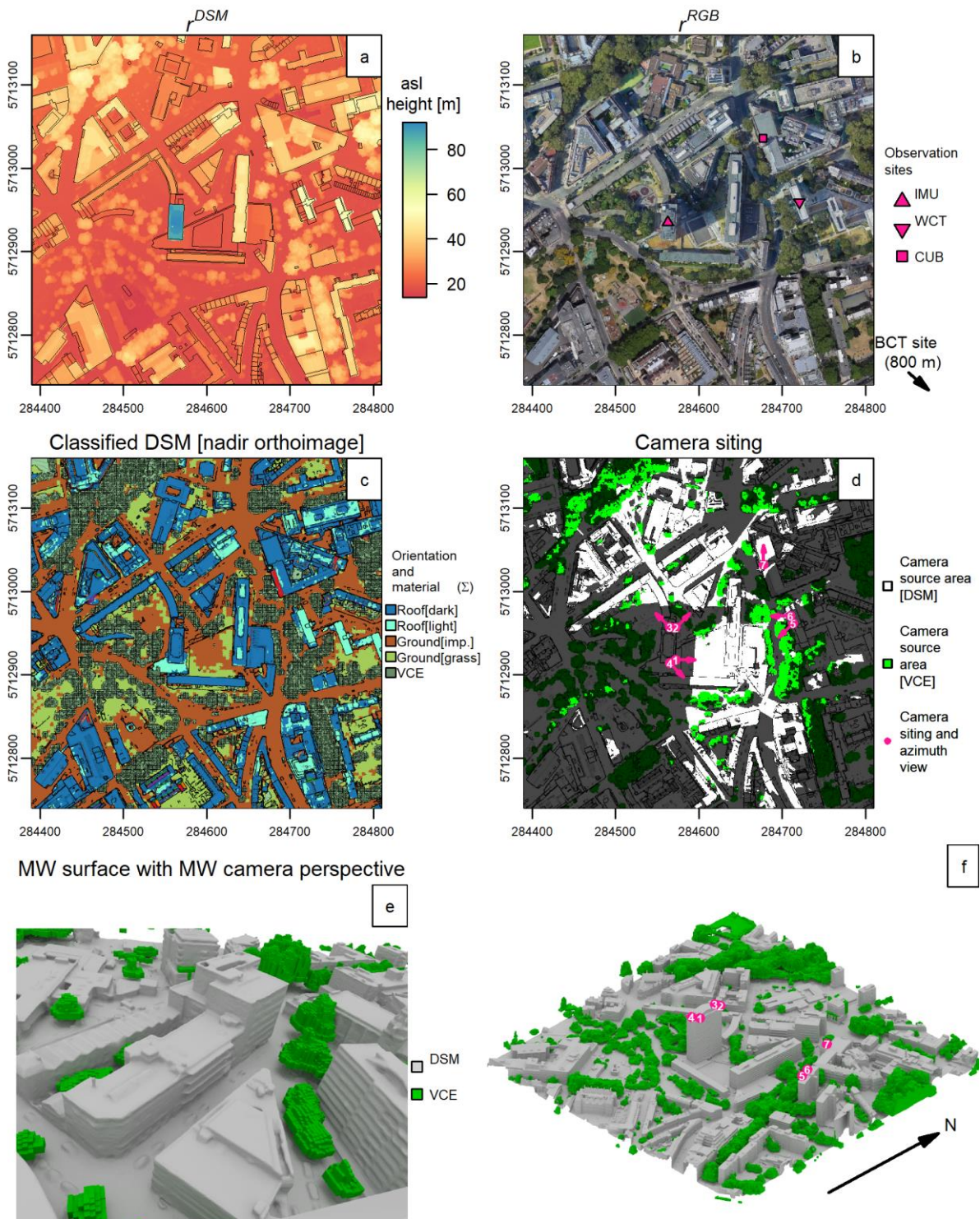


Figure 3-2. Study area characteristics: plan view of (a) above sea level raster digital surface model ( $r^{DSM}$ ) of all surfaces with (black lines) a reference building footprint model from Evans, Hudson-Smith and Batty (2006), (b) orthorectified raster RGB ( $r^{RGB}$ ) image from a mosaic of Google Earth (Google, 2019a) images (Appendix D.1) with (symbols) locations of the study sites, (c) “model world” (MW) surface geometry with surface orientation and material properties ( $\Sigma$ ), (d) impervious and grass surfaces (white) and vegetation canopy elements (VCEs, light green) seen by the LWIR cameras within the observation network (Table 3-1). Camera locations (numbers) shown as pink dots (white text) with approximate azimuthal facing (pink arrow). Dark colours are surfaces not seen by cameras. MW surface geometry rendered using Blender (Blender, 2018) for: (e) camera C2 perspective and (f) oblique orthogonal view of scene. Coordinates for (a – d) are Coordinate Reference System WGS84 UTM grid zone 31N for study area extent of 420 m x 420 m.

### 3.4.2 Instrumentation and observations

Optris PI-160 (Optris GmbH, 2018) LWIR cameras are deployed to observe the upwelling LWIR radiation (Table 3-1; Figure 3-3). The small, lightweight, industrial-grade camera uses uncooled microbolometer detectors, with  $25\ \mu\text{m} \times 25\ \mu\text{m}$  bolometer elements in a  $160 \times 120$  focal plane array. The instrument outputs digital number (DN) values for each microbolometer pixel. DN values relate to at-sensor  $7.5 - 14\ \mu\text{m}$  radiance and were radiometrically calibrated by the manufacturer two months prior to measurements using a BB reference. Each operational measurement is calibrated using an internal shutter with reference temperature and BB characteristics. During this calibration the shutter is put in the optical path of the instrument whereby its emission is sampled. The noise equivalent differential temperature (NEDT) is 0.1 K and the manufacturer's specified accuracy is  $\pm 2\ ^\circ\text{C}$  at ambient temperatures  $23 \pm 5\ ^\circ\text{C}$  (Optris GmbH, 2018), which is typical of most microbolometer LWIR camera systems available and used for such applications (e.g. Meier and Scherer, 2012; Adderley, Christen and Voogt, 2015; Lee *et al.*, 2018).

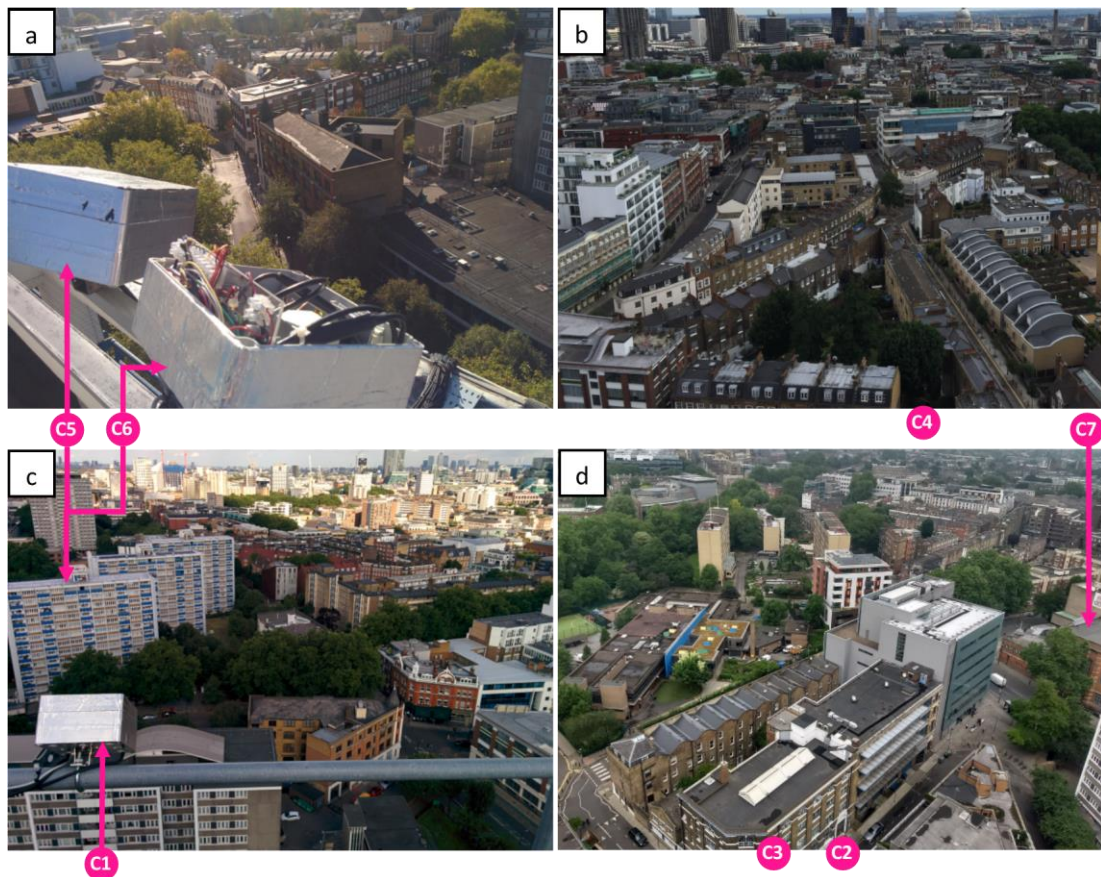


Figure 3-3. Digital camera images of: (a) cameras C5 and C6 taken at WCT site on 25<sup>th</sup> October 2017 looking southwest, with C6 enclosure shown open for maintenance, (b) southeast view from IMU site taken next to C4 on 21<sup>st</sup> July, (c) C1 enclosure taken at IMU site on 12<sup>th</sup> July looking east with WCT (C5, C6) site in background, and (d) northeast view from IMU site taken next to C2 and C3 on 30<sup>th</sup> May, with a portion of the roof at CUB site sampled by C7 (Appendix G) annotated.

The cameras have external enclosures (Figure 3-3, Appendix E) to reduce body temperature changes from strong winds and/or direct sunlight and protect against corrosion and have a derived spectral response function (Appendix F).

With seven LWIR cameras installed at IMU, WCT and CUB observation sites (Section 3.4.1) for the study period (7<sup>th</sup> July – 10<sup>th</sup> November 2017) multiple view angles of surfaces with different orientation, material, microscale structure and distances to the cameras are sampled.

The base sample resolution is 1 min. To reduce the frequency of observational gaps, the median brightness temperature through time is taken from 5 images giving (e.g. Figure 3-4a) a final temporal resolution of 5 min.

Table 3-1. Siting properties of the ground-based longwave infrared (LWIR) cameras installed on high-rise residential towers (IMU, WCT) and London City University Building roof (CUB) within the study area. Study area, sites and position of instrumentation shown in Figure 3-2 and Figure 3-3. Further camera meta data shown in Appendix B. See list of symbols and acronyms for all other definitions.

Camera name	Installation site	Field of view (°) Horizontal x vertical	Cardinal facing	Viewing zenith angle (°)	5th percentile path length (m)	Median path length (m)	95th percentile path length (m)
		FOV		$\theta$	$z^{\text{path}}$	$z^{\text{path}}$	$z^{\text{path}}$
C1	IMU	68.6 x 54.2	E	46.5	72.3	88.8	178.8
C2	IMU	62.6 x 49.1	NE	51.7	70.1	97.9	198.93
C3	IMU	62.8 x 49.2	NWW	52.9	73.1	106.6	198.2
C4	IMU	37.3 x 28.4	SE	56.7	89.0	122.7	201.2
C5	WCT	38.4 x 29.3	SW	66.6	47.1	79.0	167.4
C6	WCT	62.4 x 48.9	W	61.7	41.3	67.5	220.1
C7	CUB	38.1 x 29.0	N	~60	~15	~15	~15

The uncertainty in UTC time is assumed to be < 10 s. The cameras require a 2 h “warm up” period (Chapter 2) to allow the current-induced self-heating of the sensor elements to stabilize (Vollmer and Möllmann, 2017). Data prior to this are excluded. All data 0.5 h prior and 8 h after any rain event are excluded. A Davis Vantage Pro 2 weather station installed 114 m agl on top of a residential tower block located at the BCT site (1.1 km southeast of the IMU site) provides measurements of rain rate ( $\text{mm h}^{-1}$ ) along with  $T_a$ , RH, and atmospheric pressure (hPa) required for the atmospheric correction routine. A Kipp & Zonen CNR1 net radiometer installed at IMU next to C4 (Figure 3-2e, f) measured broadband (4.5 – 42  $\mu\text{m}$ ) LWIR irradiance downward from the sky ( $E_{\text{LW}}^{\text{sky}}$ ,  $\text{W m}^{-2}$ ) for the emissivity correction routine.

The LWIR cameras lens distortion is corrected to match the rectilinear projection of the MW cameras (Appendix A) and the MW cameras are sited in the model domain using on-site measurements of each camera location and view angle (Table 3-1) and a fine-adjustment (Chapter 2).

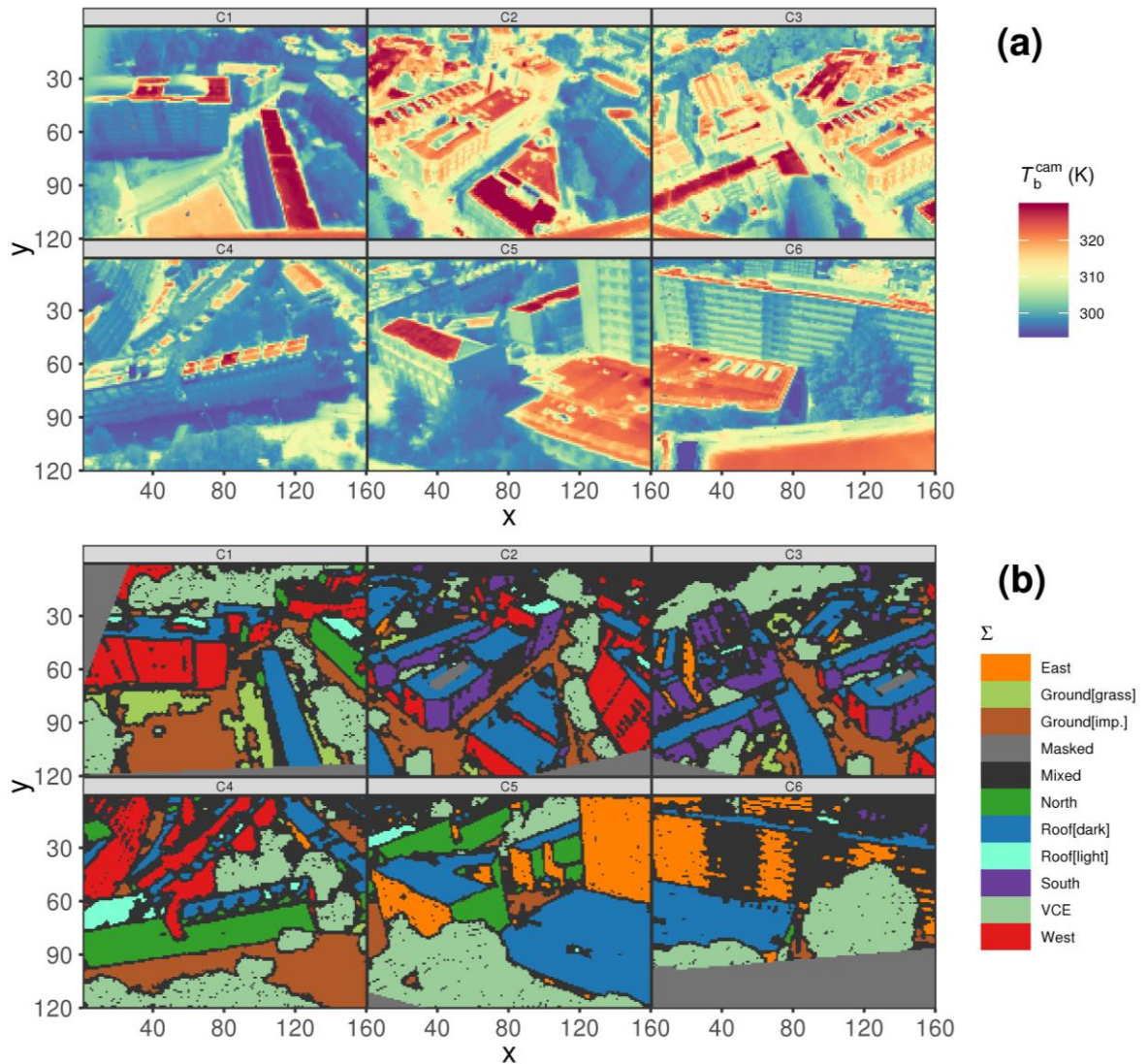


Figure 3-4. (a) Undistorted brightness temperature images ( $T_b^{\text{cam}}$ ) from Optris PI longwave infrared (LWIR) cameras at 11:30 on 27<sup>th</sup> August 2017 and (b) surface orientation and material property ( $\Sigma$ ) projected onto the image plane (IP) of each “model world” (MW) camera classified for each image pixel using the perspective projection (Chapter 2) of a similarly classified DSM (Appendix D.2).

The per-pixel orientation and material classes ( $\Sigma(x, y)$ , Figure 3-4b) uses information from the similarly classified DSM (Appendix D.2) that is projected for the MW camera perspectives following methods in Chapter 2.  $\Sigma(x, y)$  enables the inter- $\Sigma$  classification of observations for use in prescribing temperature for the DART emissivity correction (Section 3.4.3.2).

### 3.4.3 Model setup

The general model parameters for each simulation type used for the correction of observations (Table 3-2) are explained below.

Table 3-2. General model parameters set for the Discrete Anisotropic Radiative Transfer (DART) model atmospheric and emissivity correction routines.

Model parameter	Units	Atmospheric correction	Emissivity Correction
DART version	-	5.7.4 build 1094	5.7.1 build 1058 (5.7.4 build 1094)
Voxel resolution $\Delta X, \Delta Y, \Delta Z$	m	2.5, 2.5, 2.5	1, 1, 1
Voxel sub-faces	-	1	36
Wavelength(s)	$\mu\text{m}$	7 – 14, $\Delta\lambda = 0.2$	10
Discrete directions	-	628 (for image directions only)	628
BOA ray density	rays $\text{m}^{-2}$	-	1600
Surface ray density	rays $\text{m}^{-2}$	10,000	10,000
Number of scattering events	-	0	5
Surface temperature description	-	Homogeneous (300 K)	From LWIR camera $T_b^{\text{surf}}$ (see text)
Emissivity	-	1	Bulk variation across man-made surfaces using SLUM dataset (0.89 – 0.97)

### 3.4.3.1 Atmospheric correction

A vertical profile of  $T_a$  and water vapor content for each horizontal voxel layer is created from the BCT *in-situ* measurements of  $T_a$ , RH and atmospheric pressure. Each horizontal layer of air voxels has  $T_a$ , water vapour content and pressure extrapolated by DART using a midlatitude summer atmosphere profile. As the weather station is 40 m above the top of the MW surface,  $T_a$  is extrapolated down to the bottom layer of the MW using the dry adiabatic lapse rate.

Given the large number of camera observations, DART simulations for each observation timestep (5 min) are not computationally viable (8 CPU threads per simulation: ~12 min using ~8GB memory and 8 processor cores). Instead, a 60 min simulation timestep is used. Post-processed (Section 3.3.2.2) results for each band and timestep are temporally interpolated to the observational resolution using a spline (Moritz and Bartz-Beielstein, 2017). Interpolated values near timesteps without observations (e.g. maintenance, quality control) are rejected. To reduce the number of emission sources and subsequent computation time, VCE geometry is not included during atmospheric correction.

### 3.4.3.2 Emissivity correction

For the downwelling longwave radiation from the sky,  $E_{\text{LW}}^{\text{sky}}$  from the CNR1 radiometer is related to  $T_b^{\text{sky}}$  for DART, using the Stefan-Boltzmann law:

$$T_b^{\text{sky}} = \sqrt[4]{E_{\text{LW}}^{\text{sky}} / \sigma}. \quad \text{Eqn. 3.15}$$

Atmospherically corrected surface temperature ( $T_b^{\text{surf}}$ ) observations are prescribed across the MW surfaces. The median  $T_b^{\text{surf}}$  of all pixels within a certain orientation and material class ( $\Sigma$ ) is  $\langle T_b^{\text{surf}}(\Sigma) \rangle$  (class median =  $\langle \rangle$ ) are used, except for VCE. As  $T_s$  for trees is nearly equal to  $T_a$  (Meier and Scherer, 2012),  $T_a$  from the Davis weather station is used for VCE. Broadband emissivity values are allocated for each DSM surface orientation and material property. As comprehensive urban emissivity databases are not readily available (Ghandehari, Emig and Aghamohamadnia, 2018), a representative range of urban emissivity values are used for the emissivity correction. Similar to Mitraka *et al.* (2012), the broadband (8 – 14  $\mu\text{m}$ ) emissivity from all non-metal and anthropogenic materials in a spectral library (SLUM, Kotthaus *et al.*, 2014) is used as a fully opaque and grey body estimate for all non-vegetative surfaces (roof, ground, all walls) with the mean ( $\epsilon_{0.93}$ ) being used as a baseline value. Minimum ( $\epsilon_{0.89}$ ) and maximum ( $\epsilon_{0.97}$ ) values are used in a sensitivity analysis (Section 3.5.2.3). VCE have a turbid representation of leaves within each  $Vx^V$  and are given a spherical angular distribution. Leaves are given “deciduous leaf” optical properties at 10  $\mu\text{m}$  from the DART spectral database (leaf transmissivity = 0.0145, reflectance = 0.0195) with a leaf area density [leaf area within voxel / voxel volume ( $\text{m}^2 \text{m}^{-3}$ )] of 1.6 (Lalic and Mihailovic, 2004; Jeanjean *et al.*, 2017).

Rays tracked from turbid VCE directly to camera pixels are not considered. Accurate tracking of rays from turbid media across camera pixels requires higher resolution DART runs (e.g. higher density of rays and voxel sub-faces) and/or leaves determined using the discrete triangle cloud option. These factors are not tested as part of this study, so VCE pixel temperatures are not corrected for emissivity effects and are masked (e.g. Figure 3-4b). Ground-based thermography specific to urban trees and a simple emissivity correction applicable to observed VCE can be found in Meier and Scherer (2012).

## 3.5 Results

### 3.5.1 Atmospheric correction

To evaluate the atmospheric correction, cameras C2 and C7, (Table 3-1) both viewing a flat asphalt roof (CUB, Figure 3-2, Appendix G details C7 siting) are used. For C2, the  $\sim 50 \text{ m}^2$  area is  $\sim 155 \text{ m}$  ( $z^{\text{path}}$ ) away and covers seven pixels (Figure 3-4a,  $x = 35$ ,  $y = 140$ ), whereas C7 ( $z^{\text{path}} < 15 \text{ m}$ ) has a 18542 pixel view. After DART shadow distribution simulations (Chapter 2), pixels are manually selected to exclude any shaded areas during the day as found in Meier *et al.*'s (2011) evaluation. Given the short C7 path length, atmospheric effects for this camera are assumed to be negligible [i.e.  $T_b^{\text{cam}}(\text{C7}) \approx T_b^{\text{surf}}(\text{C7})$ ].

During a predominantly cloudy evaluation period (7<sup>th</sup> – 26<sup>th</sup> September 2017) the minimum (maximum)  $T_a$  was 281.4 (293.9) K and minimum (maximum) absolute humidity  $\rho_v$  was 7.03 (12.71)

g m<sup>-3</sup> (Figure 3-5c). Less cloudy daytime conditions near the end of the period (from 22<sup>nd</sup> Sep) coincide with higher  $T_a$  values. The roof is fully sunlit (Figure 3-5d) from ~40 min after sunrise (e.g. 15<sup>th</sup> September sunrise = 06:30, sample area fully sunlit at 07:05). Quality control (e.g. rain events (Figure 3-5d), camera maintenance) removed 1670 (29 %) 5 min periods of  $T_b^{\text{cam}}$  observations (Section 3.4.2). As site access prevented longer evaluation, more diverse meteorological conditions should be evaluated in future studies.

The median brightness temperature of pixels that view the roof are used from each camera at each timestep. The difference in the brightness temperature observed by the two cameras  $\Delta T_b^{\text{cam}} = T_b^{\text{cam}}(\text{C2}) - T_b^{\text{surf}}(\text{C7})$  (Figure 3-5a, blue) quantifies the atmospheric effect on the raw observations. Generally,  $\Delta T_b^{\text{cam}}$  is negative during the day and approaches zero at night, as atmospheric absorption reduces the amount of radiation leaving the surface that is received by the sensor, particularly during daytime when the surface is much warmer than the air. For clear and partly-cloudy daytime periods,  $\Delta T_b^{\text{cam}}$  is typically < -2 K (minimum -2.97, 15<sup>th</sup> September 09:15) when the brightness - air temperature differences are  $(T_b^{\text{cam}}(\text{C7}) - T_a) > \sim 10$  K. Nocturnal clear and partly-cloudy periods (e.g. 12<sup>th</sup>, 16<sup>th</sup> September, Figure 3-5d) can have high  $\Delta T_b^{\text{cam}}$  variability between timesteps. Sensor timestamp differences (~10 s) combined with fast temporal response (seconds) of  $T_s$  to changes in turbulent sensible heat fluxes (Christen, Meier and Scherer, 2012; Crawford *et al.*, 2017), intermittent cloud cover and anthropogenic heat sources may explain this variability.

After correction of atmospheric effects,  $T_b^{\text{surf}}(\text{C2})$  is significantly closer to the reference observations ( $\Delta T_b^{\text{surf}} = T_b^{\text{surf}}(\text{C7}) - T_b^{\text{surf}}(\text{C2})$  Figure 3-5a, black). The mean absolute error (MAE) between  $T_b^{\text{surf}}(\text{C7})$  and  $T_b^{\text{surf}}(\text{C2})$  is 0.39 K for all observations ( $r^2 = 0.998$ , Figure 3-6) and 0.48 K (0.28 K) for day (night) time observations, respectively. This is a significant improvement compared to the uncertainty associated with omitting the atmospheric correction particularly during daytime where  $T_b^{\text{surf}}(\text{C7})$  and  $T_b^{\text{cam}}(\text{C2})$  have 1.03 K MAE. While the magnitude of the atmospheric correction ( $T_b^{\text{cam}}(\text{C2}) - T_b^{\text{surf}}(\text{C2})$ , Figure 3-5a, red) generally follows the variations of atmospheric effect [observationally quantified by  $T_b^{\text{cam}}(\text{C2}) - T_b^{\text{surf}}(\text{C7})$ , Figure 3-5a, blue], some artefacts remain during morning when  $\Delta T_b^{\text{surf}}$  is strongly positive at times. Of the 1<sup>st</sup> percentile of  $\Delta T_b^{\text{surf}}$  (> 1.02 K), most (93 %, n = 39) occur between 07:00 – 09:00 under clear or partly-clear sky conditions. Observations with strongly negative  $\Delta T_b^{\text{surf}}$  occur in the afternoon, with 95 % (n = 42) of observations in the 99<sup>th</sup> percentile ( $\Delta T_b^{\text{surf}} < -0.97$  K) being between 12:00 – 15:00.

Both the strongly positive and negative  $\Delta T_b^{\text{surf}}$  values could partly result from uncertainties in camera calibration. During the morning, rapid changes in air temperature can cause uneven heating of the camera bodies. During the afternoon, the vertical profile of air temperature may the air temperature between the cameras to differ. Inter-camera discrepancies in the manually selected area of roof could yield differences in observations depending on the fraction of shaded surface seen by each camera during these periods (also noted by Meier *et al.*, 2011). As the dry adiabatic lapse rate rather than the

environmental lapse rate are used, humidity is not accounted for (Section 3.3.2.1). A weather station installed near ground level of the MW area to provide horizontal variability in temperature and water vapour for the correction and associated uncertainties unfortunately failed shortly prior to this period.

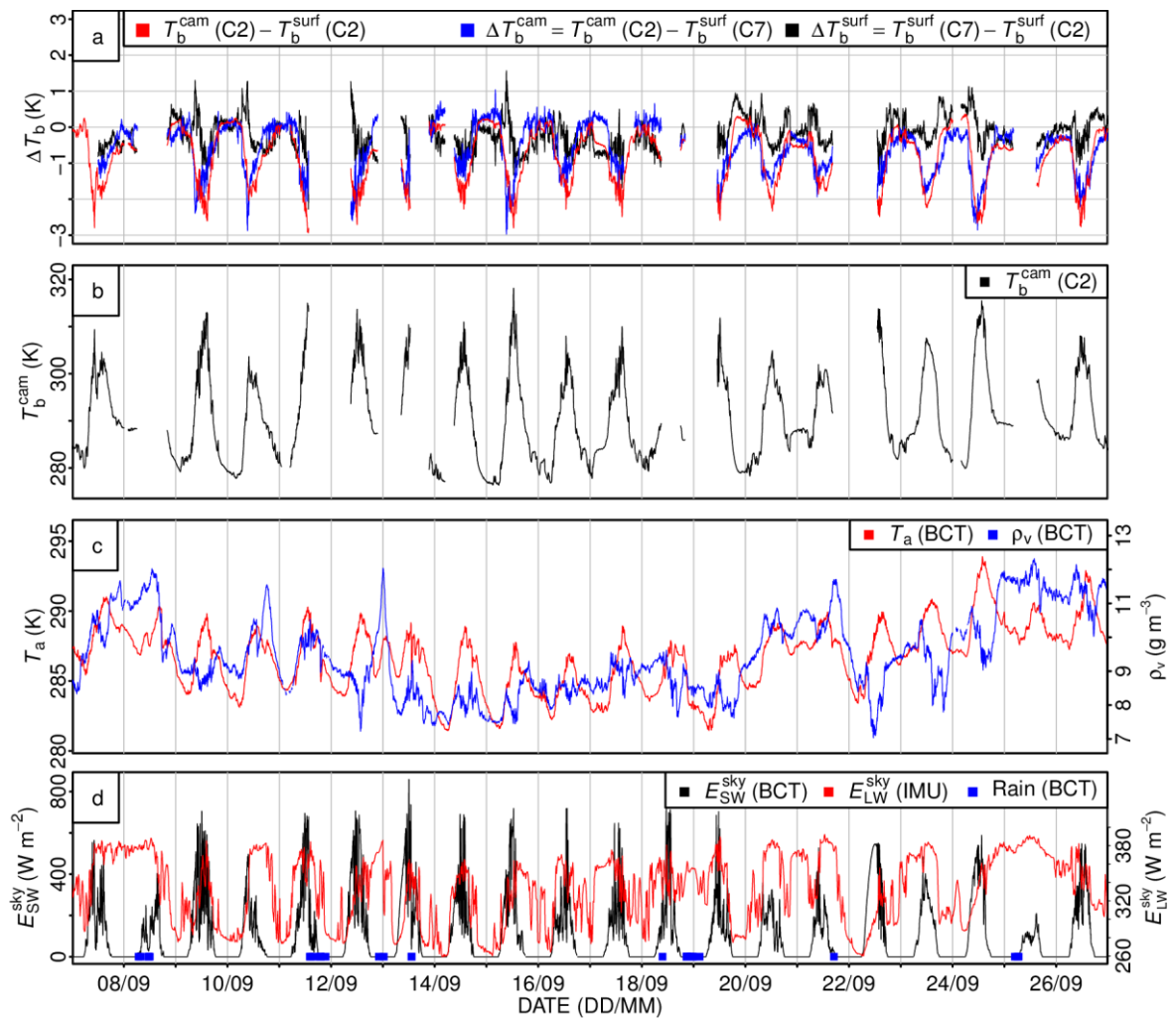


Figure 3-5. Atmospheric correction evaluation using the C2 and C7 cameras (Table 3-1, Figure 3-2, Figure 3-3) and meteorological variables (Section 3.4.2) observed at BCT and IMU sites (Figure 3-2): (a, red) uncorrected ( $T_b^{\text{cam}}$ ) minus corrected ( $T_b^{\text{surf}}$ ) surface brightness temperature for 155 m “far” path length from C2, (a, blue) uncorrected “far” minus reference ~15 m “near” path length from C7 and (a, black) corrected “far” minus “near”, (b)  $T_b^{\text{cam}}$ (C2), (c) air temperature ( $T_a$ ) and absolute humidity ( $\rho_v$ ) and (d) incoming shortwave ( $E_{\text{SW}}^{\text{sky}}$ ) and longwave ( $E_{\text{LW}}^{\text{sky}}$ ) radiation, and timing of rainfall (blue).

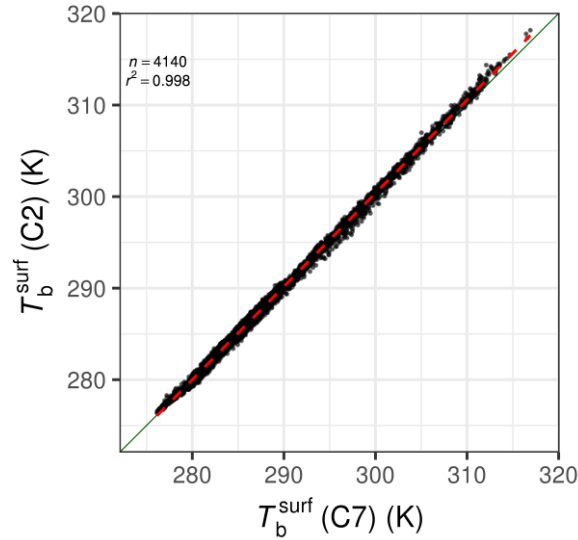


Figure 3-6. Comparison of surface brightness temperature corrected for atmospheric effects of a flat felt roof sampled with path length  $\sim 155$  m [ $T_b^{\text{surf}}(\text{C2})$ ] and surface brightness temperature of the same surface sampled with path length  $\sim 15$  m [ $T_b^{\text{surf}}(\text{C7})$ ] with negligible atmospheric effects.

When the atmospheric correction procedure is applied to all cameras with substantial path length differences (Table 3-1) for the evaluation period, the greatest differences between the uncorrected at-sensor brightness temperature  $T_b^{\text{cam}}(x, y)$  to surface brightness temperature  $T_b^{\text{surf}}(x, y)$  are seen on 24<sup>th</sup> September. The median of  $T_b^{\text{cam}}(x, y) - T_b^{\text{surf}}(x, y)$  for pixels with  $z^{\text{path}}$  between 240 – 260 m reaches a minimum of -4.53 K at 10:10. Impacts of different path lengths on this day are summarised in Figure 3-7 (see Appendix I for other days). The variability of  $T_b^{\text{cam}}(x, y) - T_b^{\text{surf}}(x, y)$  within each  $z^{\text{path}}$  bin (Figure 3-7) can be large (e.g. median -2.34 K, IQR 1.93 K at 06:00) as the magnitude of the correction varies based on the absolute value of  $T_b^{\text{cam}}(x, y)$ , which again is highly variable in the urban setting (e.g. Figure 3-4a).

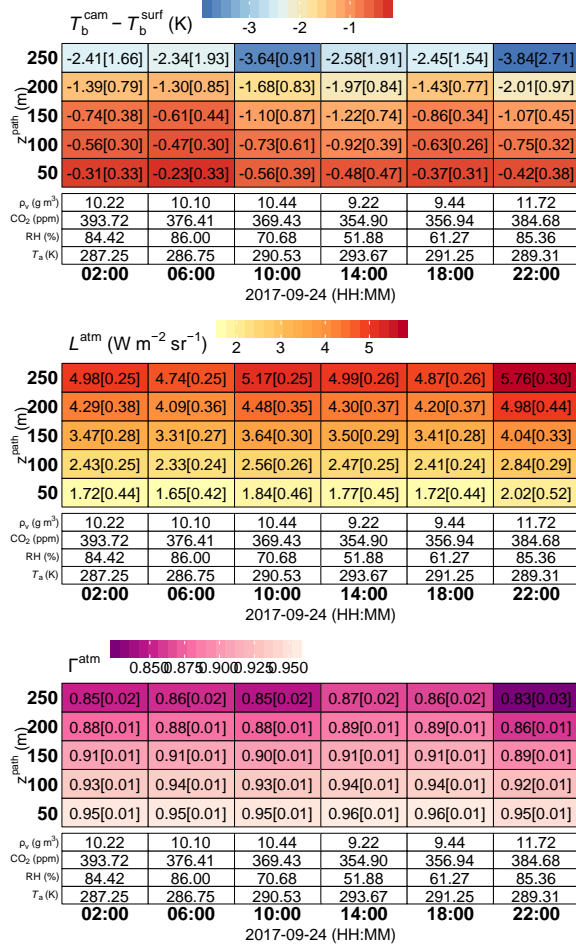


Figure 3-7. Atmospheric correction of longwave infrared (LWIR) camera observations for six timesteps on 24<sup>th</sup> September 2017, using pixels within  $\pm 10$  m of five path lengths ( $z^{\text{path}}$ ) with (white cells) meteorological input variables (coloured cells) median[IQR] values of: (a) difference between uncorrected camera brightness temperature ( $T_b^{\text{cam}}$ ) and corrected surface brightness temperature ( $T_b^{\text{surf}}$ ), (b) surface-camera path contribution of the at-sensor band integrated atmosphere radiance ( $L^{\text{atm}}$ ), and (c) surface-camera path contribution of band integrated atmospheric transmissivity ( $\Gamma^{\text{atm}}$ ). See list of symbols and acronyms for all definitions and Appendix I for other days.

Analysis of all pixels from all cameras on the 24<sup>th</sup> September (Figure 3-8a) indicates a decrease in  $T_b^{\text{cam}}(x, y) - T_b^{\text{surf}}(x, y)$  with  $z^{\text{path}}$ . This is explained by the associated increase (decrease) of  $L^{\text{atm}}$  ( $\Gamma^{\text{atm}}$ ) (Figure 3-8b, c). The outlier points (grey < 1000 pixels or 0.003 % of observations throughout the day) in Figure 3-8 are mainly from  $\Gamma^{\text{atm}}$  artefacts (Figure 3-9c). The 1<sup>st</sup> to 99<sup>th</sup> percentile range for Figure 3-8a is -3.17 to 0.06 K. Results are similar to Meier *et al.* (2011) which found  $T_b^{\text{cam}} - T_b^{\text{surf}} \approx -6.5$  K for  $z^{\text{path}} = 310$  m around midday, but are potentially underestimated compared to Adderley, Christen and Voogt (2015) where with a 15 – 75 m  $z^{\text{path}}$  range,  $T_b^{\text{cam}} - T_b^{\text{surf}}$  was up to -8.6 K. Note that inter-study comparisons are challenging, as differences in  $z^{\text{path}}$ ,  $T_b^{\text{cam}}$ , meteorological conditions and spectral response functions affect the magnitude of atmospheric effects.

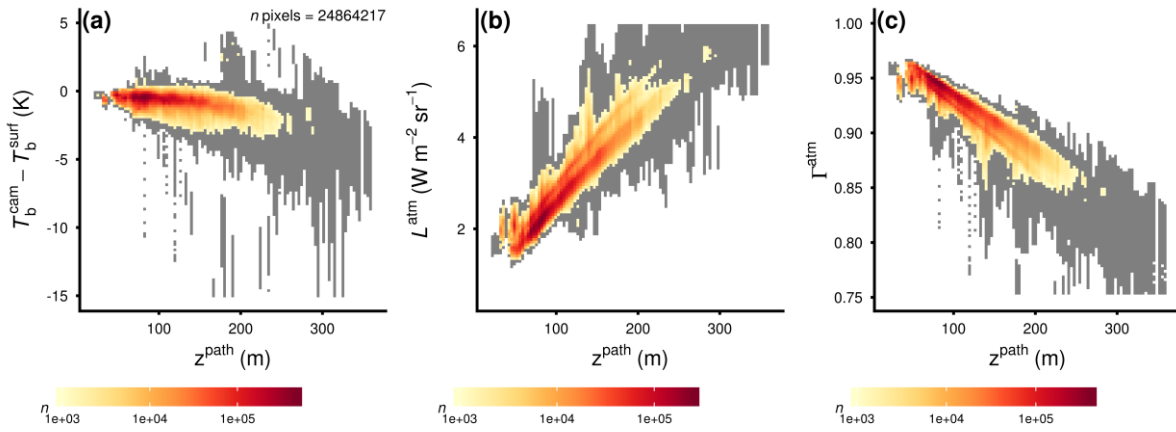


Figure 3-8. Per-pixel atmospheric correction of all longwave infrared (LWIR) camera observations at 5 min resolution on 24<sup>th</sup> September 2017, with density of pixels (coloured shading; grey < 1000 pixels) against surface-camera path length ( $z^{\text{path}}$ ) and (a) difference between uncorrected camera brightness temperature ( $T_b^{\text{cam}}$ ) and corrected surface brightness temperature ( $T_b^{\text{surf}}$ ), (b) surface-camera path contribution of the at-sensor band integrated atmosphere radiance ( $L^{\text{atm}}$ ), and (c) surface-camera path contribution of band integrated atmospheric transmissivity ( $\Gamma^{\text{atm}}$ ).

To illustrate spatial variations of the atmospheric correction components for the study area, the MW surface and cameras are used to calculate  $z^{\text{path}}$ ,  $L^{\text{atm}}$  and  $\Gamma^{\text{atm}}$  (Figure 3-9). As seen from the path lengths (Figure 3-9a), the complex real world (RW) surface geometry (Figure 3-2) is accurately reproduced, including buildings with complex footprints and multiple storeys (e.g. Figure 3-9a C3,  $x = 40$ ,  $y = 35$ ) and sloped roofs (e.g. Figure 3-9a C5,  $x = 40$ ,  $y = 50$ ; C6,  $x = 40$ ,  $y = 10$ ). Oblique view angles under RW conditions demand a high LOD surface geometry representation, as simplified MW geometry (e.g. flat roofs, planar walls) could lead to inaccuracies in modelled surface-sensor view geometry. For example, if the MW had flat roofs (i.e. low LOD) a C6 pixel viewing a sloped roof (Figure 3-9a C6,  $x = 40$ ,  $y = 10$ ) has  $z^{\text{path}} \approx 75$  m but with a low LOD geometry the roof may not be registered and instead have  $z^{\text{path}} > 250$  m and hence an error in atmospheric correction of over 3K (Figure 3-7).

Variability of  $z^{\text{path}}$  with buildings and oblique viewing geometry (Figure 3-9a) is resolved by the atmospheric emission (Figure 3-9b) and transmissivity (Figure 3-9c) components of the correction. The spatial variability of  $L^{\text{atm}}(x, y)$  and  $\Gamma^{\text{atm}}(x, y)$  is related to the building geometry and  $z^{\text{path}}$ . Typically, a greater  $z^{\text{path}}$  causes an increase (decrease) of  $L^{\text{atm}}$  ( $\Gamma^{\text{atm}}$ ) (Figure 3-7). A small number of pixels underestimate  $\Gamma^{\text{atm}}$  (e.g. Figure 3-9c C5,  $x = 65$ ,  $y = 80$ ). For the surface within the IFOV of these pixels, the density of emitted rays ( $W^{\text{surf}}$ , Section 3.3.2.1) may be too low for the accurate determination of  $L^{\text{cam}}(W^{\text{surf}})$ . These artefacts can be eliminated by increasing the voxel resolution and the density of  $W^{\text{surf}}$  at the expense of computation time. Pixels that view surfaces outside the MW area (e.g. Figure 3-9c C4,  $x = 38$ ,  $y = 5$ ) are excluded.

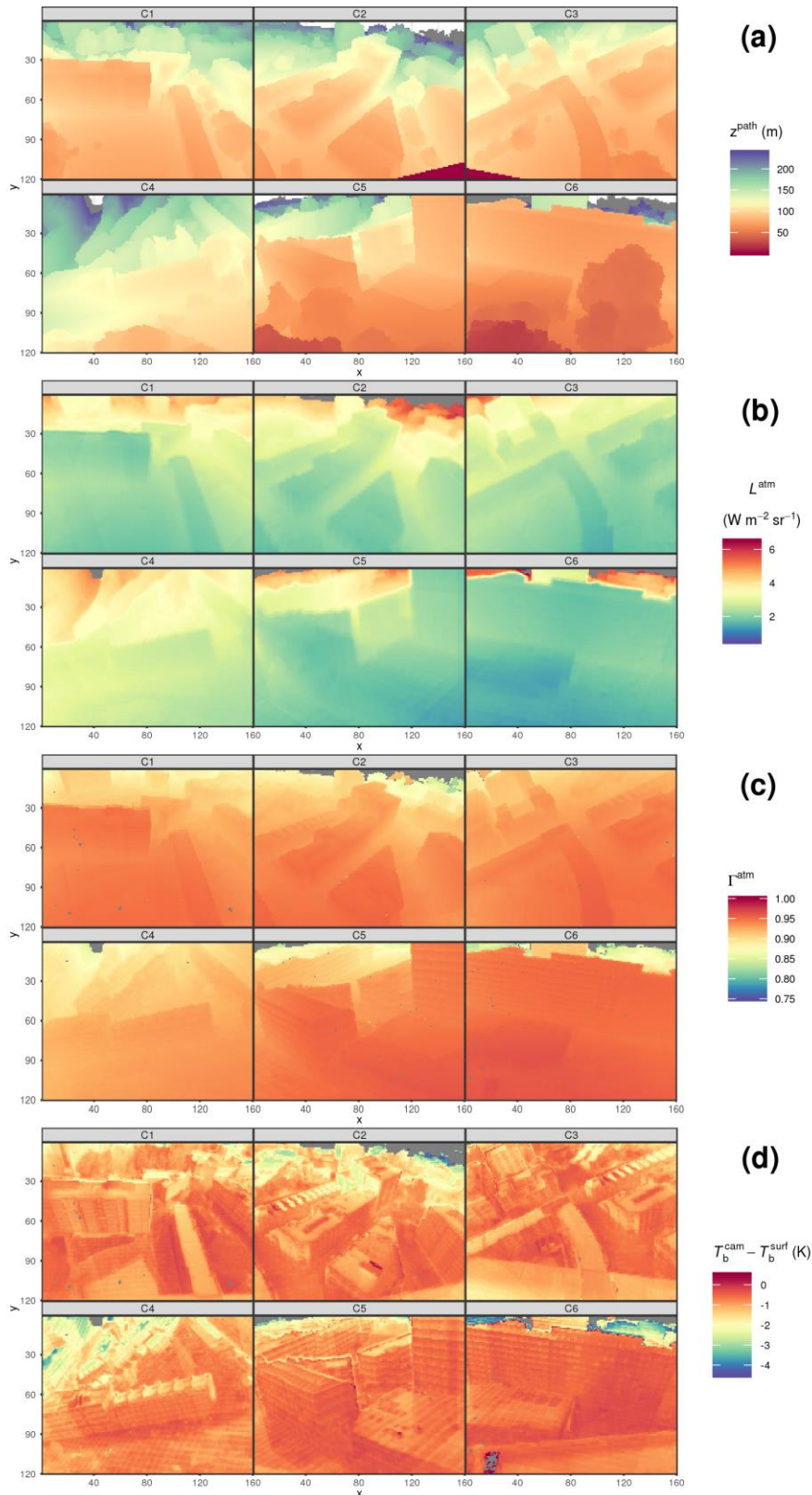


Figure 3-9. Atmospheric correction variables for each camera (Table 3-1) at 12:00 (24<sup>th</sup> September 2017): (a) Surface – sensor path length ( $z^{\text{path}}$ , m), (b) band integrated longwave emission from the atmosphere [ $L^{\text{atm}}(x, y) = \int_{7\mu\text{m}}^{14\mu\text{m}} d\lambda \cdot R_{\lambda}(x, y) \cdot L_{\lambda}^{\text{atm}}(x, y)$ ] with  $d\lambda = 0.2$  and  $R_{\lambda}(x, y)$  the sensor spectral response function, (c) band average atmospheric transmissivity. DART calculated  $\Gamma_{\lambda}^{\text{atm}}(x, y)$  and  $L_{\lambda}^{\text{atm}}(x, y)$ , and (d) final difference between uncorrected ( $T_b^{\text{cam}}$ ) and corrected ( $T_b^{\text{surf}}$ ) brightness temperature observations. C3 shows more foreground roof than in Figure 3-4 (pixels excluded from all other results) from an altered view angle between the observation dates.

### 3.5.2 Emissivity correction

#### 3.5.2.1 Temporally resolved surface temperatures and incoming LWIR radiation

The impact of the emissivity correction on the atmospherically corrected surface brightness temperatures ( $T_b^{\text{surf}}$ ) is assessed on a day with predominantly clear-skies (27<sup>th</sup> August 2017, Figure 3-10) and large variability of  $T_s$  between surfaces. As the surface emissivity is varied as part of the emissivity correction analysis, the radiance received by the surface [ $L_\lambda^{\text{DART}}(x, y, \Omega_\downarrow, \varepsilon_{0.93})$ , Eqn. 3.13] is shown instead of the  $(1 - \varepsilon)$  modified surface-leaving radiance. As broadband irradiance  $E_{\text{LW}}$  ( $\text{W m}^{-2}$ ) using the Planck function and Stefan-Boltzmann law this is:

$$E_{\text{LW}}^{\text{cam}}(x, y) = \sigma B_\lambda^{-1} [L_\lambda^{\text{DART}}(x, y, \Omega_\downarrow, \varepsilon_{0.93})]^4. \quad \text{Eqn. 3.16}$$

Canopy brightness temperature observations used to prescribe spatial variability of radiation leaving the surfaces of different surface types ( $\Sigma$ ) differ broadly as a function of the incoming shortwave radiation ( $E_{\text{SW}}^{\text{sky}}$ ) diurnal cycle (Figure 3-10b). While surfaces with a high SVF are more likely to receive shortwave energy input (Chapter 2), the inverse is true for longwave irradiance (Figure 3-10c) as surfaces within the canopy are warmer than the sky (even during the entire night). The median for north walls ( $\langle T_b^{\text{surf}}(\Sigma_{\text{North}}) \rangle$ ) generally follows the diurnal cycle of  $T_a$  as the facets are mostly shaded throughout the day.  $\langle T_b^{\text{surf}}(\Sigma_{\text{East}}) \rangle$  peaks at 10:00 (306.0 K), while the maximum (314.9 K) of  $\langle T_b^{\text{surf}}(\Sigma_{\text{South}}) \rangle$  is reached ~100 mins later. This relatively short time between maxima of east and south facing walls is explained by a predominant south-southeast facing direction of these facets (median azimuth for “South” wall is 147.9°, cf. for “East” is 91.6°).

Inter-class  $T_b^{\text{surf}}$  variations contribute to the simulated differences in  $E_{\text{LW}}(x, y, \Sigma)$  (Figure 3-10c). This has implications on the final emissivity corrected observations (Figure 3-10d). Median differences for  $E_{\text{LW}}(x, y, \Sigma)$  reach 74.3  $\text{W m}^{-2}$  between  $\Sigma_{\text{Roof[dark]}}$  and  $\Sigma_{\text{East}}$  during 13:00 – 14:55 (Figure 3-10c). The high SVF of roofs means  $E_{\text{LW}}$  for roof surfaces [ $E_{\text{LW}}(x, y, \Sigma_{\text{Roof}})$ ] is mostly composed of sky irradiance and hence is in closest agreement to the broadband radiometer observations used to specify  $E_{\text{LW}}^{\text{sky}}$ , while east facing walls receive large energy emissions from the opposing warm walls. The median for  $E_{\text{LW}}(x, y, \Sigma_{\text{Roof}})$  is up to 19.9  $\text{W m}^{-2}$  greater than the median  $E_{\text{LW}}^{\text{sky}}$  during 13:00 – 14:55 (Figure 3-10c) as the roof receives some radiation from other surfaces. Inter-wall differences in the median of  $E_{\text{LW}}(x, y)$  reach 17.4  $\text{W m}^{-2}$  between east and west walls during 13:00 – 14:55, which is driven by the lower temperatures of the shaded north facing walls.

Of the walls,  $E_{\text{LW}}$  shows greatest variability for those facing east, which is explained by very small-scale variations of these structures. Cameras C5 and C6 primarily observe non-planar, east facing walls (Figure 3-4) with complex features such as balconies. Combined with the high zenith angle of observations (Table 3-1), the cameras have a near-perpendicular view of the east walls and thus

sample both the upper and lower parts of the balconies that have contrasting view factors to the sky and ground surfaces.

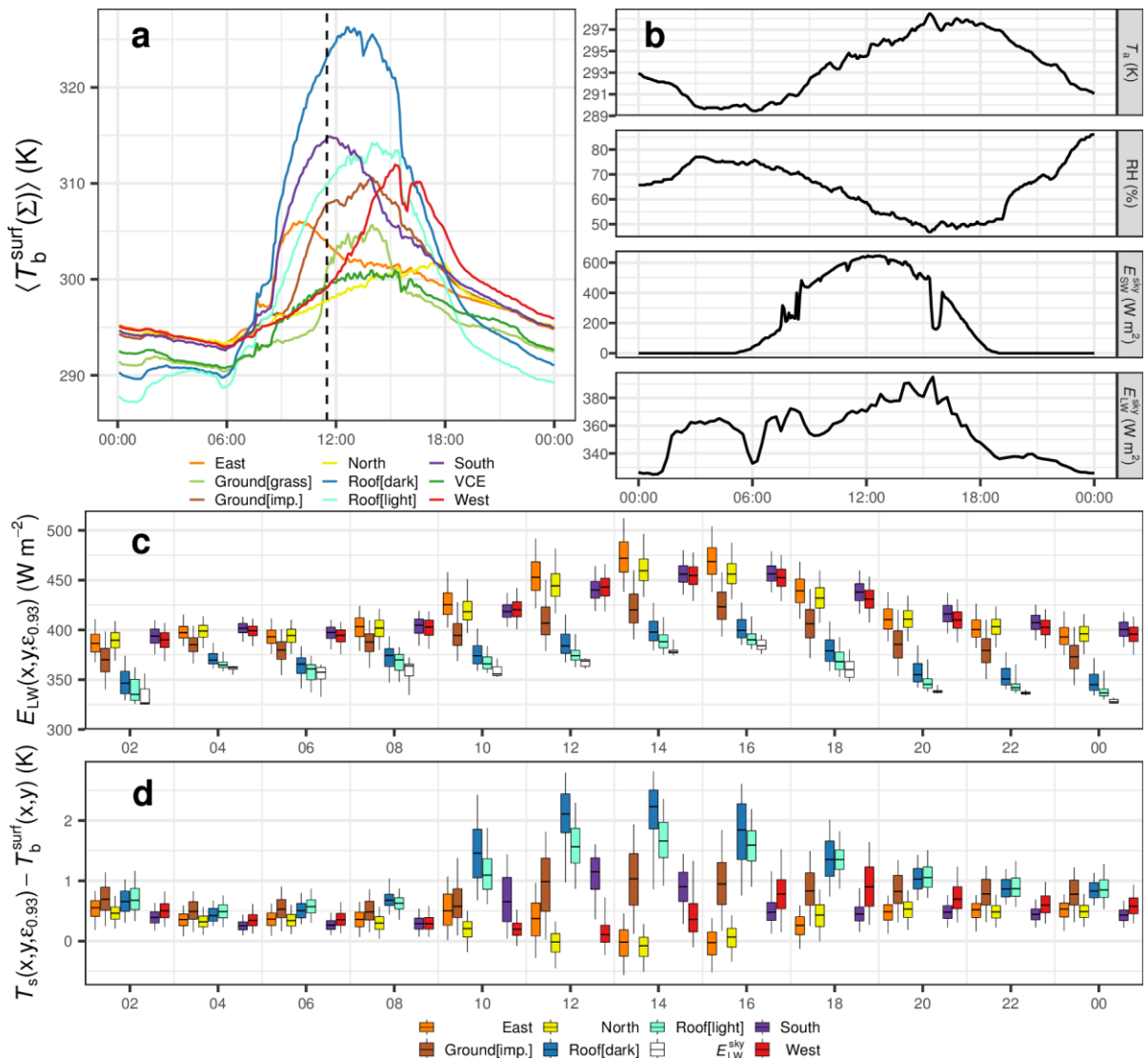


Figure 3-10. Observed and modelled data for 27<sup>th</sup> August 2017 stratified by surface orientation and material type ( $\Sigma$ ) (colours) with (a) median per-pixel surface brightness temperatures  $[T_b^{\text{surf}}(x, y)]$ . For spatial pattern of emissivity correction (11:30, dashed lined) see Figure 3-11. (b) BCT observations of air temperature, relative humidity, Kipp & Zonen CNR1 net radiometer broadband incoming shortwave ( $E_{\text{SW}}^{\text{sky}}$ ) and longwave ( $E_{\text{LW}}^{\text{sky}}$ ) radiation. (c) Broadband LWIR irradiance ( $E_{\text{LW}}$ ) onto surfaces within the camera field of view, with  $E_{\text{LW}}^{\text{sky}}$  for comparison. (d) Difference between emissivity (0.93) corrected surface temperature  $[T_s(\epsilon_{0.93})]$  for non-vegetative surfaces and surface brightness temperature. Boxplots: based on pixels from all camera images (5 min resolution, for 2 h: 07:00 – 08:55 i.e. 08:00 is between 07:00 and 09:00 vertical lines) with 5<sup>th</sup> and 95<sup>th</sup> percentiles (whiskers), interquartile range (box), and median (horizontal line).  $E_{\text{LW}}^{\text{sky}}$  boxplot uses 15 min resolution observations and min and max values (whiskers).

### 3.5.2.2 Spatially resolved longwave irradiance and emissivity correction

On the 27<sup>th</sup> August 2017 the spatially resolved emissivity correction for all cameras (Figure 3-11,  $T_b^{\text{cam}}$  in Figure 3-4a) have the maximum inter-facet variability of surface brightness temperature for within-canopy surfaces at 11:30 (Figure 3-10a, dashed line). The  $\langle T_b^{\text{surf}}(\Sigma_{\text{South}}) \rangle$  is 314.8 K, or 17.0 K higher than  $\langle T_b^{\text{surf}}(\Sigma_{\text{North}}) \rangle$ . As a single surface emissivity is used for all the non-vegetative surfaces when correcting  $T_b^{\text{surf}}$ , the magnitude of the correction (Figure 3-11b) is related to spatial differences in  $E_{\text{LW}}$  (Figure 3-11a). The  $E_{\text{LW}}$  results account for RT process across the complex geometry seen by the RW camera observations (Figure 3-4a), e.g. compare east wall balconies (C5 and C6), sloped roofs (e.g. C2  $x = 40$ ,  $y = 40$ ), complex roofs (e.g. C1,  $x = 55$ ,  $y = 35$ ; C3,  $x = 50$ ,  $y = 60$ ; C4  $x \approx 70 \rightarrow 120$ ,  $y \approx 55 \rightarrow 70$ ), and vegetation (e.g. C2,  $x = 120$ ,  $y = 80$ ; C6,  $x = 120$ ,  $y = 75$ ). The atmospheric correction is not as sensitive to such small details across building facades.

Wall  $E_{\text{LW}}$  (Figure 3-11a) has high spatial variability associated with the wall geometry complexity. The overall  $E_{\text{LW}}$  increases closer to ground level and in narrow street canyons where SVF are reduced (Figure 3-11a).  $E_{\text{LW}}$  is typically lowest for roof surfaces (i.e. high sky view factor) and increasingly varies for roofs within the canopy (e.g. C6  $x = 40$ ,  $y = 60$ ). Compared to adjoining walls,  $E_{\text{LW}}$  for ground surfaces is typically lower as there is a preferential orientation of ground surfaces to the cool sky. Overall,  $E_{\text{LW}}$  for the ground surfaces decreases with distance to buildings and is greater for ground surfaces close to trees, as these occlude the ground from most downwelling sky irradiance. Where the longwave irradiance approaches the radiation emitted by a surface, the emissivity correction is minimised (Figure 3-10b).

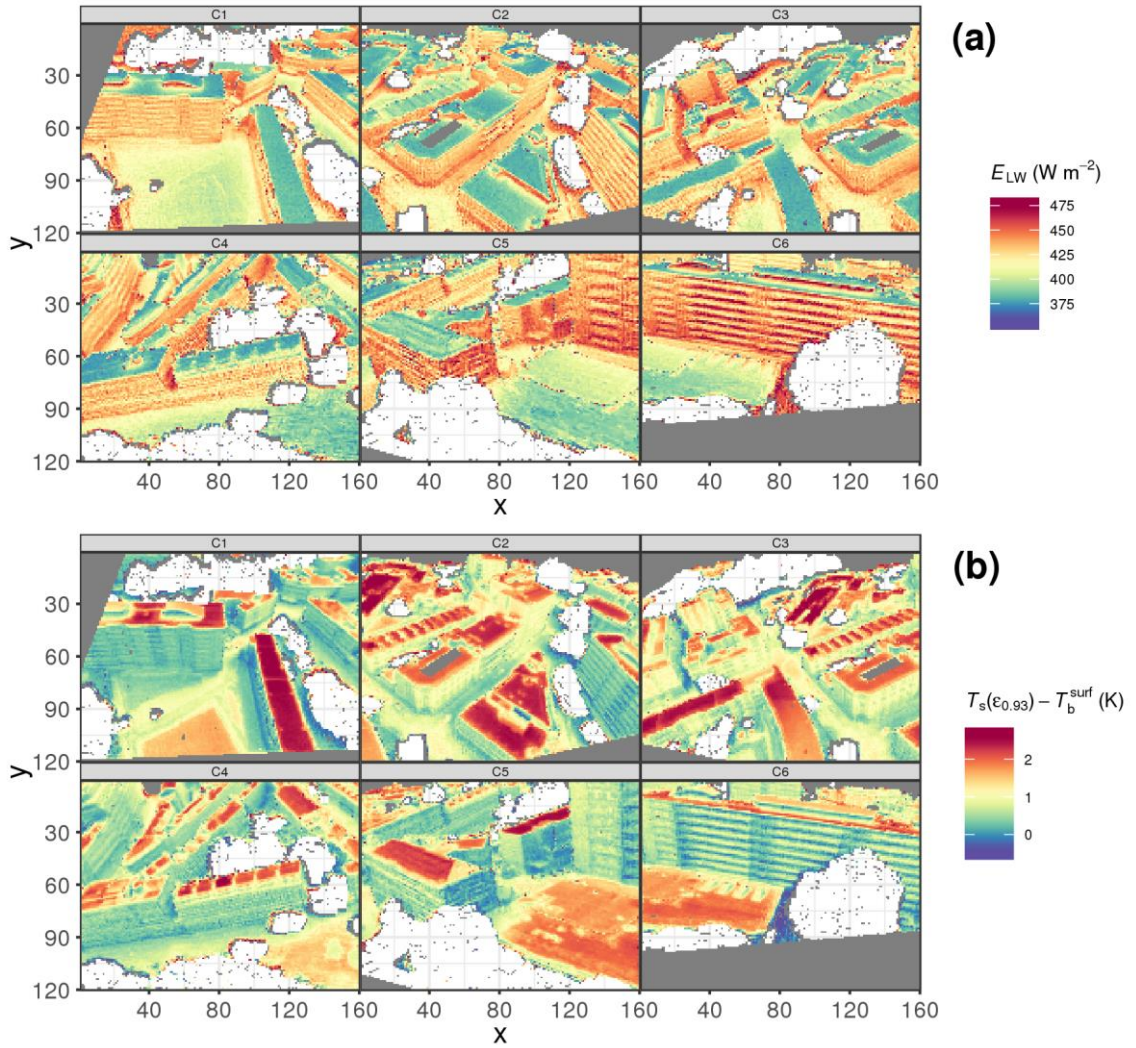


Figure 3-11. Observed and modelled results (27<sup>th</sup> August 2017 at 11:30) of (a) longwave irradiance ( $E_{LW}$ ) from broadband hemispherical radiometer (sky component) and 3D distribution of surface brightness temperatures from the network of longwave infrared cameras (canopy component) prescribed to DART to simulate the emission, irradiance and multiple scattering processes of LWIR radiation for correction of surface brightness temperature ( $T_b^{surf}$ ) to emissivity (0.93) corrected surface temperature [ $T_s(\epsilon_{0.93})$ ], (b)  $T_s - T_b^{surf}$  difference.

### 3.5.2.3 Uncertainty analysis

The variability of  $T_s$  based on the emissivity and temperature value prescribed across the non-vegetative surfaces is evaluated for each timestep. Initially with  $\epsilon_{0.93}$  a heterogeneous distribution of surface temperature is used (Figure 3-12), and then repeated using the minimum ( $\epsilon_{0.89}$ ) and maximum ( $\epsilon_{0.97}$ ) broadband emissivities for dark impervious urban materials in the Kotthaus *et al.* (2014) spectral library; and repeated again (Figure 3-13) with an isothermal surface temperature that resolves the RT process similarly to the SVF approach of Adderley, Christen and Voogt (2015).

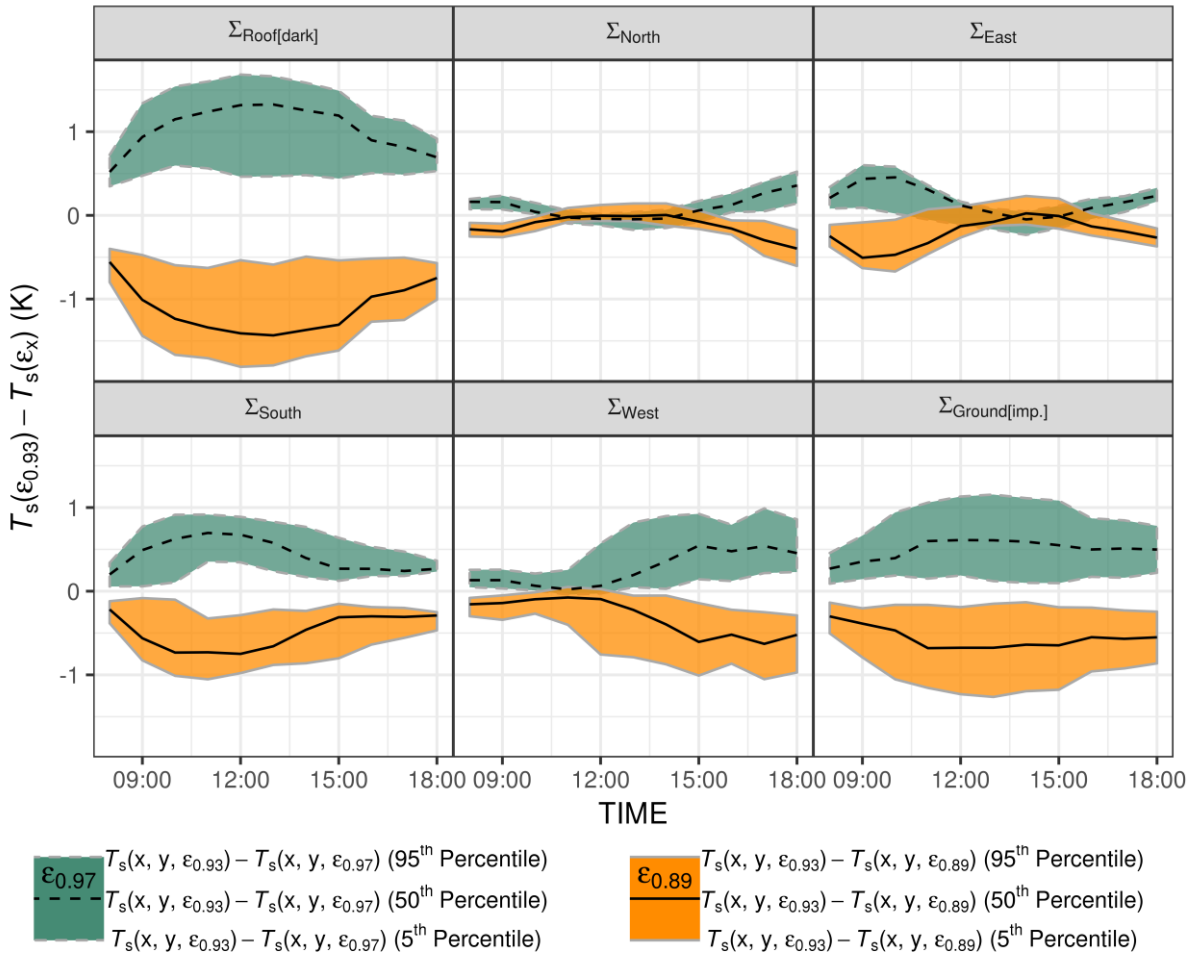


Figure 3-12. Per-pixel emissivity corrected surface temperature  $T_s$  differences (median = black lines, inter-quartile range = shaded) from LWIR camera observations (27<sup>th</sup> August 2017, 60 min resolution) using different spectral library (Kotthaus *et al.*, 2014) broadband emissivity values: mean ( $\epsilon_{0.93}$ ), minimum ( $\epsilon_{0.89}$ , orange) and maximum ( $\epsilon_{0.97}$ , aqua) for non-vegetative surfaces (walls E, N, S, W; ground, roof) simulated using DART.

The facet most sensitive to changes in surface emissivity is the roof as its high  $T_b^{\text{surf}}$  and SVF, and low incoming (sky) LWIR radiation combine to produce large contrasts between received and emitted radiation. On this day the emissivity effect for roof surfaces is most pronounced at 13:00, when median difference between the surface temperature derived using an emissivity of 0.93 is 1.4 K higher (1.3 K lower) than with an emissivity of 0.89 (0.93) (Figure 3-12). Although ground surfaces also mostly receive radiance from the cold sky, temporal variability in  $T_s(x, y, \Sigma_{\text{Ground}})$  is lower compared to roof surfaces as the diurnal amplitude of surface temperatures of this facet type is lower due to the relatively lower shortwave energy received (Figure 3-10a).

For the wall facets, the magnitude of the emissivity effect is impacted by the wall's orientation (Figure 3-12). Depending on the emissivity value used, the sign of the differences between surface temperatures obtained can even change throughout the day. For east and south facing walls the uncertainty is greatest in the morning when the surfaces are insolated and have high  $T_s$ , while their

opposite walls (west and north) are shaded with low  $T_s$ . By the afternoon, differences for east facing walls are minimised when the west facing walls are insolated and have similar temperature to east facing walls. The asymmetry of the uncertainty for south facing walls around solar noon, with greater uncertainty before noon, is linked to the preferential view of south-southeast walls and resulting diurnal cycle of  $T_b^{\text{surf}}(\Sigma_{\text{South}})$  (Figure 3-10a). Although east walls have a similar distribution of orientations to west walls, they respond differently to changes in prescribed emissivity. This is associated with the high diurnal variability of observed brightness temperatures in this class (Figure 3-10).

To assess the impact of variations in LWIR radiation leaving the canopy surfaces, the correction to  $T_s(\epsilon_{0.93})$  is performed using two different distributions of surface brightness temperature across the MW area. The “heterogeneous” temperature ( $T_b^{3D}$ ) is derived from the full temperature distribution [ $T_b^{\text{surf}}(X, Y, Z, \Sigma)$ ]. This is compared to an “isothermal” case ( $T_b^{\text{iso}}$ ) with two classes: roof (including both  $\Sigma_{\text{Roof[dark]}}$ ,  $\Sigma_{\text{Roof[light]}}$ ), and “within canopy” (i.e. walls and ground). The combination of isothermal within-canopy temperatures and isotropy of surface emissivity and downwelling sky radiance means  $T_b^{\text{iso}}$  is analogous to the SVF approach of Adderley, Christen and Voogt (2015). Median of per-pixel surface brightness temperatures are calculated and assigned to surfaces of the respective groups. The isothermal distribution of temperatures eliminates strong contrasts between the walls, such as  $\langle T_b^{\text{surf}}(\Sigma_{\text{South}}) \rangle$  up to 14.6 K greater than the median brightness temperature for the overall “within canopy” class at 11:30.

Assigning a more realistic temperature distribution ( $T_b^{3D}$ ) allows the heterogeneous urban canopy influences to impact the derived surface temperature [ $T_s(x, y, T_b^{3D})$ ] compared to the isothermal case [ $T_s(x, y, T_b^{\text{iso}})$ ]. A reduced emissivity enhances the surface temperature differences between the heterogeneous [ $T_s(x, y, T_b^{3D})$ ] and isothermal [ $T_s(x, y, T_b^{\text{iso}})$ ] cases (Figure 3-13). As the proportion of reflected radiation increases, the effect of assigning contrasting brightness temperature distributions increases with decreasing emissivity. Simulations using  $\epsilon_{0.97}$  have a 5<sup>th</sup> – 95<sup>th</sup> percentile range of  $T_s(x, y, \epsilon_{0.93}, T_b^{3D}) - T_s(x, y, \epsilon_{0.93}, T_b^{\text{iso}})$  that is typically less than 0.1 K (Figure 3-13, blue). The range for simulations using  $\epsilon_{0.89}$  [5<sup>th</sup> – 95<sup>th</sup> percentile,  $T_s(x, y, \epsilon_{0.89}, T_b^{3D}) - T_s(x, y, \epsilon_{0.89}, T_b^{\text{iso}})$ ] is greatest for  $\Sigma_{\text{Ground[imp.]}}$  surfaces (up to 0.4 K at 11:00). As  $\Sigma_{\text{Roof}}$  have low wall view factors, the sensitivity of this class to incoming LWIR radiation from within canopy surfaces is low throughout the day. The emissivity effect for the other within-canopy surfaces varies through the day with the brightness temperature of the opposite facets (Figure 3-10a). Given that the impact of surface emissivity is increased when the facing wall has a very different temperature (Figure 3-12), the relative temperature distribution between walls is important. For  $\Sigma_{\text{North}}$ , the 5<sup>th</sup> percentile of  $T_s(x, y, \epsilon_{0.89}, T_b^{\text{iso}})$  overestimates the 5<sup>th</sup> percentile of  $T_s(x, y, \epsilon_{0.89}, T_b^{3D})$  by 0.25 K in the period 11:30 – 12:00. This effect of temperature distribution within the canopy on the emissivity correction can therefore be larger than when changing the actual emissivity value used for north walls, as the 5<sup>th</sup> and 95<sup>th</sup>

percentile differences in  $T_s(x, y, \epsilon_{0.89}) - T_s(x, y, \epsilon_{0.97})$  are within  $\pm 0.2$  K during the same 11:30 – 12:00 period (within  $\pm 0.5$  K for 08:00 – 18:00) (Figure 3-12). These results highlight that assuming emitted radiation is only a function of SVF (Adderley, Christen and Voogt, 2015) does not account for the real complex thermal heterogeneity of the urban canopy and can contribute towards uncertainty in the emissivity correction.

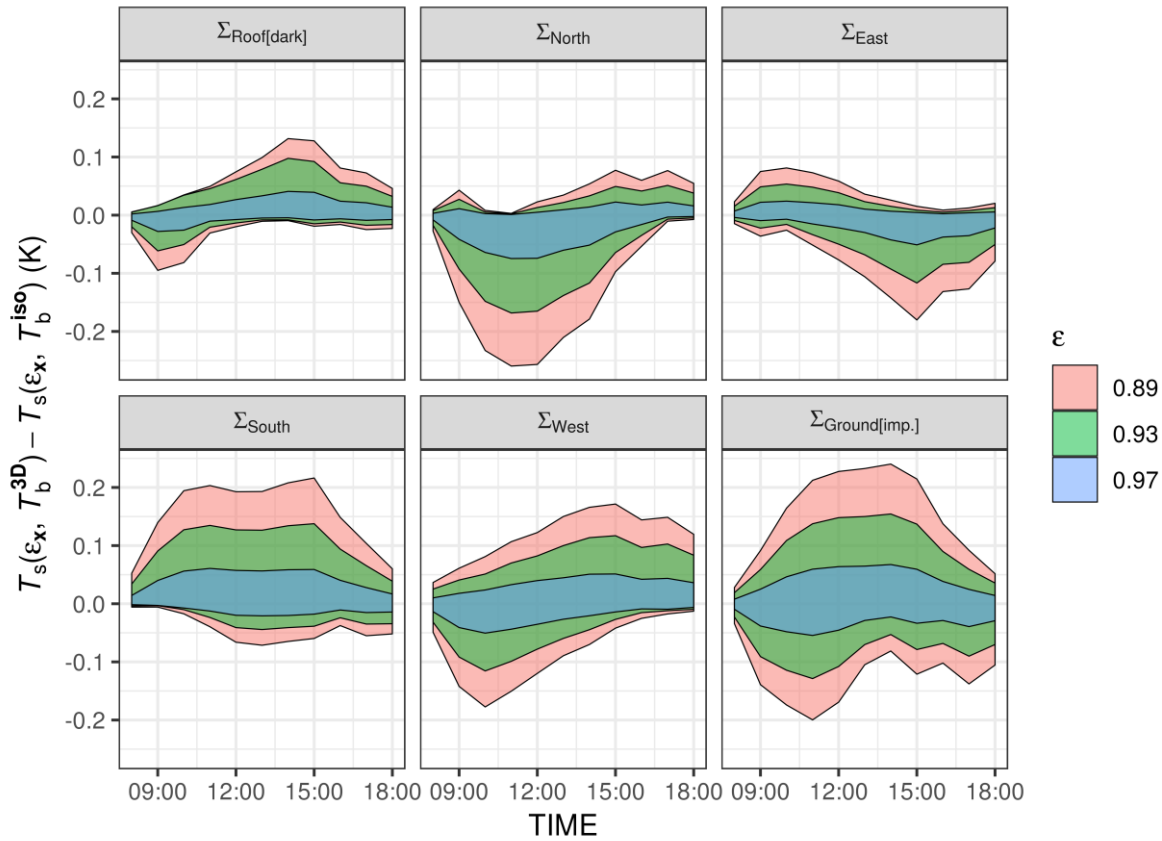


Figure 3-13. Difference in surface temperature  $T_s$  (60 min resolution, 27<sup>th</sup> August 2017) derived from LWIR camera observations based on emissivity ( $\epsilon$ ) corrections with a heterogeneous ( $T_b^{3D}$ ) and isothermal ( $T_b^{iso}$ ) assumption, respectively, using a range of  $\epsilon$  values (non-vegetative surfaces) according to dark impervious materials in the Kotthaus *et al.* (2014) spectral library. As observations are not areally weighted, the lower and upper extent of the distributions can still represent large fractions of the surface seen by the LWIR cameras.

## 3.6 Discussion

### 3.6.1 Flexibility in the correction framework

The correction methodology presented for a complex urban area is applicable to different observation sites and applications. Our single case-study in central London does not demonstrate the myriad of potential ways this approach can be applied.

For the atmospheric correction, climate model or reanalysis data could be used as input data instead of the more costly and challenging *in-situ* weather station observations used here. A trade-off may

exist with model grid resolution and skill, but the horizontal and vertical distribution of air temperature, pressure and water vapour from the model may be more accurately resolved than that observed. Alternatively, standard gas and aerosol models are available within the DART database. In addition to vertical atmospheric variations, the 3D RT approach is unique in that any horizontal variability (e.g. associated with localised point sources or distributions of water vapour or soot) can be specified. We aimed for atmospheric correction processing at close to real time (< 5 min simulation time). The final ~12 min simulation time per timestep across all cameras means the sensitivity of the model resolution (e.g. voxels, number of rays) to the simulated results requires more investigation and there is much scope for reduction in simulation time.

The emissivity correction uncertainty analysis could be expanded to consider more spatially variable materials and anisotropy in surface emissivity such as specular reflections from glass. The DO nature of DART means spectral properties and scattering phase functions can be determined either manually or from the DART database. In general, the distribution of material properties for the correction is only limited by the input data. More detailed optical property information is expected in the future and could be obtained by incorporating other datasets and classification techniques. Given that a primary benefit of ground-based RS in urban areas is that observations can be made of the full 3D structure including vertical surfaces, a description of the material composition of the vertical surfaces is particularly important and can be used here. Google Street View has been applied in urban climate studies (Gong *et al.*, 2018; Zeng *et al.*, 2018a) and could be used to obtain structure and material composition information for within-canopy surfaces across large areas (Lindberg *et al.*, 2019).

To further understand uncertainties with emissivity correction from changes in surface temperature distributions, the surface temperature distribution can be pre-processed by DART (e.g. Wang, Chen and Zhan, 2018) or by user-defined approaches (Chapter 2) to resolve its variability from shadow patterns.

We assumed downwelling radiance from the sky to be an isotropic source to isolate variance from the other effects studied. However, an anisotropic sky radiance can be prescribed which uses the full above-BOA (bottom of atmosphere) radiative transfer capabilities of DART.

Additional sensitivity analyses for all these processes could contribute to a benchmarking effort to reduce simulation times (each emissivity correction takes ~12 h using 4 cores, 40 GB ram) along with simplifications (e.g. using first order scattering of LWIR radiation only) and/or by reducing the resolution (e.g. fewer voxels and lower density of rays).

### **3.6.2 Future application of corrected ground-based observations**

To enhance the applicability of ground-based thermography observations for studying physical exchange processes, the correction of atmospheric and emissivity effects is crucial. Surface kinetic temperature ( $T_s$ ) from high resolution LWIR RS on ground-based platforms in urban areas are

increasingly required for a wide range of applications. The role of complex geometry to 3D RT processes is important to understand, particularly as modelling typically uses low LOD geometry restricted by data availability (e.g. Ghandehari, Emig and Aghamohamadnia, 2018) or the nature of the model as a 2D (Harman, Best and Belcher, 2004) or simplified 3D (Krayenhoff and Voogt, 2007; Aoyagi and Takahashi, 2012) scheme. The corrected ground-based observations are expected to have application in the following specific fields: ground-truthing of airborne or space-borne surface temperatures by assessment of the anisotropy (directional variability) of upwelling LWIR radiation (Lagouarde *et al.*, 2014; Krayenhoff and Voogt, 2016), estimation of complete urban surface temperatures (Voogt and Oke, 1997), evaluation of urban surface (e.g. Masson, 2000; Harshan *et al.*, 2018) and building (Bueno *et al.*, 2012) energy balance models, studies of shadow hysteresis effects (Meier, Scherer and Richters, 2010a), inputs to unstably stratified large eddy simulations (Gronemeier, Raasch and Ng, 2017) and data assimilation (e.g. Ghent *et al.*, 2010; Li and Bou-Zeid, 2014).

### 3.7 Conclusions

As high-resolution thermal imagery starts to be gathered in urban settings for long periods, detailed automatic correction techniques are required. As building structures and vegetation may have different patterns and heterogeneity in the city centre compared to residential areas, flexible methods are needed that account for the specific urban morphology. Here, a radiative transfer model is used to convert brightness temperature observations to kinetic surface temperature from a network of seven thermal cameras deployed in a complex, central city area. The methods applied to correct atmospheric and emissivity effects are advantageous over earlier work as: (a) the correction is applied within one modeling framework, (b) a large number of cameras with varying properties can be corrected simultaneously with minimal increase to computational cost, (c) a very high level of detail and realistic surface model is created and explicitly models buildings with sloped roofs, micro-scale structures (such as balconies), and vegetation, (d) multiple scattering of radiation within the urban atmosphere and between building structures is accounted for, and (e) the heterogeneous distribution of temperatures within the urban canopy is used.

Six cameras have path lengths to the viewed surfaces of  $\sim 50 - 250$  m. The analysis ( $> 20$  days) covers varying meteorological conditions. The atmospheric correction is greatest during the day (up to 4.53 K for  $\sim 250$  m path length) coinciding with high daytime brightness temperatures. This correction is evaluated using concurrent observations of a surface from both a “near” ( $\sim 15$  m) and corrected “far” ( $\sim 155$  m) distance using a seventh camera. The mean absolute error is 0.39 K ( $r^2 = 0.998$ ). New insights are gained about path length variability by using a high level of detail surface geometry model. By using detailed surface geometry, the pixel path length is accurately registered

even for complex features such as sloped roofs, where a more simplified geometry may give inaccurate results.

The emissivity correction has a diurnal pattern and varies by surface type. On a clear-sky day, the correction is greatest around midday with roofs over 3 K warmer when corrected. An error in material emissivity is most important for roofs. A baseline correction using an emissivity of 0.93 ( $\epsilon_{0.93}$ ) across all built surfaces gives around  $\pm 1.4$  K variation compared to using a reasonable range of expected emissivity values for dark building materials ( $\epsilon_{0.89}$  and  $\epsilon_{0.97}$ , Kotthaus *et al.*, 2014). Driven by varied surface temperatures and sky view factors, the irradiance across the surfaces is highly variable (intra-pixel differences  $> 70$  W m<sup>-2</sup>). South facing walls are up to 17 K warmer than north walls. The latter generally follow the air temperature and have cooler temperature when corrected ( $< -0.25$  K around midday). Without variation in surface temperature, which is analogous to a sky view factor correction (Adderley, Christen and Voogt, 2015), the correction changes by around 0.25 K (0.1 K) using the low (high) emissivity values of  $\epsilon_{0.89}$  ( $\epsilon_{0.97}$ ). Thus, the uncertainty introduced from using a simplified SVF approach could be larger from the uncertainty introduced from material emissivity choice. Roofs likely have the greatest uncertainty in estimated  $T_s$ . Because of their high sky view factor, error sources are from the prescribed material emissivity and longwave sky irradiance. A more general error source is rapid changes in camera body temperature during clear-sky mornings which correspond to relatively poor agreement between modelled and observed atmospheric correction magnitudes ( $\sim 1$  K difference). More work on the calibration and housing of longwave infrared cameras for outdoor settings is required.

Overall, the technique introduced is flexible and corrects for atmospheric and emissivity effects at an unprecedented level of detail. Once a “model world” is defined that describes the observational area (i.e. observed surface geometry and sensor perspective), the use of an anisotropic radiative transfer model (DART, Gastellu-Etchegorry *et al.*, 2015) simplifies this challenging and complex correction procedure. There is flexibility in the choice of model inputs and parameters including the: 3D distributions of atmospheric optical properties, surface temperatures and (directional) surface emissivity; anisotropic downwelling longwave radiance from the sky; surface and vegetation geometry; remote sensing observations from different platforms and design (e.g. cameras and narrow-wide FOV radiometers) which may be important for configurations where the observations and model resolve more detailed material properties, including anisotropic emissivity and specular reflections. By using a network of cameras with observations of a broad range of urban surface types and surface-camera distances, the approach encompasses a range of these parameters which will invariably be relevant as a benchmark for future applications.

## List of symbols and acronyms [units]

3D	Three dimensional
agl	Above ground level (m)
$B_\lambda$	Black-body Planck radiance [ $\text{W m}^{-2} \text{sr}^{-1} \mu\text{m}^{-1}$ ]
BB	Black-body
BCT	Observation site for weather data (~1 km outside study area)
BOA	Bottom of atmosphere
C#	Nonspecific camera (C) and unique reference number (#)
$c_1$	First radiation constant [ $1.191042 \times 10^9 \text{ W m}^{-2} \text{sr}^{-1} \mu\text{m}^{-1}$ ]
$c_2$	Second radiation constant [ $1.4387770 \times 10^4 \mu\text{m K}$ ]
CUB	Observation site within the study area
DART	Discrete Anisotropic Radiative Transfer model
DO	Discrete ordinate
DSM	Digital surface model (3D vector-based)
$\Delta T_b^{\text{cam}}$	Atmosphere effect for C2 (no correction) as $T_b^{\text{cam}}(\text{C2}) - T_b^{\text{surf}}(\text{C7})$ [K]
$\Delta T_b^{\text{surf}}$	Atmosphere effect corrected for C2 as $T_b^{\text{surf}}(\text{C2}) - T_b^{\text{surf}}(\text{C7})$ [K]
$E_{\text{LW}}$	Broadband incoming longwave radiation flux (irradiance) [ $\text{W m}^{-2}$ ]
$E_{\text{LW}}^{\text{sky}}$	Broadband incoming longwave radiation flux (irradiance) from sky [ $\text{W m}^{-2}$ ]
$\epsilon$	Emissivity
FOV	Field of view [ $^\circ$ ]
IFOV	Instantaneous field of view
IMU	Observation site within the study area
L	Band radiance [ $\text{W m}^{-2} \text{sr}^{-1}$ ]
$\lambda$	Wavelength [ $\mu\text{m}$ ]
LOD	Level of detail
LUT	Lookup table
LWIR	Longwave infrared
$L_\lambda$	Spectral radiance [ $\text{W m}^{-2} \text{sr}^{-1} \mu\text{m}^{-1}$ ]
$L_\lambda^{\text{atm}}$	Spectral atmospheric radiance contribution along $z^{\text{path}}$ [ $\text{W m}^{-2} \text{sr}^{-1} \mu\text{m}^{-1}$ ]
$L_\lambda^{\text{cam}}$	At-sensor radiance [ $\text{W m}^{-2} \text{sr}^{-1} \mu\text{m}^{-1}$ ]
MLOS	Multi line of sight
MW	Model world
$\Omega$	Solid angle [sr]
$\Omega_{\downarrow}$	Solid angle [sr] associated with radiation received by a surface
$\Omega_{\uparrow}$	Solid angle [sr] associated with radiation leaving a surface
$\phi$	Zenith angle [ $^\circ$ ]
p	Scattering phase function
r	Nonspecific raster spatial dataset (nadir orthorectified)
$r^{\text{DSM}}$	Raster digital surface model (ground and building height agl)
RH	Relative humidity [%]
$\rho_v$	absolute humidity [ $\text{g m}^{-3}$ ]
$r^{\text{RGB}}$	True-colour raster RGB image
RT	Radiative transfer
RW	Real world
$R_\lambda$	Camera relative spectral response function
$\Sigma$	Surface property of orientation and material
$\sigma$	Stefan-Boltzmann constant [ $5.67 \times 10^{-8} \text{ W m}^{-2} \text{K}^{-4}$ ]
SEB	Surface energy balance
SLUM	Spectral Library of impervious Urban Materials (Kotthaus <i>et al.</i> , 2014)
$T_a$	Air temperature [K]
$\tau$	Optical depth
$\Gamma^{\text{atm}}$	Transmittance of atmosphere
$\Gamma_\lambda^{\text{atm}}$	Spectral transmittance of atmosphere
$T_b^{3\text{D}}$	Three-dimensional parameterisation of brightness temperature across MW surfaces
$T_b^{\text{cam}}$	Camera brightness temperature [K]
$T_b^{\text{iso}}$	Isothermal parameterisation of brightness temperature across MW surfaces
$T_b^{\text{surf}}$	Surface brightness temperature [K]
$\theta$	Azimuth angle [ $^\circ$ ]
$T_s$	Surface temperature [K]

VCE	Vegetation canopy element: e.g. trees, bushes or shrubs taller than 1.5 m agl
$V_x^s$	Surface voxel (intersected by DSM triangles)
$V_x^v$	VCE voxel
x, y	Nonspecific coordinate in 2D camera image
X, Y, Z	Nonspecific coordinate of 3D space
$z^{\text{path}}$	Path length between camera and target surface [m]

## Acknowledgements

This work is funded by Newton Fund/Met Office Climate Science for Service Partnership China (CSSP China, SG), EU H2020 UrbanFluxes, NERC ClearLo, NERC/Belmont TRUC, EUf7 emBRACE, EUf7 BRIDGE and the National Research Foundation (NRF) Singapore through the Singapore-MIT Alliance for Research and Technology's Centre for Environmental Sensing and Modeling (SMART-CENSAM) interdisciplinary research program. We thank Islington Council (Esther Lamontagne and Paul Stokes) and City University (Prof. Sir Paul Curran and Dean Beeden) for arranging access to observation sites, Daniel Clewley of the NERC Airborne Research Facility for assistance with the airborne hyperspectral dataset, Kjell Zum Berge (University of Reading) for assistance with the observations and Bryam Orihuela for assistance with the 3D modelling. We thank NERC ARSF, Martin Wooster and all those who contributed to the airborne measurement campaign 2010/154.

## Chapter 4 Urban satellite view uncertainty assessed with ground-based thermography

### Abstract

Ground-based thermal camera observations are used to determine the surface temperature ( $T_s$ ) of a central urban study area to quantify view angle uncertainties in satellite land surface temperatures. Observations with high temporal (5 min) and spatial ( $\sim 0.5 \rightarrow 2.5$  m) resolution cover a large source area (3.9 ha). A detailed model of the urban surface combined with sensor view modelling is used to quantitatively classify camera observations by geometry and material properties (e.g. surface orientation, albedo, solar irradiance and shadow history) at an unprecedented level of detail. Unsupervised shadow tracking within images reveals the recently shaded ( $< 30$  min) ground is up to 18.6 K warmer than concurrent ambient surface temperatures. The ground cools at a similar rate to walls but three times slower than roofs. Based on the classified observations the surface temperature distribution across a large area (430 x 430 m) is characterised at high (1 m) resolution. This is used to simulate the directional surface-leaving radiance (effective thermal anisotropy), accounting for multiple scattering within the canopy as opposed to only considering the changing view fraction of surfaces. Virtual surface temperature observations from an EO satellite ( $T_s^{\text{EO}}$ ) are simulated, taking into account emissivity effects. On a mainly clear-sky day,  $T_s^{\text{EO}}$  varies by up to 5.1 K in response to view angle variations of up to  $50^\circ$  off-nadir, which is common for EO satellites (e.g. Aqua/Terra MODIS). This magnitude of effective thermal anisotropy is generally lower than observed or modelled by prior studies. Uniquely, the inter-class variability of observed  $T_s$  is here quantified for a complex surface geometry (cf. simplified geometry in prior studies) and (relatively cool) urban trees are explicitly resolved.  $T_s^{\text{EO}}$  has generally good agreement with concurrent MODIS observations. From a nadir view,  $T_s^{\text{EO}}$  overestimates the areally averaged surface temperature (“complete” surface temperature) by up to 1.9 K during the day. Realistic simulation of thermal anisotropy can inform further idealised descriptions of urban geometry (e.g. TUF-3D, Krayenhoff and Voogt, 2007; GUTA, Wang, Chen and Zhan, 2018) for future operational retrievals of  $T_s^{\text{EO}}$  over urban areas.

### 4.1 Introduction

Urban surface temperature  $T_s$  is closely linked to the surface energy balance (Krayenhoff and Voogt, 2007). High-quality observations are needed to develop and evaluate parameterisations that address more realistically complex land surfaces in numerical weather prediction (NWP), climate models, thermal computational fluid dynamics (CFD) models and building energy models required to provide a wide range of integrated urban services (e.g. urban planning, heat stress warnings, Baklanov *et al.*, 2018). Across entire cities, earth observation (EO) satellites can resolve  $T_s$  ( $T_s^{\text{EO}}$ ) at a local-scale to observe the urban heat island phenomenon (e.g. Roth, Oke and Emery, 1989; Kandel, Melesse and

Whitman, 2016), effects of land use change (e.g. Dousset and Gourmelon, 2003; Weng and Lu, 2008) and derive SEB components of  $Q_H$  (e.g. Voogt and Grimmond, 2000; Xu, Wooster and Grimmond, 2008; Crawford *et al.*, 2018) and  $\Delta Q_s$  (e.g. Kato and Yamaguchi, 2007; Chrysoulakis *et al.*, 2018; Lindberg *et al.*, 2019). Further,  $T_s$  determined by urban climate models as part of their underlying physical equations can use  $T_s^{EO}$  for evaluation (e.g. Ghent *et al.*, 2010; Li and Bou-Zeid, 2014).

Despite the advances of thermal infrared monitoring from space, there are several limitations with the approach (Roth, Oke and Emery, 1989; Voogt and Oke, 2003).  $T_s^{EO}$  only provides an instantaneous snapshot at a given moment of the varied diurnal cycle. In addition, any remote sensing (RS) observation is taken from a limited view angle (Jiang *et al.*, 2018) with a two-dimensional perspective of the surface-leaving radiance in which to determine  $T_s$ . Over urban areas, the three-dimensional (3D) morphology and complex surface materials create a varied  $T_s$  distribution and anisotropic surface-leaving radiance (Krayenhoff and Voogt, 2016, Chapter 2). As a result, surface-leaving radiance sampled by a remote sensor can change depending on the view angle. For example, an observation viewing directly downward (nadir) is biased to the surface-leaving radiance from horizontal surfaces and misses the large wall area. Anisotropy of surface-leaving radiance across urban canopies is defined as an “effective” thermal anisotropy, to differentiate from thermal anisotropy exhibited by individual surface components (Voogt and Oke, 1998b).

Effective urban thermal anisotropy and view bias of urban thermal RS has been observed from helicopters, which enable multi-angular observations across scales representative of satellite pixels (local-scale i.e. 100 – 5000 m; Oke *et al.*, 2017) with maximum anisotropy of up to 9 K (Voogt and Oke, 1998b) and over 10 K (Lagouarde *et al.*, 2010). Long time-series satellite observations have drawn similar conclusions (Hu *et al.*, 2016). Observations from these platforms cannot determine the diurnal development of thermal anisotropy. For this, surface temperatures at high temporal resolution over an extended time period are required, as urban surface temperatures have high temporal variability even over relatively short intervals (Christen, Meier and Scherer, 2012). RS observations from ground-based platforms can provide such information and observe the micro-scale (< 100 m) processes that contribute to effective thermal anisotropy at high temporal resolution from potentially concurrent observations of both the horizontal and vertical surfaces of the urban canopy. As the observations are at micro-scales but  $T_s^{EO}$  is at local-scale, comparison to EO data requires “upscaling” the observations across the whole surface area within the satellite pixel (i.e. micro-scale → local-scale). This can be achieved by classifying which parts of the urban surface are “seen” (e.g. walls, roofs, ground) by the ground-based observations and allows their relative distribution across surfaces within the satellite pixel area to be determined. Prior studies using ground-based thermography may use manual inspection of images to determine which pixels view different surfaces such as walls, roofs and ground (e.g. Christen, Meier and Scherer, 2012), or may relate any contrasting distributions of observed values to different surface characteristics by clustering and frequency distribution

analysis, requiring a-priori decisions on the end-members (e.g. Voogt and Oke, 1997; Hénon *et al.*, 2012). These methods can be time consuming, qualitative, and have not been shown to reliably classify many complex micro-scale features such as surface materials and vegetation and have generally been upscaled across relatively homogeneous (Adderley, Christen and Voogt, 2015) or scale model (Chapter 2) morphology.

Models enable analysis of effective thermal anisotropy for longer time series and under controlled conditions. Sensitivity of  $T_s$  to urban morphology cf. material properties have received attention (e.g. Krayenhoff and Voogt, 2016) because of the complexity in material distributions and properties. Surface geometry implemented in current modelling frameworks is created based on building plan area index (PAI), building height, sky view factor (SVF), building aspect ratio and street direction (Krayenhoff and Voogt, 2016; Jiang *et al.*, 2018). These parameters are translated to surface models of simplified geometry, i.e. using planar wall facets, flat roofs and regular repeating arrays of buildings. Geometry simplification can underestimate maximum anisotropy (Krayenhoff and Voogt, 2016) and likely overestimate the influence of certain view directions due to any repeating features of the surface model geometry (Chapter 2). Few studies include vegetation or details of buildings smaller than the building scale. Surface temperatures have been prescribed across facets derived from energy balance modelling (Krayenhoff and Voogt, 2007) or from sub-facet assimilation of observations (Wang *et al.*, 2018, Chapter 2).

In this paper, ground-based observations are used with high-resolution 3D radiative transfer modelling (Discrete Anisotropic Radiative Transfer (DART) to investigate effective thermal anisotropy and to develop a unique upscaling approach. Six ground-based infrared cameras provide the surface temperature at high spatial (sub-facet) and temporal (5 min) resolution in a city area. Ground-based remote sensing is highly directional and challenging to interpret across scales of satellite pixels as only a subset of all surfaces in any area are captured. To explore this, a 3D surface model with realistic surface geometry is used with classes based on sun-surface geometry, shadow history and materials. These are used to parameterise the observed surface temperature variability, creating a novel high resolution (< 1 m) surface temperature distribution applicable to a large area (430 x 430 m) that is spatially representative of a  $T_s^{\text{EO}}$  pixel; i.e. this new upscaling technique is applicable to complex urban areas. All of the surface classes are associated with sun-surface geometry which drives effective thermal anisotropy (Krayenhoff and Voogt, 2016). The upscaled 3D surface temperature is used with DART to simulate the radiative transfer processes and directional variability of  $T_s^{\text{EO}}$  at an unprecedented level of detail.

## 4.2 Methods

Surface temperature ( $T_s$ ) across a “real world” (RW) urban study area is determined using a network of longwave infrared (LWIR) cameras (Section 4.2.1). Results are presented for one case study day.

A “model world” (MW, Section 4.2.2) describes geometry and instrumentation of the RW area. It facilitates the classification of observations quantitatively compared to qualitatively in earlier ground-based studies. Classified observations are upscaled across the MW geometry giving a 3D temperature distribution with local-scale extent (Section 4.2.3), enabling simulation of effective thermal anisotropy and comparison to satellite imagery (Section 4.2.4).

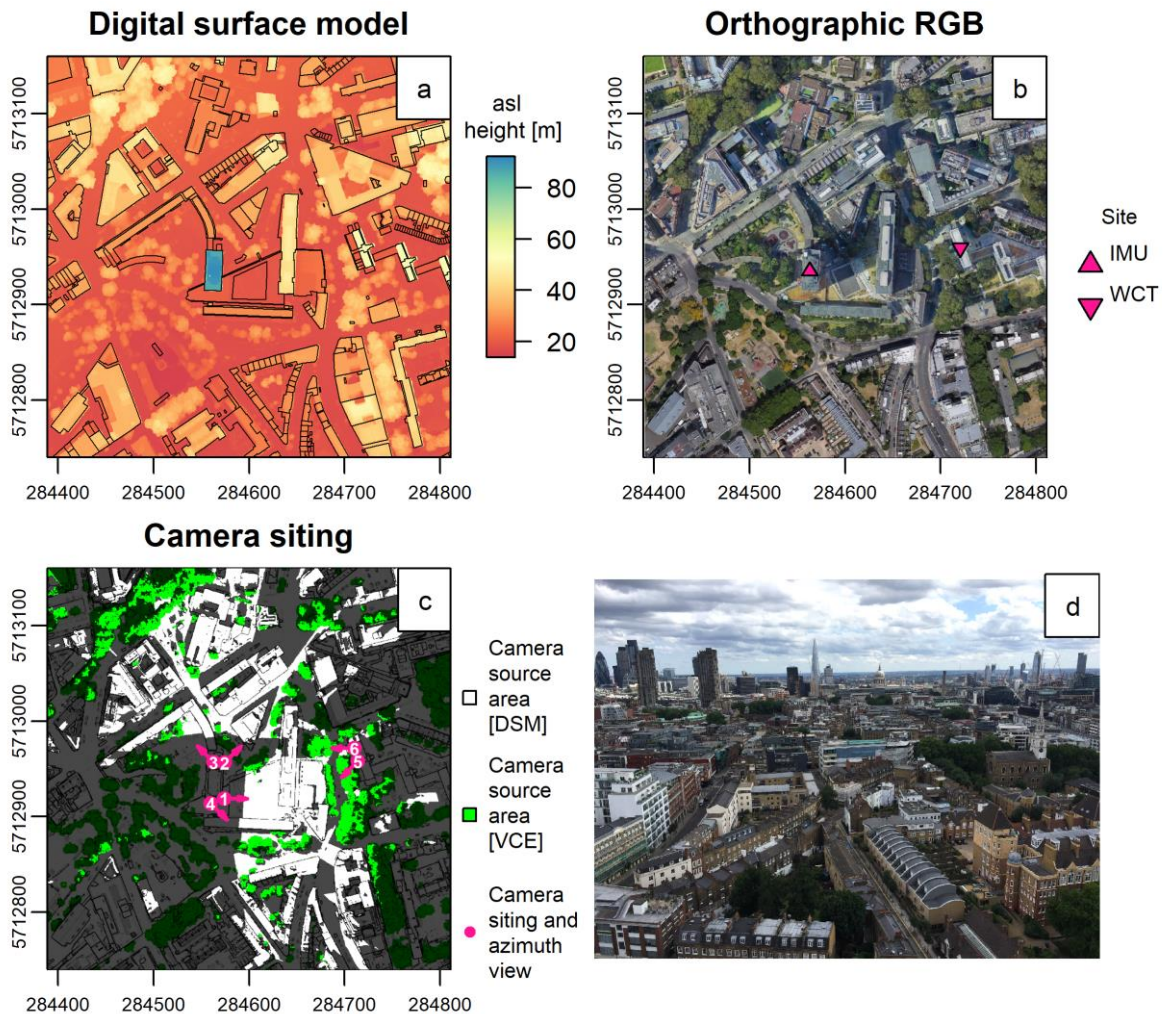


Figure 4-1. Plan view of study area with: (a) height of all surfaces above sea level (asl) with building footprints (black lines, from Evans *et al.*, 2011), (b) orthorectified RGB image from a mosaic of Google Earth (Google, 2019a) images with locations (symbols) of the study sites, (c) a render of the “model world” (MW) digital surface model (DSM) and vegetation canopy element (VCE) geometry with DSM (white) and VCEs (green) seen by the cameras located (pink dots) around the observation sites with different view directions (pink arrows) and unique camera identification (white) numbers (Table 4-1 gives details), (d) Digital camera image looking southeast and next to camera number 4 (C4) on 25<sup>th</sup> Oct 2017. (a – c) use Coordinate Reference System WGS84 UTM grid zone 31N.

#### 4.2.1 Real world study area and observations

The RW study area, in the Borough of Islington, London, UK (51°31'35" N, 0°06'19" W), has observation sites on top of two high rise residential tower blocks (hereafter IMU at 74 m agl (above

ground level); WCT 36 m agl) (Figure 4-1a). The study area streets have an irregular pattern and are often lined with deciduous trees. Buildings are residential and commercial, often four to six storeys, arranged in terrace rows or large single units.

Optris PI-160 (Optris GmbH, 2018) LWIR cameras (Table 4-1) measure upwelling longwave radiation from the study area (Figure 4-1c). The cameras, installed on tall buildings, have multiple view angles (Table 4-2) allowing various facets of the complete canopy surface to be sampled. A representative monitoring of the 3D surface is crucial for the upscaling of observations. More details about the study area and the observations are given in Chapter 3, including camera siting, measurement procedure, and the atmospheric and emissivity correction of observations to estimate  $T_s$  from the at-sensor brightness temperatures.

Table 4-1. Measurement and corrections used to determine surface temperature ( $T_s$ ) from LWIR cameras.

Property	Description
Platform	Static ground-based
Sample rate	1 min
Temporal resolution	5 min (median of samples at end of interval)
Image resolution	160 x 120 pixels
Temperature resolution	0.1 K
Number of cameras	6
Observation campaign period	7 <sup>th</sup> July – 10 <sup>th</sup> Nov 2017
Enclosure	Custom built enclosures (Chapter 3)
Radiometric calibration	Manufacturer calibrated 2 months prior to study
Accuracy	$\pm 2$ K
Spectral range	7 – 14 $\mu$ m
Image distortion correction	See Chapter 2
Atmosphere correction	See Chapter 3
Emissivity correction	See Chapter 3

Table 4-2. Siting properties of the ground-based longwave infrared (LWIR) cameras installed on two high-rise residential towers (IMU, WCT) within the study area (Figure 4-1).

Camera	Located	Field of view (°) Horizontal x vertical	Cardinal facing	Viewing zenith angle ( $\theta$ , °)	Median path length (m)
C1	IMU	68.6 x 54.2	E	46.5	88.8
C2	IMU	62.6 x 49.1	NE	51.7	97.9
C3	IMU	62.8 x 49.2	NWW	52.9	106.6
C4	IMU	37.3 x 28.4	SE	56.7	122.7
C5	WCT	38.4 x 29.3	SW	66.6	79.0
C6	WCT	62.4 x 48.9	W	61.7	67.5

Meteorological observations used include air temperature ( $T_a$ , K) and downwelling shortwave (SW) irradiance ( $E_{SW\downarrow}$ ,  $W\ m^{-2}$ ) from a Davis Vantage Pro 2 weather station located 114 m agl, 1.1 km southeast of IMU, and broadband (4.5 – 42  $\mu\text{m}$ ) downwelling longwave irradiance ( $E^{LW\downarrow}$ ,  $W\ m^{-2}$ ) from a Kipp & Zonen CNR1 net radiometer at IMU.

#### 4.2.2 Model world

The RW study area and instrumentation are represented in a “model world” (MW) environment to facilitate the analysis of observations and simulation of effective thermal anisotropy. The MW uses a vector-based 3D digital surface model (DSM) with a 3D mesh of triangles and a voxelated representation of vegetation covering the RW study area (Figure 4-1). It is discretised into voxels  $V_x$  of uniform size in a 3D raster format at high resolution ( $\Delta X = \Delta Y = \Delta Z = 1\ \text{m}$ ). The spatial resolution of the MW surface is the portion of DSM triangles ( $S$ ) that occupies the volume of one surface voxel (a “surface element”,  $S^{V_x}$ , Figure 4-2). The voxel array stores a series of surface properties as a surface class (Table 4-3) and the surface temperature of MW surface elements. By using surface elements, surface features such as geometry, material, optical and temperature properties can be determined at a flexible spatial resolution, instead of at the triangle scale of the DSM (e.g. radiosity models of Emig, 2017 and Ghandehari *et al.*, 2018; SOLENE model of Hénon *et al.*, 2012).

Many features of the MW are created and managed by the Discrete Anisotropic Radiative Transfer (DART) model (Gastellu-Etchegorry, Grau and Lauret, 2012). DART allows 3D radiative transfer (RT) processes to be simulated in both natural and urban landscapes in the visible to LWIR regions of the electromagnetic spectrum using a ray tracing approach. Here DART is used to:

- 1) resolve the triangle-voxel intersection and store the surface class, upscaled surface temperature observations and optical properties for each surface element (Figure 4-2)
- 2) simulate the 3D distribution of direct incoming SW radiation across the MW surface for surface and image classification based on sun-surface geometry
- 3) simulate surface-leaving radiance from the perspective of EO satellites at various view angles using the MW surface geometry, temperatures and optical properties.

For a full description of DART see Gastellu-Etchegorry *et al.* (2015).

The vegetation canopy elements (VCE, any vegetation taller than 1.5 m) are a voxel array ( $VCE^{V_x}$ ) with  $\Delta X = \Delta Y = 1\ \text{m}$  and  $\Delta Z = 0.1\ \text{m}$  resolution (Figure 4-2). The final MW geometry (Figure 4-3) is determined from a series of Google Earth (Google, 2019a) images photogrammetrically processed as a 3D point cloud using Agisoft PhotoScan Professional software (Agisoft LLC, 2013) and subsequently post-processed (Appendix D) to separate the DSM and VCE.

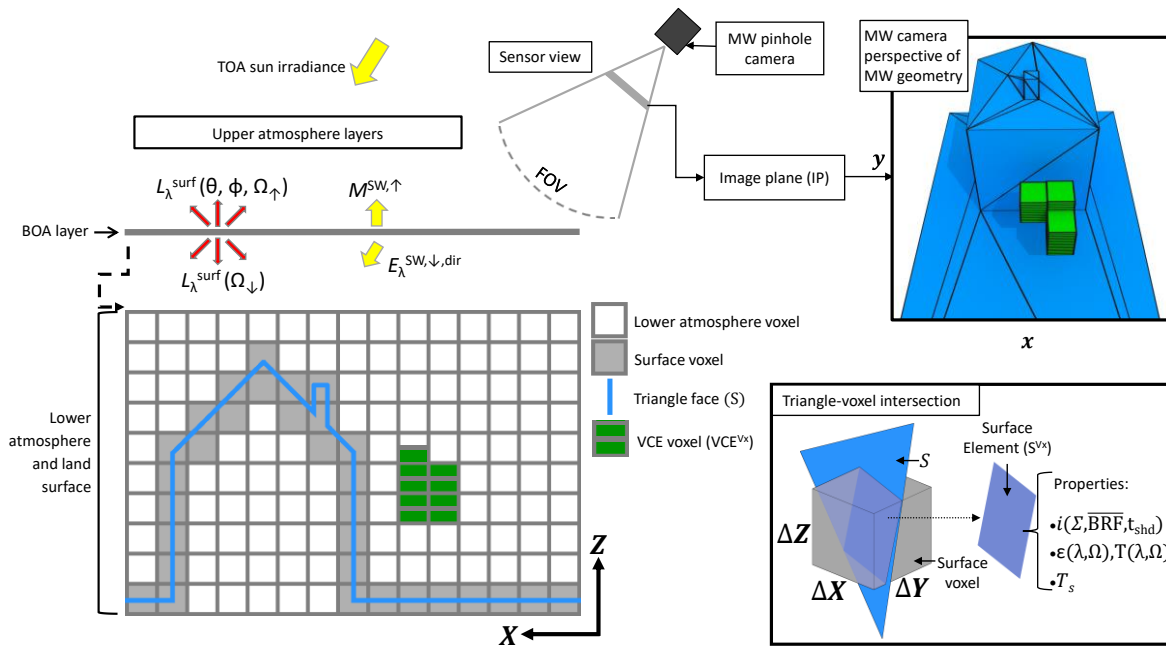


Figure 4-2. Surface representation and interaction in the “model world” (MW) that is used to interpret the “real world” (RW) urban area and observations, with radiative processes and triangle-voxel intersection managed by the DART model. The pinhole camera can also be below the bottom of atmosphere (BOA) layer. See list of symbols and acronyms for definitions.

Each surface element (Figure 4-2) is assigned three properties: orientation and material ( $\Sigma$ ), sun-surface geometry (bidirectional reflectance factor, BRF) and shadow history (time in shade,  $t_{\text{shd}}$ , min) which are all used to inform the upscaling of observed surface temperatures. The three properties (Table 4-3) combine to a unique surface class  $i$  at timestep  $t$  resulting in a 3D voxel array of surface classes  $[V_x(X, Y, Z, i, t)]$ .

Table 4-3. Surface properties of orientation and material ( $\Sigma$ ), bidirectional reflectance factor (BRF) and shadow history ( $t_{\text{shd}}$ ) assigned to each surface element (Figure 4-2) of the “model world” (MW) at  $\Delta X = \Delta Y = \Delta Z = 1$  m spatial and 5 min temporal resolution. A surface element has three surface properties:  $i(\Sigma, \overline{\text{BRF}}, t_{\text{shd}})$ .

	Property	Method	Description	Values	Fig. e.g.	
$\Sigma$	Orientation and material	Blender 3D modelling Land cover map Airborne hyperspectral	Cardinal orientation and material	Roof[dark] Roof[light] Ground[imp.] Ground[grass] North East	South West Down Mixed Masked	Figure 4-3 Figure 4-5b
$\overline{\text{BRF}}$	Sun-surface geometry	DART simulation	DART BRF simulation	BRF binned ( $\overline{\text{BRF}}$ ) as $0 \rightarrow 2$ at $\Delta 0.25$ (unitless). Shaded surfaces ( $\text{BRF} < 0.05$ ) are assigned $\text{BRF} = -1$	Figure 4-4	
$t_{\text{shd}}$	Shadow history	DART simulation	Time in shade	$0 \rightarrow 2\tau \Delta 5$ (min)	Figure 4-5d	

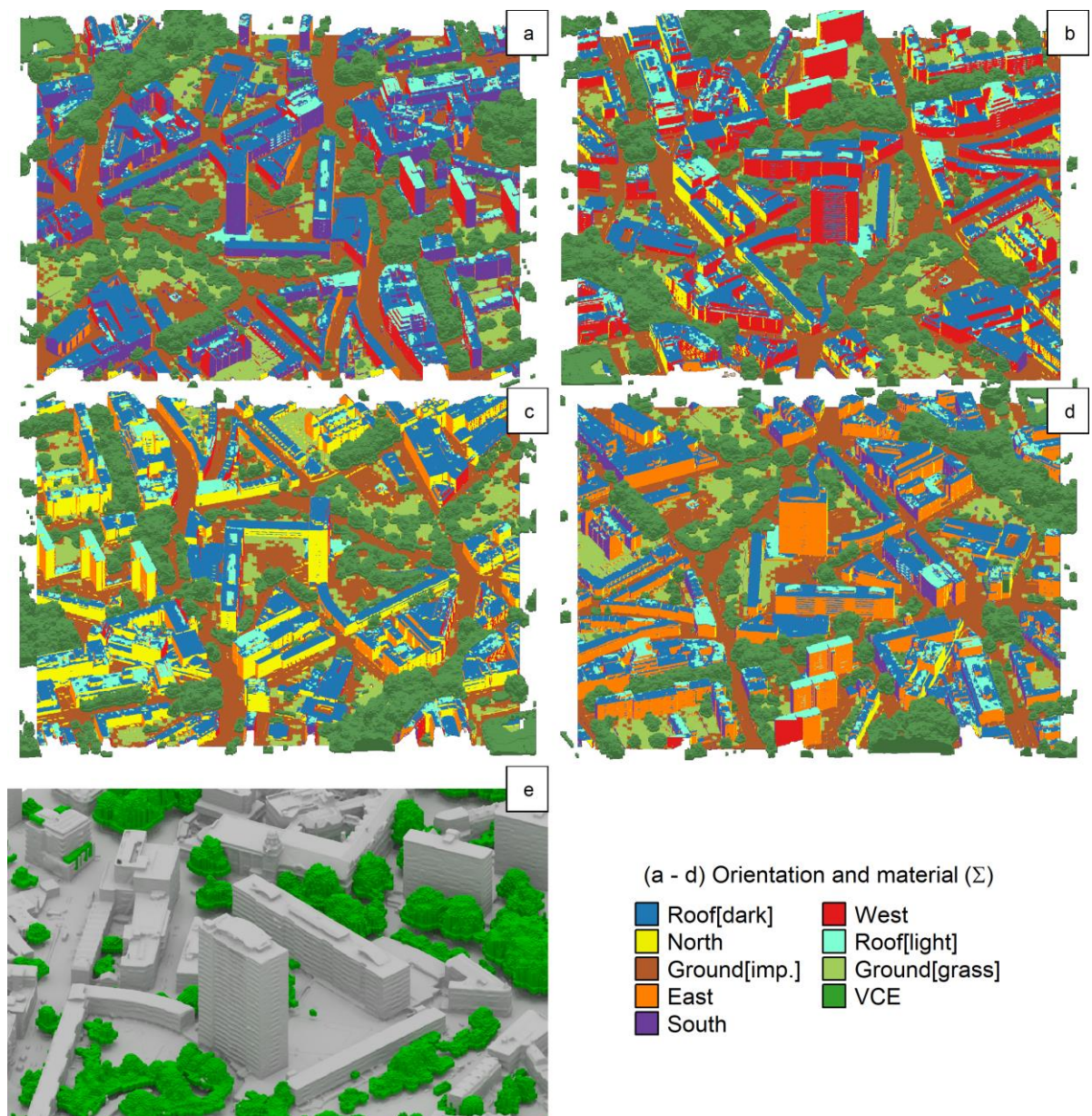


Figure 4-3. Digital surface model (DSM) and vegetation canopy elements (VCE) for the study area created from Google Earth (Google, 2019a) imagery (Appendix D) with (colours) orientation and material surface properties ( $\Sigma$ ), rendered in Blender (Blender, 2018) for off-nadir view directions facing: (a) north, (b) east, (c) south, (d) west and (e) northeast with focus on the study sites and surface geometry, rendered without  $\Sigma$ . The VCE product covers slightly larger area than the DSM.

The DSM triangle orientation property (walls by cardinal orientation, roofs, ground and downward) is extracted from the surface model using the Blender 3D modelling software version 2.79b (Blender, 2018). Incorporating a 4 m raster land cover dataset (Lindberg and Grimmond, 2011) and a roof albedo classification derived from a 1 m airborne hyperspectral image (NERC ARSF, 2010) allows for the surface classes to be enhanced. Ground is subdivided into grass (Ground[grass]) and impervious (Ground[imp.]) while roofs are either of high albedo (Roof[light]) or low albedo

(Roof[dark]). Further details can be found in Chapter 3 and Appendix D. The final DSM with  $\Sigma$  assigned to each triangle (Figure 4-3) is intersected with the voxel array to determine  $\Sigma$  for each surface element.

#### 4.2.2.1 Surface-sun geometry

DART simulations of direct incoming SW radiation across the MW surface (Figure 4-4) are used to determine the sun-surface geometry of each surface element through time, and the shadowing of surface elements by other surface elements and VCEs.

All surface elements are defined in DART as Lambertian reflectors. Direct downwelling spectral irradiance ( $E_{\lambda}^{\downarrow,dir}$ ) is simulated by DART at 0.5  $\mu\text{m}$  wavelength ( $\lambda$ ,  $\Delta\lambda = 0.01 \mu\text{m}$ ) with solar angles calculated using NOAA solar calculator equations (NOAA, 2016). Rays from the BOA (bottom of atmosphere, Figure 4-2) layer ( $625 \text{ rays m}^{-2}$ ) are tracked with spectral radiant flux density  $E_{\lambda}(\theta, \phi, \Omega, t)$  ( $\text{W m}^{-2} \mu\text{m}^{-1}$ ) along solid angle  $\Omega$  (sr) and direction  $(\theta, \phi)$  through the lower atmosphere and land surface at timestep  $t$ .  $E_{\lambda}(\theta, \phi, \Omega, t)$  that is intercepted by  $S^{Vx}(X, Y, Z)$  is scattered isotropically for all possible scattering directions, according to its position and orientation. Energy from rays scattered from the surfaces are stored by the voxel of  $S^{Vx}(X, Y, Z)$ .

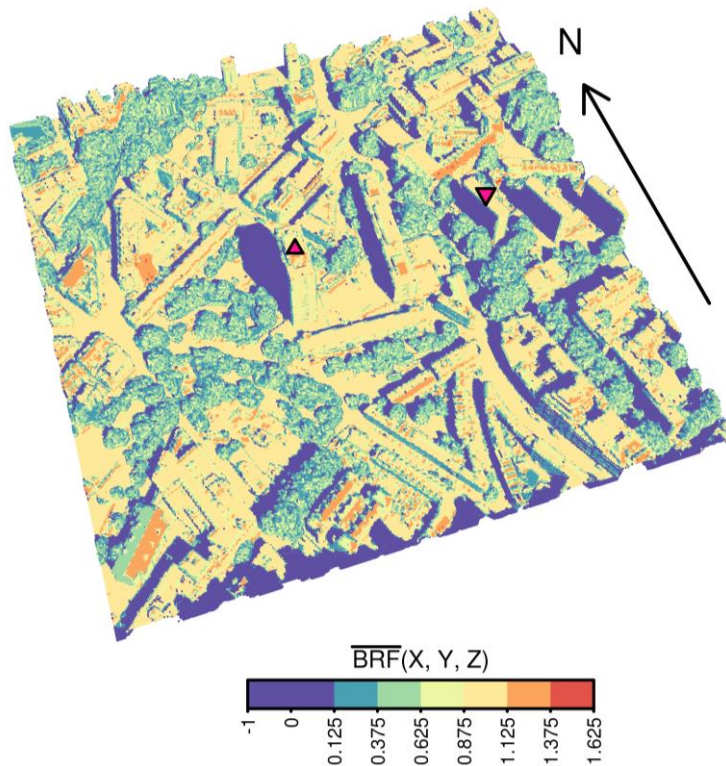


Figure 4-4. Surface geometry of the “model world” (MW) with bi-directional reflectance factor ( $\overline{\text{BRF}}$ ) (bins) from direct incoming solar radiation simulated using DART for 27<sup>th</sup> August 2017 11:00 and stored as a 3D array of voxels. See Figure 4-1b for (pink symbols) observation sites.

Across the entire scene this produces a 3D array of voxels with values of locally scattered radiation (SR) for a given timestep [ $M_\lambda(X, Y, Z, t)$ ,  $W\ m^{-2}$ ]. The fraction  $fSR_{DART}$  references any sun-surface geometry to spectral irradiance for a flat surface:

$$fSR_{DART}(X, Y, Z, t) = \frac{M_\lambda(X, Y, Z, t)}{E_\lambda^{\downarrow,dir}(X, Y, Z = \text{top}, t)} \quad \text{Eqn. 4.1}$$

by normalising with the downwelling spectral irradiance at the BOA layer [ $E_\lambda^{\downarrow,dir}(X, Y, Z = \text{top}, t)$ , Figure 4-2]. Based on  $fSR_{DART}(X, Y, Z, t)$ , a 3D distribution of bidirectional reflectance factor  $BRF(X, Y, Z, t)$  is derived (Appendix J). The final surface property  $\overline{BRF}(X, Y, Z, t)$  (Figure 4-4) is created from the BRF binned (indicated by overbar) from  $0 \rightarrow 2$  with a bin width of 0.25. To differentiate shaded surfaces [ $BRF(X, Y, Z, t) \approx 0$ ] from the lowest  $\overline{BRF}$  bin ( $\overline{BRF} = 0 \rightarrow 0.25$ ), surface elements with  $BRF(X, Y, Z, t) < 0.05$  are assigned  $\overline{BRF}(X, Y, Z, t) = -1$ . The same is done for timesteps without direct solar radiation, determined based on  $E_{SW}^\downarrow$  observations (Section 4.2.1).

#### 4.2.2.2 Shadow history

The time series of  $\overline{BRF}(X, Y, Z, t)$  is used to estimate the time a surface element has spent in shade ( $t_{shd}$ , min).  $\overline{BRF}(X, Y, Z, t)$  is compared to the prior timestep [ $\overline{BRF}(X, Y, Z, t - 5\text{min})$ ] (Table 4-1). If a surface element becomes shaded at time  $t$ , it has spent  $t_{shd}(X, Y, Z, t) = 5$  min in shade. For the timestep prior to this ( $t - 5$  min), the surface element has spent zero minutes in shade and has  $t_{shd}(X, Y, Z, t - 5\text{min}) = 0$  min. A surface element that continues to be in shade [i.e.  $\overline{BRF}(X, Y, Z, t + 5\text{min}) = -1$ ] has  $t_{shd}(X, Y, Z, t + 5\text{min}) = 10$  min at the next timestep, etc. A surface element can be part sunlit and part shaded, even across multiple timesteps, however, each surface is reassigned as fully sunlit or fully shaded based on a 50 min window around each timestep. If a surface element has  $\overline{BRF}(X, Y, Z, t) > -1$ , is sunlit at  $t - 25$  min and shaded at  $t + 25$  min, then it is assumed that the surface element could be partially sunlit. In these cases, the following threshold is used to determine if the surface element is more shaded than sunlit, and used to update  $t_{shd}$  by:

$$t_{shd}(X, Y, Z, t) = \begin{cases} 0 & \text{if } \overline{BRF}(X, Y, Z, t) < [0.75 \cdot \overline{BRF}(X, Y, Z, t - 25\text{min})] \\ 5 & \text{otherwise} \end{cases} \quad \text{Eqn. 4.2}$$

When  $t_{shd}(X, Y, Z, t) = 0$ , surface elements are allocated the maximum  $\overline{BRF}(X, Y, Z)$  that occurred up to 5 timesteps prior (i.e.  $\max\{\overline{BRF}(X, Y, Z, t - 25\text{min} \rightarrow 0)\}$ ) to assign partially shaded surfaces with a fully sunlit status.

#### 4.2.2.3 Instrumentation and image classification

RW images are classified using the MW surface and “instrumentation”. Sensor view modelling replicates the RW LWIR camera perspectives in the MW, with  $(X, Y, Z)$  elements of the MW surface geometry projected on to the MW camera image plane (IP). Pinhole cameras (Hartley and Zisserman, 2004) are used. Each have a location, view angle and field of view within the MW. The pinhole

camera rectilinear perspective projection causes 3D straight lines to be straight lines in the images. The RW cameras are geometrically calibrated to match the pinhole camera projections (i.e. image distortion correction applied, see Chapter 2 and Appendix A for details). MW surface elements projected onto the MW camera IP provide the RW image classes (e.g. Figure 4-5a) per-pixel  $(x, y)$ : surface properties of  $\Sigma(x, y)$ ,  $\overline{\text{BRF}}(x, y)$  and  $t_{\text{shd}}(x, y)$  (Figure 4-5).

Surface property  $\Sigma$  for each camera pixel [ $\Sigma(x, y)$ , Figure 4-5b] is obtained using Blender, with colours from each DSM triangle property (Figure 4-3) projected for the MW camera perspective (see Chapter 2 for details). A pixel is  $\Sigma_{\text{mixed}}(x, y)$  (dark grey, Figure 4-5b) if more than one surface and orientation property is rendered within the pixel's instantaneous field of view (IFOV). RW pixels viewing surfaces beyond the MW (e.g. Figure 4-5b C2, top of image) are assigned  $\Sigma_{\text{mixed}}(x, y)$ . Near-field pixels that are challenging to align (e.g. IMU and CUB roofs) include a metal roof (C2, Figure 4-5b) and the corner of the C1 enclosure (Figure 4-5b, top left); these are manually assigned the additional class  $\Sigma_{\text{masked}}(x, y)$  and excluded from further analysis.

Per-pixel surface properties of BRF [ $\text{BRF}(x, y, t)$ , Figure 4-5c] are determined using DART. Rays scattered from the surface of each fSR( $X, Y, Z$ ) (Eqn. 4.1) simulation for 3D classification of sun-surface geometry are tracked across the IP of each MW camera (Yin, Lauret and Gastellu-Etchegorry, 2015). These sensor-tracked rays are used by DART to calculate at-sensor spectral radiance [ $L_{\lambda}^{\text{cam}}(x, y, t)$ ,  $\text{W m}^{-2} \text{sr}^{-1} \mu\text{m}^{-1}$ ] with:

$$\text{BRF}(x, y, t) = \frac{\pi L_{\lambda}^{\text{cam}}(x, y, t, \Omega)}{E_{\lambda}^{\downarrow, \text{dir}}(t)}. \quad \text{Eqn. 4.3}$$

As a low density of rays incident on a surface cause inaccuracies and erroneous patterns in  $\text{BRF}(x, y)$ , isolated “sunlit” pixels [ $\text{BRF}(x, y) > 0$ ] (i.e. none of the surrounding 8 pixels have  $\text{BRF}(x, y) > 0$ ) are reassigned to  $\Sigma_{\text{mixed}}(x, y)$ . A low density of incident rays occurs if the direct-beam solar radiation is near-perpendicular to surfaces and/or when the sun angle is low relative to the surface.

Again, pixel values of  $\text{BRF}(x, y)$  are binned as  $\overline{\text{BRF}}(x, y)$ .  $\overline{\text{BRF}}(x, y)$  provides the time the surface sampled by each pixel has spent in shade [ $t_{\text{shd}}(x, y)$ ] in the same way as  $t_{\text{shd}}(X, Y, Z, t)$  (i.e. 2D pixels rather than 3D voxels).

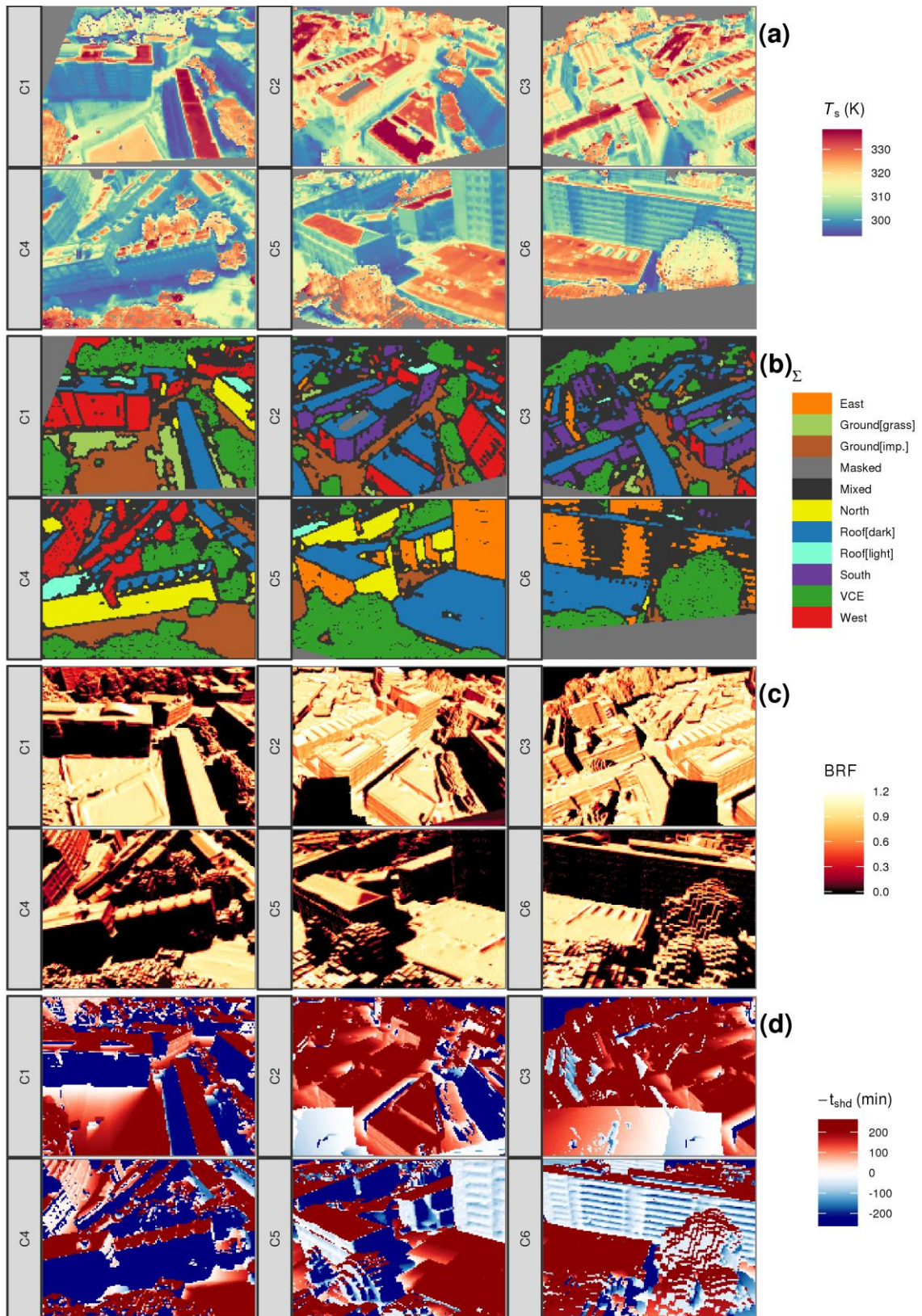


Figure 4-5. (a) Optris PI longwave infrared (LWIR) camera observations for 27<sup>th</sup> August 2017 12:00 UTC and (b – d) simulated surface properties projected onto the image plane (IP) of “model world” (MW) cameras that simulate the perspective of (a). Surface properties are: (b) orientation and material ( $\Sigma$ ), (c) shortwave bidirectional reflectance factor (BRF) assuming Lambertian reflecting surfaces, and (d) time surfaces have spent in shade ( $t_{shd}$ , white  $\rightarrow$  blue) or sun (white  $\rightarrow$  red). The cameras (Table 4-2) are indicated to the left of each image.

### 4.2.3 Upscaling classified surface temperature across model world

Classified observations are upscaled across the MW surface to give a 3D surface temperature distribution  $[T_s^{3D}(X, Y, Z, t)]$ . According to class  $i$  (combination of  $\Sigma$ ,  $\overline{\text{BRF}}$  and  $t_{\text{shd}}$ , Table 4-3), per-pixel surface temperature observations  $[T_s(x, y, i, t)]$  at timestep  $t$  are aggregated to give per-class values of surface temperature  $[T_s(i, t)]$ . These are then gap-filled and allocated to all surface elements based on the 3D surface classes  $[S^{Vx}(X, Y, Z, i, t)]$ .

Initial per-pixel surface temperature aggregation uses  $\Sigma$  and  $\overline{\text{BRF}}$  for each timestep  $[T_s(\Sigma, \overline{\text{BRF}}, t)]$ , excluding “mixed” and/or “masked” pixels. As there are more  $T_s(\Sigma, \overline{\text{BRF}}, t_{\text{shd}}, t)$  combinations than observed, a per-class shaded temperature  $[T_s(\Sigma, \overline{\text{BRF}} = -1, t)]$  is used. To account for the hysteresis effect inherent to the cooling of shaded surfaces (Meier, Scherer and Richters, 2010b; Chapter 2), a “cooling event” time window is defined. A cooling event starts when a pixel is sunlit for the last time ( $t_{\text{shd}}(x, y) = 0$  min) and ends when it is substantially cooled ( $t_{\text{shd}}(x, y) > n\tau$ ), with time constant  $\tau$  (min) and multiplicative factor  $n$ . To determine a representative length of time for cooling events,  $\tau(x, y)$  is calculated using an exponential rate of cooling (Vollmer, 2009) from all pixels that enter shade as:

$$T_s[\text{a}] = T_s[\text{b}] + (T_s[\text{c}] - T_s[\text{d}])e\left(-\frac{t}{\tau}\right) \quad \text{Eqn. 4.4}$$

based on different surface temperature observations (Table 4-3).

Table 4-4. Surface temperature sub-classes used to determine exponential cooling (Eqn. 4.4). See text and list of symbols and acronyms for definitions.

	Surface temperature ( $T_s$ ) description	Full definition
$T_s[\text{a}]$	Pixel $T_s$ with time in shade no longer than $n\tau$ minutes.	$T_s(x, y, \Sigma, \overline{\text{BRF}} > -1, t_{\text{shd}} > 0 \ \& \ \leq n\tau, t)$
$T_s[\text{b}]$	Ambient $T_s$ at time $t$ , aggregated (median) from pixels in shade for more than $n\tau$ minutes.	$T_s(\Sigma, \overline{\text{BRF}} = -1, t_{\text{shd}} > n\tau, t)$
$T_s[\text{c}]$	Pixel $T_s$ at the timestep prior to shading ( $t_{\text{shd}} = 0$ ), i.e. at the start of the cooling event ( $t = 0$ ).	$T_s(x, y, \Sigma, \overline{\text{BRF}} > -1, t_{\text{shd}} = 0, t = 0)$
$T_s[\text{d}]$	Ambient $T_s$ at the timestep prior to shading ( $t = 0$ ), aggregated (median) from pixels in shade for more than $n\tau$ minutes.	$T_s(\Sigma, \overline{\text{BRF}} = -1, t_{\text{shd}} > n\tau, t = 0)$

Cooling event lengths ( $n\tau$ ) need to be initially estimated. Using all pixels within a day,  $n\tau$  is set at 15 min and increased in increments of 15 min until the majority of observations are at ambient surface temperature; i.e. when  $> 75\%$  of pixels with  $t_{\text{shd}}(x, y) = n\tau$  have an exponentially cooled  $T_s$  ( $T_s[\text{a}]$ ) lower than ambient temperature ( $T_s[\text{b}]$ , median) plus one standard deviation. Only considered are cooling events where the pixel has a recorded temperature at  $t_{\text{shd}}(x, y) = 0$  and  $t_{\text{shd}}(x, y) = n\tau$ .

In Eqn. 4.4, the temperature difference between the recently shaded surface and the ambient surface temperature throughout the cooling event ( $T_s[\text{a}] - T_s[\text{b}]$ , Table 4-2 and Figure 4-6b) isolates the rate of cooling from any ambient variations in temperature. After  $\tau$  minutes, the temperature difference is reduced to  $1/e$  ( $\sim 0.368$ ) of the value at  $t_{\text{shd}} = 0$  (Vollmer and Möllmann, 2017). The established

time window for observations within cooling events (e.g. Figure 4-6a) enables the estimation of  $\tau(x, y, t)$  using a nonlinear least squares (NLS) fit of Eqn. 4.4 (e.g. Figure 4-6b) for all per-pixel cooling events. The NLS fit of  $\tau(x, y, t)$  is rejected if (1) it contains less than 5 timesteps, (2) the pixel surface property becomes “mixed” (Section 4.2.2.3) at any point during the event, (3) the NLS fit fails to converge, or (4)  $\tau(x, y, t) > 1000$  min. A final daily value of  $\tau$  uses the median value of  $\tau(x, y, t, \Sigma)$  determined from all eligible cooling events as one representative time constant for three surface types: roofs, walls, and ground [ $\tau(\Sigma)$ ]. From this, the initial estimate of  $n\tau$  is updated to use  $\tau(\Sigma)$  and a value of  $n$  that is explicitly defined (here  $n = 2$ ).

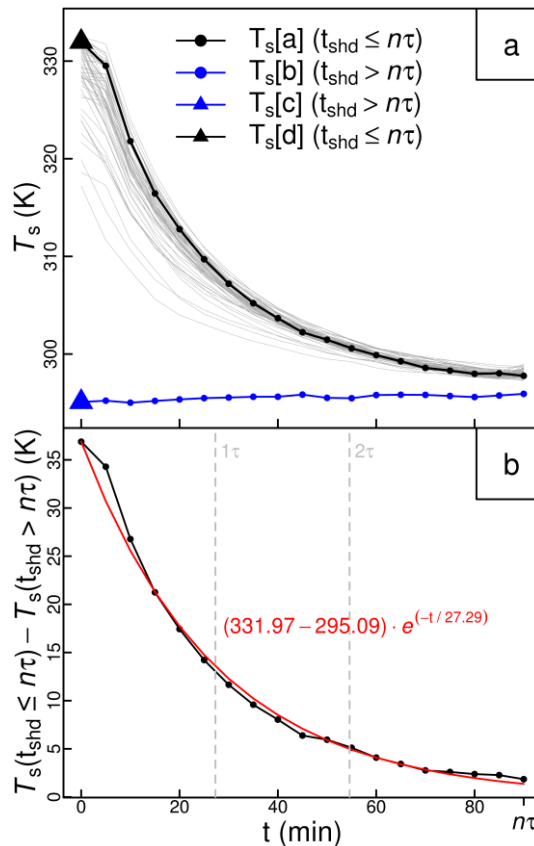


Figure 4-6. All C3 camera (Table 4-2) roof-viewing pixels shaded from  $t = 0$  and  $t = 90$  (min) (10:00 and 11:30 on 27<sup>th</sup> August 2017): (a) all samples (grey lines) and one (random, black) cooling event with the background surface temperature (blue) line) (b) an exponential fit (red, Eqn. 4.4) to one (black line from a) to one cooling event.

Meier *et al.* (2010) describe surface heating rates under controlled conditions in an urban courtyard with homogeneous surface materials. However, for our complex site we could not generate a parameterisation for recently sunlit surfaces as the required “well sunlit” reference temperature is challenging to define given the greater variability in sunlit temperatures compared to shaded temperatures.

#### 4.2.3.1 Gap-filling per-class surface temperatures

As observations do not cover all facets of the entire study area, there are more 3D classes  $S^{Vx}(X, Y, Z, i, t)$  than aggregated per-class observations  $[T_s(i, t)]$ . This requires observations to be gap-filled. The multiple and static cameras sample all  $\Sigma$  except for downward facing surfaces ( $\Sigma_{\text{down}}$ ) (e.g. under a balcony, rendered as  $\Sigma_{\text{mixed}}(x, y)$ , Figure 4-5b). These are gap-filled using per-pixel observations from all shaded walls.

Bins of  $T_s(\Sigma, \overline{\text{BRF}})$  with less than 96 pixels (0.5 % of an image) are gap-filled with the nearest lower bin [e.g.  $T_s(\Sigma, \overline{\text{BRF}} = 0.5)$  filled with  $T_s(\Sigma, \overline{\text{BRF}} = 0.25)$ ] consecutively until all gaps are filled. For gap-filling the lowest possible BRF bin (i.e.  $\overline{\text{BRF}} = -1$ ), observations from all per-pixel shaded temperatures [i.e.  $T_s(x, y, \overline{\text{BRF}} = -1)$ ] are used.

For cooling events with an ambient temperature at  $t = 0$  that is greater than the sunlit temperature at  $t_{\text{shd}} = 0$  min, the ambient temperature is used throughout the cooling event. If the recently shaded surface temperature becomes less than the well shaded temperature ( $T_s[\text{b}]$ , Table 4-2) then this temperature and all subsequent temperatures with a greater time in shade are given the ambient temperature ( $T_s[\text{b}]$ ).

#### 4.2.3.2 Extrapolating observations to 3D and complete surface temperature

$T_s(i, t)$  is allocated to the 3D space  $[S^{Vx}(X, Y, Z, i, t)]$  to create 3D surface temperature  $[T_s(X, Y, Z, i, t)]$ . A surface element can have multiple triangles with multiple properties of  $\Sigma$ . For example, a voxel at the edge of a roof may contain a surface element comprising  $\Sigma_{\text{Roof}}$  and  $\Sigma_{\text{North}}$  DSM triangles. In these cases, the mean temperature of all classes involved is allocated to the respective surface element.

Interpretation of thermal anisotropy and satellite directional view bias uses the complete surface temperature ( $T_c$ , K) or areally averaged 3D surface temperature rather than a directional surface temperature from RS (Voogt and Oke, 1998b; Jiang *et al.*, 2018).  $T_c$  is important as surface-atmosphere exchanges involve (to some extent) all surfaces in contact with the atmosphere. Each surface element has an area  $[S^{Vx}(X, Y, Z), \text{m}^2]$  that is incorporated to weight  $T_s(X, Y, Z, i, t)$ :

$$T_c(t) = \sum_{X,Y,Z}^n T_s(X, Y, Z, i, t) \left[ \frac{S^{Vx}(X, Y, Z)}{\sum_{X,Y,Z}^n S^{Vx}(X, Y, Z) + A^{\text{VCE}}} \right] + T_s^{\text{VCE}} \left[ \frac{A^{\text{VCE}}}{\sum_{X,Y,Z}^n S^{Vx}(X, Y, Z) + A^{\text{VCE}}} \right] \quad \text{Eqn. 4.5}$$

where  $A^{\text{VCE}}$  ( $\text{m}^2$ ) is the VCE surface area across the domain and  $T_s^{\text{VCE}}$  the VCE surface temperature. Similar to Voogt and Oke (1997),  $A^{\text{VCE}}$  is taken as plan area of all VCEs, here derived from a 0.2 m raster mask of the VCE distribution. Vegetation can exhibit complex thermal anisotropy but on average is nearly equal to  $T_a$  (Meier and Scherer, 2012), so  $T_s^{\text{VCE}}$  is approximated by  $T_a$  from the weather station (Section 4.2.1) rather than thermography.

#### 4.2.4 Simulation of satellite surface temperature

In order to simulate the effective thermal anisotropy, surface-leaving spectral radiance ( $L_{\lambda}^{\text{surf}}$ ) from the MW area is simulated with DART for a series of discrete upward directions [ $L_{\lambda}^{\text{surf}}(\phi, \theta, \Omega)$ ].

Optical properties at 11.02  $\mu\text{m}$  are used to correspond with the centre of MODIS (Moderate Resolution Imaging Spectroradiometer) band 31 (10.780 – 11.280  $\mu\text{m}$ ). For  $\Sigma_{\text{Ground[grass]}}$  the mean of all dry grass samples ( $\epsilon_{11.02\mu\text{m}} = 0.955$ ) in MODIS UCSB (University of California, Santa Barbara) spectral library (Wan, Ng and Dozier, 1994; Snyder, Wan and Zhang, 1997) is used. As the surface material and associated emissivity are not well known for other DSM elements, the mean spectral emissivity ( $\epsilon_{11.02\mu\text{m}} = 0.945$ ; min = 0.900, max = 0.968, n = 60) from all non-metal and non-plastic impervious materials in the SLUM spectral library (Kotthaus *et al.*, 2014) is used.

VCE optical properties are parameterised using a spatially homogeneous turbid representation of leaves with a spherical angular distribution (Wang, Li and Su, 2007; Pisek, Ryu and Alikas, 2011) within each VCE<sup>Vx</sup>. Leaves are given “deciduous leaf” optical properties from the DART spectral database (leaf transmissivity = 0.020, reflectance = 0.027) with a leaf area density [leaf area within voxel / voxel volume ( $\text{m}^2 \text{m}^{-3}$ )] of 1.6 estimated for summertime conditions (Lalic and Mihailovic, 2004; Jeanjean *et al.*, 2017).

DART is used with the MW geometry, surface temperature  $T_s(X, Y, Z, i, t)$  and the optical property distribution with  $\Delta\lambda = 0.01$  bandwidth.  $E^{\text{LW},\downarrow}$  from the CNR1 radiometer determines the sky brightness temperature ( $T_b^{\text{sky}}$ ) by inversion of the Stefan-Boltzmann law. It is used in DART to determine an isotropic source of downwelling spectral radiance received from the BOA layer [ $L_{\lambda}^{\text{sky}}(\Omega_{\downarrow})$ ] with the Planck function at the simulation wavelength (11.02  $\mu\text{m}$ ). The emission and multiple scattering of radiation across the surfaces is tracked across a large number of individual rays (Appendix K). Rays that cross the BOA determine a spectral radiance image with the BOA cell resolution for each upward direction [ $L_{\lambda}^{\text{surf}}(x, y, \phi, \theta, \Omega)$ ] that is averaged across each image pixel to give  $L_{\lambda}^{\text{surf}}(\phi, \theta, \Omega)$ .

$L_{\lambda}^{\text{surf}}(\phi, \theta, \Omega)$  is combined with  $L_{\lambda}^{\text{sky}}(\Omega_{\downarrow})$  and a representative bulk spectral emissivity used for EO land surface temperature (LST) applications ( $\epsilon_{\lambda}^{\text{EO}}$ ) to give a directional LST estimate [ $T_s^{\text{EO}}(\phi, \theta)$ ] using:

$$T_s^{\text{EO}}(\phi, \theta, \Omega) = c_2 / \left[ \lambda \cdot \ln \left( \frac{c_1}{\lambda^5 \frac{L_{\lambda}^{\text{surf}}(\phi, \theta, \Omega) - (1 - \epsilon_{\lambda}^{\text{EO}}) \frac{1}{\pi} E_{\lambda}}{\epsilon_{\lambda}^{\text{EO}}} + 1} \right) \right] \quad \text{Eqn. 4.6}$$

with  $c_1 = 1.191042 \times 10^9$  ( $\text{W m}^{-2} \text{sr}^{-1} \mu\text{m}^{-1}$ ) and  $c_2 = 1.4387770 \times 10^4$  ( $\mu\text{m K}$ ) the first and second radiation constants. Operational determination of  $\epsilon_{\lambda}^{\text{EO}}$  (Li *et al.*, 2013) uses land cover datasets for

the split-window approach (Wan, 1996; Snyder and Wan, 1998) or concurrent estimation with land surface temperature following the temperature emissivity separation method (Wan, 1997). Here the emissivity for band 31 from the MODIS M\*D11A1 collection 6 (Wan, 2014) split-window product is used to replicate the MODIS land surface temperature product.

The M\*D11A1 collection 6 processed by MODIS<sub>Stp</sub> (Busetto and Ranghetti, 2016) have temperature, emissivity and quality control products with a 927 m pixel resolution. EO data of the pixel covering the IMU site are compared to simulated directional surface temperatures.

### 4.3 Results

#### 4.3.1 Assessment of the morphometric and land cover characteristics of the MW area

To assess how representative the study area is compared the spatial extent of the complete city and also a single satellite pixel, the morphometric and land cover characteristics are analysed for a ~ 4 km x 4 km area around the site (Figure 4-7a). South and east of the site is the central business district (CBD). Building height ( $z_b$ ) and building plan area index ( $\lambda_p$ ) on average decrease northwards and higher vegetation fractions coincide with more residential areas. The study area is generally similar to the larger area (Figure 4-7), except with respect to VCE and grass fraction (Table 4-5) which are higher than the 75<sup>th</sup> percentile of the larger area (cf. Figure 4-7b, c). The park in the study area has a large amount of vegetation (Figure 4-1b, centred on grid coordinates 284500, 5712850) while there is an overall lower fraction of vegetation to the south around the CBD and River Thames.

The study area has a higher urban density than prior ground-based thermography studies. For example, the area-weighted building height of 6.23 m from Adderley *et al.* (2015) and 1.5 m from Chapter 2 are both much lower than the median height of 13.5 m in this study (Table 4-5). The vegetation density is most likely lower than in the area studied by Meier and Scherer (2012).

Table 4-5. Study area (Figure 4-1) land cover fractions in the MW (from raster data) and variability of morphometric parameters indicated by percentiles ( $P$ ).

MW parameter	Symbol	MW	$P_{25}$	$P_{50}$	$P_{75}$
Plan area fraction:					
VCE		0.17			
Grass		0.17			
Building (plan area index)	$\lambda_p$	0.37			
Building height (m)	$z_H$		6.90	13.49	19.10
Sky view factor	$\psi^{sky}$		0.41	0.57	0.75

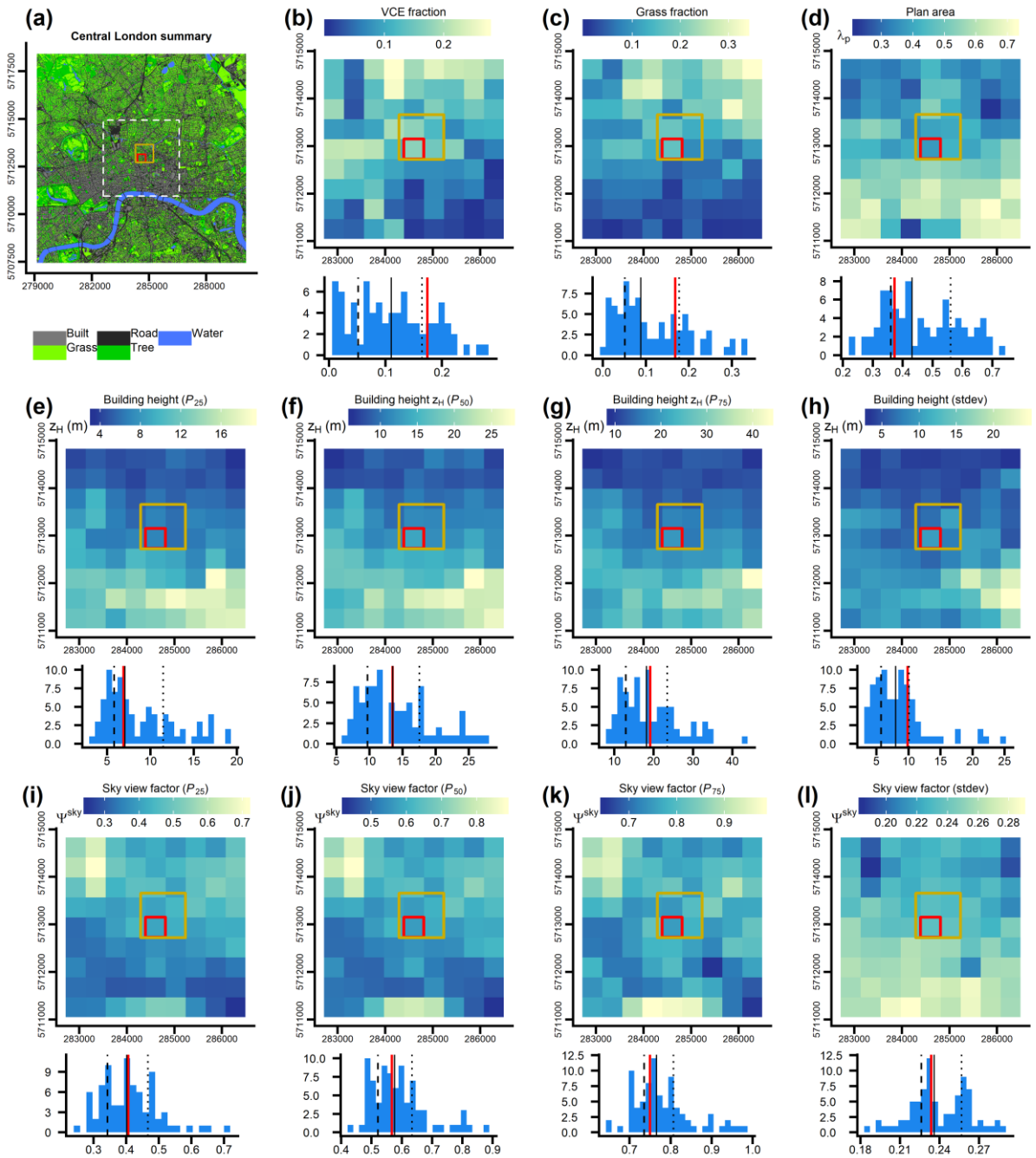


Figure 4-7. Variability of surface characteristics in central London (49 areas of 420 m x 420 m) oriented to grid north (WGS84 UTM grid zone 31N) around the study area (red) and MODIS M\*D11A1 pixel (orange) with (upper) maps and (lower) histograms with  $n^{\text{th}}$  percentiles ( $P_n$ ) of (dashed lines)  $P_{25} \rightarrow P_{75}$ , (solid line)  $P_{50}$  for the study area. (a) Land cover (4 m) central London with (white dashed box) extent of maps in b – l and (red) the study area (Figure 4-1). Surface characteristics: (b) plan area fraction of tall vegetation ( $> 2$  m) (c) plan area fraction of grass (d) plan area fraction of buildings (i.e. plan area index), (e – h) building height, (i – l) sky view factor (Dozier and Frew, 2002) calculated in R (R Core Team, 2017) with the “horizon” package (Doninck, 2018), and (g, l) standard deviation of the respective parameter.

### 4.3.1.1 Observational source area and image classification

The observational source area is critical to understand as surface temperatures upscaled across the entire study area are derived from inherently sub-sampled measurements. Although this source of uncertainty exists in previous ground-based studies, it has never been quantified. Given the complexity and heterogeneity of the present study area, it is particularly critical to assess the extent to which the observations capture the full diversity of the total study area.

Of the total MW surface area  $A_{TOTAL}$  ( $4.1 \times 10^5 \text{ m}^2$ , Figure 4-8), 88.0 % is composed of DSM triangles and the remainder (12.0 %) is from the VCE plan area. East and west walls are 23.3 % of  $A_{TOTAL}$  compared to 18.3 % for north and south walls. These numbers are not equal given the MW buildings are not necessarily cuboid and are frequently cut off at the MW edges (Figure 4-3). The ground surfaces (30.6 %) (i.e. streets, parks, courtyards etc.) have greater area than the roofs (15.6 %). The latter mostly have low albedo (Roof[dark], 12.8 %). The fraction of downward facing surfaces is very small (0.9 %) so their required gap-filling has little impact.

Using Blender, the DSM vertices that are completely within the FOV of any camera are selected. Adding the area of all selected DSM triangles gives the overall camera source area ( $A_{CAM}$ ,  $\text{m}^2$ ) which is 9.5 % of  $A_{TOTAL}$  (3.9 ha).  $A_{CAM}$  excludes VCEs directly but resolves the occlusion of other surfaces by VCEs. Where cameras have overlapping source areas (Figure 4-1c, Figure 4-5) the overlapping area is allocated arbitrarily to the camera with lowest numeric ID (Table 4-2). As  $A_{CAM}$  is calculated directly from the DSM and not from rendered images (Section 4.3.1.1),  $A_{CAM}$  includes all mixed (“complex” geometry) and masked (near field objects, e.g. roofs directly beneath cameras, Figure 4-5b) pixel leading to a small overestimation of  $A_{CAM}$ . Still, it is expected that  $A_{CAM}$  underestimates the actual source area for classified pixels because triangles that are partially visible through the MW camera FOV are rejected.

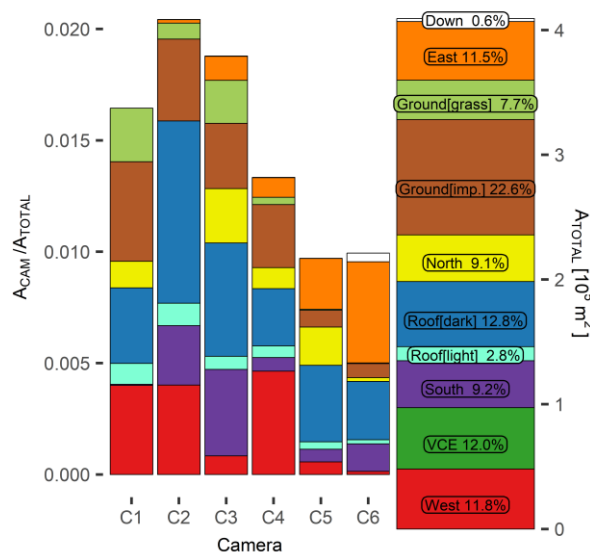


Figure 4-8. Area of surface ( $\text{m}^2$ ) across ( $A_{TOTAL}$ ) the total three-dimensional study area and ( $A_{CAM}$ ) seen by the LWIR cameras (Table 4-2) for (colours) different surface and orientation properties.

Inter-camera differences in  $A_{CAM}$  result from camera siting height, zenith view angle and the occlusion of far-field surfaces by near-field objects. Located 75 m agl with an oblique view angle, camera C2 has the largest source area (2 % of MW area, Figure 4-8) whereas C5 and C6, mounted at 37 m agl, have the smallest source areas ( $\sim 1$  % of MW each). In contrast to RS from spaceborne platforms, ground-based sampling is not limited to predominantly capture the horizontal facets (ground, roof). Due to oblique view angles, vertical facets substantially contribute to the observational source area. Still, while roof and ground surfaces are observed by all cameras, the vertical facets sampled depend on the camera azimuth (Table 4-2). Cameras can appear to view surfaces from opposing directions (e.g. east and west) due to the grouping of the heterogeneous wall facings into the four cardinal directions (Figure 4-9).

The azimuth and zenith of DSM triangles within each camera pixel IFOV are given in Figure 4-9. The distribution of surface azimuth angles for the walls is uneven (Figure 4-9a). Some angles have many samples (maximum 2677 pixels for  $342.5^\circ \rightarrow 347.5^\circ$ ) and others far fewer (minimum 130 pixels for  $127.5^\circ \rightarrow 132.5^\circ$ ) as building walls have a few fixed directions and sensors observe only limited views (Table 4-2). Given the complexity of the study area geometry, the azimuthal facings are well distributed within each wall orientation bin (Figure 4-9a, between vertical dashed lines) except for the  $\Sigma_{South}$  where a view bias of southeast facing ( $\theta \approx 135^\circ \rightarrow 150^\circ$ , Figure 4-9a) surfaces is found. This can be explained by the southwest-to-northeast street orientation seen by the northward facing cameras (C2 and C3, Figure 4-1). The  $\overline{BRF}$  values associated with southwest walls have fewer samples or require gap-filling (Section 4.2.3.1) using the well-sampled southeast facing observations. Sloped roofs, chimneys and balconies, etc. resolved in the DSM widen the surface zenith angle distribution (Figure 4-9b). Most observed walls are vertical (median  $90.83^\circ$ ) with variability ( $\pm 11.07^\circ$  standard deviation) from the sub-facet wall geometry (e.g. balconies). Roof pixels are mainly flat (median  $176.74^\circ$ ). Here, slight slopes (8579 pixels are between  $177.5^\circ$  and  $178.25^\circ$ ) may result from inaccuracies in the DSM, as these pixels most likely view flat roofs in the RW.

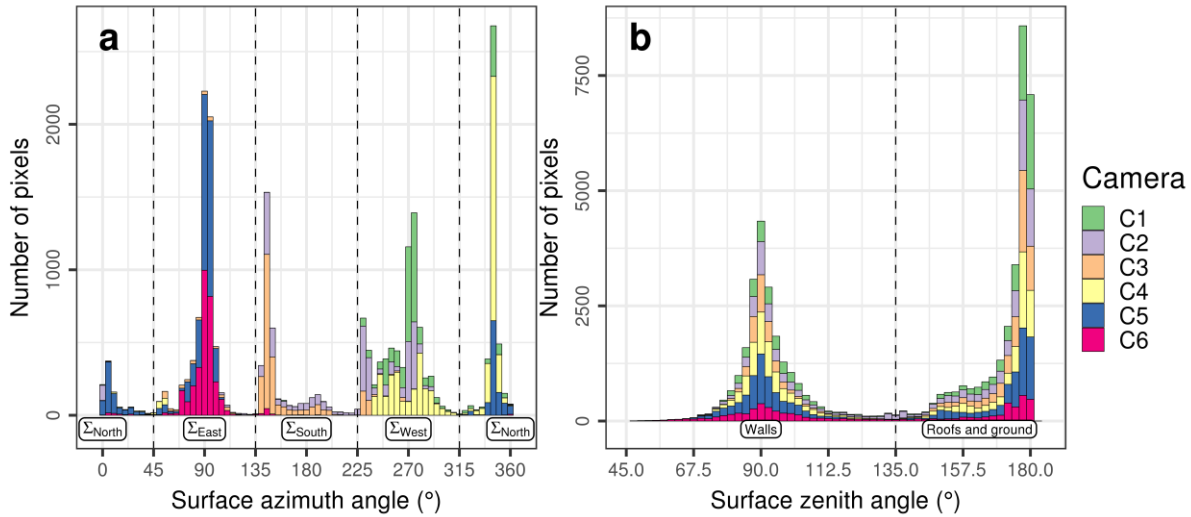


Figure 4-9. Frequency of pixels by surface orientations within the instantaneous field of view of each camera (excluding VCE but including “mixed” and “masked” pixels) for (a) azimuth facing (zenith angle  $<135^\circ$ ), and (b) zenith angles of pixels. Azimuth angle of  $0^\circ$  ( $180^\circ$ ) is north (south) for WGS84 UTM grid zone 31N. Pixels with a zenith angle of  $90^\circ$  ( $180^\circ$ ) face vertically (horizontally).

### 4.3.2 Drivers of observed surface temperature variability

The surface properties impact surface temperature variability and effective thermal anisotropy. To quantify the role of various drivers, results from the sensor view and 3D modelling are used with the controls on variability considered by scale: (i) building scale variability (facet, orientation and material  $\Sigma$ ), Section 4.3.2.1), (ii) sub-facet within a surface orientation (e.g. different roof slopes) related to the sun-surface geometry ( $\overline{\text{BRF}}$ , Section 4.3.2.2) and (iii) high spatial resolution shadow histories ( $t_{\text{shd}}$ , Section 4.3.2.3).

#### 4.3.2.1 Variability from surface orientation and material at the building scale

The building facets, orientations and their materials provide the coarsest surface characteristics for explaining surface temperature variability. Initially all observations (i.e. except for  $\Sigma_{\text{VCE}}$ ,  $\Sigma_{\text{mixed}}$  or  $\Sigma_{\text{masked}}$  pixel classes) are considered together (pre-classified – white, Figure 4-10a) to understand the overall variability of  $T_s$  observed during the day. Differences of 37.5 K are found between the 5<sup>th</sup> percentile ( $P_5$ )  $\rightarrow P_{95}$  during the period 12:00 – 12:55 (hereafter defined as time ending, i.e. 13:00). The mixed pixels (Figure 4-10a, grey) have a smaller hourly and diurnal range than the pre-classified temperatures. Mixed pixels are primarily associated with walls, as those often have complex small-scale features (e.g. balconies - C6, Figure 4-5a, b). These are generally cooler than roof and ground surfaces. Unresolved balconies can create complex shading patterns and may be cooler than facets with simpler more planar geometry.

As expected (e.g. Adderley, Christen and Voogt, 2015; Chapter 2), roofs have the greatest diurnal  $T_s$  range (Figure 4-10b, median  $\Sigma_{\text{roof[dark]}} T_s$  290.6  $\rightarrow$  329.0 K). The change in  $\Sigma_{\text{roof[dark]}} T_s$  across timesteps representative of Aqua and Terra satellite overpasses (10:30 and 13:30, respectively) is around 5 K (median  $\Sigma_{\text{roof[dark]}} T_s$  increases from 321.7 K at 11:00 to 326.9 K at 14:00, which is less than in early morning when the roofs are first sunlit (e.g. between 09:00 and 10:00, median  $T_s$  for  $\Sigma_{\text{roof[dark]}}$  pixels increases from 303.9 K to 315.0 K). Within each hour, roofs have consistently large  $T_s$  variability driven by insolation (Section 4.3.2.2 and 4.3.2.3). The generally higher albedo of  $\Sigma_{\text{roof[light]}}$  surfaces means less shortwave radiation is absorbed which leads to lower surface temperatures. Hence median  $\Sigma_{\text{roof[light]}}$  (313.8 K) at 13:00 is 14.2 K lower than the coinciding  $\Sigma_{\text{roof[dark]}}$  temperature. Prior to an overcast period in the afternoon (15:30 – 15:55, Appendix L) the two roof types have distinct  $T_s$  distributions. The fewer  $\Sigma_{\text{roof[light]}}$  are mainly sunlit throughout the day, whereas  $\Sigma_{\text{roof[dark]}}$  have some within-canopy surfaces affected by prolonged ( $> 1$  h) shading. With the overcast conditions the distributions begin to converge as the contrasting albedos have reduced effect when only diffuse solar radiation is incident. After the overcast period, the overall shortwave radiative forcing is weaker because of the lower sun angles. These results have important implications for effective thermal anisotropy modelling. If (as often applied) homogeneous material properties are assigned to the urban surfaces, potential variations may not be captured by sensitivity analyses. The response of surface temperature to albedo may have a significant impact on the anisotropy of an urban area, which is rarely considered as part of  $T_s^{\text{EO}}$  uncertainties. This effect is expected to be particularly important for roof surfaces for two reasons: (a) their high SVF generally correlates with greater access to direct solar radiation and (b) near-nadir RS observations have a view bias of horizontal facets (Hu and Wendel, 2019).

Grass ( $\Sigma_{\text{Ground[grass]}}$ )  $T_s$  has a smaller diurnal range than impervious ground ( $\Sigma_{\text{Ground[imp.]}}$ ). From the grass, evaporative cooling and some shading from grass blades (i.e. leaf area index is greater than 1) are likely to occur while the impervious areas lack moisture (4 days since rainfall). Also, the generally higher heat capacities of  $\Sigma_{\text{Ground[imp.]}}$  causes more heat to be stored during the day and released slowly over night. Uncertainty in grass temperature may arise from a potential sample bias as only one camera (C1) captures grass surfaces compared to all cameras having some  $\Sigma_{\text{Ground[imp.]}}$  in their view (Appendix M). The relatively coarse (4 m) land cover dataset may introduce unquantified classification uncertainties.

Wall pixels by cardinal orientation follow the expected general trend from insolation (Appendix M).  $\Sigma_{\text{East}}$  ( $\Sigma_{\text{West}}$ ) pixels are warmest during morning (afternoon), with median  $T_s$  reaching 306.1 (310.6) K at 11:00 (17:00).  $\Sigma_{\text{West}}$  surfaces peak at higher temperatures  $\Sigma_{\text{East}}$ , as the latter are among the first to be heated in morning while  $\Sigma_{\text{West}}$  surfaces have already been heated throughout the day.  $\Sigma_{\text{South}}$  are warmest during representative Aqua and Terra overpasses.  $\Sigma_{\text{West}}$  remains warm past sunset, with differences in per-pixel medians of 1.2 K to  $\Sigma_{\text{North}}$  at 23:00. This is reasonable given that  $T_s$  of  $\Sigma_{\text{North}}$

pixels are consistently low with reduced variability as they are mainly shaded throughout the day. Only just prior to sunset,  $\Sigma_{\text{North}}$  surfaces receive a little direct solar irradiation, causing their temperatures to be slightly higher than those of  $\Sigma_{\text{East}}$  in the evening.

The south-east sampling bias (Section 4.3.1.1) causes the median  $T_s$  for  $\Sigma_{\text{South}}$  to peak (315.8 K) at 12:00, i.e. earlier than expected for a wall distribution centred around  $180^\circ$  azimuth. Before sunrise, median  $T_s$  differences for wall orientations are less than 0.8 K but are up to 4.9 K warmer than  $\Sigma_{\text{Roof[dark]}}$  at 01:00 during a clear-sky period. During daytime, walls are generally much cooler than roofs and the complex geometry and materials contribute to these variations. Roofs are mostly planar with small features (e.g. chimneys and air conditioning units) whereas walls have many balconies and other shade causing features that reduce their overall temperature. The emissivity of glass is unaccounted for and is expected to cause wall temperature overestimation.

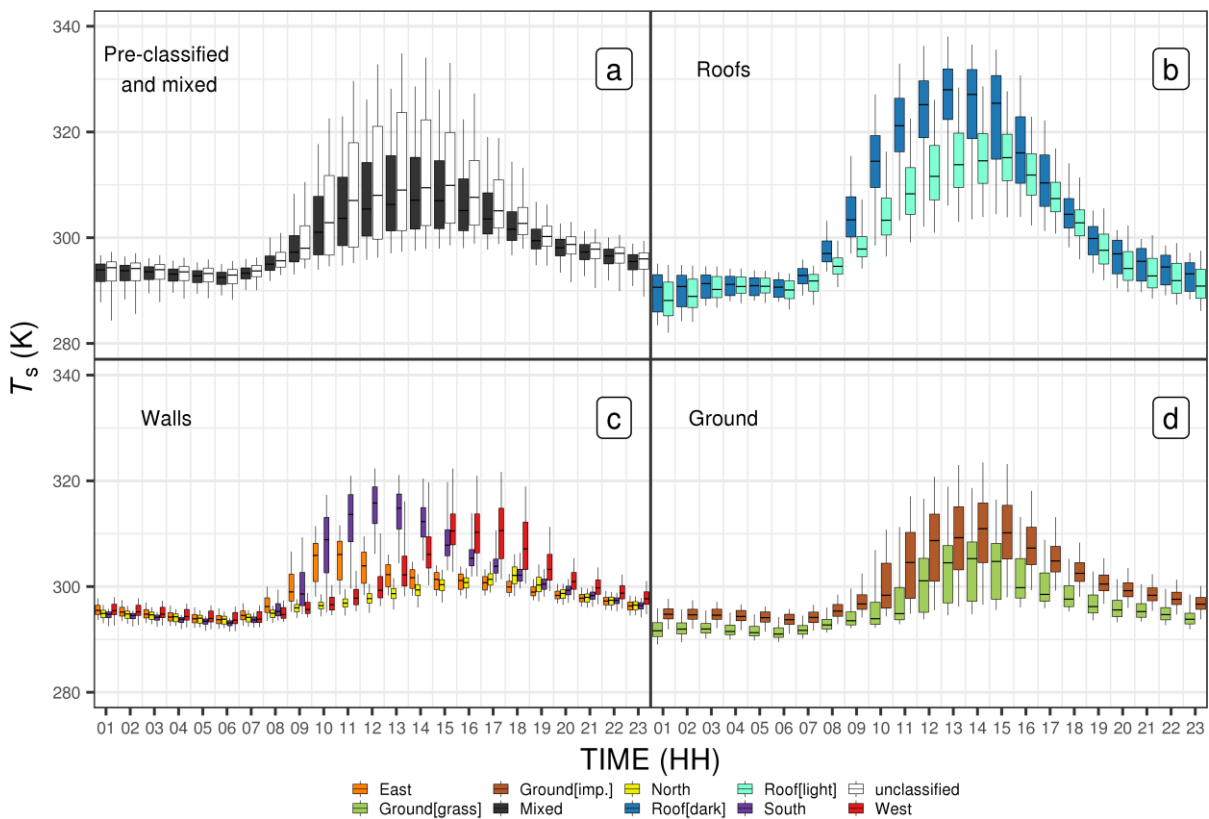


Figure 4-10. Variability of LWIR camera derived surface temperature ( $T_s$ ) for 27<sup>th</sup> August with observations classified as (a) all classes (white) (except VCE and “masked” and “mixed” (grey) pixels, (b) roofs, (c) walls, and (d) ground. Boxplot are from all camera images (5 min samples) by group (colour) during 1 h (e.g. first hour is 00:00  $\rightarrow$  00:55 for Time (HH)) “01” between vertical lines) with interquartile range (box), median (horizontal line) and 5 and 95 percentiles (whiskers) of pixel values.

#### 4.3.2.2 Variability from shortwave irradiance

The facet (orientation and material) observations are stratified by irradiance using  $\overline{\text{BRF}}$  as  $T_s$  are positively correlated with this variable (cf. Figure 4-5b, c).

Despite the importance of roofs for upwelling longwave radiation sampled from space ( $T_s^{EO}$ ), prior studies typically simplify their radiative, geometric and material characteristics. Here the complex geometry of this facet type is uniquely observed and modelled. To assess the importance of BRF as a driver for temperature variability of the low albedo roofs ( $\Sigma_{\text{Roof[dark]}}$ ), the difference between sunlit flat [ $T_s(\text{BRF} \approx 1)$ ] and all [ $T_s(\overline{\text{BRF}})$ ] roofs (Figure 4-11) is calculated through a day. Overall there is clear separation in  $T_s$  between  $\overline{\text{BRF}}$  bins. At 09:15, median  $T_s$  differences for sloped roofs facing the sun reach 13.2 K [ $T_s(\overline{\text{BRF}} = 1.5) - T_s(\text{BRF} \approx 1)$ , Figure 4-11]. Sloped roofs with  $\overline{\text{BRF}} < 1$  but still sunlit have median  $T_s$  up to 23.3 K cooler than the flat roofs at 11:55. Contributions to the observed  $T_s$  variability within each  $\overline{\text{BRF}}$  class at a given timestep are the variable time in sun (Figure 4-5d), differences in surface albedo and emissivity within the  $\Sigma_{\text{Roof[dark]}}$  surface property, and uncertainties in atmosphere and emissivity corrections Chapter 3.

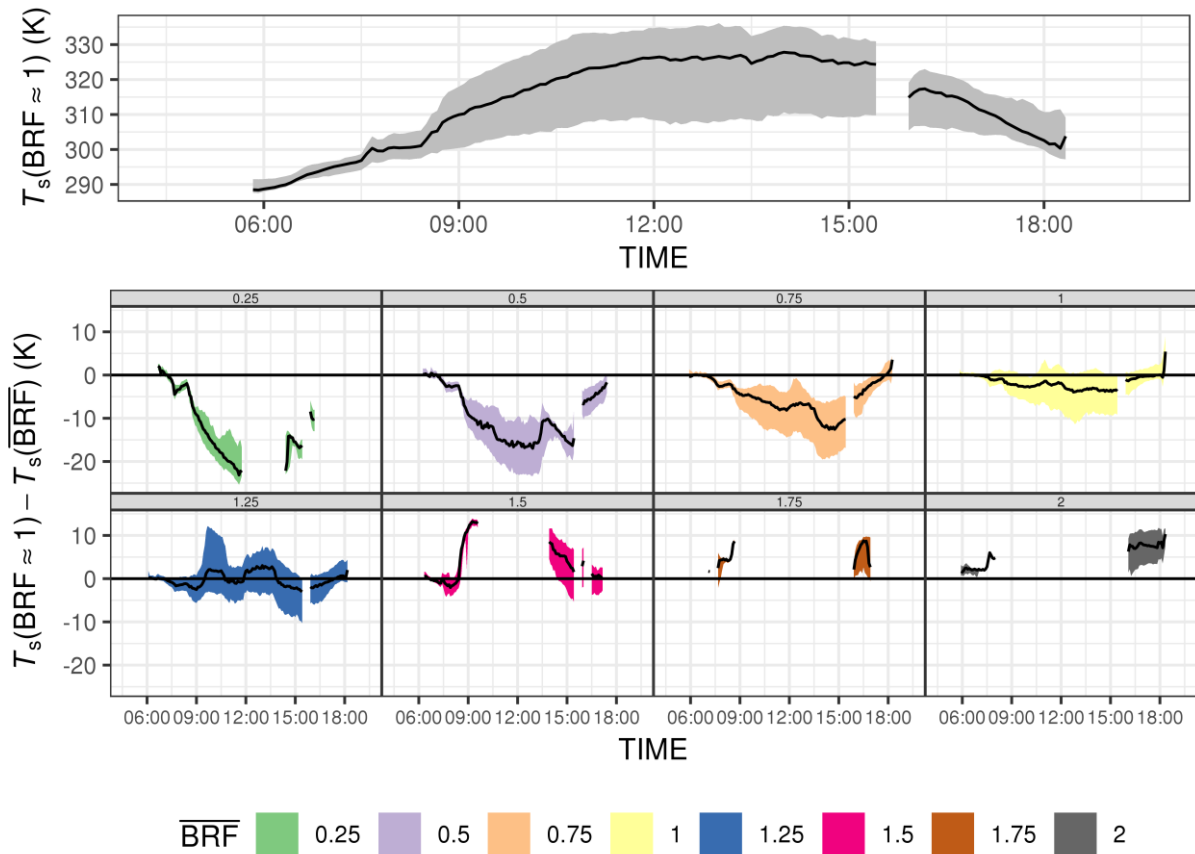


Figure 4-11. Observed daytime surface temperature ( $T_s$ ) for 27<sup>th</sup> August for (top) pixels viewing surfaces with bidirectional reflectance factor (BRF, Schaepman-Strub *et al.*, 2006) equivalent to solar irradiance for a flat surface ( $\text{BRF} \approx 1$ ) and (bottom) BRF for any given daytime sun angle and binned values of BRF ( $\overline{\text{BRF}}$ , bin width 0.25) across all observed sun-surface geometries (shown as difference to  $\text{BRF} \approx 1$  i.e. top). BRF calculated using DART assuming Lambertian surfaces.

The overcast period (15:30 – 15:55) has  $\overline{\text{BRF}} = -1$  for all surfaces. This may explain the smaller differences in  $T_s(\overline{\text{BRF}})$  during the afternoon and into the evening (Figure 4-11). There are fewer and

less consistent observations of sloped roofs compared to flat roofs, causing temporal gaps in  $T_s(\overline{\text{BRF}})$  (e.g.  $T_s(\overline{\text{BRF}} = 0.25)$ ) for around 12:00 → 14:00). Large gaps (> 4 h) for high BRF bins occur during high sun angles which correspond to peaks in  $E_{\lambda}^{\downarrow, \text{dir}}$  (Eqn. 4.3) and a preferential view of roofs to the sun at these high sun angles. This combines to give  $T_s(\overline{\text{BRF}} \leq 1.25)$  the highest physically possible values around midday ( $\pm \sim 2.5$  h). When repeated for ground and wall surfaces (Appendix M), analysis confirms that the sun-surface geometry of vertical facets is mostly captured by the orientation and material property, with ground surfaces also showing small variations.

### 4.3.2.3 Variability from shadow history

The instantaneous sun-surface geometry drives surface temperature variability (Section 4.3.2.2) but does not explain the transient effects of shadowing. The history of shading is potentially significant given the thermal inertia of urban materials (e.g. concrete). It has not previously been quantified using quantitative shadow distributions for a high-resolution set of observations and is often not considered as part of what is “seen” by simulated remote sensors in the study of effective thermal anisotropy or any other LST analysis.

On the study date, a cooling time window  $\tau(x, y, t, \Sigma)$  (Eqn. 4.4) was determined (Figure 4-12) for  $1.15 \times 10^6$  per-pixel cooling events. The starting times occur across the day and their  $P_{25} \rightarrow P_{75}$  statistics are distributed with 12:00 → 17:00. This distribution is reasonable as more cooling events are expected in the afternoon and more surfaces are becoming sunlit in the morning. To assess the goodness of fit of  $\tau(x, y, t, \Sigma)$  and the variability in cooling, observed (e.g. Figure 4-6b, black) and modelled per-pixel cooling events (e.g. Figure 4-6b, red) are compared (Figure 4-12). Generally, the fits are good for all three surface types with mean absolute error (MAE) of 0.7 K (ground, roof) or 0.6 K (walls) and are linear (red dashed line, Figure 4-12) across the range of temperature differences (approx. 0 → 30 K). A small number of points have negative differences meaning the shaded temperature is warmer than the sunlit. This gives the flat “tail” to the scatter, as negative modelled values are not permitted. Negative differences account for 1.3 % of all cooling events and reach -2.5 K at  $P_5$ .

To model surface temperature cooling, the coefficients are determined from medians by surface type (Figure 4-12, row 2). As  $\tau(x, y, t, \Sigma)$  is highly variable (e.g. 25<sup>th</sup> → 75<sup>th</sup> percentile of 91.08 → 196.27 min for ground surfaces), using a single set of coefficients results in a greater spread between observed and modelled results (Figure 4-12 cf. row 1 and 2). There is generally good agreement but with some large (> 10 K) departures when facets have distinctly different thermal properties. Uncertainty for roofs is increased as roof pixels’ shading during daytime can only be from nearby taller buildings (e.g. Figure 4-5b, foreground of C2 and C3) which is only for short periods. This reduces the number of pixels available for the background shaded temperature. Additionally, the

emissivity correction uncertainty is greatest for roof surfaces because of the large contrast between LWIR irradiance (from the relatively cool sky) and LWIR exitance (Chapter 3).

Uncertainties may arise for ground pixels from the highly contrasting material properties (impervious and grass), whereas for walls the more complex surface geometry may lead to uncertainties in shadow patterns and history. Walls also have a mix of glass and masonry/concrete with their contrasting thermal properties and cooling rates not accounted for.

As walls and ground have slower cooling rates than roofs, they take longer to reach the well shaded temperature. The  $P_{95}$  temperature differences between recently shaded and well shaded are 21.6 K (walls), 27.5 K (ground) and 16.5 K (roof) at 10 min after entering shade ( $t_{\text{shd}} = 10$  min). After 30 min the corresponding differences are 18.6 K, 17.3 K, 14.7 K greater (assuming the well shaded temperature remains constant).

In previous studies, shaded surfaces seen by a sensor have been assumed to all have the same temperature (e.g. Voogt, 2008) which presumably accounts for some uncertainties in their results. Variability in  $\tau$  is directly related to variability in heat transfer rate (radiative, convective and conductive), material heat capacities, density, volume and overall mass of the observed surface structures. These properties are central to surface energy balance partitioning and therefore the resulting urban heat island. Both the storage of heat during the day and its release at night are impacted. Cooling rates associated with storage heat flux can be modelled based on bulk material properties (Roberts *et al.*, 2006) and detailed knowledge on cooling rates is valuable for the evaluation and improvement of bulk parameterisations of storage heat flux. the generally shorter cooling time constant of roofs (median  $\tau(\Sigma) = 43.13$  min), may be explained by a list of characteristics, including roofs are often thinner (lower mass facilitating conductive heat loss), have higher sky view factor (facilitating radiative heat transfer), and are more exposed to higher wind speeds (facilitating convective heat transfer).

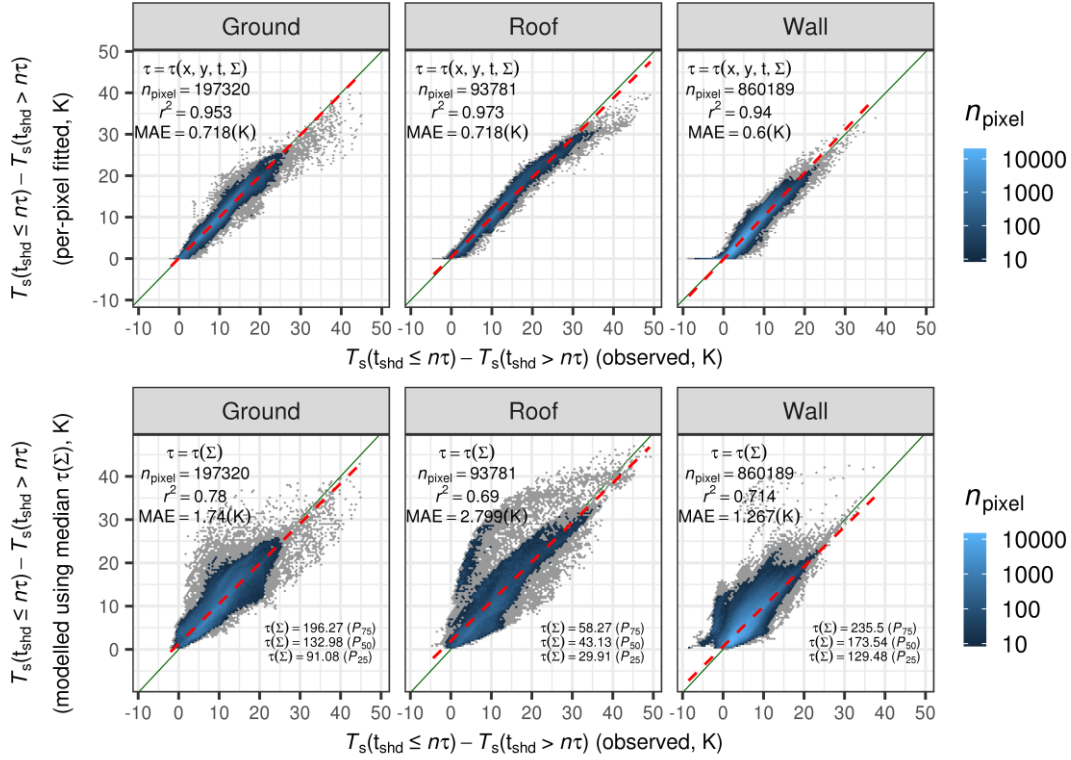


Figure 4-12. Surface temperature ( $T_s$ ) cooling rates observed (x axis) and estimated (using Eqn. 4.4) for each pixel with colours indicating number of pixels ( $n_{\text{pixel}}$ ) with (row 1) fitted time constant  $\tau$  per pixel [ $\tau(x, y, \Sigma)$ ] and (row 2) modelled time constant as median  $\tau(x, y, t, \Sigma)$  per surface type [ $\tau(\Sigma)$ ] for (column 1) ground (grass and impervious), (column 2) roof (light and dark) and (column 3) walls (N, E, S, W). Statistical metrics: coefficient of determination ( $r^2$ ), mean absolute error (MAE).

### 4.3.3 Crossing scales between satellite and ground-based observations

The surface-leaving radiance varies markedly across complex 3D geometry. However, the effective thermal anisotropy that causes this is not captured by current models that are mainly using simple surface parameters. Using high resolution fixed-platform observations, the view angle uncertainties can be assessed in a way similar to airborne studies (Lagouarde *et al.*, 2010) but at much higher temporal resolution to explore the diurnal evolution of the anisotropy phenomena.

$T_s$  differences between surface types are greatest during daytime (Section 4.3.2). Hence,  $T_s^{\text{EO}}(\phi, \theta, \Omega)$  sampled from space is particularly sensitive during this time to the surface types seen by the satellite instrument. Characterising effective thermal anisotropy is crucial for the correct interpretation and implementation of thermal EO products over cities.

#### 4.3.3.1 Spatially resolved thermal anisotropy

Thermal anisotropy is explored at  $< 1$  m resolution (Section 4.2.3.2) for a sub-sample of DART simulated view directions. The high spatial resolution and directional upwelling radiance simulated by DART [ $L_{\lambda}^{\text{surf}}(x, y, \phi, \theta, \Omega)$ , Section 4.2.4] based on high-LOD DSM geometry (Figure 4-2, Figure

4-4) and high-resolution surface temperature observations combines as a unique dataset to explore effective thermal anisotropy at an unprecedented level of detail. The high-resolution images (Figure 4-13) are shown using brightness temperatures ( $T_b$ ) as the bulk emissivity correction to give  $T_s^{EO}(\phi, \theta, \Omega)$  is only applicable across satellite pixel scales. Appendix K explains why the gaps at the edge of the images occur.

Depending on the view angle, different surfaces are seen in the images (Figure 4-13) which reveal unique brightness temperature distributions. Roof, ground and vegetation are viewed from the nadir direction. Off-nadir view angles also have wall surfaces visible, many with complex  $T_b$  distributions. With simple planar surface geometry,  $T_b$  across a wall would vary only from building shadows and shadow hysteresis. However, the sub-facet wall geometry creates contrasting temperatures around sunlit portions and cooler shaded areas (e.g. recesses, from balconies) or with oblique sun-surface angles. Similarly, for roofs, complex shadow patterns from roof geometry detail lowers their average  $T_b$ . Differences in  $T_b$  from shadowing are less distinct from the sunlit surfaces in the afternoon image (14:00) than the morning. Larger differences between sunlit and shaded temperatures in the afternoon drive this spatial variation.

VCE create spatial patterns in contrast to impervious surfaces due to their lower temperatures and generally homogeneous  $T_b$  ( $T_s$  prescribed based on air temperature). The average tree crown temperature is approximated by  $T_a$  but sub-tree variations in  $T_b$  result from variable exposure to the sun (shortwave irradiance) and other canopy elements (LWIR and shortwave diffuse irradiance).

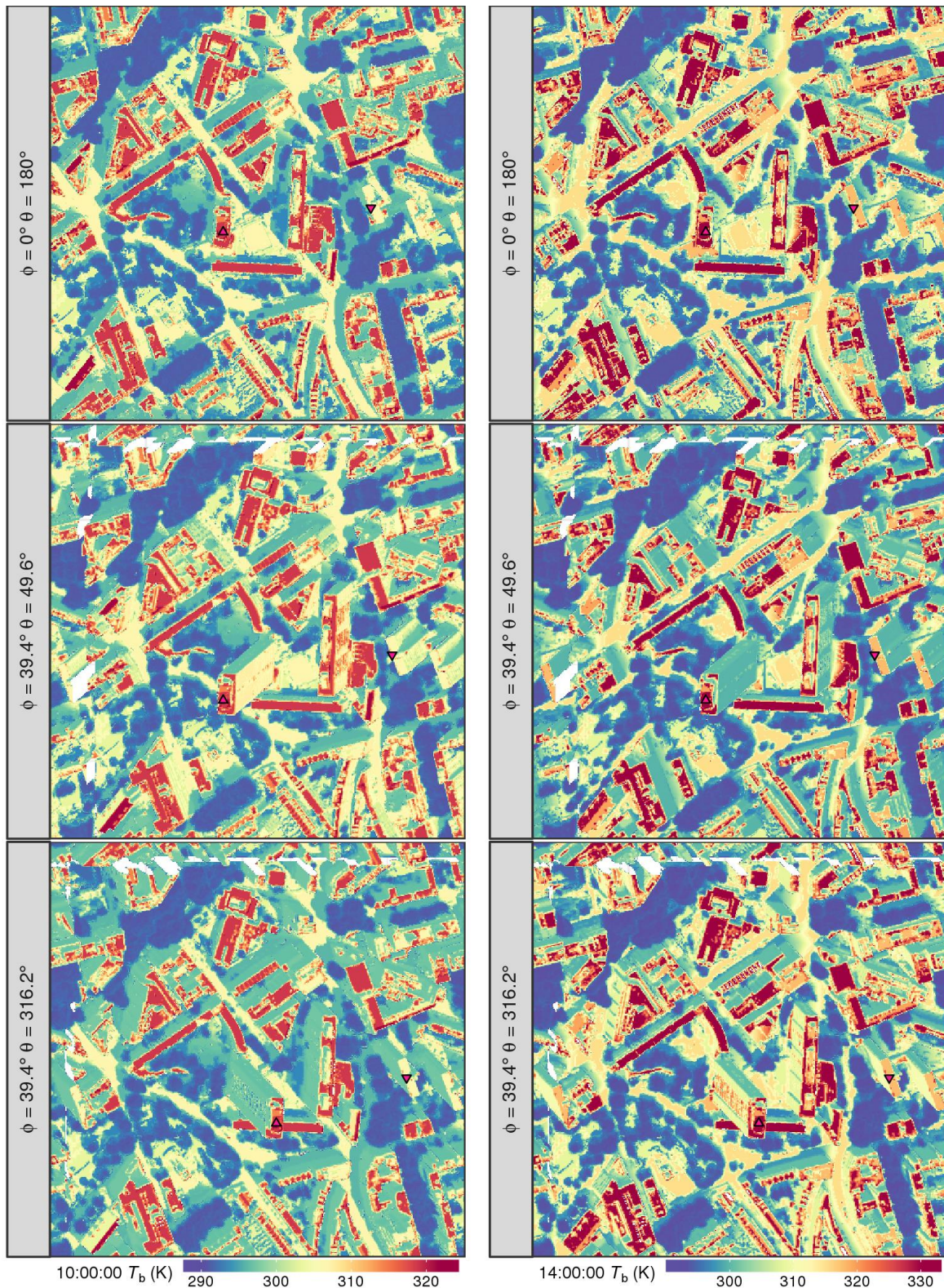


Figure 4-13. Surface-leaving radiance across the study area as brightness temperatures ( $T_b$ ) simulated using observationally derived and three-dimensional (3D) surface temperature and the DART model for 27<sup>th</sup> August at (left) 10:00 and (right) 14:00 for (top) nadir and (middle – bottom) off-nadir zenith ( $\phi$ ) angles and (triangles) IMU and CUB sites (Figure 4-1b). Images projected onto the bottom of atmosphere horizontal plane (Figure 4-2) with (grey labels) surface  $\rightarrow$  sky directions, with  $\theta = 0^\circ$  grid north and e.g.  $\theta = 90^\circ$  grid east (WGS84 UTM grid zone 31N) and  $\phi = 0^\circ$  ( $\phi = 90^\circ$ ) perpendicular (horizontal) to the surface. Rotating images view angle by ( $\theta, \phi$ ) gives orthographic projections.

### 4.3.3.2 Time series of thermal anisotropy

While airborne studies can provide an instantaneous view of the complex surface geometry, the present study allows for anisotropy to be characterised at 30 min resolution across an extended time period (e.g. an entire study day, Figure 4-14). Before sunrise, the more homogeneous  $T_s$  between surface classes gives near-isotropic  $T_s^{\text{EO}}(\phi, \theta, \Omega)$ , with greatest absolute difference in temperature between any two  $T_s^{\text{EO}}(\phi, \theta, \Omega)$  directions with up to  $50^\circ$  zenith angle (maximum anisotropy,  $\Lambda$ ) of less than 0.5 K.

Half-hourly simulations after sunrise show greater  $T_s^{\text{EO}}(\phi, \theta, \Omega)$  for off-nadir view angles with markedly higher temperatures in small angular regions (hot spots) that are up to 2.9 K warmer than the nadir view (302.5 K) at 10:00 ( $\Lambda = 4.95$  K). The maximum anisotropy is at 10:30 ( $\Lambda = 5.1$  K) and is 3.52 K across  $\pm 30^\circ$  off-nadir angles. Across  $\pm 10^\circ$  off-nadir, maximum anisotropy is typically within 1 K (e.g. 1.06 K at 10:30). A small bias in the nadir temperature and the model domain edges negligibly impact modelled results (Appendix K). The hot spot present near the sun direction is consistent with prior mid-latitude observations and with simplified geometry (Hu and Wendel, 2019; Chapter 2). Previously, the directional temperature near the sun hot spot has been found to decrease rapidly with small azimuth angle increments. Here, the hot spot effect occurs across a greater angular region around the sun direction (i.e. not as concentrated around small angular regions). Simplified geometry with regularly repeating features mean a small change in azimuth angle can have a large effect on the streets and walls seen (Hu and Wendel, 2019) and may contribute towards the formation of multiple hotspots (e.g. Krayenhoff and Voogt, 2016). These are not found in the real world, non-uniform wall orientations and sub-facet heterogeneities (e.g. balconies) studied here, which are resolved in the satellite image simulations (Figure 4-13) used to calculate the anisotropy.

To assess implications of these anisotropy results (Figure 4-14) on differences in surface temperatures, two surface temperature estimates are compared:  $T_s^{\text{EO}}$  sampled by a satellite sensor at a given viewing geometry and the complete surface temperature  $T_c$  which accounts for the full 3D temperature distribution across the urban canopy. This helps to put temporally sporadic satellite data into context of near-continuous observations. MODIS observations (Table 4-6) are compared to both the continuous surface data assuming the same viewing direction ( $T_s^{\text{EO}}$ , 30 min resolution) and using  $T_c$  (5 min resolution) (Figure 4-15) as  $T_c$  is uniquely non-directional (Voogt, 2000). The high angular and temporal resolution of  $T_s^{\text{EO}}$  means MODIS sampling characteristics can be closely matched with respect to view angle (within  $\sim \pm 5^\circ$  for azimuth and zenith) and sampling time ( $< 30$  min).

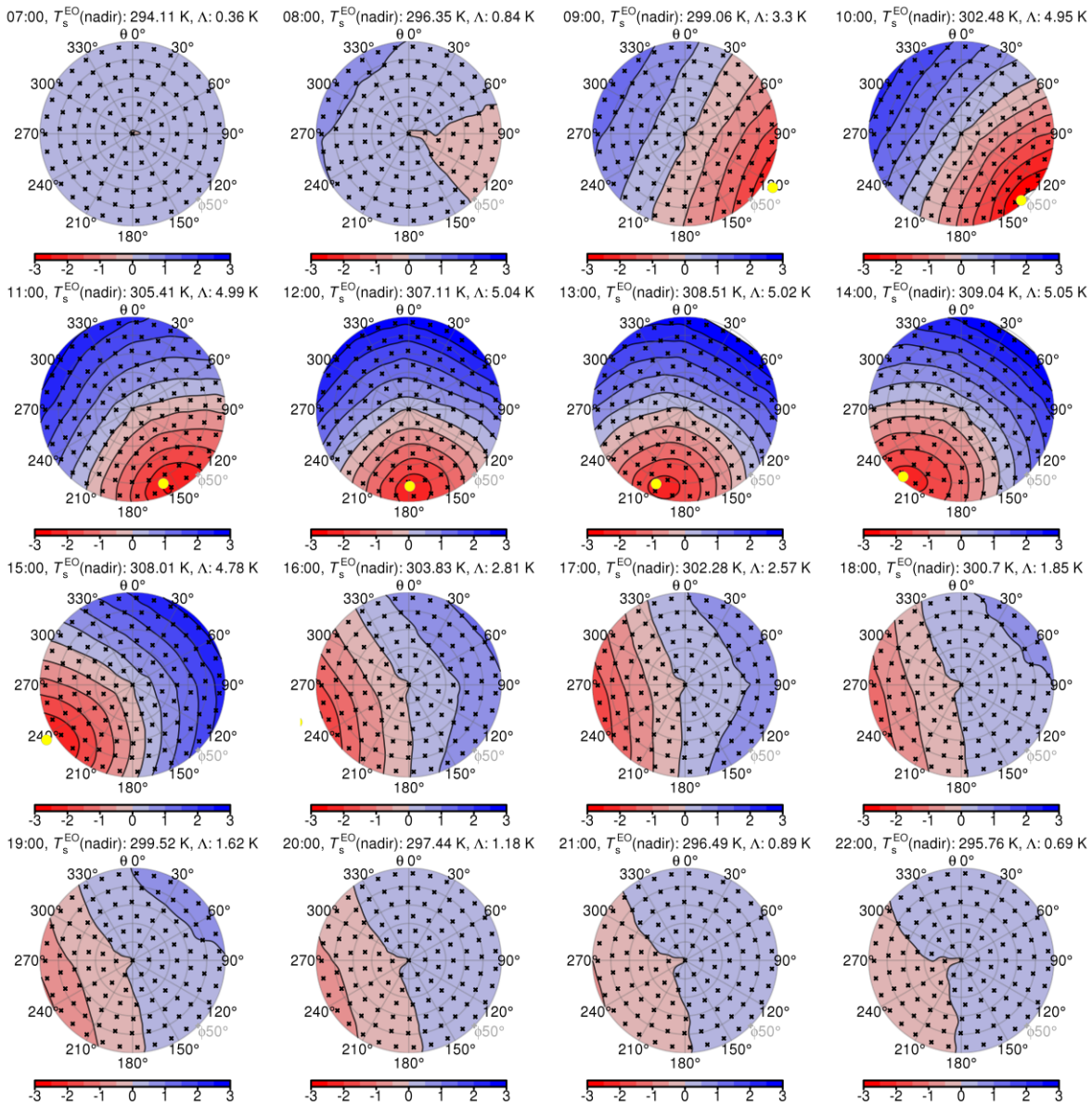


Figure 4-14. Polar plots with difference in surface temperature  $[T_s(\theta, \phi, \Omega)]$  from nadir temperature  $[(T_s(\theta, \phi = 0, \Omega) - T_s(\theta, \phi, \Omega))]$  for upward directions with zenith angle  $(\phi) \leq 50^\circ$  simulated using observationally derived, three-dimensional (3D)  $T_s$  across the study area (Figure 4-1). DART is used to simulate surface-leaving radiance for (black crosses) discrete directions. Directions and (yellow dot) the sun position are oriented with a surface  $\rightarrow$  sky perspective, with  $\theta = 0^\circ$  grid north,  $\theta = 90^\circ$  grid east, etc (WGS84 UTM grid zone 31N) and  $\phi = 0^\circ$  ( $\phi = 90^\circ$ ) perpendicular (horizontal) to the surface. Grey lines have (radial)  $\Delta\phi = 10^\circ$  (straight)  $\Delta\theta = 30^\circ$ . The maximum absolute difference  $\Lambda$  and nadir temperatures are given at each timestep.

The diurnal  $T_c$  pattern (Figure 4-15) highlights a gap-filling constraint for the recently shaded observations and sampled surface types through time. Prior to 18:00, C1 and C4 view the most sunlit ground pixels (Appendix K). After 18:00 the ground sampled by these pixels becomes shaded and the sunlit ground is seen by relatively few pixels from C2 and C3 that are cooler than the well shaded

ground. This prevents calculation of a cooling rate until these surfaces are heated to above the well shaded ground temperature, which occurs at 18:25 and is seen as a step change in  $T_c$  at 18:25 (Figure 4-15).

Table 4-6. MODIS collection M\*D11A1 land surface temperature and emissivity for the grid cell intersecting the study area. Products obtained using MODIS<sub>tp</sub> package (Busetto and Ranghetti, 2016).

<b>Time (UTC)</b> <b>27<sup>th</sup> August</b> <b>2017</b>	<b>Platform</b>	<b>LST error</b> <b>(± K)</b>	<b>Emissivity</b> <b>value</b> <b>(Band 31)</b>	<b>Emissivity</b> <b>error</b>	<b>View</b> <b>zenith</b> <b>angle (°)</b>	<b>View azimuth</b> <b>angle (°)</b>
10:30	Terra	≤ 3	0.982	± 0.02	48	98.2 (east)
12:18	Aqua	≤ 1	0.982	± 0.01	44	98.2 (east)
21:42	Terra	≤ 3	0.982	± 0.04	7	81.8 (east)

The IQR estimate of  $T_c$  (Figure 4-15) provides an uncertainty estimate for the upscaling of observations. There is generally more uncertainty during the day (maximum 4.9 K at 13:00) than at night (minimum 1.6 K at 07:20). The IQR distribution indicates the unresolved  $T_s$  variability from using the selected surface properties (Section 4.3.2). It is much smaller than if unclassified observations were used, as this IQR is over 20 K (Section 4.3.2.1). By incorporating more surface properties (e.g. materials, insolation history) intra-class per-pixel distributions could be reduced and translate to more certain  $T_c$  with smaller IQR.

In agreement with Adderley *et al.* (2015),  $T_s^{EO}$  has greater diurnal range than  $T_c$ . During the night,  $T_c$  is higher than  $T_s^{EO}$  as walls are more represented by  $T_c$  and generally have higher  $T_s$  than horizontal surfaces (Figure 4-10). When  $T_s$  for roof and ground are higher during the day,  $T_s^{EO}(\text{nadir}) - T_c$  reaches its maximum (1.9 K at 12:30).  $T_s^{EO}(\text{nadir})$  is within 0.5 K of  $T_c$  during morning (up to 10:00) and after 16:00. Around 09:00 – 10:00  $T_s^{EO}(\text{nadir}) \approx T_c$ . Anisotropy is more evident after sunset than after sunrise as afternoon sunlit surfaces cool overnight but by sunrise are near homogeneous.

The satellite-derived surface temperatures from MODIS (Table 4-6) and the nearest concurrent view angle from  $T_s^{EO}$  have varying agreement. Clearly, the nocturnal MODIS observation underestimates (-3.4 K) the corresponding  $T_s^{EO}$ . However, the MODIS error flag for this observation is ≤ 3 K (Table 4-6), i.e. significantly worse than for an optimal retrieval (≤ 1 K). During daytime,  $T_s^{EO}$  underestimates MODIS by 1.4 K (1.8 K) for the 10:30 (12:18) MODIS observation [error flags: ≤ 3 K (≤ 1 K), Table 4-6]. This comparison demonstrates how ground-based observations and modelling can complement satellite observations to support data assimilation for NWP or urban climate modelling applications (e.g. surface energy balance fluxes) and aid evaluation of EO land surface temperature products.

The choice of surface temperature definition remains an open question (Adderley, Christen and Voogt, 2015), with no consensus on if  $T_c$  is more appropriate than  $T_s^{EO}$  in the context of surface-atmosphere exchanges and urban – rural temperature differences, described as the surface urban heat island (SUHI). As  $T_c$  is more representative than  $T_s^{EO}$  of all the surfaces, prior studies using  $T_s^{EO}$  for

SUHI without consideration or correction to  $T_c$  may have overestimate or underestimate the SUHI during the day and night, respectively. This is further confounded by how the SUHI is determined, whereby the SUHI intensity ( $\Delta$ SUHI) is usually calculated as the temperature difference between urban pixels and suburban or rural reference pixels (Peng *et al.*, 2012; Clinton and Gong, 2013), the latter likely having more homogeneous terrain and reduced view angle effects. Thus, a distinction between land use over land form is needed in such  $\Delta$ SUHI studies. At night the  $\Delta$ SUHI may be underestimated, explained by the  $\sim 1$  K underestimation of  $T_c$  by  $T_s^{\text{EO}}$ . This is significant given  $\Delta$ SUHI magnitudes have been reported with similar ranges; between 0.5 – 1.2 K in London from MODIS observations (Zhou *et al.*, 2016),  $\sim 1 - 2$  K in Beijing (Meng *et al.*, 2018) and also  $< 2$  K ( $\pm \sim 1.5$  K standard deviation) globally from  $\sim 193,000$  “cities” (Clinton and Gong, 2013). During daytime the opposite may be true following the overestimation of  $T_c$  by  $T_s^{\text{EO}}$  found here. This is supported by Hu *et al.* (2016) who find anisotropic effects account for 25 – 50 % of the satellite derived  $\Delta$ SUHI in New York City and Chicago.

For surface-atmosphere exchanges and the broader study of surface energy balance components from space (e.g. Chrysoulakis *et al.*, 2018), a difference of 1 K is significant. Such uncertainties could represent the difference between stably and unstably stratified nocturnal boundary layers with impact on nocturnal boundary layer depth and pollution dispersion (Kotthaus and Grimmond, 2018; Lee *et al.*, 2019).

Daytime application of  $T_s^{\text{EO}}$  to estimate  $\Delta$ SUHI is far more complex due to the pronounced variations in surface temperatures and thermal anisotropy. Hence, anisotropy has not been considered beyond the removal of extreme view angles from observations (Hu *et al.*, 2014). Similar to the sunlit treetops in forest stands (Sun and Mahrt, 1995), it may be that roof surfaces have a bias contribution to the exchange of heat from the surface to the atmosphere (Loridan *et al.*, 2010). Harman and Belcher (2006) and Porson *et al.* (2010) find that roof properties are crucial to the surface-atmosphere coupling in urban surface energy balance modelling. The rooftop bias has potential synergy with the satellite view bias of roofs meaning  $T_s^{\text{EO}}$  may be an appropriate measurement if the view angle variation was accounted for by e.g. adjusting temperatures from off-nadir to nadir (Hu *et al.*, 2016).

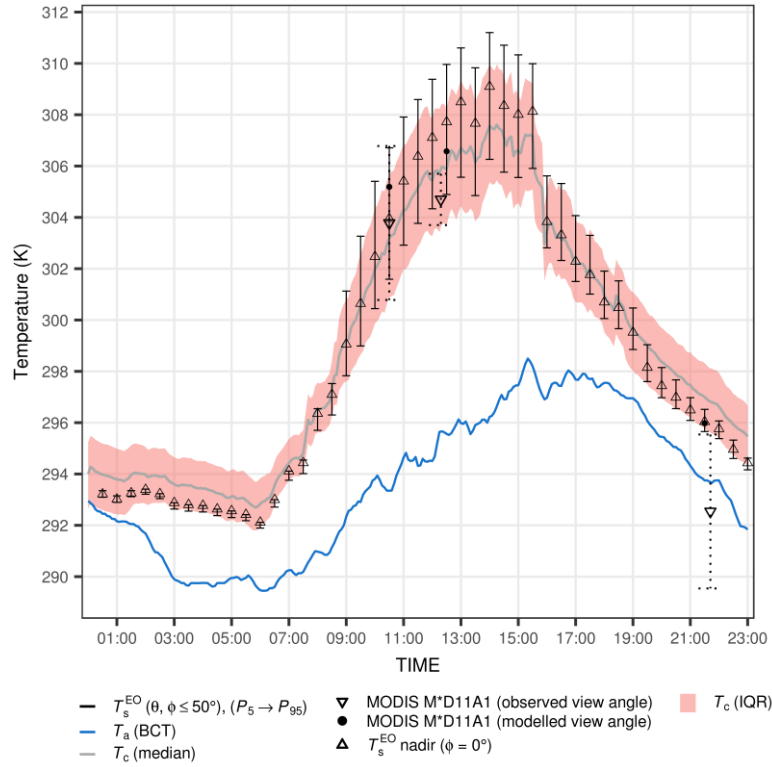


Figure 4-15. Temperatures for 27<sup>th</sup> August 2017 with: (grey line) complete surface temperature ( $T_c$ ) from median ( $P_{25}$  and  $P_{75}$ , shading) of intra-class observations and extrapolated as a three-dimensional (3D)  $T_s$  and then areally weighted across the complete surface of the study area, ( $T_s^{EO}(\theta, \phi, \Omega)$ , black) directional surface temperature simulated using 3D  $T_s$  (median of intra-class observations) and the DART simulation (triangles, centre point in Figure 4-14 polar plots) for  $T_s^{EO}$  at (upward triangles) nadir view and (vertical lines) minimum and maximum range for  $0^\circ \rightarrow 50^\circ$  off-nadir view directions, (black dots) MODIS collection 6 LST with (dashed lines) error from quality assurance data flags and (blue line) air temperature ( $T_a$ ) from nearby weather station.

The relative contribution of walls, roofs and other individual surface types to modelled  $T_s^{EO}(\theta, \phi)$  is explored. An inter-class fractional contribution ( $f_\Sigma$ ) to the radiance value used to calculate  $T_s^{EO}(\theta, \phi)$  is determined using DART outputs. The separation of radiance by surface type resolved by DART constitutes the surface-leaving (cf. surface-emitted) radiance. The sum of  $f_\Sigma$  for the  $n$  surface types of orientation and material is unity and across each timestep, view direction and surface type  $\Sigma$ ,  $f_\Sigma(\phi, \theta)$  is:

$$f_\Sigma(\phi, \theta) = \frac{\sum_{(x_\Sigma, y_\Sigma)}^{n_{px}} L_{\lambda, \Sigma}(x_\Sigma, y_\Sigma, \phi, \theta, \Omega)}{\sum_{(x, y)}^{n_{px}} L_\lambda(x, y, \phi, \theta, \Omega)} \quad \text{Eqn. 4.7}$$

with  $L_\lambda(x, y, \phi, \theta, \Omega)$  the per-pixel radiance for a DART orthographic image (e.g. Figure 4-13 without the Planck conversion to  $T_b$ ) and  $n_{px}$  the total number of image pixels.  $L_{\lambda, \Sigma}(x, y, \phi, \theta, \Omega)$  in Eqn. 4.7 is the same except only considers the radiance leaving surface type  $\Sigma$ , from pixels that view surface

type  $\Sigma$  ( $x_\Sigma$ ,  $y_\Sigma$ ). Unlike prior work, where  $f_\Sigma$  is a geometric view fraction (e.g. Hu and Wendel, 2019) often with idealised urban geometry (e.g. Wang, Chen and Zhan, 2018),  $f_\Sigma$  from Eqn. 4.7 is more realistic as it varies according to the temperature, emissivity, SVF and incoming longwave radiation of surfaces within the IFOV of each DART image pixel and also uses the realistic DSM.  $f_\Sigma$  across different view zenith angles (Figure 4-16, azimuth angles are aggregated) shows  $f_\Sigma$  differs most at near-nadir view angles between surface types ( $f_{\Sigma=\text{Wall}}$  is north, east, south, west walls combined). For near-nadir view angles, the ground has the largest contribution to the observed radiance ( $f_{\Sigma=\text{Ground}} > 0.4$ ) for  $\phi < 20^\circ$ . For view angles with larger  $\phi$ , more walls are visible which also occlude the ground, meaning  $f_{\Sigma=\text{Wall}}$  ( $f_{\Sigma=\text{Ground}}$ ) generally increases (decreases) with view zenith angle. The greatest variation in  $f_\Sigma$ , between timesteps on the study day occurs between sunrise ( $\sim 06:00$ ) and shortly prior to the overcast period (14:00), is attributed to the large diurnal variation in roof temperatures (Figure 4-10) i.e. roofs are much cooler at night relative to other surfaces and thus the contribution of radiance leaving these surfaces is less than during the day when the roofs are notably warmer. Azimuthal variations increase with  $\phi$ , with 5th – 95th percentile  $f_{\Sigma=\text{Wall}}$  differences increasing from around  $\pm 0.1$  at  $\phi = 9^\circ$  (i.e. near-nadir and very small fraction of visible walls) to  $\pm 0.023$  for oblique view angles ( $\phi = 57^\circ$ ). Changes in (e.g.)  $f_{\Sigma=\text{Roof}}$  with azimuth angle (Figure 4-16, shading) may result from micro-scale roof geometry and occlusion of roofs by larger buildings for given view angles. Modelled  $T_s^{\text{EO}}$  (Figure 4-15) therefore has highly varied contributions from the different surfaces types, with a near-equal contribution of surfaces (not including wall direction) at oblique view angles.

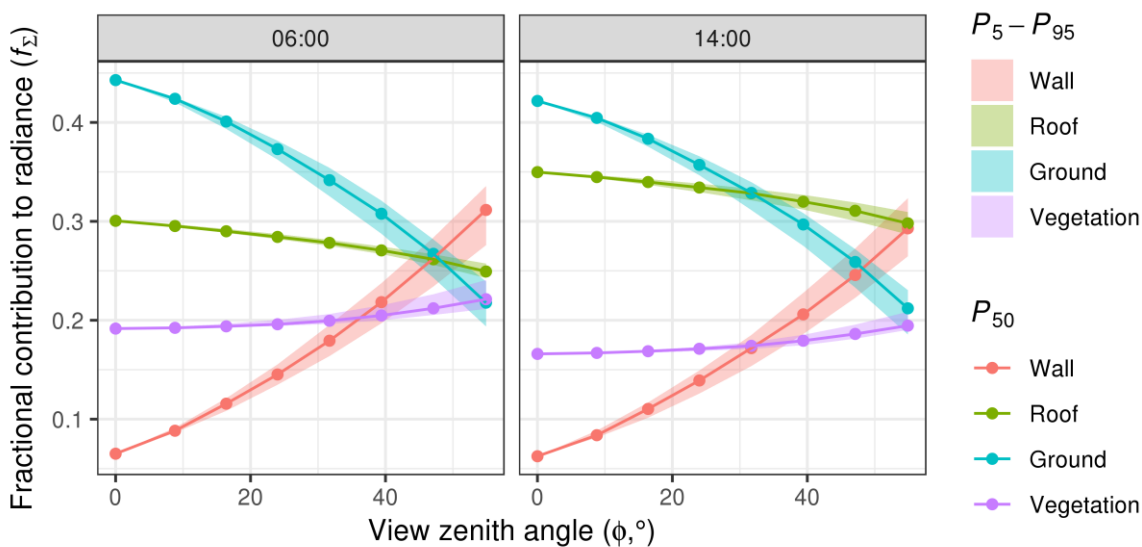


Figure 4-16. Temporal and angular variation (on 27<sup>th</sup> August 2017 06:00 to 14:00) in the fractional contribution of different surface types (colours) to upwelling radiance, with median (dots) 5<sup>th</sup> – 95<sup>th</sup> percentile (shading) of all azimuth angle variations for the given zenith angle ( $\phi$ ).

## 4.4 Conclusions

Ground-based thermography observations are combined with detailed modelling of urban geometry, materials, sensor views and radiative transfer processes to explore view angle uncertainties in satellite land surface temperatures. The study is conducted in central London using data for a mainly clear-sky summer day. The methods presented allow for various drivers of surface temperature variations in a complex, urban area to be quantified. Thermal data are quantitatively interpreted and upscaled from sub-facet ( $\sim 1$  m) to a high level of detail (LOD) 3D distribution of  $T_s$  across a large (430 m x 430 m) area using a novel technique. This distribution is used to explore view angle effects of  $T_s$  derived from earth observation satellites, overcoming constraints of prior studies, including (a) simple geometry descriptions, (b) modelled surface temperatures, and (c) limited temporal representation of observations (from airborne platforms).

In the upscaling process, surfaces are classified from camera observations using detailed source area analysis that allows for assessment of the measurement characterisation of a larger study area and satellite pixels. With a very high LOD surface description and integrated sensor view modelling, the footprint analysis is unprecedented for such a complex urban setting. The objective image classification separates drivers of surface temperature variability without requiring *a-priori* decisions on the number of clusters or manual image classification. Observed temperature are highly variable, with 5<sup>th</sup> – 95<sup>th</sup> percentile differences in per-pixel  $T_s$  observations up to 37.5 K during the daytime. Diurnal patterns of  $T_s$  for surfaces with different orientation show general agreement with prior studies at similar latitude. The high detail of image classification allows for quantification of  $T_s$  variability in direct relation to the sun-surface geometry features. This determines the amount of short- and long-wave radiation incident onto a surface, driving shadow patterns, direct solar irradiance and radiation trapping between buildings. Material properties are especially important for roof surfaces with increased access to solar radiation and high exposure to the cold sky.

Variability of  $T_s$  is significantly driven by a surface's orientation to the sun. While differences in surface temperatures between facets such as walls, roofs and ground have been quantified before, here they are shown relative to more complex sub-facet geometry. Differences in surface temperature between flat and sloped roofs reach 23.3 K due to sun-surface geometry effects while roofs with high albedo are up to 14.2 K colder than roofs with low albedo. Inter-facet variability is of similar magnitudes with median differences between wall orientations reaching 18.1 K, while walls, roof and ground facets reach contrasting temperatures by up to 29.3 K.

The second important driver of surface temperature variability is shading. For the first time, the effect of shadows is explicitly quantified. The energetic history of recently shaded surfaces greatly affects their  $T_s$ , e.g. recently shaded roof surfaces are up to 27.5 K warmer than those in shade for long periods. Cooling characteristics are derived from observations. Cooling characteristics were found

exponential with time constants ( $\tau$ ) estimated relative to long-term shaded surface temperatures describing the duration a certain surface requires to stabilise its thermal state. Clear contrasts were found between facet types with roofs on average cooling much faster  $\tau(\Sigma_{\text{Roof}}) = 43.13$  min than ground  $\tau(\Sigma_{\text{Ground}}) = 132.98$  min and walls  $\tau(\Sigma_{\text{Walls}}) = 173.54$  min. Surfaces shaded at sunset will have cooled to within 5 % of the ambient temperature by  $\sim 3\tau$  i.e. over 6 h and 8.5 h into the night for ground and walls, respectively. The developed shadow history methodology could be extended to study recently sunlit temperatures in the future. Quantifying heating and cooling characteristics of the urban surface is critical to advance the understanding of the storage heat flux, which is notoriously difficult to measure (Meyn and Oke, 2009) particularly over a large urban area (Kato and Yamaguchi, 2007; Chrysoulakis *et al.*, 2018). Models to quantify the storage heat flux in urban areas (e.g. ESTM, Offerle *et al.* 2005) require observational inputs and evaluation (Roberts *et al.*, 2006).

Material properties determine the amount of incoming energy absorbed. Using simple albedo characteristics (i.e. two classes “light” (high albedo) and “dark” (low albedo); excluding any metal or glass) clearly explains differences in observed temperature distributions. Dark roofs are up to 14.2 K warmer during the day as more solar radiation is absorbed. The material classification of roofs could be expanded if high spatial resolution datasets of surface optical material properties are available.

Effective urban thermal anisotropy, modelled with high-resolution surface geometry and  $T_s$  distribution, includes the effect of sloped roofs for the first time. The daytime maximum thermal anisotropy (up to 5.1 K) is generally lower than prior observational studies (e.g. Lagouarde *et al.*, 2010) particularly for near-nadir measurements (anisotropy for  $\pm 10^\circ$  off-nadir is nearly always within 1 K). Care should be taken with such inter-study comparisons, as Lagouarde *et al.* (2010) found maximum anisotropy across  $60^\circ$  zenith angles, whereas here it is at  $50^\circ$ . More generally, seasonality, urban geometry and materials are all variable between cities and studies. Notably, North American grid-like cities differ from more heterogeneous European cities.

The few prior ground-based studies used simplified or suburban models to describe the study areas for source area analysis whereas here a realistic, high resolution representation of a diverse central urban area (e.g. little repeating building patterns) is implemented. Critically, it shows less abrupt directional variation, particularly around the sun angle. Overall the combination of a relatively large fraction of vegetation, complex geometry and associated surface temperature distributions and 3D radiative transfer modelling give a unique temporally continuous case-study compared to other studies.

The high LOD observations and modelling combined here could provide a benchmark for computationally cheaper (e.g. Krayenhoff and Voogt, 2016) and analytical (Wang *et al.*, 2018) approaches which cannot explicitly resolve sub-building scale geometry or related  $T_s$  variability and radiative transfer processes. Future work could include a sensitivity analysis to quantify the relative

contribution of surface characteristics to thermal anisotropy, including e.g. sub-facet geometry,  $T_s$  classes, flat vs sloped roofs, vegetation, or street “clutter” (e.g. cars). This has challenges given the myriad of configurations of the urban form and material distributions. Specific to the 3D vector digital surface model (DSM) and its sensitivity towards effective thermal anisotropy, any changes in the DSM geometry description would require careful consideration as it is more challenging to alter a complex 3D model than a more simple urban morphology description, e.g. in form of raster datasets or bulk parameterisations (Biljecki *et al.*, 2015).

The classified  $T_s$  observations and 3D distribution has potential for application in other areas of urban climate study, including as inputs for large eddy simulation modelling and evaluation of the prognostic surface temperature from urban climate models. Further, they could aid in challenges with *in-situ* satellite verification over more homogeneous non-urban areas, where sensor positioning, source area uncertainties and micro-scale temperature variations are still problematic during daytime (Wang, Liang and Meyers, 2008; Duan *et al.*, 2019).

## List of symbols and acronyms [units]

3D	Three dimensional
agl	Above ground level (m)
$A_{v_x}$	Surface area of a surface element [ $m^2$ ]
$B_\lambda$	Planck black-body spectral radiance [ $W m^{-2} sr^{-1} \mu m^{-1}$ ]
BB	Black-body
BOA	Bottom of atmosphere
BRF ( $\overline{BRF}$ )	Surface property of bidirectional reflectance factor (binned)
C#	Nonspecific camera (C) and unique reference number (#)
CBD	Central business district
DART	Discrete Anisotropic Radiative Transfer model
DSM	Digital surface model (vector based)
DSM	Digital surface model
$E$	Broadband incoming radiation flux (irradiance) [ $W m^{-2}$ ]
$E_\lambda$	Incoming spectral radiation flux (spectral irradiance) [ $W m^{-2} \mu m^{-1}$ ]
$E^{LW,\downarrow}$	Broadband incoming longwave radiation flux (irradiance) [ $W m^{-2}$ ]
$E^{SW,\downarrow}$	Broadband incoming direct and diffuse shortwave radiation flux (irradiance) [ $W m^{-2}$ ]
$E_{\lambda,\downarrow,dir}$	Incoming direct spectral radiation flux (spectral irradiance) [ $W m^{-2} \mu m^{-1}$ ]
EO	Earth observation
$\varepsilon$	Emissivity
$\varepsilon_\lambda$	Spectral emissivity
FOV	Field of view [ $^\circ$ ]
fSR	Fraction of scattered radiation (to BOA irradiance)
$i$	Surface class containing ( $\Sigma$ , $\overline{BRF}$ , $t_{shd}$ ) surface properties
$\lambda$	Wavelength [ $\mu m$ ]
$L_\lambda^{cam}$	At-sensor spectral radiance [ $W m^{-2} sr^{-1} \mu m^{-1}$ ]
$L_\lambda^{sky}$	Spectral radiance from the sky [ $W m^{-2} sr^{-1} \mu m^{-1}$ ]
$L_\lambda^{surf}$	Surface-leaving spectral radiance [ $W m^{-2} sr^{-1} \mu m^{-1}$ ]
LOD	Level of detail
LWIR	Longwave infrared
$M_\lambda$	Spectral exitance [ $W m^{-2} \mu m^{-1}$ ]
MW	Model world
NLS	Nonlinear least square
$\Omega$	Solid angle [sr]
$\phi$	Zenith angle [ $^\circ$ ]
$P_n$	$n^{th}$ percentile
RT	Radiative transfer
RW	Real world
S	Triangle(s) of digital surface model mesh [ $m^2$ ]
$S^{V_x}$	Triangle(s) intersecting a voxel (a surface element) [ $m^2$ ]
$\Sigma$	Surface property of orientation and material
$\sigma$	Stefan-Boltzmann constant [ $5.67 \times 10^{-8} W m^{-2} K^{-4}$ ]
SR	Scattered radiation
SVF	Sky view factor
SW	Shortwave
t	Nonspecific timestep
$\tau$	Time constant [min]
$T_b^{EO}$	Surface brightness temperature from satellite earth observation platform [K]
$\theta$	Azimuth angle [ $^\circ$ ]
$T_s$	Surface temperature [K]
$T_s^{EO}$	Surface temperature from satellite earth observation platform [K]
$t_{shd}$	Surface property of time in shade [min]
UHI	Urban heat island
VCE	Vegetation canopy element
$VCE^{V_x}$	Vegetation canopy element within a voxel space
$V_x$	Nonspecific voxel
x, y	Nonspecific coordinate in 2D camera image
X, Y, Z	Nonspecific coordinate of 3D space

## **Acknowledgements**

This work is funded by Newton Fund/Met Office Climate Science for Service Partnership China (CSSP China, SG), EPSRC DARE, EU H2020 UrbanFluxes, NERC ClearfLo, NERC/Belmont TRUC, EUf7 emBRACE and EUf7 BRIDGE. We thank Jean-Philippe Gastellu-Etchegorry, Tiangang Yin, Nicolas Lauret, Jordan Guilleux and all others of the DART team for ongoing and support and advice regarding the model. We thank Islington Council (Esther Lamontagne and Paul Stokes) for arranging access to observation sites, Daniel Clewley of the NERC Airborne Research Facility for assistance with the airborne hyperspectral dataset, Kjell Zum Berge (University of Reading) for assistance with the observations and Bryam Orihuela for assistance with the 3D modelling.

## Chapter 5 Conclusions

Ground-based thermography is applied to determine the effective thermal anisotropy in urban areas that contributes to uncertainties in satellite derived land surface temperatures critical for urban climate studies. As ground-based thermography has only been used occasionally in urban climate research, a major contribution of this work is to the advancement of the observational technique. Two case studies are undertaken: (1) at the Comprehensive urban Scale MOdel (COSMO) site (Kanda *et al.*, 2007) with an array of concrete cubes that provide a simplified urban geometry and material properties; and (2) in central London with a complex mix of residential, commercial and recreational park land-use.

### 5.1 Main contributions and conclusions

#### 5.1.1 Application and interpretation of ground-based thermography

A unique multi-camera approach developed for ground-based thermography allows the urban surface to be viewed from different angles to measure a more representative and larger 3D source area than in previous studies. This new approach uses simple static platforms rather than mechanical rotating masts (Adderley, Christen and Voogt, 2015) or vehicle transects (Voogt and Oke, 1997) so it is not limited to providing temporally sporadic data. It also reduces the trade-off between temporal resolution and spatial extent found in other remote sensing observations. In London, six cameras view 9.5 % of the 430 x 430 m study area.

To understand the drivers of surface temperature variability captured by the camera images, 3D modelling and perspective projection techniques are developed that combined to create a new quantitative interpretation of the surface geometry, including both building facets and vegetation, effects of sunlit/shaded conditions and surface orientation for each camera pixel. For London, this classification is enhanced to include discrete irradiance bins and a shadow history.

With these advances and applications of the methods, the following conclusions are drawn from the interpreted observations:

- (1) There are several technical challenges regarding the application and interpretation of observations. Continuous measurements at 1 min resolution means cameras capture over 10,000 raw thermographs ( $1.94 \times 10^7$  data points) for the London study across each day. Compared to other ground-based imaging studies using fewer cameras on different platforms, or more conventional meteorological instrumentation such as radiometers or weather stations, the capture and storage of this large amount of data cannot readily adopt more flexible approaches such as wireless and cellular networking. Instead the multiple cameras require mains power across

multiple wired connections that can also accommodate high bandwidth data transfer. These challenges compound with the need to have access to appropriate sites.

- (2) For both the COSMO and London studies, the observations are highly variable. During clear-sky conditions on summer days, temperatures around midday (12:00 – 13:00 local time) for the simpler COSMO surface have a 313 – 331 K brightness temperatures ( $T_b^{\text{cam}}$ ) range whereas the more complex London surface temperature ( $T_s$ ) range is even greater (297 – 335 K). The London (hourly resolution)  $T_s$  diurnal range reaches 38.4 K for roofs but is significantly less for natural surfaces (e.g. grass, < 12 K) and the predominantly shaded north walls (8.3 K). The latter generally follow the diurnal range of air temperature (8.9 K).
- (3) The sky view factor is shown to influence inter-class variability. At COSMO, roofs are cooler than other surfaces at night (up to 2 K) and warmer during the day (up to 15 K). Similar results are found in London but, with more detailed surface classes, the more complex surface and material characteristics can be accounted for. A simple description of the roof albedo (either light or dark) shows dark roofs are up to 14.2 K warmer during the day due to the greater absorption of solar radiation. The high level of detail in this study allows for the effect of roof slopes to be assessed. The difference in  $T_s$  between flat roofs (assumed in low level of detail modelling) and sloped roofs (in the high level of detail modelling here) reaches 23.3 K.
- (4) With a calculated sunlit/shaded status of pixels on the COSMO surfaces, the corresponding distribution of temperatures are not always bimodally distinguishable. This is a critical finding as previous studies using manual digitisation or frequency distribution approaches usually assume the two thermal states are clearly separated. The distributions are least distinguishable for afternoon periods when thermal inertia of the concrete gives a thermal hysteresis effect relating to the shadowing history.
- (5) The shadow hysteresis observed at COSMO is parameterised in London using an exponential cooling model by determining the time a surface has spent in shade. From this, recently shaded roof surfaces are up to 27.5 K (95<sup>th</sup> percentile) warmer than those in shade for long periods.
- (6) Across a day at the London site, the cooling surfaces are shown to follow an exponential rate with time constants ( $\tau$ , min) differentiated by facet (roof = 43.13 min, ground = 132.98 min, walls 173.54 min). Individual pixels also closely follow an exponential rate.
- (7) Walls that enter shade at sunset will have cooled to within 5 % of the “ambient” shaded surface temperature after  $\sim 3\tau$ . The slow cooling is a primary cause of the nocturnal urban heat island (Oke, 1981).

### 5.1.2 Retrieval of surface temperature

In general, retrieval of  $T_s$  from ground-based remote sensing (RS) is a very challenging process. A unique correction procedure is developed in this thesis using the Discrete Anisotropic Radiative Transfer (DART) three-dimensional radiative transfer (3D RT) model for the London case study,

accounting for both atmospheric and emissivity effects. It is concluded that the correction methodology is streamlined by using one model. Prior studies either use multiple models or do not account for both atmospheric and emissivity effects. The designed approach is flexible, having utility with any ground-based or even airborne observation campaign allowing any degree of complexity of the urban surface.

General characteristics of the atmospheric and emissivity effects for the London study can be quantified:

Across six cameras viewing the surface with  $\sim 50 - 250$  m path lengths over 20 days with varied meteorological conditions, the atmospheric correction is greatest during the day (up to 4.53 K for  $\sim 250$  m path length) coinciding with high daytime brightness temperatures. Evaluated using concurrent observations from cameras with a “near” and “far” distance to a reference surface, the correction has 0.39 K mean absolute error ( $r^2 = 0.998$ ). The approach is shown to be scalable with multiple instruments in the model area with minimal impact on computation time and applicable for operational use for observations at 5 min resolution.

For the emissivity correction, spatially variable descriptions of surface emissivity and emitted LWIR radiation across the canopy were successfully resolved by the DART model. The approach is shown to model RT processes at a level of detail and resolution not seen before in prior studies, where the exchange of LWIR radiation within the urban canopy is also resolved across realistic geometry whereby the buildings have balconies, sloped roofs, etc. and vegetation has a realistic canopy structure. An anisothermal case that used surface temperatures varying by surface orientation is compared to an isothermal case where all temperatures in the canopy are the same. Inter-case differences reach  $\pm 0.25$  K mainly for walls with high view factors of surfaces with contrasting (up to 17 K) temperatures, such as when west walls are facing the warm east walls in the morning, and vice-versa in the afternoon. Non-3D RT approaches (e.g. using the sky view factor - SVF) are constrained to the isothermal case (e.g. Adderley, Christen and Voogt, 2015). The correction is generally more sensitive to variation in the surface emissivity, which is varied according to a spectral library of urban materials (Kotthaus *et al.*, 2014). As roofs have the highest SVF, with the sky is much cooler than the surfaces under the mainly clear-sky conditions, varying the roof material emissivity from 0.89 – 0.97 from the baseline value of 0.93 resulted in  $T_s$  of more than  $\pm 1.5$  K during daytime, when roof temperatures are generally high (surface brightness temperatures up to 325.5 K). From the same variation in emissivity, the multiple scattering and lower sky view factor for within-canopy surfaces (walls, ground) gives a typically lower ( $\pm 1$  K) range.

### 5.1.3 Urban effective thermal anisotropy

Previous studies have combined ground-based or airborne observations with 3D modelling to study satellite view angle uncertainties from urban effective thermal anisotropy. However, this is the first

method combining observations from a network of cameras with detailed, anisotropic radiative transfer for both simplified urban geometry (COSMO) and a real urban area (London).

Across the two sites, the maximum difference in angular temperatures (maximum absolute anisotropy,  $\Lambda$ , K) is generally greatest at the COSMO site ( $\Lambda_{\max} = 6.18$  K at 13:00) but less than reported previously (e.g. over 10 K for airborne brightness temperatures, Lagouarde *et al.*, 2010). Despite the greater intra-pixel daytime range of temperatures in London, the site has lower maximum anisotropy (maximum  $\Lambda = 5.1$  K at 10:30). Across both study areas, the low night-time minimum in  $\Lambda$  ( $< 0.5$  K) is consistent with the literature. Conclusions relating to inter-site and inter-study differences in  $\Lambda$  are challenging to draw given the unique study dates, meteorological conditions, surface temperature distributions, etc. Further, COSMO results do not consider the emissivity effect and use brightness temperatures (as in Lagouarde *et al.*, 2010). A reference non-directional surface temperature that accounts for all surfaces without view bias (the “complete” surface temperature,  $T_c$ ) is determined for London. Simulated surface temperatures as seen from a satellite with directional view bias ( $T_s^{\text{EO}}$ ) are  $\sim 1$  K lower than  $T_c$  at night, which is significant in the context of nocturnal surface urban heat island intensity. The opposite is true during the day when  $T_s^{\text{EO}}$  for nadir views overestimates  $T_c$  by up to 1.9 K, in part because of its view bias of warm roofs. For low frequency revisit platforms such as Landsat (off-nadir view angles  $\sim 10^\circ$ ) maximum anisotropy is relatively low (typically  $< 1$  K). As the view angle increases, as occurs for platforms with more frequent revisit times (e.g. twice daily for Aqua/Terra satellites), the retrieved temperature includes these vertical facets that better represent  $T_c$ , but clearly require some correction or consideration of angular variation before application (e.g. surface urban heat island analysis). Without correction, any near-nadir satellite observations can be considered close to  $T_c$  in the morning, Night-time observations have small angular variation. Off-nadir measurements outside these time windows should be treated with greater care. Future operational corrections will benefit from verification using the datasets and methods shown here, particularly given the fractional contribution to total radiance is shown to be more evenly distributed among the roofs, walls and ground for more oblique view angles. If left uncorrected, any conclusions drawn based on temporal variations in  $T_s^{\text{EO}}$  should include uncertainty estimates for anisotropy. More simulation case studies for (e.g.) different cities and times of year may reveal further limitations on the current scientific value of urban  $T_s^{\text{EO}}$  observations, particularly when studies conduct multi-timestep and multi-city analyses.

This work both advances the methods for future ground-based case studies and demonstrates case studies at an unprecedented level of detail. A significant conclusion regarding the differences in anisotropy between the study areas in this thesis relate to the directional patterns of anisotropy through time. For the COSMO site, patterns have similar characteristics to prior modelling work with simple geometry, with steep gradients across narrow solid angles that align with bulk geometry features such as the building wall facings and the sun angle. This can occur when buildings are

arranged in repeating arrays with walls with the same cardinal direction (Krayenhoff and Voogt, 2016); but is generally not found when random orientations are used (Wang, Chen and Zhan, 2018). For the real urban surface geometry at the London site with a wide range of wall orientations, the directional temperature around the sun angle decreases more gradually across larger increments of azimuth angle. Further, the zenith view angle has similar or greater importance to the anisotropy in the real urban setting. This suggests that features of complex geometry found in the London area that are not well represented by simple geometry descriptions are substantially driving the thermal anisotropy. No vegetation is present at COSMO and many prior modelling studies neglect the green infrastructure (Krayenhoff and Voogt, 2016; Wang, Chen and Zhan, 2018; Hu and Wendel, 2019). However, for the central London study area, 12.0 % of the total area is canopy vegetation, and the contribution of vegetation is realistically modelled here for the first time.

## 5.2 Recommendations for future work

Based on the findings and contributions presented in this thesis, recommendations for future work relate to:

### Ground-based thermography observations

- A primary benefit of ground-based RS platforms is the temporally continuous nature of observations. Additional value has been demonstrated ranging from days to months. However, future studies may benefit from an inter-seasonal range of observations.
- Presented methods now enable streamlined correction and analysis of observations from a network of thermal cameras. Implementing multi-camera approaches of ground-based thermography now allows for the 3D thermal characteristics even of complex urban settings to be captured. With thermal camera technology becoming increasingly affordable with use in many commercial and industry sectors, operating a network of sensors with varying view angles becomes increasingly feasible.
- Two distinct study areas are assessed here, demonstrating the applicability of methods both in a simplified setting (COSMO) and a highly complex area (London) that encompasses many of the challenges associated with measurements in “real” urban areas. These case studies can inform future studies across a wide range of cities. The approach may face additional challenges in e.g. high-rise central business districts that can have very distinct surface geometry and material properties. With high fractions of glass, the lower emissivities and specular reflections in these areas may require cameras with different spectral responses and the emissivity correction may have a greater range of uncertainty unless more comprehensive material datasets are available. The geometry of compact high-rise areas may also limit the source area of measurements, unlike the open high-rise geometry of the London area and prior studies (e.g. Meier *et al.*, 2011), or generally low-rise surfaces of COSMO or

other prior studies (Meier, Scherer and Richters, 2010a; e.g. Adderley, Christen and Voogt, 2015). Longer distance and wider angled siting approaches (Yang and Li, 2009; e.g. Ghandehari, Emig and Aghamohamadnia, 2018) have potential to overcome this issue.

- The interpreted and corrected datasets compiled here have potential for the evaluation of surface energy balance models that resolve the canopy at increasingly high resolution (Grimmond *et al.*, 2010), especially given surface schemes simulate surface temperatures separately for roofs, walls and ground and also distributed by solar radiation (Masson, 2000). The derived cooling rates and shadow histories have much scope for further study given the slowed release of heat by urban surfaces forms the basis of the nocturnal urban heat island effect.

### **3D modelling of urban areas**

- Urban mapping is anticipated to produce more readily available and higher level of detail 3D urban models in the future as a result of ever-increasing use of photogrammetry, computer vision and 3D geometry in a variety of fields (Biljecki *et al.*, 2015). As 3D surface models form the basis of much of the image interpretation, correction and radiative transfer modelling in this thesis, such advances should be used to positively impact future applications of the work shown here.
- Material property distributions across urban surfaces in 3D and at high spatial resolution and extent are not well documented compared to the material-specific emissivity estimates (Kotthaus *et al.*, 2014), which is important for a range of urban climate applications and in particular for both emissivity correction and effective thermal anisotropy shown here. A better understanding of urban material properties at high spatial resolution will complement the projected future availability of 3D urban models. A combination of relatively recent advances in computer vision, machine learning and crowd sourced or open access “big data” may help with this effort, for example by using Google Street view imagery (Zeng *et al.*, 2018b), unmanned aerial vehicles (e.g. Kirsch *et al.*, 2018) and the Open Street Map framework (Jokar *et al.*, 2015) which could be particularly advantageous for surveying the horizontal surfaces that are not always seen from typical airborne and satellite platforms.
- The London case study uses a very high level of detail 3D model. However, once the model is created it is hard to modify or simplify it as part of a sensitivity analysis to complement many of the findings in this thesis. As most 3D modellers are interested in increasing the level of detail (Biljecki, Ledoux and Stoter, 2017), ways to reliably and quickly reduce the level of detail have not been explored as much. In general it is harder to modify complex 3D models compared to idealised 3D or 2.5D raster digital elevation models (Biljecki *et al.*, 2015). Future work should aim to address this issue to enable geometry related sensitivity studies such as the effect on the effective thermal anisotropy. To date, the latter has only

been investigated by Krayenhoff and Voogt (2016) using variations of highly idealised geometry in a similar configuration to COSMO.

### **Surface temperature retrieval from ground-based thermography**

- For the atmospheric correction, the observational evaluation could benefit from a longer (annual) campaign to capture more variation in meteorological conditions. The sensitivity of the correction to the assumed atmosphere profiles of temperature and water vapour could be explored, including the use of different input data such as from climate model output or reanalysis.
- For the emissivity correction, information on the directional nature of surface emissivity and downwelling longwave radiation from the sky would be beneficial. Uncertainty analysis could explore the relative importance of these processes which are not well known but are readily applicable using this emissivity correction methodology. This analysis would also help to optimise the computational cost of future simulations.
- Generally, the 3D RT approach requires a benchmarking framework to understand the trade-offs associated with the various model parameters that can be set by the user, such as voxel resolution and the number of rays tracked. Challenges are associated with the complex model output when considered across the multiple cameras each with different viewing perspectives of the model domain.

### **Modelling of effective thermal anisotropy**

- The interpreted thermography observations were not compared against high resolution energy balance model outputs (e.g. TUF-3D, Krayenhoff and Voogt, 2007) and there is generally a lack of observational evaluation of such models. Using the thermography interpretation framework shown in this thesis, observations can be used more effectively for the evaluation and improvement of models. With improved and evaluated models, their high-resolution surface temperature can be used more confidently over observations.
- The high-resolution modelling of effective thermal anisotropy shown throughout this thesis can inform future parameterisations of effective thermal anisotropy in urban areas. Future work should aim to evaluate recent advances in more simple parameterisations (e.g. GUTA, Wang *et al.*, 2018b) such that generic morphometric parameters and sun-surface geometry can be used for the operational correction of view angle effects on land surface temperature products from earth observation satellites.
- Using the present model setup, a sensitivity analysis could inform the development of future model parameterisations. By incrementally simplifying modelled aspects, such as the surface geometry, material properties, RT processes and surface temperature distributions, their relative contribution to effective thermal anisotropy can be better quantified.

## **Application for architects, building planners and energy management studies**

- The high resolution (e.g. spatial, angular, spectral) 3D building and RT modelling in this thesis lends itself to further uncertainty analyses with thermography for (e.g.) building envelope studies that often use brightness temperatures to infer results that actually demand a retrieved kinematic surface temperature.
- With glass and metal commonplace in urban design, there is increasing need for more realistic RT modelling of the undertaken as these surfaces have a strong specular reflection component that. If not accounted for during architectural design phases can result in unexpected micrometeorological impacts and costly building retrofits.

## **Infrared camera metrology**

- The thermal stability and accuracy of thermal cameras, affected by their sampling conditions, has been considered. Radiation shields successfully protected the instruments from differential heating from direct sunlight.
- Aspirated enclosures developed here have potential to reduce large and rapid variation in body temperature experienced in outdoor environments. More work is required to quantify the impact of enclosures on the accuracy of infrared cameras through time in these environments.

## Appendix A: Thermal camera lens distortion correction

A rig was designed to calibrate the Optris PI-160 (Optris GmbH, 2018) longwave infrared (LWIR) cameras for lens distortion effects. A geometric calibration or “resectioning” of the camera intrinsic or “internal” parameters of focal length, scale factor (aspect ratio of pixels), principal point offset (misalignment of the camera focal plane array with the centre of the image) and lens distortion were undertaken. The fundamentals of computer vision and camera calibration are detailed in Hartley and Zisserman (2004).

The calibration rig (Figure A-1) was designed to be detectable in the LWIR portion of the electromagnetic spectrum. Thermal images of the calibration rig were analysed using the Matlab “camera calibration toolbox” (Bouguet, 2008) to perform the geometric calibration of the LWIR cameras presented.

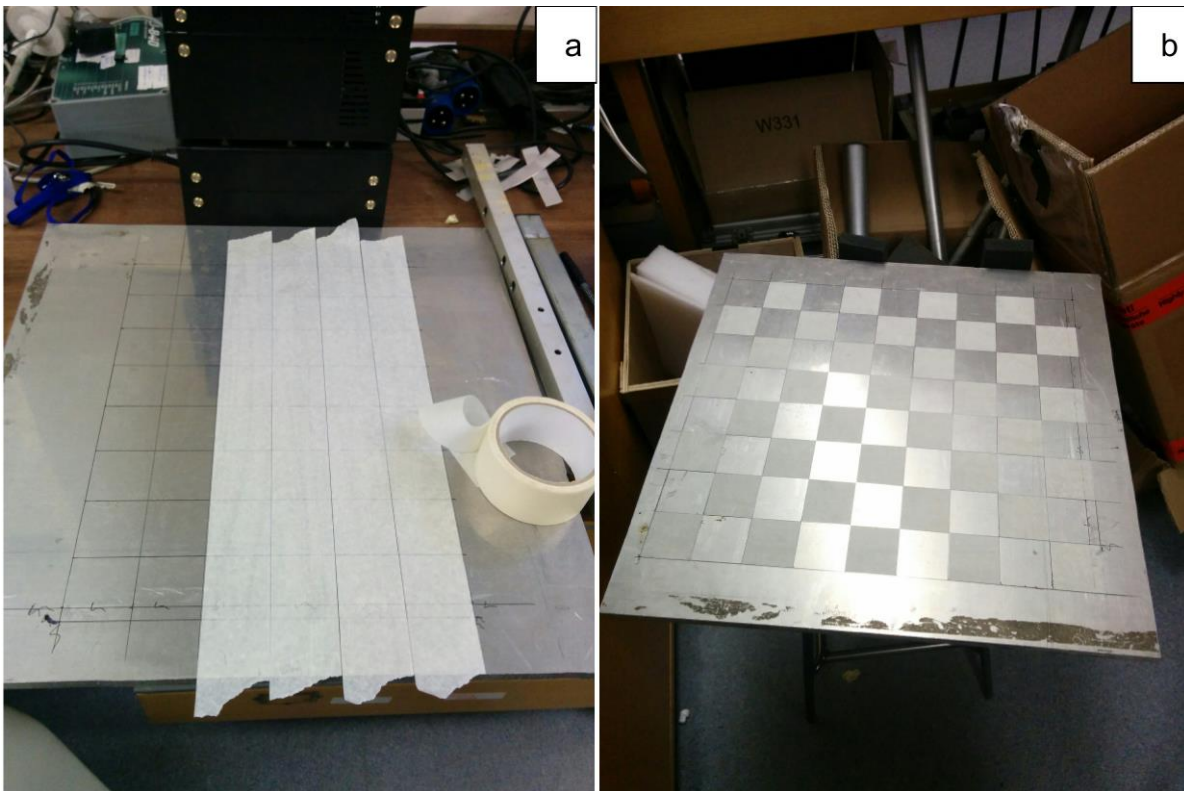


Figure A-1. (a) Preparation of and (b) final construction of the calibration rig used for the calibration of the Optris PI-160 longwave infrared cameras used. The metal plate is a 0.5 m x 0.5 m steel plate highly reflective in the infrared (emissivity  $\epsilon < 0.1$ ) populated with masking tape 0.05 m wide with a contrasting low reflectance ( $\epsilon \approx 0.95$ ), which was taped onto the plate and cut into a grid of 8 x 7 cells each 0.05 m x 0.05 m.

Images are taken with the Optris PI-160 longwave infrared camera (Figure A-2) of the calibration rig when it is outside under clear skies. For an image, the Matlab *camera calibration toolbox* is run to detect the corners of each grid cell (green points) and the origin of the grid cell (yellow) which

have known “real world” dimensions. Multiple images (> 20) of the grid are captured, from different view angles and parts of the camera image.

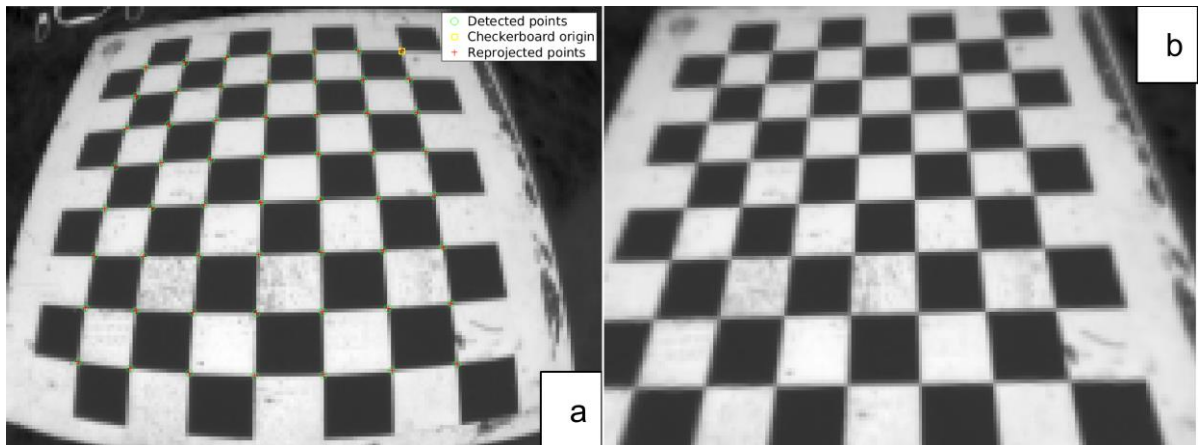


Figure A-2. Output images from the Matlab camera calibration toolbox of the calibration rig, with (a) the distorted image originally taken by an Optris PI-160 longwave infrared camera with points (green) detected and (red) estimated by the Matlab camera calibration toolbox and (b) the undistorted image determined using the camera parameters. Black (white) relates to low (high) camera brightness temperatures. Camera (lens) serial number 12080017 (17050013).

The location and orientation of the camera during each image capture (Figure A-3) and the re-projected grid points (Figure A-2a, red) is estimated by the combination of the known “real world” dimensions and the detected grid points. The differences between the detected and re-projected points are evaluated, and the process is repeated until the error is minimised in a least squares sense, at which point the best distortion correction parameters are saved and referenced manually to the serial number of the given camera and its installed lens.

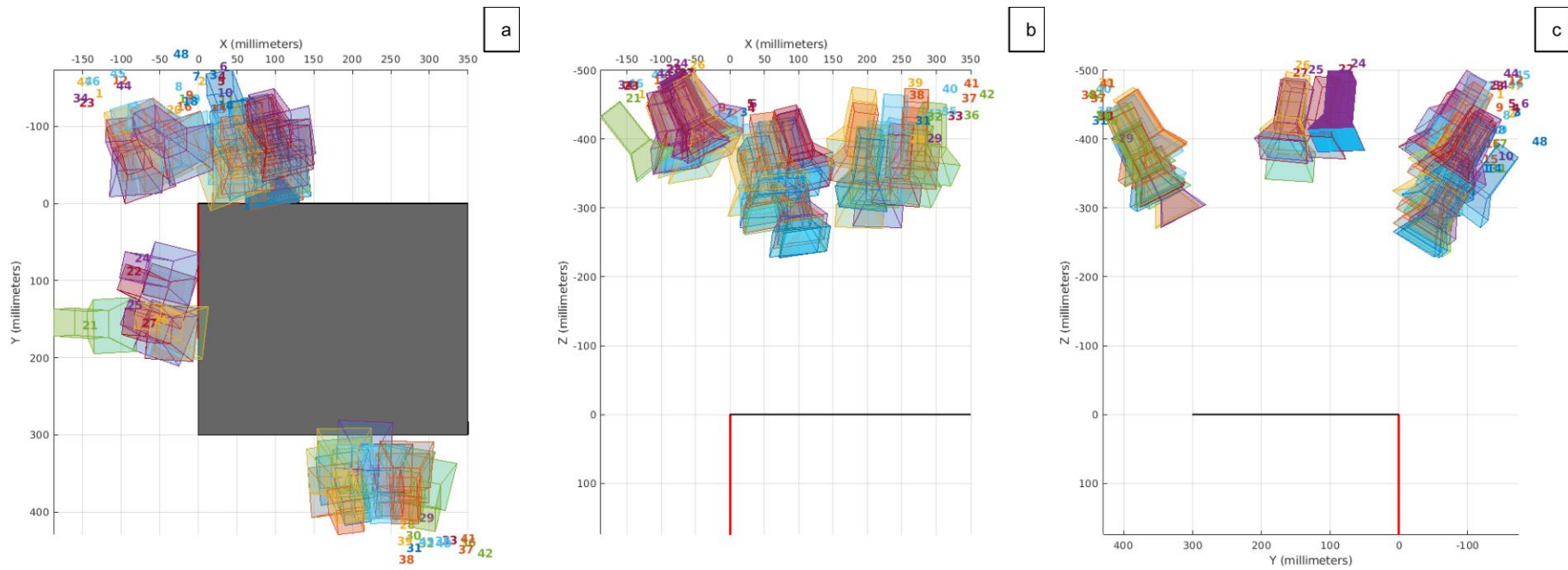


Figure A-3. Output images from the Matlab camera calibration toolbox showing in three-dimensions the estimate of the relative position and orientation of the calibration rig (grey square) to the camera during the capture of 48 images (coloured boxes with frustums) of the plate. Relative positions plotted in 3D and shown with perspective along the (a) vertical Z axis (b) horizontal X axis and (c) horizontal Y axis.

## Appendix B: Longwave infrared camera meta data

Table B-1. Meta data for all Optris PI cameras installed during the two observation campaigns in this thesis with (deployment) the time window where a camera has a static location and rotation and (internal meta data ID) a reference to the London Urban Climate metadata system ([www.urban-climate.net](http://www.urban-climate.net)) used to manage the observational meta data.

Camera reference in thesis	Deployment start date (DD/MM/YYYY)	Deployment end date (DD/MM/YYYY)	Observation site	Serial number (body)	Serial number (lens)	Internal meta data ID
C <sup>North</sup>	16/06/2014	26/09/2014	COSMO	12070026	12060012	363
C <sup>South</sup>	16/06/2014	26/09/2014	COSMO	12060057	12060030	364
C <sup>North</sup>	16/06/2014	26/09/2014	COSMO	12070026	12060012	365
C1	13/07/2017	27/07/2017	IMU	12080019	17050029	444
C4	17/07/2017	02/08/2017	IMU	12080017	17050013	443
C1	22/07/2017	02/08/2017	IMU	12080019	17050029	444
C4	22/07/2017	02/08/2017	IMU	12080017	17050013	443
C2	22/07/2017	02/08/2017	IMU	12080016	16060004	403
C6	22/07/2017	02/08/2017	WCT	12070069	17050015	406
C5	22/07/2017	02/08/2017	WCT	12060057	16080014	405
C3	22/07/2017	02/08/2017	IMU	12080103	17050030	401
C4	22/07/2017	02/08/2017	IMU	12080017	17050013	443
C2	22/07/2017	02/08/2017	IMU	12080016	16060004	403
C1	22/07/2017	02/08/2017	IMU	12080019	17050029	402
C4	22/07/2017	02/08/2017	IMU	12080017	17050013	443
C1	22/07/2017	24/10/2017	IMU	12080019	17050029	402
C2	22/07/2017	24/10/2017	IMU	12080016	16060004	403
C3	04/08/2017	10/11/2017	IMU	12080103	17050030	453
C4	04/08/2017	10/11/2017	IMU	12080017	17050013	404
C6	04/08/2017	10/11/2017	WCT	12070069	17050015	441
C5	04/08/2017	10/11/2017	WCT	12060057	16080014	442
C1	17/08/2017	10/11/2017	IMU	12080019	17050029	437
-	17/08/2017	10/11/2017	IMU	12080017	17050013	439
C7	17/08/2017	10/11/2017	CUB	12070026	12060012	431
C3	17/08/2017	10/11/2017	IMU	12080103	17050030	434
-	17/08/2017	10/11/2017	IMU	12080017	17050013	439
C2	17/08/2017	10/11/2017	IMU	12080016	16060004	403
C1	17/08/2017	10/11/2017	IMU	12080019	17050029	437
-	17/08/2017	10/11/2017	IMU	12080017	17050013	439
-	17/08/2017	10/11/2017	IMU	12080016	16060004	440
C1	17/08/2017	10/11/2017	IMU	12080019	17050029	437
-	17/08/2017	10/11/2017	IMU	12080016	16060004	440

## Appendix C: Camera image emissivity maps from the DART model

An emissivity map is required for the emissivity correction of longwave infrared (LWIR) cameras. A map covers the perspective of a camera image and has emissivity values across the image pixels informed by the surfaces observed and their associated material and optical properties. With an isotropic emissivity, the view angle of the camera does not alter the observed surface emissivity, thus an emissivity map can be created that is referenced to any prior image classification (e.g. surface orientation and material maps, Figure 3-4a). For anisotropic emissivity situations, DART can be used to calculate a pre-processed emissivity map that considers the view angle dependence of surface emissivity for any given camera and its pixels. For this, the surfaces in the DART model world (MW) would be configured to have materials with scattering phase functions ( $p$ ) to give an anisotropic and spectral emissivity  $\varepsilon_{\lambda,p}$ . A DART simulation similar to that used for the non-black-body (non-BB) radiance calculation ( $L_{\lambda}^{\text{DART}}(x, y, \Omega_{\uparrow}, \varepsilon_{\lambda,p} < 1)$ ,  $\text{W m}^{-2} \text{sr}^{-1} \mu\text{m}^{-1}$ , see Section 3.3.3) is used and adjusted to have: one known surface temperature ( $\bar{T}_s$ ) across all surfaces, no sky emission (sky brightness temperature  $T_b^{\text{sky}} = 0 \text{ K}$ ) and no scattering events. This gives a non-BB surface-leaving radiance product [ $L_{\lambda}^{\text{DART}}(x, y, \Omega_{\uparrow}, \varepsilon_{\lambda,p} < 1, T_b^{\text{sky}} = 0, \bar{T}_s)$ ] used to determine  $\varepsilon_{\lambda,p}(x, y)$  across the MW camera perspective with:

$$\varepsilon_{\lambda,p}(x, y) = \frac{L_{\lambda}^{\text{DART}}(x, y, \Omega_{\uparrow}, \varepsilon_{\lambda,p} < 1, T_b^{\text{sky}} = 0, \bar{T}_s)}{B_{\lambda}(\bar{T}_s)} \quad \text{Eqn. C.1}$$

where  $B_{\lambda}(\bar{T}_s)$  is the expected at-sensor Planck radiance for a black-body (i.e.  $\varepsilon_{\lambda,p} = 1$ ) at the given homogeneous temperature.

## Appendix D: Creation and classification of complex 3D surface and vegetation models

Photogrammetry techniques are used to build a high level of detail (LOD) description of the surface geometry within the central London study area (Chapter 3 and Chapter 4).

### D.1: Creation

Urban surface geometry of buildings, roads, and vegetation (Figure D-1) are resolved to include sub-facet details (e.g. sloped roofs and balconies). The model world (MW) area has an initial horizontal extent of 450 x 450 m.

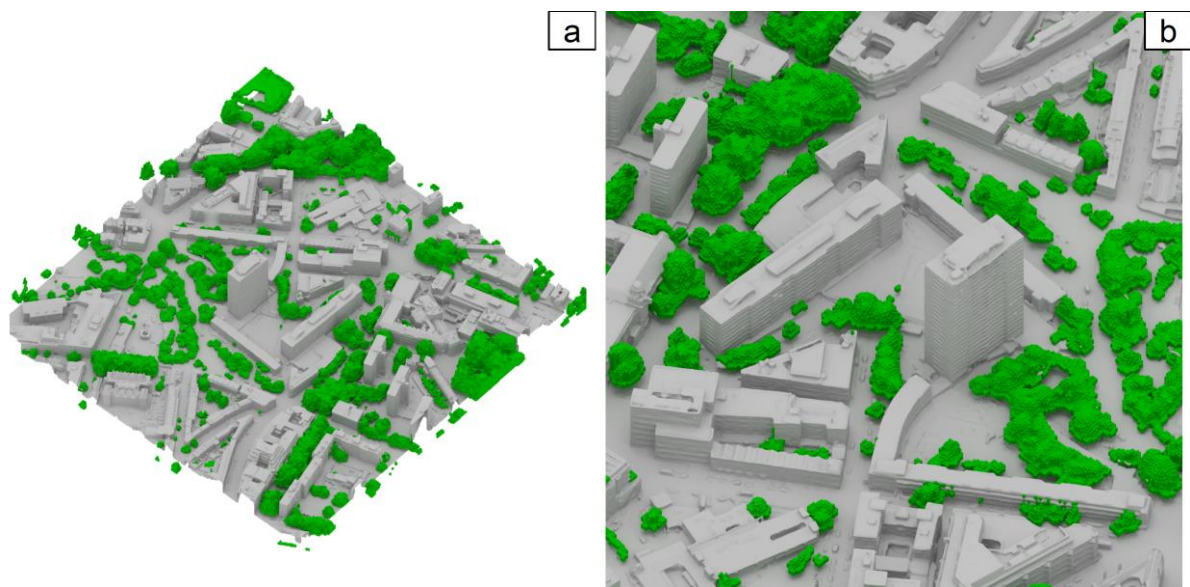


Figure D-1. Urban surface geometry as (grey) a vector-based 3D surface model and (green) a voxel-based model of vegetation canopy elements for the central London (UK) study area (Chapter 3 and Chapter 4) rendered using Blender (Blender, 2018).

The MW area is first split into nine 150 m x 150 m georeferenced tiles (3 x 3 array). In Google Earth Pro (Google, 2019a), a programmed “tour” takes 32 images per tile at 200 m from the centre of each tile with a 45° zenith angle at 11.25° azimuth angle steps (tile height: mean height above ground level (centre), derived from Google Maps API, Google, 2019b). The tour, saved in .kml file format, can be read by Google Earth. By taking images around a centre point, most of the Google Earth 3D surface present within a tile is captured (Figure D-2).



Figure D-2. Sample images captured by Google Earth using a pre-programmed Google Earth “tour”. Images are used to create a dense point cloud “tile” in Agisoft PhotoScan Professional (Figure D-3).

Agisoft PhotoScan Professional (Agisoft LLC, 2013) photogrammetry software suite (“PhotoScan”) Version 1.3.4 build 506 is used to process the Google Earth images. The relative position and rotation of the cameras stored in the .kml file is verified by Photoscan using unsupervised detection of inter- and intra-image control points. For each tile, image depth mapping with Photoscan is used to construct a dense 3D point cloud (120,000 – 160,000 points) of Google Earth surfaces containing the 3D coordinate (X, Y, Z), surface normal and RGB attributes (Figure D-3).

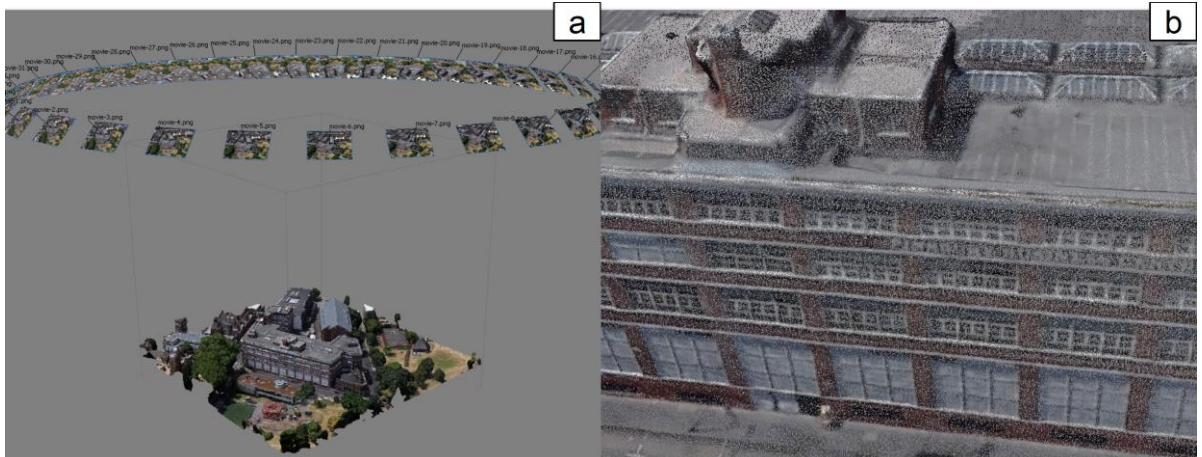


Figure D-3. Screen captures from the Agisoft PhotoScan Pro user interface (Version 1.3.4 build 506) with (a) a dense point cloud ( $1.56 \times 10^7$  points) across a  $150 \times 150$  m “tile” centred on WGS UTM 31N coordinates ( $x = 284450$ ,  $y = 5712800$ ) with the camera position for the Google Earth images shown above and (b) a close-up of the sample dense point cloud.

Point clouds for each tile are rasterised at 0.2 m resolution to give raster ( $r$ ) digital surface models ( $r^{\text{DSM}}$ , e.g. Figure D-4a) for each tile which are then merged.

As the Google Earth images only sample the top and sides of convoluted urban surfaces, the complete vegetation canopy is underrepresented by the point cloud. Thus, vegetation canopy points are extracted from the point cloud and modelled separately. Ground points within each point cloud are automatically classified with Photoscan and rasterized to create a raster digital elevation model ( $r^{\text{DEM}}$ ) at 0.2 m resolution ( $r^{\text{DEM}}$ , Figure D-4b) which is aggregated to 5 m using the median values and resampled back to 0.2 m. Green vegetation canopies are selected using an RGB colour filter applied to an orthorectified true-colour raster of the Google Earth surface ( $r^{\text{RGB}}$ , Figure D-4d) combined with an above ground level (agl) height threshold ( $[r^{\text{DSM}} - r^{\text{DEM}}] > 1.5$  m). Manual digitisation is used to select any shaded or non-green vegetation not selected, and to deselect any raster cells incorrectly identified (e.g. artificial turf). The combined automated filter and manual digitised vegetation forms a vegetation map ( $r^{\text{VEG}}$ ). Any point cloud points with horizontal coordinates that intersect a vegetation cell from  $r^{\text{VEG}}$  are moved to the height of the corresponding  $r^{\text{DEM}}$  cell, to produce a modified point cloud that excludes all vegetation canopy elements (VCE). A VCE is defined as any vegetation taller than 1.5 m agl (e.g. trees, bushes or shrubs).

The modified point cloud is converted to a 3D vector DSM using Poisson surface reconstruction (Kazhdan and Hoppe, 2013). As surfaces near ( $<10$  m) each edge of the DSM extent are poorly reconstructed with this method, they are removed; hence, the final horizontal extent of the DSM is  $430 \times 430$  m.

The geometry of VCE is contained with a 3D array of voxels ( $Vx^V$ ) at  $\Delta X = \Delta Y = 1$  m,  $\Delta Z = 0.1$  m, that either are filled with VCE or empty.  $r^{\text{VEG}}$  cells that intersect  $Vx^V$  determines the horizontal

distribution of VCE. The vertical distribution of  $Vx^V$  uses a canopy top and base height, between which all voxels are filled. The canopy top is assumed to be the 95<sup>th</sup> percentile height of the corresponding  $r^{DSM}$  and  $r^{VEG}$  cells. The canopy base height is determined for each VCE. First, individual VCE crowns are identified by applying a local maxima filter (Roussel and Auty, 2018) to  $r^{DSM}$  cells mapped as  $r^{VEG}$ . The horizontal extent of each VCE crown, determined using a watershed algorithm (Plowright, 2018), produces a polygon outline for each (Figure D-4d). The “Virtual London” building footprint model (Evans, Hudson-Smith and Batty, 2006; Figure 3-2a) is used to determine if a VCE is on top of or near a building. A VCE polygon that intersects > 90 % of the area of a building footprint polygon is assumed to originate from a roof surface. The base height of each  $Vx^V$  within a roof VCE is set to the 25<sup>th</sup> percentile height of all  $r^{DSM}$  pixels within 0.5 m of the roof VCE perimeter. For the voxels within each non-roof VCE, the base or “trunk” height is assumed as 0.25 of the 95<sup>th</sup> percentile height of  $r^{DSM}$  pixels within the VCE polygon.

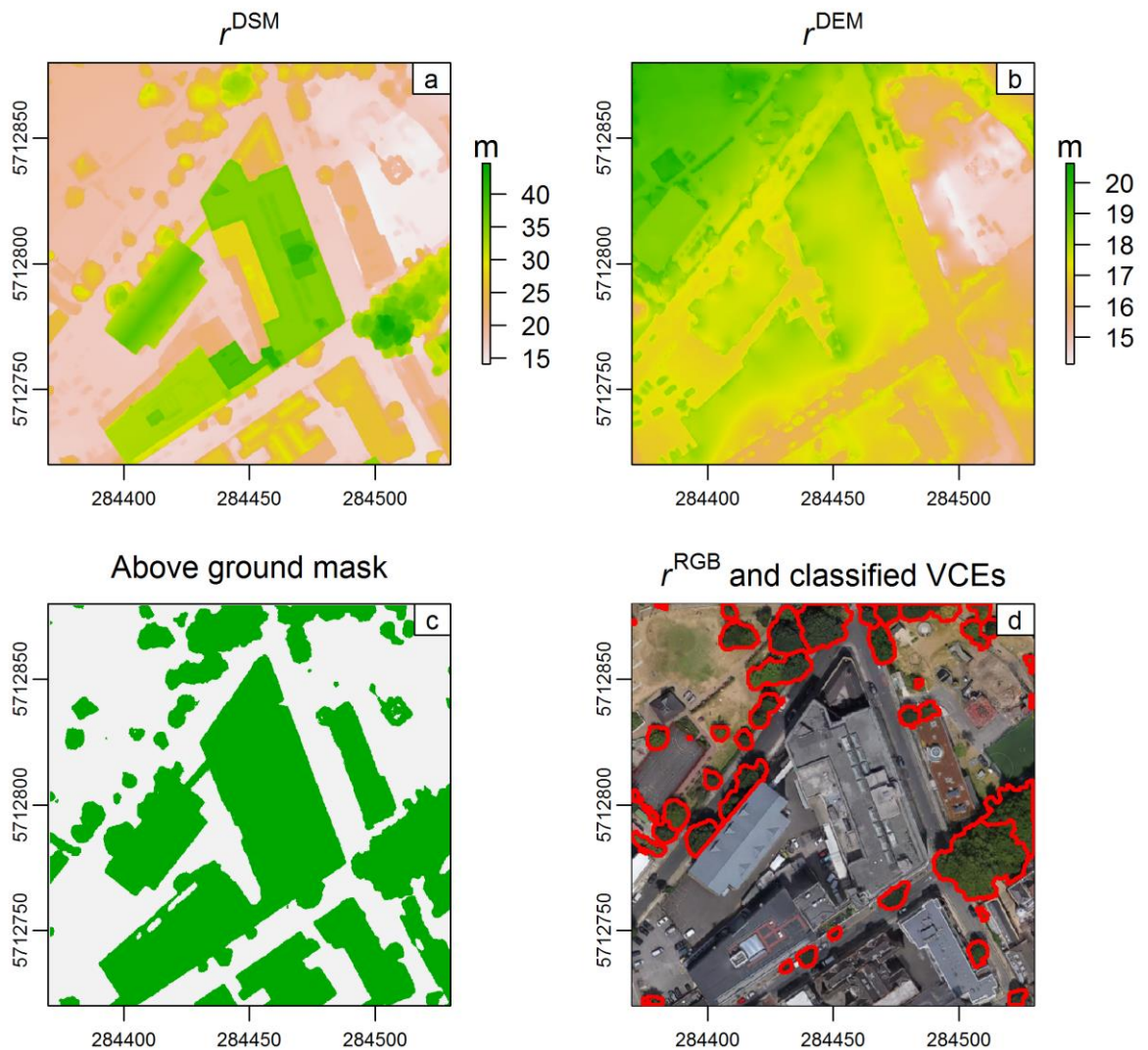


Figure D-4. Raster ( $r$ ) products for one 150 x 150 m “tile” of the larger study area, photogrammetrically processed from the 3D point cloud with (a) digital surface model ( $r^{\text{DSM}}$ ) (b) base resolution (0.2 m) digital elevation model ( $r^{\text{DEM}}$ ) (c) above ground (green) surfaces and (d) orthoimage determined by Agisoft using the raw Google Earth images and classified vegetation canopy elements (VCE, red lines). All rasters are (i) used to determine a 3D distribution of VCE (ii) shown in grid coordinate system UTM 31N (m) and (iii) above sea level (m) where appropriate.

## D.2: Classification

The final classified London surface geometry is shown in Figure 3-2a and e.g. Figure 4-3. To create this, each triangle of the DSM is assigned an “orientation” (either north, east, south or west facing wall, roof or ground) using Blender 3D modelling software version 2.79 (Blender Foundation, 2018, hereafter “Blender”). The orientation of each triangle is defined by the smallest angular difference between the normal of a DSM triangle and the normal of each cardinal and upward (downward) direction. To differentiate upward facing triangles as roof or ground, the height of the centroid of each upward facing triangle (i.e. triangles not assigned a cardinal orientation) is compared to the

height of the corresponding  $r^{\text{DSM}}$  (e.g. Figure D-4) cell. A triangle is classified as ground if its centroid height is within 2 m of the corresponding  $r^{\text{DSM}}$  cell. Remaining upward triangles are assigned as roofs.

Land cover ( $r^{\text{LC}}$ ) and hyperspectral reflectance ( $r_{\lambda}^{\circ}$ ) maps are used to assign simple materials of: Roof [light | dark] and Ground [imp. (impervious) | grass] (Figure 3-2).  $r^{\text{LC}}$  contains built surfaces, grass and “tree” classes at 4 m resolution (Lindberg and Grimmond, 2011). As VCE are modelled (Section D.1) and classified separately, the ground below each VCE within  $r^{\text{LC}}$  is assigned as Ground[grass] for pixels that intersect the Ordnance Survey Greenspace dataset (Ordnance Survey, 2018) or otherwise as impervious (Ground[imp.]).  $r_{\lambda}^{\circ}$  is derived from Specim AISA “Eagle” pushbroom sensor (0.40 – 0.97  $\mu\text{m}$ , 253 channels) mounted on the Natural Environment Research Council (NERC) Airborne Research and Survey Facility (ARSF) Dornier 228 plane observed on 3<sup>rd</sup> June 2010 (NERC ARSF, 2010). The radiometrically calibrated observations are georeferenced using flight navigation data and orthorectified using on-board Light Detection and Ranging (LiDAR) data with NERC-ARF-DAN (Natural Environmental Research Council Airborne Research Facility Data Analysis Node) APL (Airborne Processing Library) software (NERC-ARF, 2016) at 1 m spatial resolution and cropped to the MW area extent. After rejecting shaded pixels and atmospheric absorption bands,  $r_{\lambda}^{\circ}$  is classified using k-means ( $k = 3$ ) clustering (Leutner and Horning, 2016). The three clusters identified are: low reflectance, high reflectance and vegetation. Low reflectance and shaded surface clusters are assigned to “dark” pixels in the  $r_{\lambda}^{\circ}$  dataset and high reflectance clusters are assigned to “light” pixels. Google Earth imagery between 2010 and 2017 suggests land use and surface materials remain largely unchanged within the study area. Processes such as weathering and re-roofing that may impact the classification are not accounted for.

Roof and ground DSM triangles are assigned materials using  $r^{\text{LC}}$  and  $r_{\lambda}^{\circ}$  based on the intersection of the (X, Y) coordinates of a triangle centroid and the (X, Y) coordinates of each raster cell. Ground surfaces are assigned ground[grass] from  $r^{\text{LC}}$ . Roof surfaces are assigned Roof[dark] or Roof[light] from  $r_{\lambda}^{\circ}$ . Ground surfaces are not assigned any further material properties as they are often shaded and occluded by trees and buildings when viewed from airborne platforms (Weng, 2012). Materials of vertical surfaces cannot be informed by the plan view raster datasets. Almost universally limited high-resolution urban land cover and material datasets makes further land cover classes and surface material classification challenging to include.

## Appendix E: Thermal camera enclosures

During the years 2015-16 when the LWIR cameras (Optris PI-160) were installed in central London (Figure E-1), damage occurred from exposure despite being advertised as having complete protection against both dust contact and water immersion up to 1 m depth (“IP67” rating from IEC 60529 international standard) and therefore new enclosures were designed. The original aluminium enclosures covered the top of each camera (Figure E-1) to limit differential and rapid warming of the camera body from direct sunlight.



Figure E-1. Example setup of Optris PI-160 LWIR camera (years 2015-16) at the IMU site with (a) overall mounting of south facing camera (photo looking southwest) (b) close-up of the Optris PI-160 camera in original aluminium housing, and (c) front of the camera within the aluminium housing.

Examples of the degradation of the lens anti-reflective coating include a sensor installed at 110 m residential tower facing into the prevailing winds (south-westerly) for 11 months (Figure E-2b, right). The degradation is evident when compared to a new lens (e.g. Figure E-2a, left; Figure E-2b, left). Unfortunately, the overall effect of the degradation is an unaccountable reduction in transmissivity of the lens over time. This reduction in observational accuracy made images appear to be out of focus (image aberrations). Attempts to clean the lenses during and after the 2015-16 campaign concluded the lenses were damaged beyond repair.

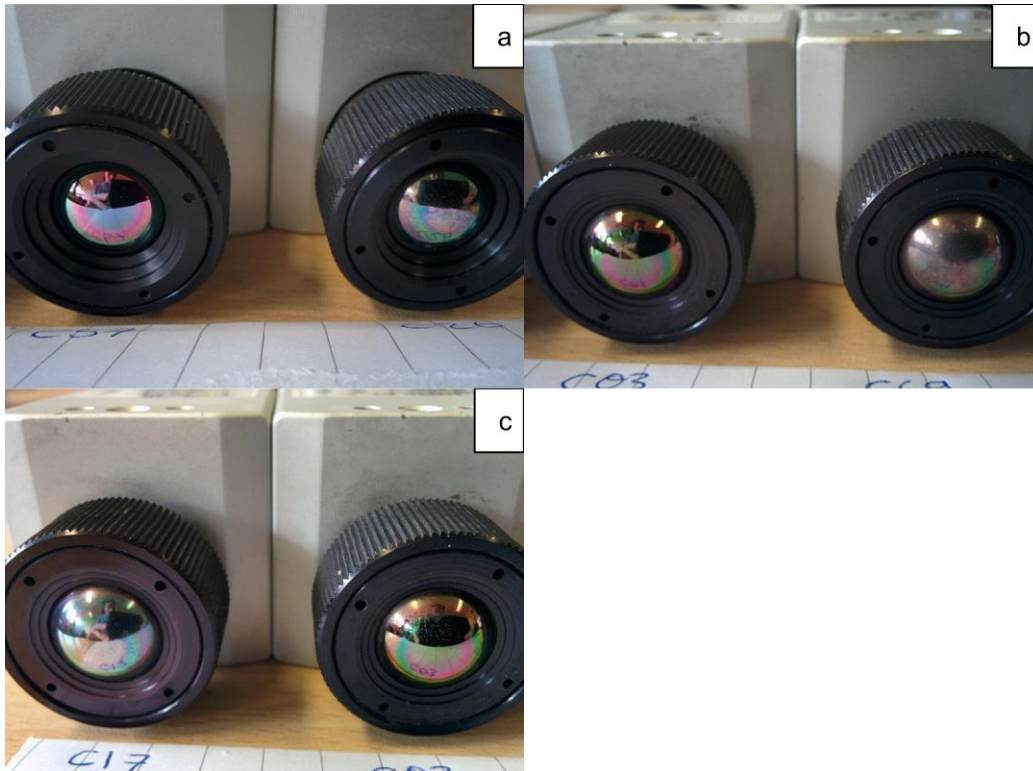


Figure E-2. Camera lenses after the 2015-16 observation campaign, camera body serial numbers ending in (a) 57 and 26 (b) 03 and 69 (c) 17 and 03 (see Appendix B).

New designs for housing the cameras considered sealed enclosures but as these require LWIR-transparent windows they were not used as the windows 1) may also be susceptible to the same degradation, and 2) would gradually and unaccountably reduce the transmittance of the camera system. The solution developed (Figure E-3) protects the lenses without directly interfering with the camera system.

Each enclosure (Spelsberg TK-PS IP66 polystyrene enclosures, 182 mm x 180 mm x 111 mm) housed a camera, a Raspberry Pi model B computer and a servo motor (Hitec HS-322HD) that controlled an external shutter. Enclosures are covered in reflective aluminium tape to minimise absorption of radiation. The Raspberry Pi controlled the servo motor, the internal shutter motor of the camera, and recorded the internal body temperature sensor of the camera. A shutter mounted on the servo motor occluded an opening in the enclosure located in front of the camera. A schematic for the components used inside each enclosure is shown in Figure E-4 and supplemented by Table E-1.

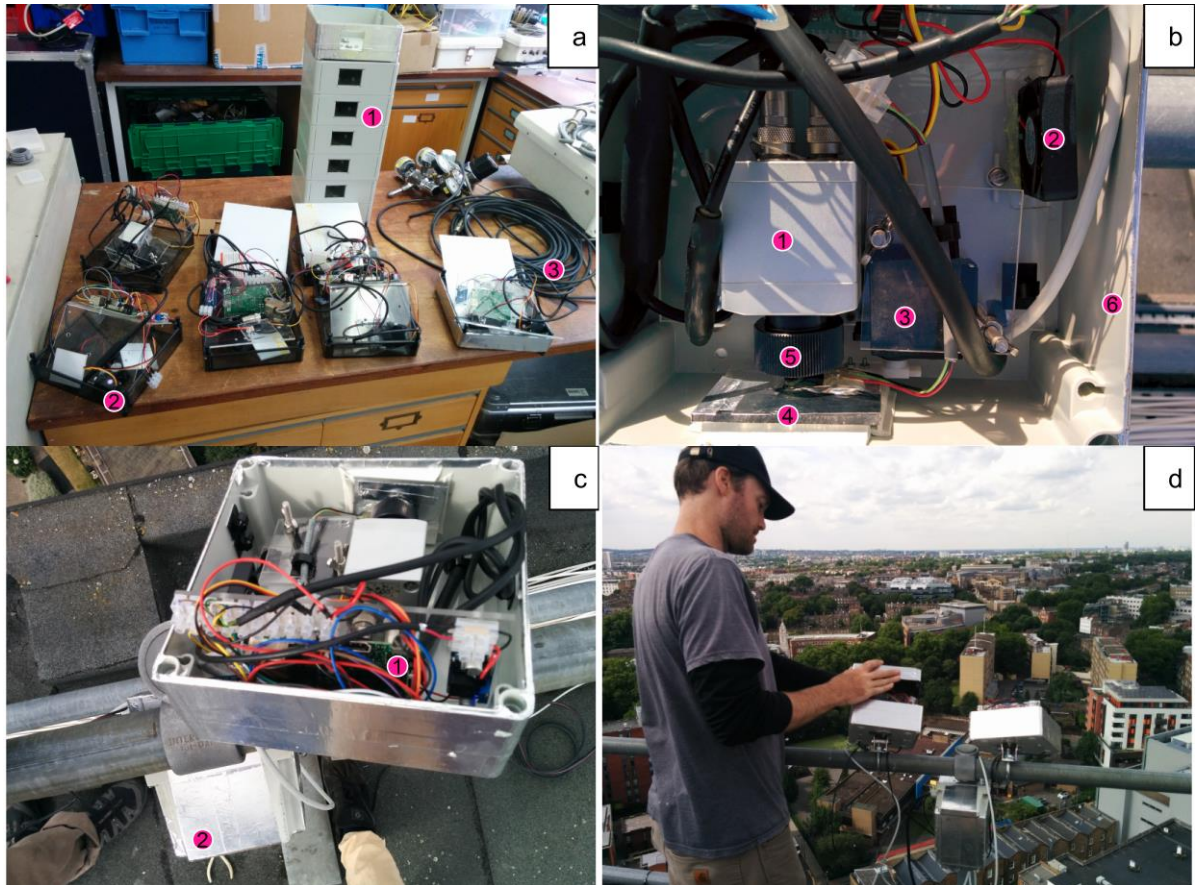


Figure E-3. (a) Construction of the 7 enclosures used for the LWIR camera observations in the thesis with (1) Spelsberg TK-PS IP66 polystyrene, 182 mm x 180 mm x 111 mm enclosure housings without aluminium tape, (2) lids for the enclosure housings prior to aluminium tape application and temporarily holding the electronics for each enclosure, (3) 20 m USB data transfer cable between the camera and data collection computer, (b) completed enclosure with (1) Optris PI-160 LWIR camera, (2) 30 mm fan with 5 mm holes underneath to promote the circulation of air within the enclosures, (3) Hitec HS-322HD servo motor attached to (4) a shutter that covers the opening in the enclosure, (5) camera lens assembly (6) enclosure housing, (c) enclosure installed at the IMU site with the camera facing northeast with (1) the Raspberry Pi and electronics housed at the back of the enclosure on an L-shaped acrylic plate, (2) additional housing for an ethernet switch and 12V power supply, (d) final installation of the camera (shown in c) with Dr Ben Crawford closing lid.

Table E-1. Description of process interface (PIF) connectors for Optris PI-160 cameras (Optris GmbH, 2018), referenced numerically in Figure E-4.

PIF port # (Figure E-4)	Short name	Description
1	PIF_VIN	Power: 5V DC +ve
2	Shield	-
3	PIF_AO1	Analog output
4	PIF_AIN1	Analog input
5	PIF_DIN1	Digital input
6	PIF_GND	Ground

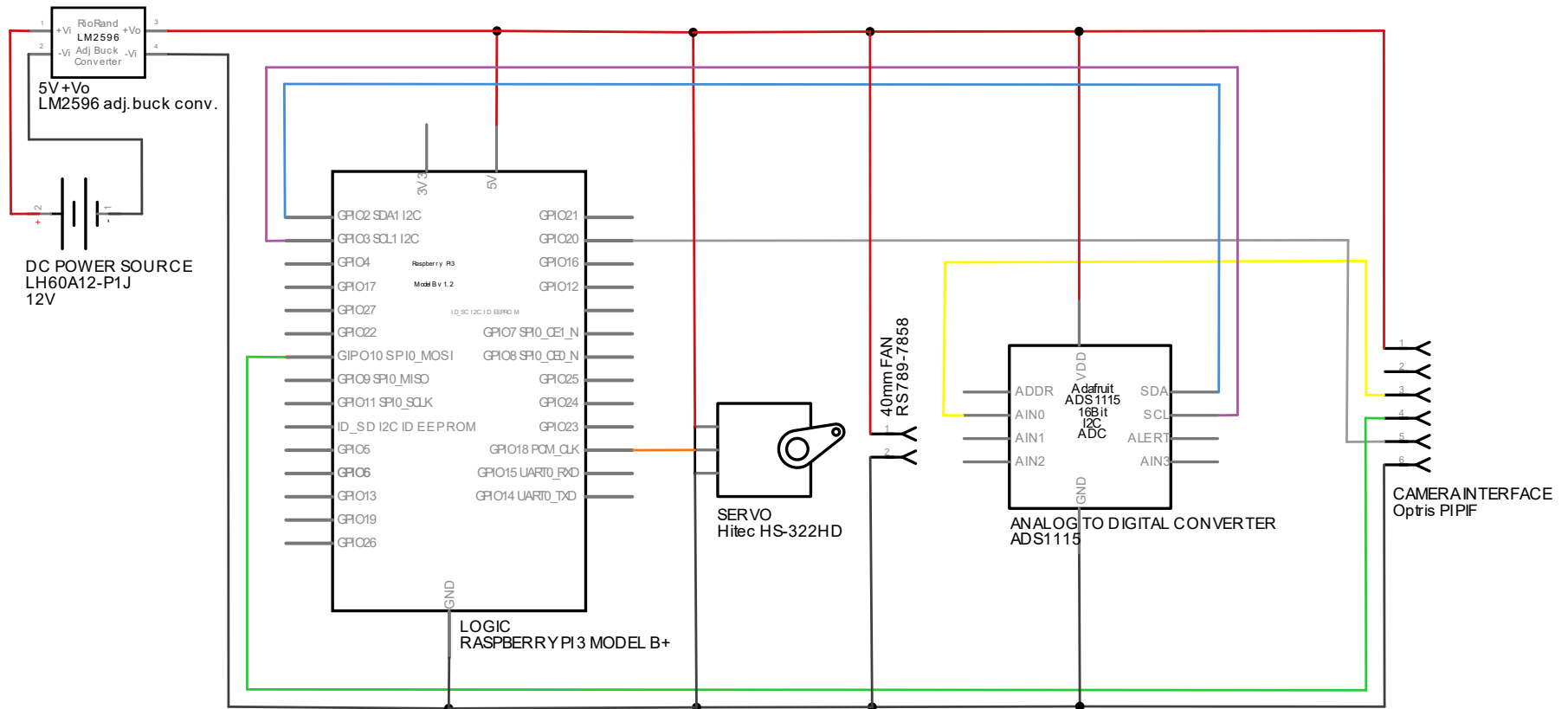


Figure E-4. Component and wiring configuration for Optris PI camera enclosures. Camera process interface (PIF) terminals shown in Table E-1. Raspberry Pi also connected via Cat 5 Ethernet to give an internet connection over a local area network.

## Appendix F: Camera spectral response function

As the spectral response function (SRF) for the cameras is unavailable from the manufacturer except for a generic focal plane array (FPA) detector response function, the full camera response function that includes the FPA and lens is derived (Figure F-1) from laboratory experiments for camera C2 (Table 3-1) from 6 – 14  $\mu\text{m}$  at 0.1  $\mu\text{m}$  resolution using a Bentham TMS300 single monochromator emission source, with reference measurements of the emission source using a Bentham Py-CAL pyroelectric detector. The emission source is sampled by C2 using the camera digital number (DN) output across a 9 x 3 region of pixels that observe the centre of the projected emission source at the monochromator exit slit. The per-pixel DN values were normalised and the median of this was compared to the normalised signal from the Py-CAL detector which has a flat response function across the entire bandwidth. From the two normalised responses of the emission source across the spectral range, the SRF was determined and applied across each pixel of each camera.

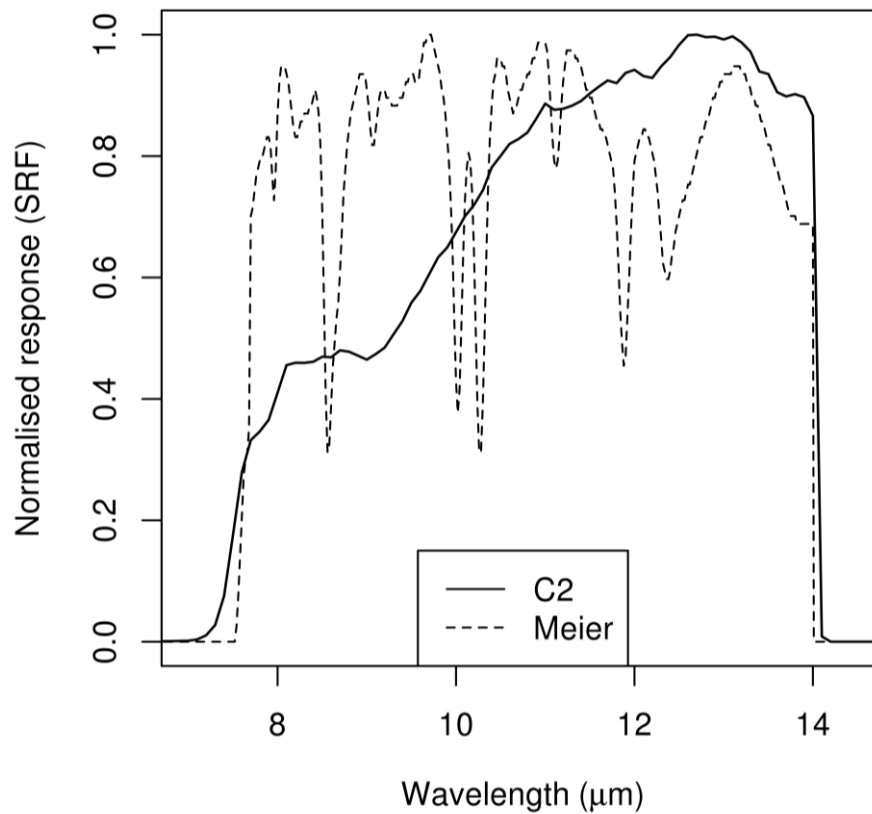


Figure F-1. Spectral response function experimentally derived for camera C2 (solid line) and from the camera used by Meier *et al.*, (2011) (dashed line) (Fred Meier *personal communication* 2018).

## Appendix G: Siting of camera for observational evaluation of atmospheric correction

A longwave infrared camera (C7) was installed at the atmospheric correction evaluation site (“CUB” site, Section 3.4, Figure G-1). The flat asphalt felt roof ( $\sim 600 \text{ m}^2$ ) is surrounded by a low ( $< 2 \text{ m}$ ) metal railing and connected by a metal stairway.

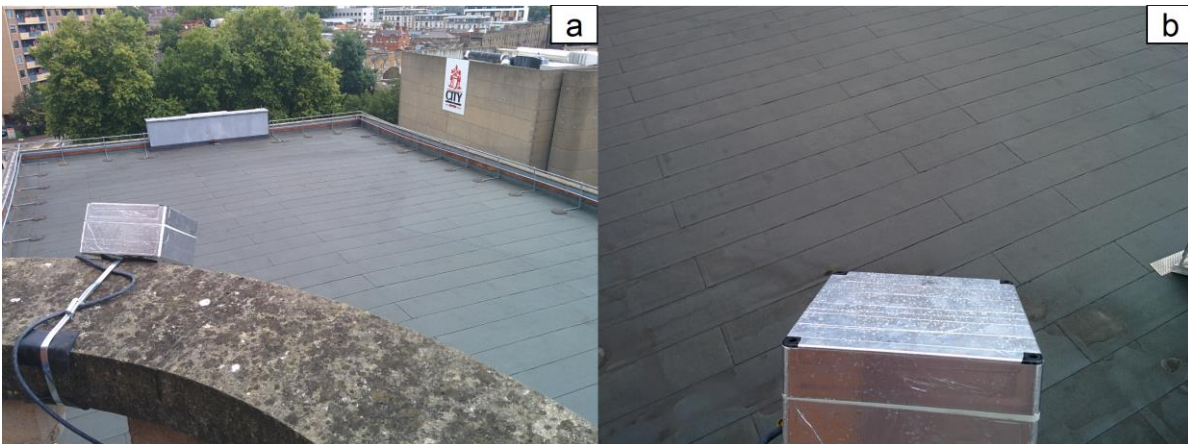


Figure G-1. Enclosed longwave infrared camera (camera C7) installed at the CUB site for atmospheric correction evaluation with its “short” roof-camera path length (a) mounted on a bell tower to the southwest of the target roof. Images taken on 7<sup>th</sup> September 2017.

A bell tower ( $\sim 12 \text{ m}$  taller than the roof) to the southwest of the roof was used to mount the enclosed (Appendix E) camera at  $\sim 6.5 \text{ m}$  above the roof facing northeast and pointing towards the flat roof below. To the east and west of the roof, there are no taller buildings in close proximity ( $\sim 100 \text{ m}$ ), allowing the camera target area in the centre of the roof to be mostly sunlit even during low sun angles around sunrise and sunset.

## Appendix H: Time series images of atmospheric and emissivity correction

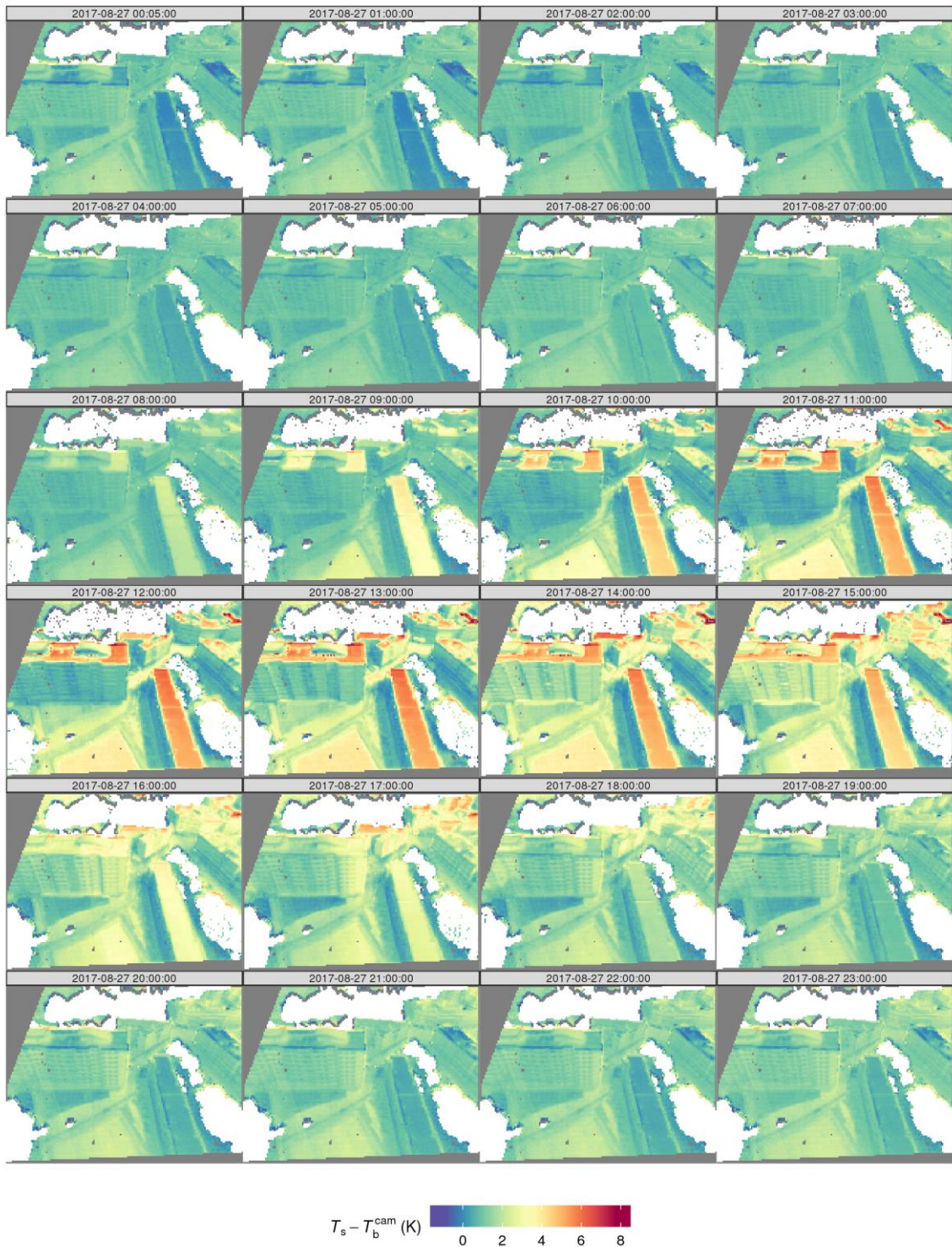


Figure H-1. Difference between at sensor-radiance as brightness temperature ( $T_b^{\text{cam}}$ ) (K) and corrected surface temperature ( $T_s$ ) accounting for atmosphere and emissivity effects for camera C1. Each image is the instantaneous value of  $T_s - T_b^{\text{cam}}$  (K) using emissivity of 0.93 for all non-vegetative surfaces.

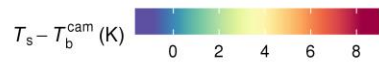
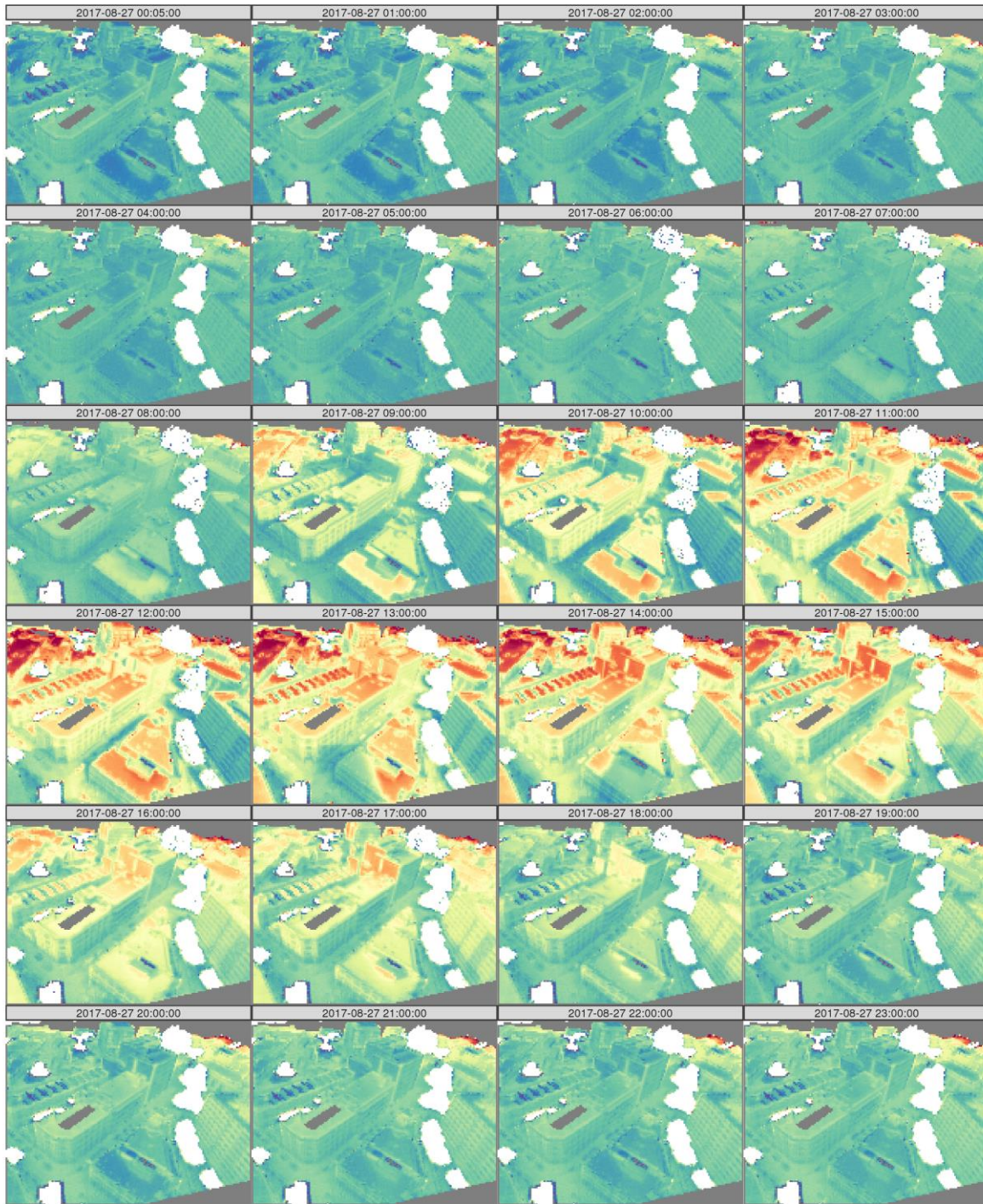


Figure H-2. As Figure H-1 but for C2.

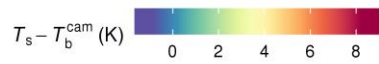
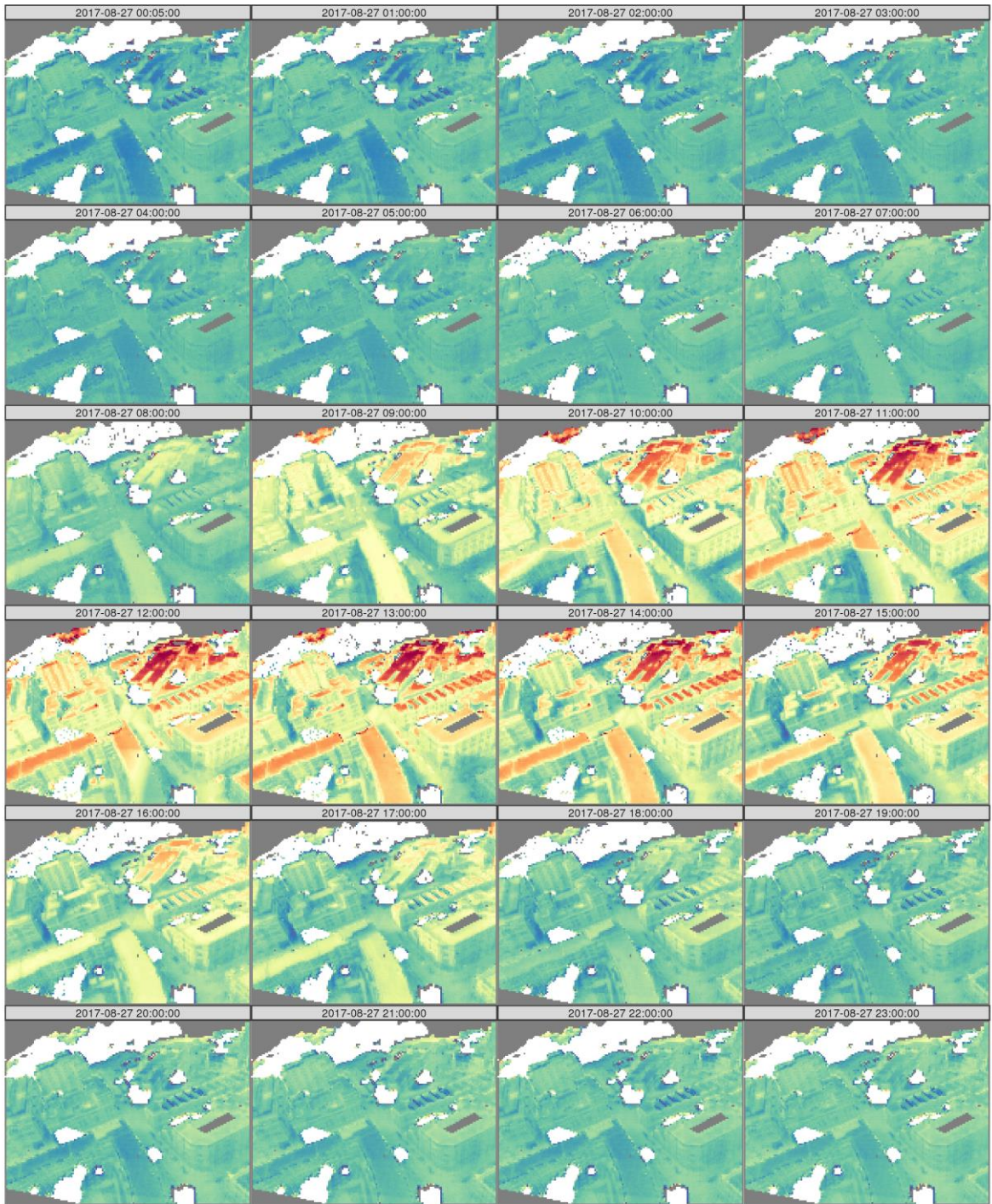


Figure H-3. As Figure H-1 but for C3.

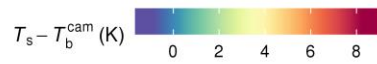
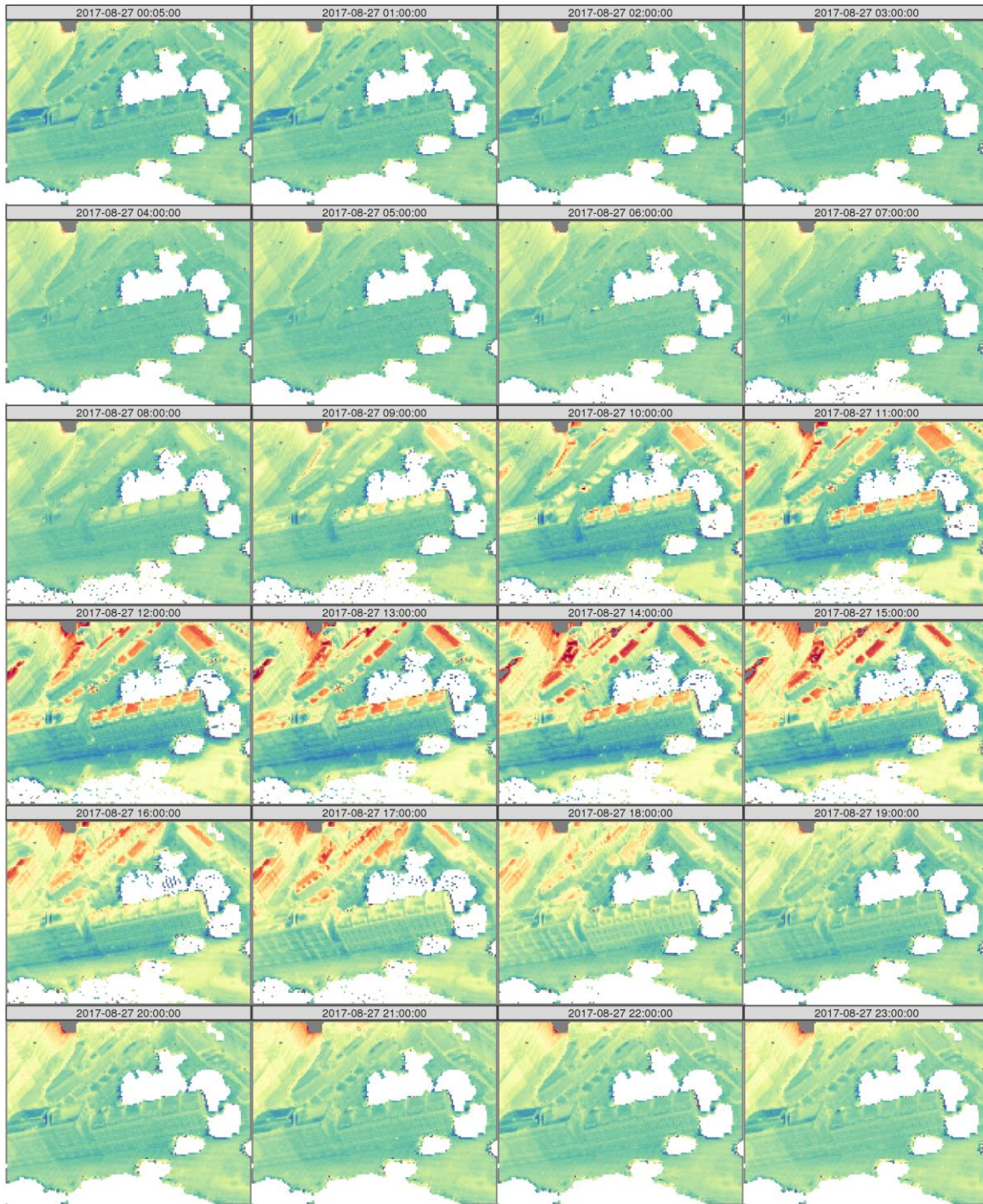


Figure H-4. As Figure H-1 but for C4.

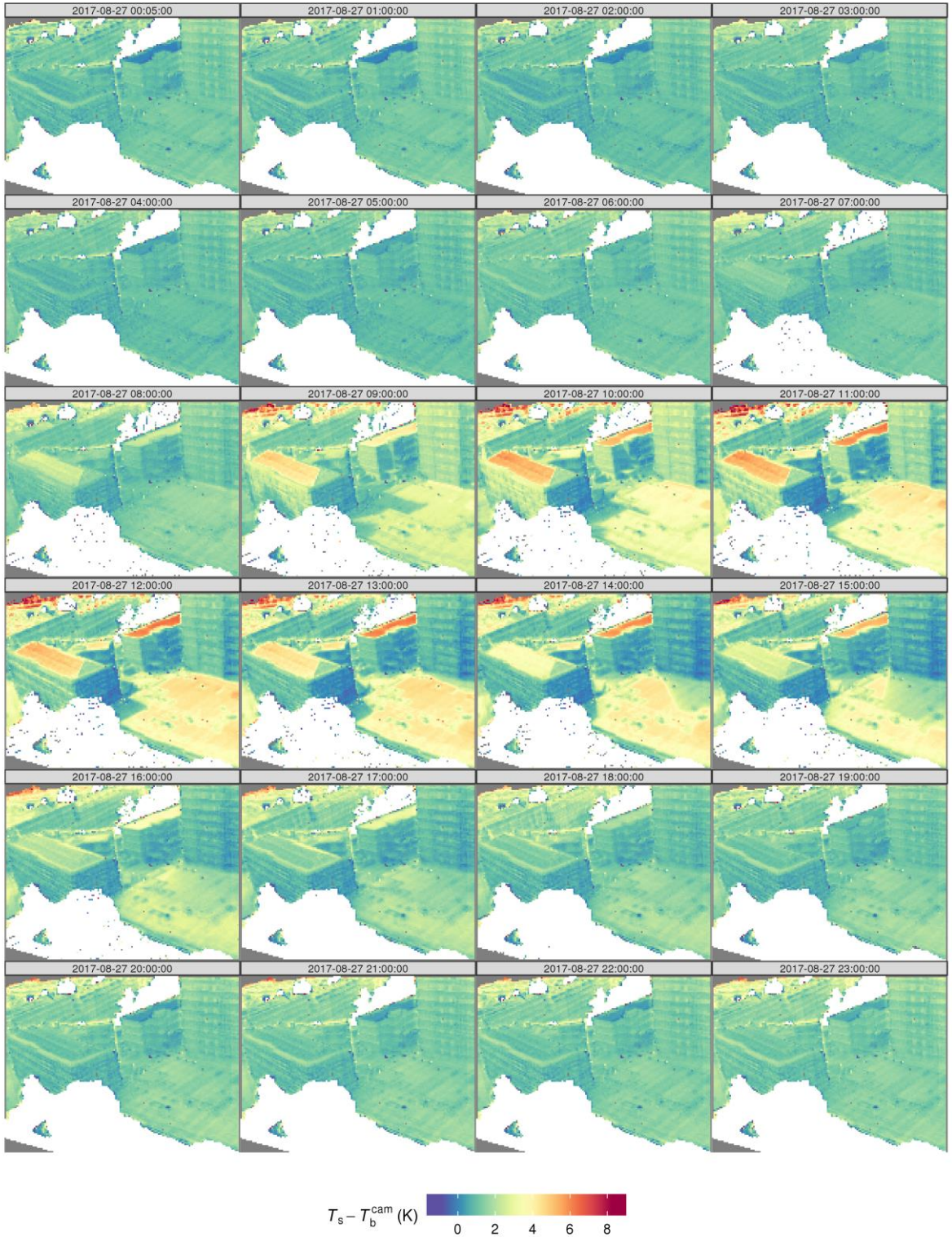


Figure H-5. As Figure H-1 but for C5.

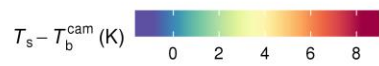
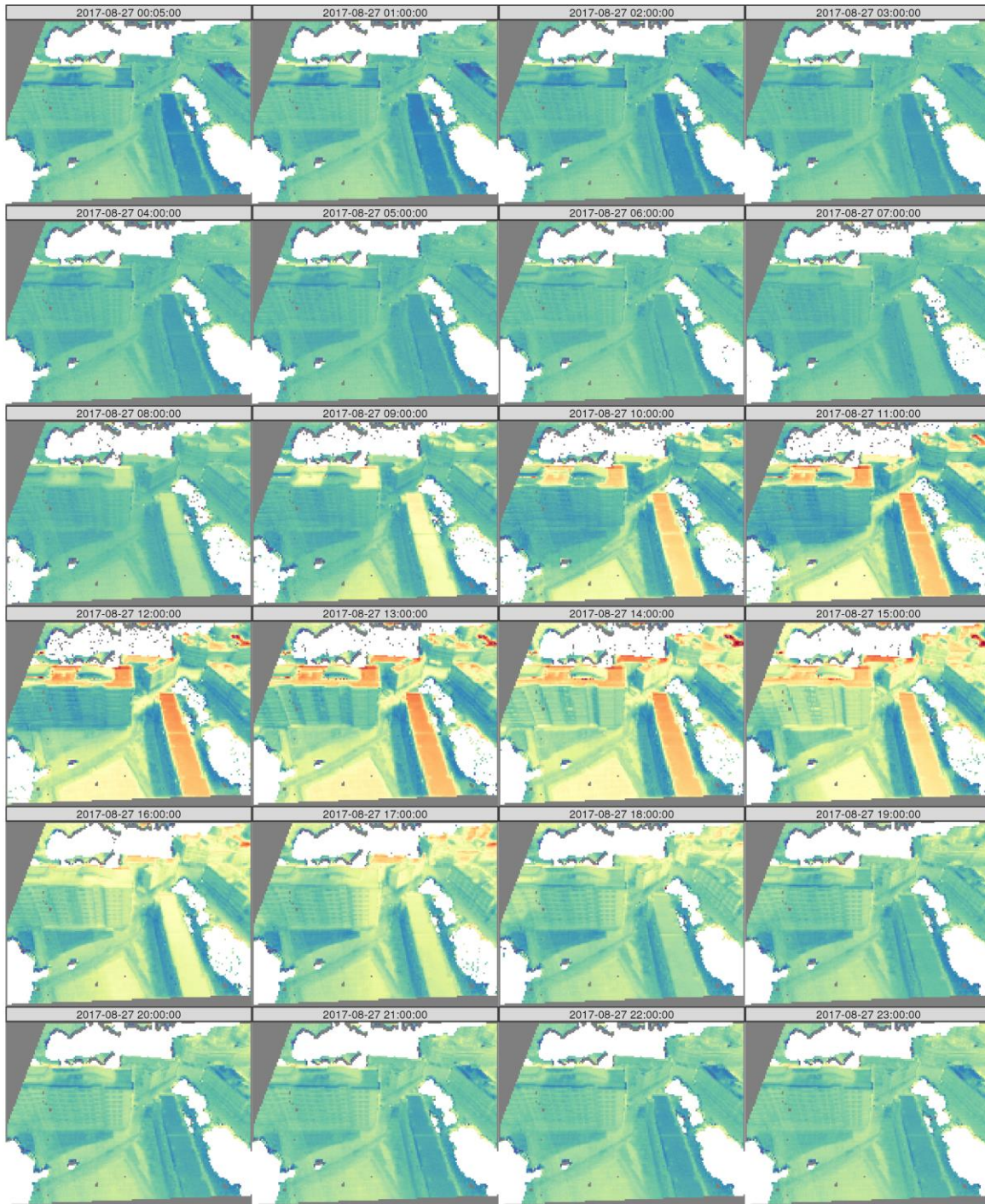


Figure H-6. As Figure H-1 but for C6.

# Appendix I: Statistics for atmospheric correction

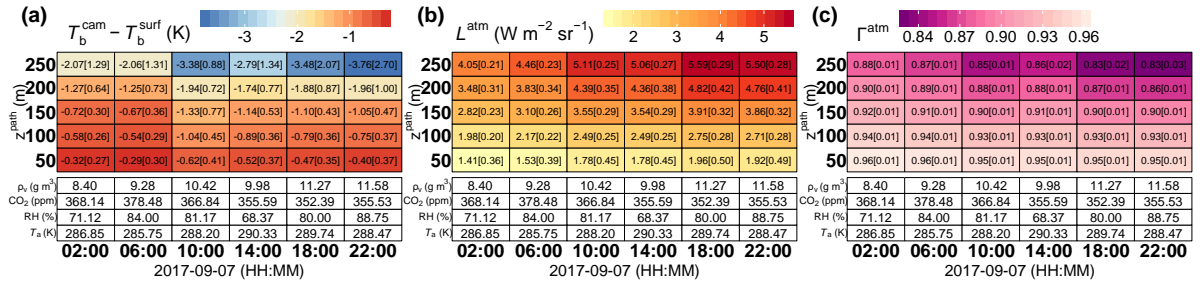


Figure I-1. Atmospheric correction of longwave infrared (LWIR) camera observations for six timesteps on 7<sup>th</sup> September 2017, using pixels within  $\pm 10$  m of five path lengths ( $z^{\text{path}}$ ) with (white cells) meteorological input variables (coloured cells) median[IQR] values of: (a) difference between uncorrected camera brightness temperature ( $T_b^{\text{cam}}$ ) and corrected surface brightness temperature ( $T_b^{\text{surf}}$ ), (b) surface-camera path contribution of the at-sensor band integrated atmosphere radiance ( $L^{\text{atm}}$ ), and (c) surface-camera path contribution of band integrated atmospheric transmissivity ( $\Gamma^{\text{atm}}$ ). See list of symbols and acronyms in Chapter 3 for all other definitions.

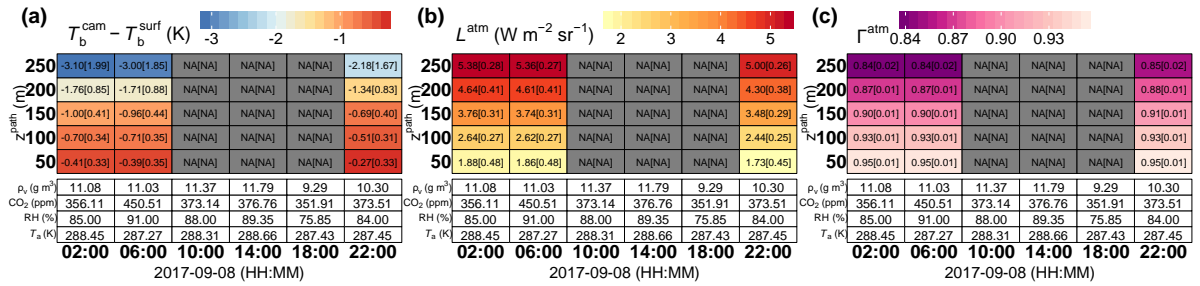


Figure I-2. As Figure I-1 but for 8<sup>th</sup> September.

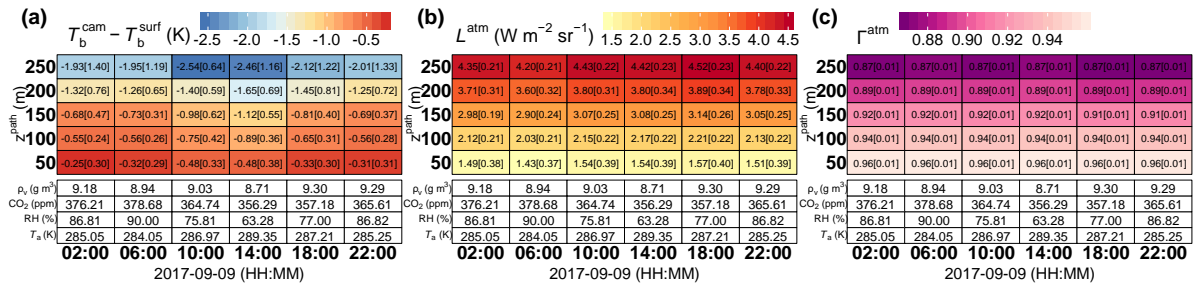


Figure I-3. As Figure I-1 but for 9<sup>th</sup> September.

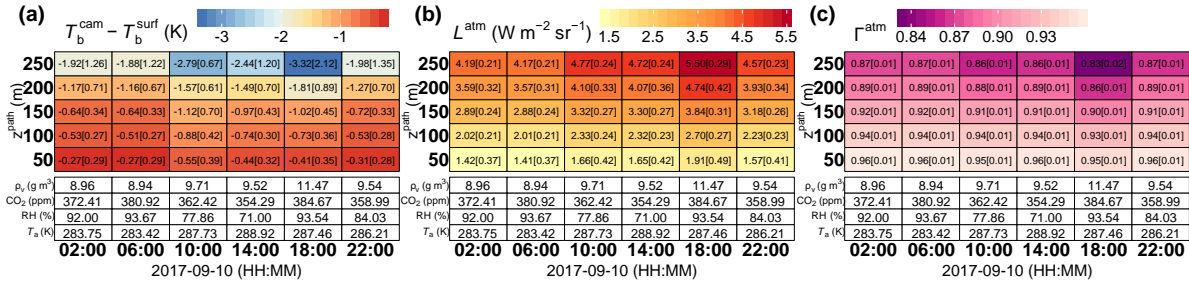


Figure I-4. As Figure I-1 but for 10<sup>th</sup> September.

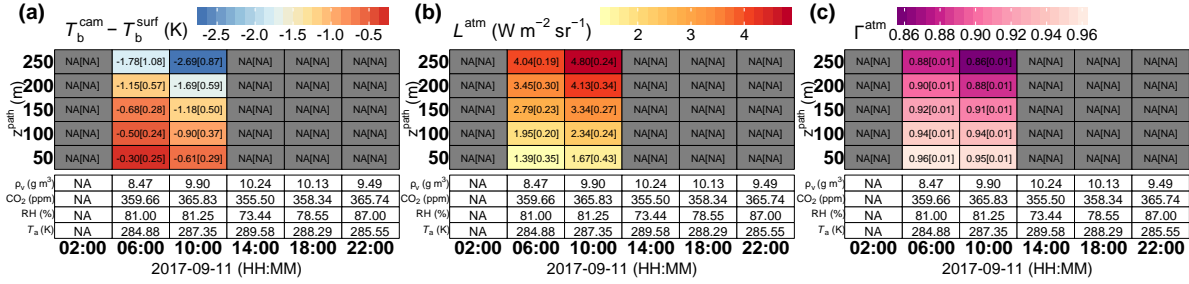


Figure I-5. As Figure I-1 but for 11<sup>th</sup> September.

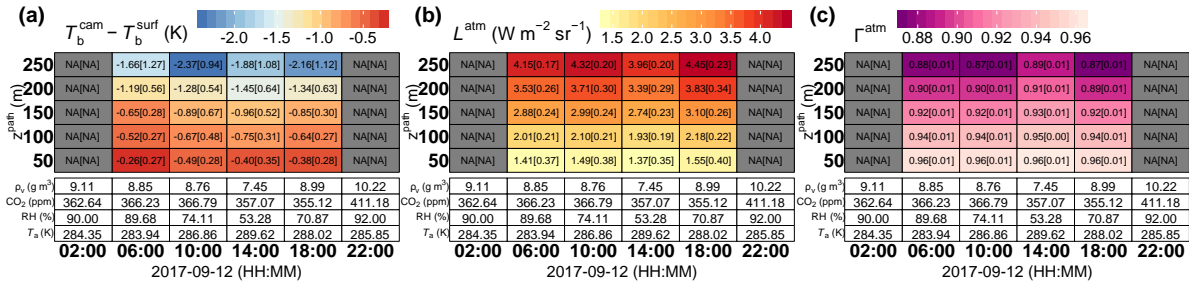


Figure I-6. As Figure I-1 but for 12<sup>th</sup> September.

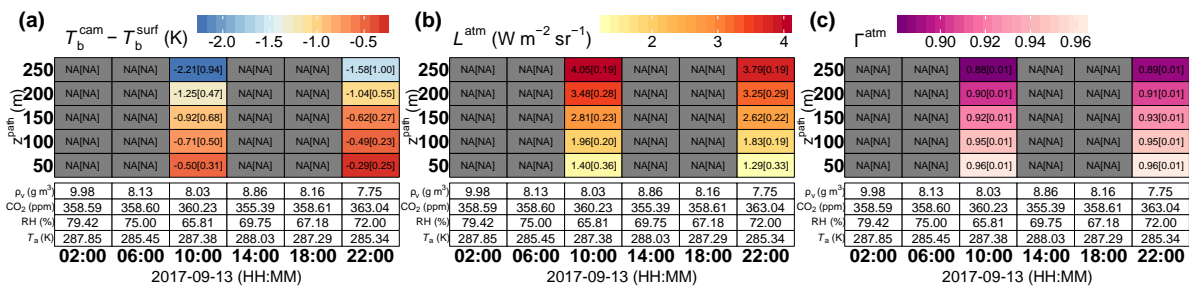


Figure I-7. As Figure I-1 but for 13<sup>th</sup> September.

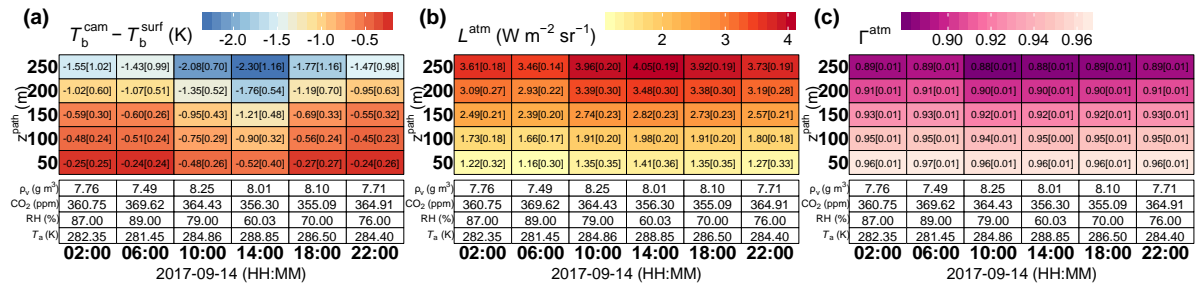


Figure I-8. As Figure I-1 but for 14<sup>th</sup> September.

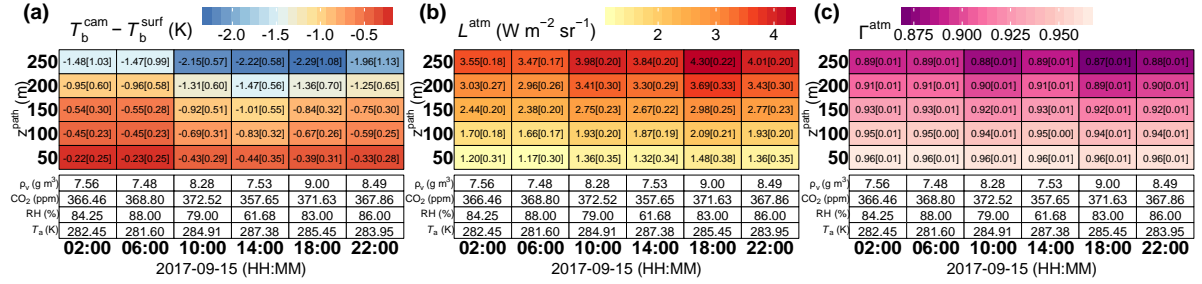


Figure I-9. As Figure I-1 but for 15<sup>th</sup> September.

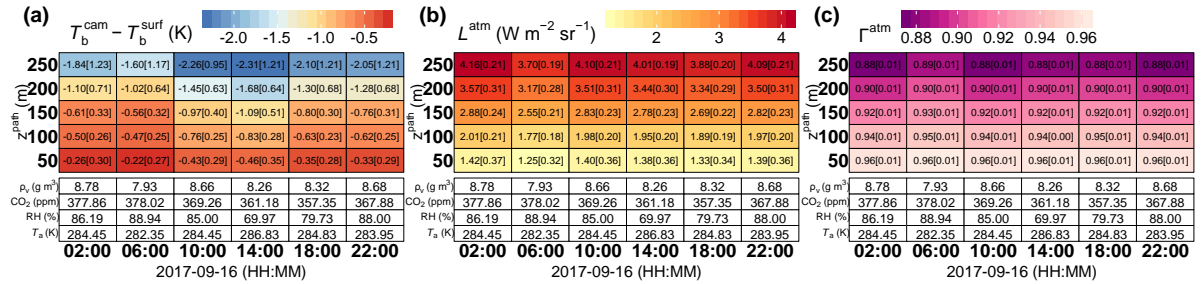


Figure I-10. As Figure I-1 but for 16<sup>th</sup> September.

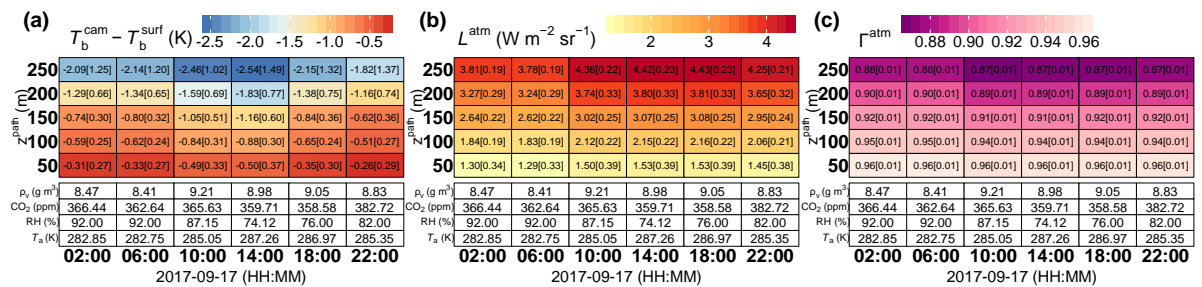


Figure I-11. As Figure I-1 but for 17<sup>th</sup> September.

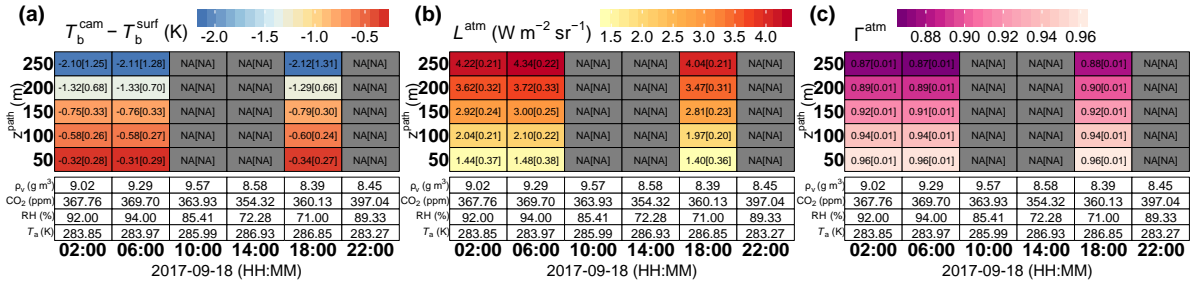


Figure I-12. As Figure I-1 but for 18<sup>th</sup> September.

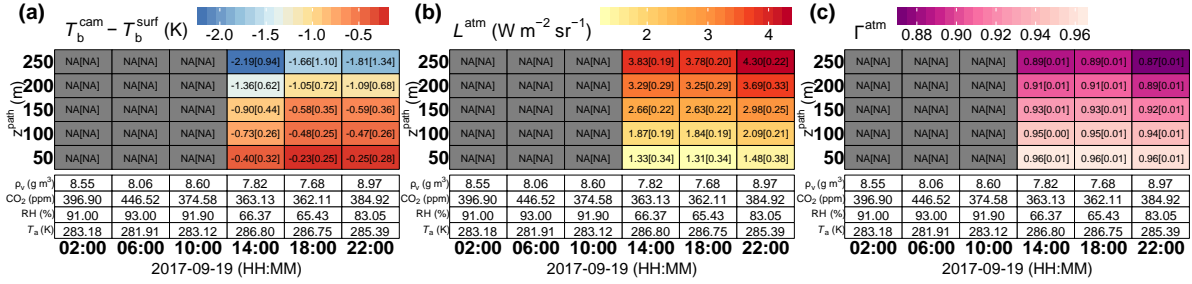


Figure I-13. As Figure I-1 but for 19<sup>th</sup> September.

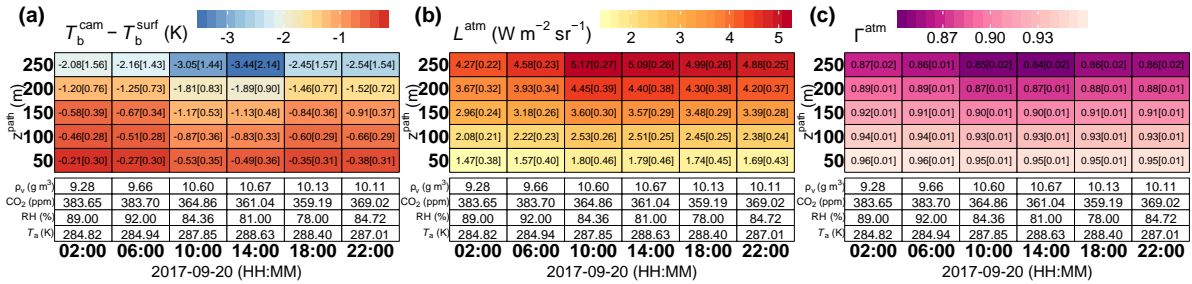


Figure I-14. As Figure I-1 but for 20<sup>th</sup> September.

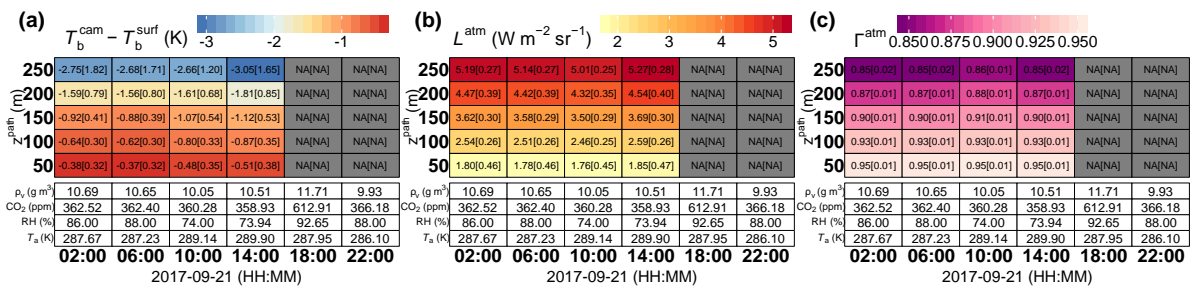


Figure I-15. As Figure I-1 but for 21<sup>st</sup> September.

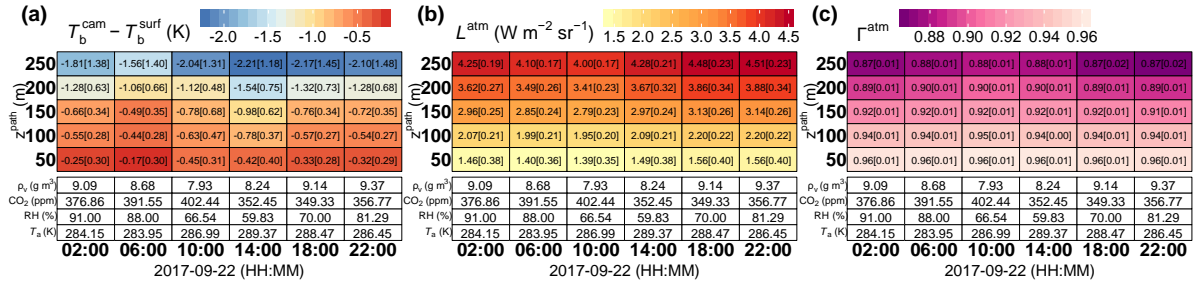


Figure I-16. As Figure I-1 but for 22<sup>nd</sup> September.

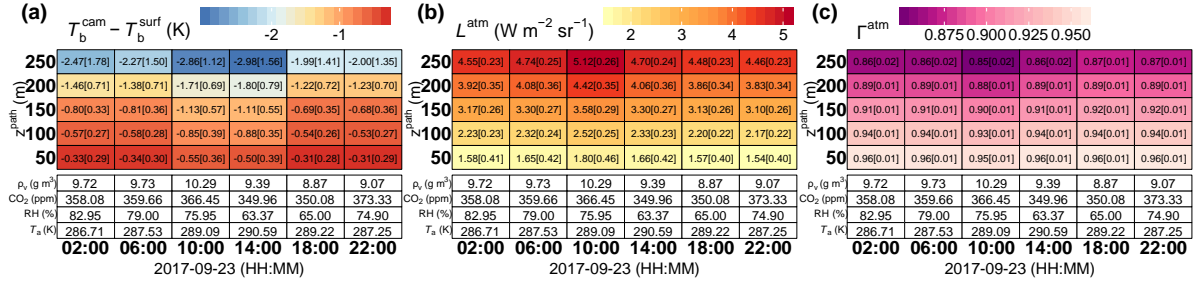


Figure I-17. As Figure I-1 but for 23<sup>rd</sup> September.

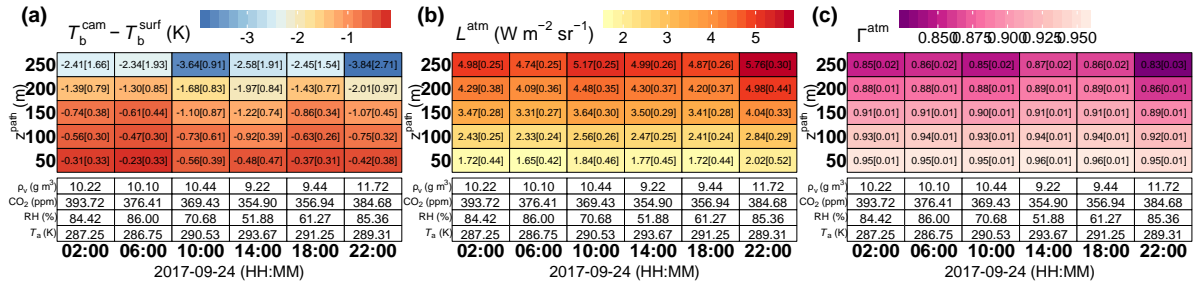


Figure I-18. As Figure I-1 but for 24<sup>th</sup> September.

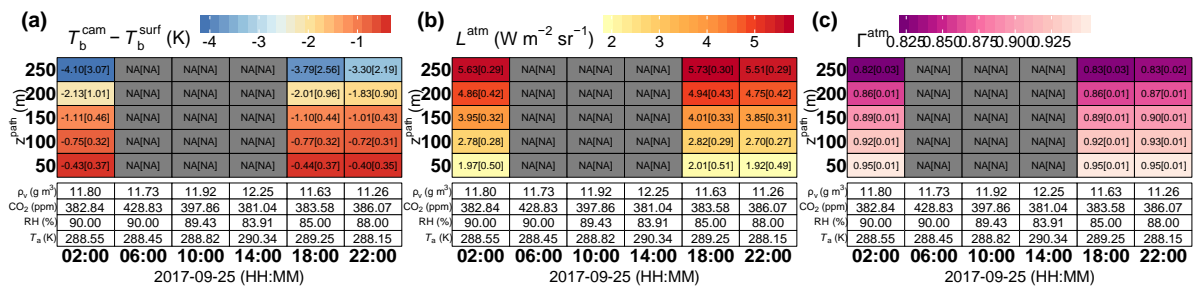


Figure I-19. As Figure I-1 but for 25<sup>th</sup> September.

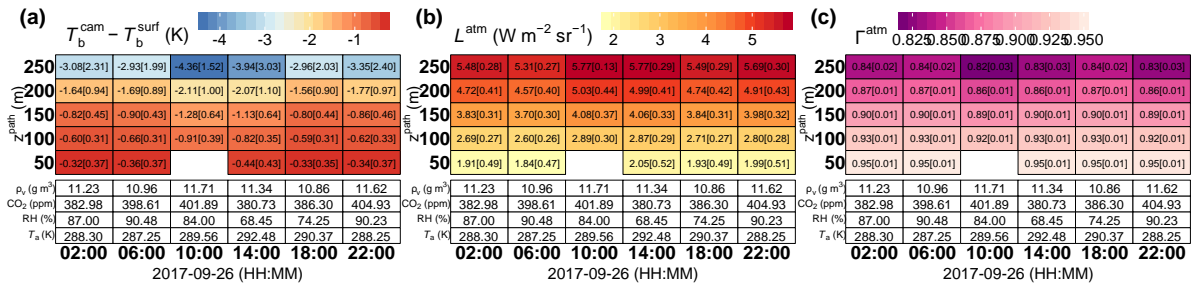


Figure I-20. As Figure I-1 but for 26<sup>th</sup> September.

## Appendix J: Three-dimensional bidirectional reflectance factor from DART

The fraction of scattered radiation (fSR) for each surface voxel [fSR(X, Y, Z, t)] simulated as fSR<sub>DART</sub> by the Discrete Anisotropic Radiative Transfer (DART) model (Gastellu-Etchegorry, Grau and Lauret, 2012) for each observational timestep t is corrected to a 3D bidirectional reflectance factor (BRF). This correction is required because fSR is a DART radiation budget product while BRF is inherently a remote sensing product.

As there can be insufficient density of solar illumination rays compared to the voxel and surface geometry resolution, when the area of a surface element [ $A_{Vx}(X, Y, Z)$ , m<sup>2</sup>] is small, fSR<sub>DART</sub> for the associated voxel can be lower than expected due to insufficient rays of the DART incoming spectral radiant flux [ $E_{\lambda}(\theta, \phi, \Omega, t)$ ] intercepting the surface element. The effect is corrected for by determining  $A_{Vx}$  for “non-shifted” [ $A_{Vx}(X, Y, Z)$ ] and “shifted” [ $A_{Vx}(X', Y', Z)$ ] DSM positions, shown for simple urban geometry in Figure J-1.  $A_{Vx}(X', Y', Z)$  is calculated by moving the DSM horizontally by half the horizontal resolution of the voxels [ $(\Delta X, \Delta Y)/2$ ]. Non-shifted [fSR<sub>DART</sub>(X, Y, Z, t)] and shifted [fSR<sub>DART</sub>(X', Y', Z, t)] cases are then simulated and merged as fSR(X, Y, Z, t) as:

$$fSR(X, Y, Z, t) = \begin{cases} fSR_{DART}(X, Y, Z, t) & \text{if } A_{Vx}(X, Y, Z) > n\Delta X\Delta Y \\ fSR_{DART}(X', Y', Z, t) & \text{if } A_{Vx}(X, Y, Z) \leq n\Delta X\Delta Y \text{ and } A_{Vx}(X', Y', Z) > n\Delta X\Delta Y \\ 0 & \text{otherwise} \end{cases} \quad \text{Eqn. J.1}$$

with  $\Delta X\Delta Y$  the horizontal area of a voxel (m<sup>2</sup>) and  $n$  a threshold factor ( $n = 0.98$ ). Remaining voxels in fSR(X, Y, Z, t) (purple cells, Figure J-1) unable to be filled from fSR<sub>DART</sub>(X, Y, Z, t) or fSR<sub>DART</sub>(X', Y', Z, t) are filled using the average of fSR values within co-planar voxels with fSR(X, Y, Z, t) > 0.

In addition to the correction for ray density, the amount of energy that can be intercepted and subsequently scattered by a voxel is modified by the available surface area  $A_{Vx}$  and requires correction. For a planar surface element with horizontal or vertical alignment with the voxel array,  $A_{Vx}(X, Y, Z)$  is equal to the horizontal model resolution ( $\Delta X\Delta Y$ ). This means fSR(X, Y, Z) is equal to BRF(X, Y, Z) for the voxel that contains these surface elements as the projected area of the surface element is equal to the horizontal surface area considered for  $E_{SW}^{l,dir}(X, Y, Z = \text{top}, t)$  (Eqn. 4.1 in main text).  $A_{Vx}$  is typically larger than  $\Delta X\Delta Y$  for sloped and heterogeneous surface elements and smaller than  $\Delta X\Delta Y$  if the surface element only partially intersects the voxel. The “effective” horizontal surface area of a voxel is therefore calculated as  $A_{Vx}(X, Y, Z) / \Delta X\Delta Y$  and used to approximate BRF(X, Y, Z) by:

$$BRF(X, Y, Z, t) \cong \frac{fSR(X, Y, Z, t)}{A_{Vx}(X, Y, Z) / \Delta X\Delta Y} \quad \text{Eqn. J.2}$$

This approximation is reasonable for surface elements with relatively simple geometry and uniform irradiance (e.g. planar sloped roofs and not building edges, balconies), whereas Lambertian surfaces with complex geometry at scales smaller than the voxel resolution can still have highly anisotropic reflectance. This limitation can be mitigated by using a high-resolution voxel array (e.g.  $\Delta X = \Delta Y = \Delta Z \leq 1$  m used in the thesis) which is still computationally viable. Recent updates in development versions of DART (e.g. 5.7.3 V1079) allow fSR to be stored for each voxel face instead of per-voxel, which was not explored here but has potential to enhance these methods.

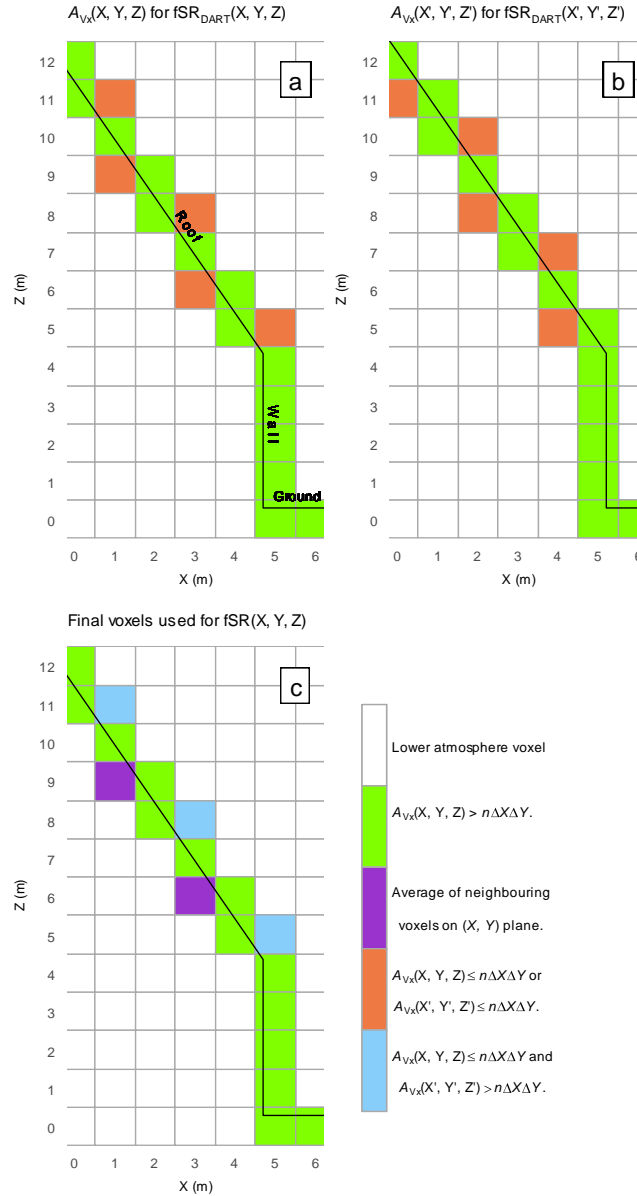


Figure J-1. Procedure for correcting the fraction of scattered radiation simulated by DART ( $fSR_{DART}$ ) using DSM elements (black lines) stored per-voxel and timestep [ $fSR_{DART}(X, Y, Z, t)$ , coloured squares] shown as vertical  $(X, Z)$  cross section of a theoretical sloped roof building that is infinitely long on  $Y$  axis. The voxel-surface intersection is resolved for DSM geometry that is (a) unshifted and (b) shifted by half the horizontal resolution of the voxels [ $(+\Delta X, +\Delta Y)/2$ ]. The area ( $A$ ) of DSM intersecting a voxel ( $A_{Vx}$ ) is calculated. For the unshifted case (a), if  $A_{Vx}(X, Y, Z) \leq n\Delta X\Delta Y$  (orange),  $fSR_{DART}(X, Y, Z)$  can be poorly resolved and is replaced using the corresponding voxel from (b) [i.e.  $fSR_{DART}(X', Y', Z, t)$ , Eqn. J.2] and used as a surface voxel in the corrected product ( $fSR(X, Y, Z, t)$ , blue voxels, c). Remaining voxels where  $A_{Vx}(X, Y, Z) \leq n\Delta X\Delta Y$  in (a) and  $A_{Vx}(X', Y', Z) \leq n\Delta X\Delta Y$  in (b) are filled using the average fSR from neighbouring horizontal voxels (purple, c).

## Appendix K: Details of DART longwave infrared simulation

The Discrete Anisotropic Radiative Transfer (DART) model (Gastellu-Etchegorry, Grau and Lauret, 2012) is used to simulate the radiative transfer (RT) processes associated with longwave infrared (LWIR) emission and multiple scattering from complex surfaces to correct a series of LWIR cameras for emissivity effects and also simulate effective thermal anisotropy. This appendix details the RT process for the “model world” (MW) in central London (Chapter 3, Chapter 4) which extends across a London study area observed by the cameras and is modelled for the camera perspectives.

Across the MW surfaces, emitted rays are tracked across 628 discrete directions ( $\Omega$ ) over the  $4\pi$  space with equal solid angle ( $\Delta\Omega \approx 0.02$  sr). Under a state of thermodynamic equilibrium all rays are emitted and tracked to other surfaces where energy from the is scattered based on the surface reflectance ( $1 - \epsilon$ ). Scattering is repeated for up to 5 iterations, with a threshold for stopping rays scattered with a very small intensity. Rays exiting any MW vertical side re-enter on the opposite side with the same direction but with a height adjusted by any topographic differences in the built surface and underlying ground between the exit and re-entry points.

The approach to simulate the effective thermal anisotropy (Section 4.3.3) is validated using a simple surface temperature configuration. Any radiance that leaves the side of the MW area is cycled to the opposite MW area edge to the cross the bottom of atmosphere (BOA) layer (Figure 4-2) at a point outside the MW extent. For off-nadir radiances, this process produces gaps around the inside space of buildings that are at the MW edge (Figure 4-13, white), where the buildings obstruct the rays that would otherwise exiting the MW sides. It is anticipated that the effect does not impact the simulated directional spectral radiance [ $L_{\lambda}^{\text{surf}}(\phi, \theta, \Omega)$ ] and is validated using a DART simulation with black-body surfaces, homogeneous  $T_s$  (300 K) and no vegetation canopy elements (VCE). Area-integrated results have maximum directional brightness temperature at nadir (300.05 K) and a 299.97 K median (standard deviation 0.02 K, mean absolute error 0.03 K) and minimum (299.9 K). Theoretically, the directional radiance is isothermal with a 300 K equivalent  $T_b$ . Errors likely result from a small number of lost rays at the edge of the scene, and also across the entire scene where the resolution of DART voxels and sub-voxels is too coarse for some areas of very complex sub-meter scale geometry.

## Appendix L: Meteorological conditions for 26<sup>th</sup> – 27<sup>th</sup> August 2017

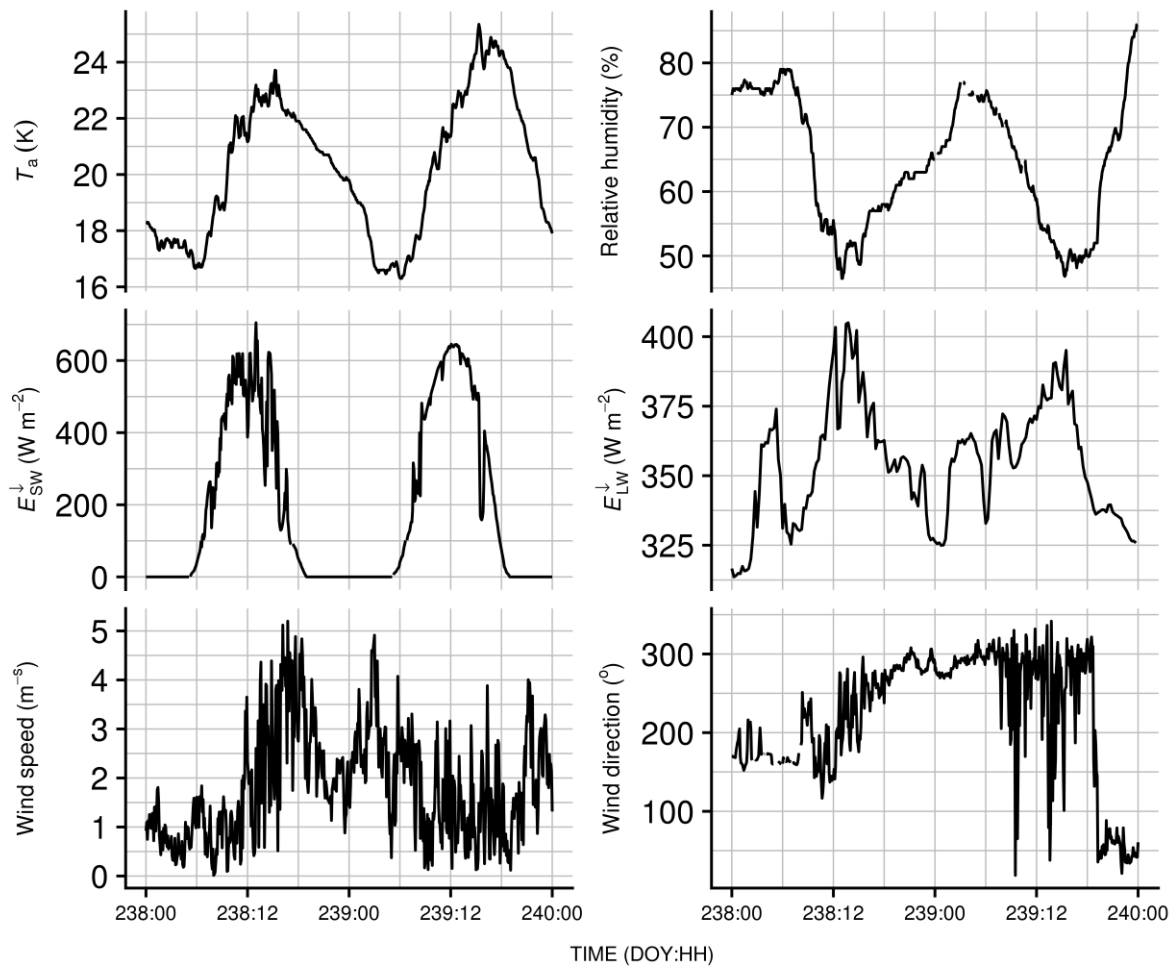


Figure L-1. Meteorological observations prior and on 27<sup>th</sup> August 2017 (day of year - DOY - 239). A Davis Vantage Pro 2 weather station located  $\sim 1$  km southeast of the study area (114 m above ground level) measured ( $T_a$ ) air temperature, relative humidity, wind speed and direction. A Kipp and Zonen CNR1 net radiometer at the IMU site (Section 4.2.1) measured ( $E_{SW}^{\downarrow}$ ) broadband incoming shortwave ( $W m^{-2}$ ) and ( $E_{LW}^{\downarrow}$ ) broadband incoming longwave radiation fluxes. Last recorded rain was  $11.8 \text{ mm h}^{-1}$  on 22<sup>nd</sup> August 2017 at 22:45.

## Appendix M: Time series and per-pixel classification of observations

The fraction of surface properties of orientation and material  $[\Sigma(x, y)]$  seen by each camera pixel are well sampled except for  $\Sigma_{\text{Down}}$  and  $\Sigma_{\text{Roof[light]}}$  (Figure M-1). Multiple factors determine the inter-camera differences in the fraction of  $\Sigma(x, y)$  sampled. As expected, the camera view angles determine the surface orientations seen (e.g. west facing cameras (C5, C6) view east facing surfaces that become sunlit after 06:00 and shaded after 12:10) (Figure M-1, orange). For non-mixed and masked values of  $\Sigma$ ,  $\Sigma_{\text{Roof[dark]}}$  ( $\Sigma_{\text{Roof[light]}}$ ) is the most (least) well sampled with maximum 14 % (0.9 %) of pixels across all cameras. Light roofs are generally rare in the study area (Figure 4-3). 36.6 % (32.9 %) of pixels are  $\Sigma_{\text{Mixed}}$  during daytime (nighttime).

The absence of  $\Sigma_{\text{Down}}$  pixels is because of the downward facing view angle of all cameras. C2 and C3 images contain the highest proportion of mixed pixels (42.8 % and 44.5 %) as these observations have longer path lengths, increasing pixel IFOV and the likelihood of viewing multiple surface properties therein.

C2 and C3 view more surfaces outside the MW area. Mixed pixels within images (Figure 4-5b) are associated with complex surface geometry at sub-pixel resolution (e.g. east wall in C6, south wall in centre of C2, roof at top right of C1; corresponding to balconies, sun-shades and an irregular shaped roof, respectively). More mixed pixels are present during daytime from an “isolated pixel” filter for  $\text{BRF}(x, y)$  (Section 4.2.2.3).

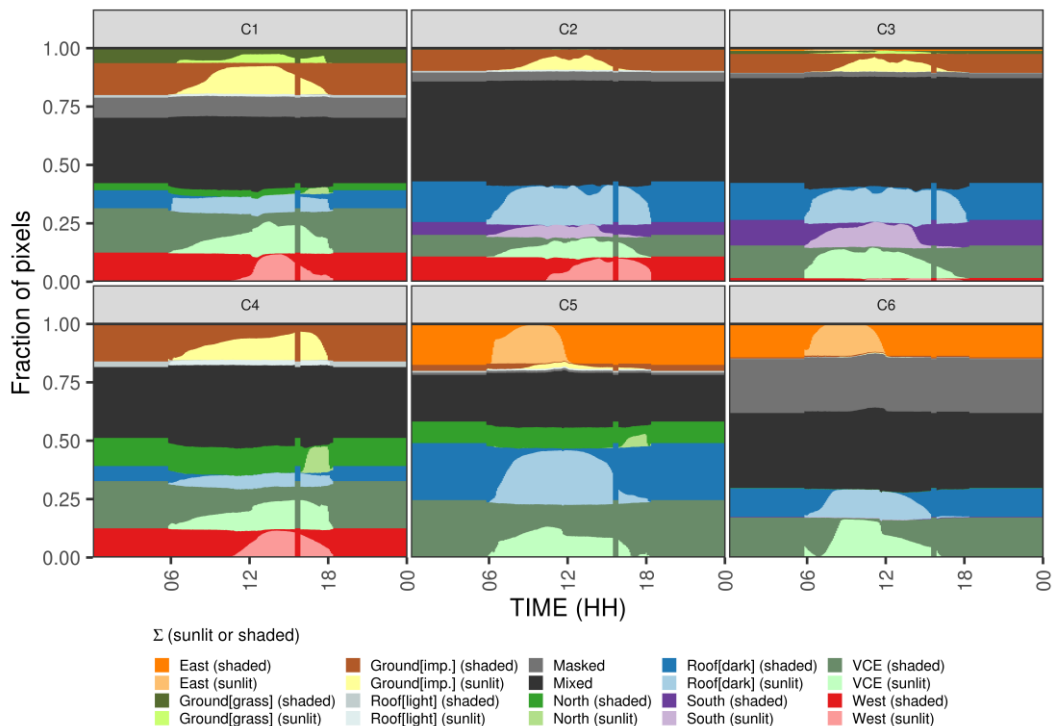


Figure M-1. Fraction of all pixels (19200) in a camera (C#) image that are assigned an orientation and material surface property ( $\Sigma$ ) and sun status during the case study day in central London (27<sup>th</sup> August 2017) at 5 min temporal resolution. Interval of daytime shadow (~15:30) is from an overcast period. Mixed pixels contain multiple  $\Sigma$  values or are isolated pixels (Section 4.2.2.3). See Section 4.2.1 for overview of study area and instrumentation.

## Appendix N: Surface temperature variability by shortwave irradiance – extended

More complete per-pixel  $T_s$  observations with surface properties of orientation and material [ $\Sigma(x, y)$ ] to the sun-surface geometry of surfaces (bidirectional reflectance factor, BRF) are provided in Figure N-1.

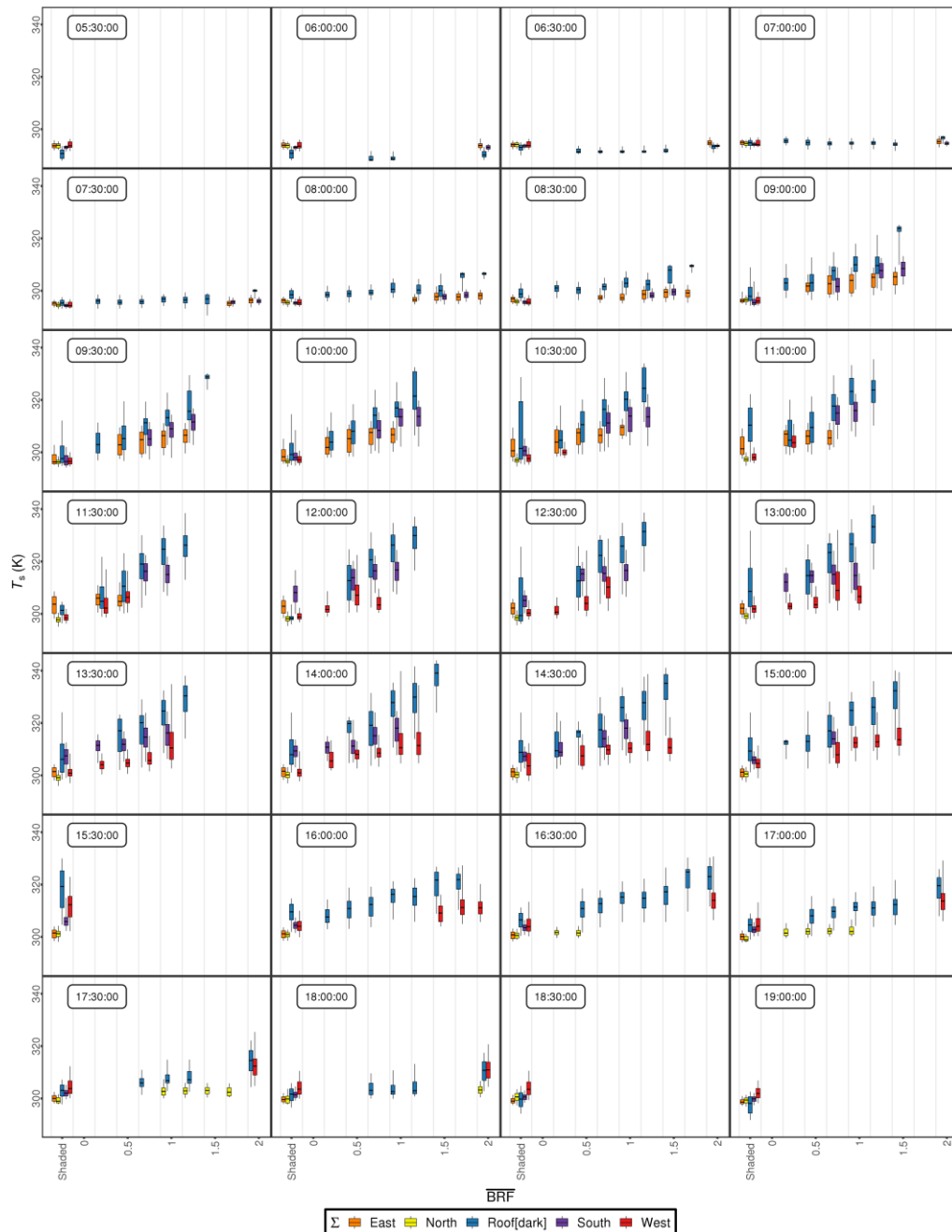


Figure N-1. Longwave infrared camera derived surface temperature ( $T_s$ ) for 28 timesteps (sub-plots) on 27<sup>th</sup> August 2017 grouped by surface properties (colour) of orientation and material ( $\Sigma$ ) and incoming shortwave radiation (bidirectional reflectance factor, BRF) with BRF = 1 equivalent to irradiance for a flat surface for any daytime sun angle. BRF binned ( $\overline{BRF}$ ) by 0.25 bin widths with shaded values ( $BRF \approx 0$ ) binned as -1. BRF determined using the Discrete Anisotropic Radiative Transfer (DART) model. Boxplots excluded if number of pixels < 50. Ground and Roof[light] excluded from analysis as most surfaces have  $BRF \approx 1$ . Boxplots include median (horizontal line), interquartile range (box), and 5 and 95 percentiles (whiskers).

## References

- Adderley, C., Christen, A. and Voogt, J. A. (2015) 'The effect of radiometer placement and view on inferred directional and hemispheric radiometric temperatures of an urban canopy', *Atmospheric Measurement Techniques*, 8(7), pp. 2699–2714. doi: 10.5194/amt-8-2699-2015.
- Agisoft LLC (2013) *Agisoft PhotoScan Professional*, <http://www.agisoft.ru/products/photoscan/professional/>. Available at: <http://www.agisoft.ru/products/photoscan/professional/> (Accessed: 23 March 2017).
- Aoyagi, T. and Takahashi, S. (2012) 'Development of an Urban Multilayer Radiation Scheme and Its Application to the Urban Surface Warming Potential', *Boundary-Layer Meteorology*, 142(2), pp. 305–328. doi: 10.1007/s10546-011-9679-0.
- Arnfield, A. J. (1982) 'An approach to the estimation of the surface radiative properties and radiation budgets of cities', *Physical Geography*, 3(2), pp. 97–122. doi: 10.1080/02723646.1982.10642221.
- Baklanov, A. *et al.* (2018) 'From urban meteorology, climate and environment research to integrated city services', *Urban Climate*. Elsevier B.V., 23, pp. 330–341. doi: 10.1016/j.uclim.2017.05.004.
- Balaras, C. A. and Argiriou, A. A. (2002) 'Infrared thermography for building diagnostics', *Energy and Buildings*, 34(2), pp. 171–183. doi: 10.1016/S0378-7788(01)00105-0.
- Barata, M. *et al.* (2011) 'Climate change and human health in cities', in *Climate Change and Cities: First Assessment Report of the Urban Climate Change Research Network*. Cambridge, UK: Cambridge University Press, pp. 179–213.
- Becker, F. and Zhao-Liang Li (1995) 'Surface temperature and emissivity at various scales: definition, measurement and related problems', *Remote Sensing Reviews*, 12(3–4), pp. 225–253. doi: 10.1080/02757259509532286.
- Biljecki, F. *et al.* (2015) 'Applications of 3D City Models: State of the Art Review', *ISPRS International Journal of Geo-Information*, 4(4), pp. 2842–2889. doi: 10.3390/ijgi4042842.
- Biljecki, F., Ledoux, H. and Stoter, J. (2017) 'Does a Finer Level of Detail of a 3D City Model Bring an Improvement for Estimating Shadows?', in van Oosterom, P. *et al.* (eds). Berlin, Heidelberg: Springer Berlin Heidelberg (Lecture Notes in Geoinformation and Cartography), pp. 31–47. doi: 10.1007/978-3-319-25691-7\_2.
- Blender (2018) 'Blender 2.79b'. Blender Institute, Amsterdam. Available at: <https://www.blender.org/>.
- Bouguet, J.-Y. (2008) *Camera calibration toolbox for matlab*, [http://www.vision.caltech.edu/bouguetj/calib\\_doc](http://www.vision.caltech.edu/bouguetj/calib_doc). doi: citeulike-article-id:7121849.
- Budzier, H. and Gerlach, G. (2015) 'Calibration of uncooled thermal infrared cameras', *Journal of Sensors and Sensor Systems*, 4(1), pp. 187–197. doi: 10.5194/jsss-4-187-2015.
- Bueno, B. *et al.* (2012) 'Development and evaluation of a building energy model integrated in the TEB scheme', *Geoscientific Model Development*, 5(2), pp. 433–448. doi: 10.5194/gmd-5-433-2012.
- Busetto, L. and Ranghetti, L. (2016) 'MODISstsp: an R package for preprocessing of MODIS Land Products time series', *Computers & Geosciences*, 97, pp. 40–48. doi: 10.1016/j.cageo.2016.08.020.
- Chen, F. *et al.* (2016) 'Effect of emissivity uncertainty on surface temperature retrieval over urban areas: Investigations based on spectral libraries', *ISPRS Journal of Photogrammetry and Remote Sensing*, 114, pp. 53–65. doi: 10.1016/j.isprsjprs.2016.01.007.
- Christen, A., Meier, F. and Scherer, D. (2012) 'High-frequency fluctuations of surface temperatures

in an urban environment', *Theoretical and Applied Climatology*, 108(1–2), pp. 301–324. doi: 10.1007/s00704-011-0521-x.

- Christen, A. and Vogt, R. (2004) 'Energy and radiation balance of a central European City', *International Journal of Climatology*, 24(11), pp. 1395–1421. doi: 10.1002/joc.1074.
- Chrysoulakis, N. *et al.* (2018) 'Urban energy exchanges monitoring from space', *Scientific Reports*, 8(1), p. 11498. doi: 10.1038/s41598-018-29873-x.
- Clarke, T. A., Wang, X. and Fryer, J. G. (1998) 'The principal point and CCD cameras', *Photogrammetric Record*, 16(92), pp. 293–312. doi: 10.1111/0031-868X.00127.
- Clinton, N. and Gong, P. (2013) 'MODIS detected surface urban heat islands and sinks: Global locations and controls', *Remote Sensing of Environment*. Elsevier Inc., 134, pp. 294–304. doi: 10.1016/j.rse.2013.03.008.
- Costanzo, V., Evola, G. and Marletta, L. (2016) 'Energy savings in buildings or UHI mitigation? Comparison between green roofs and cool roofs', *Energy and Buildings*. Elsevier B.V., 114, pp. 247–255. doi: 10.1016/j.enbuild.2015.04.053.
- Crawford, B. *et al.* (2017) 'Spatial and temporal patterns of surface–atmosphere energy exchange in a dense urban environment using scintillometry', *Quarterly Journal of the Royal Meteorological Society*, 143(703), pp. 817–833. doi: 10.1002/qj.2967.
- Crawford, B. *et al.* (2018) 'Variability of urban surface temperatures and implications for aerodynamic energy exchange in unstable conditions', *Quarterly Journal of the Royal Meteorological Society*, 144(715), pp. 1719–1741. doi: 10.1002/qj.3325.
- Doninck, J. Van (2018) 'horizon: Horizon Search Algorithm'. Available at: <https://cran.r-project.org/package=horizon>.
- Dousset, B. and Gourmelon, F. (2003) 'Satellite multi-sensor data analysis of urban surface temperatures and landcover', *ISPRS Journal of Photogrammetry and Remote Sensing*, 58(1–2), pp. 43–54. doi: 10.1016/S0924-2716(03)00016-9.
- Dozier, J. and Frew, J. (2002) 'Rapid calculation of terrain parameters for radiation modeling from digital elevation data', *IEEE Transactions on Geoscience and Remote Sensing*. IEEE, 28(5), pp. 963–969. doi: 10.1109/36.58986.
- Duan, S. B. *et al.* (2019) 'Validation of Collection 6 MODIS land surface temperature product using in situ measurements', *Remote Sensing of Environment*. Elsevier, 225(March), pp. 16–29. doi: 10.1016/j.rse.2019.02.020.
- Dyce, D. R. and Voogt, J. A. (2018) 'The influence of tree crowns on urban thermal effective anisotropy', *Urban Climate*. Elsevier B.V., 23, pp. 91–113. doi: 10.1016/j.uclim.2017.02.006.
- Emig, T. (2017) 'Temperature distribution and heat radiation of patterned surfaces at short wavelengths', *Physical Review E*, 95(5), pp. 1–8. doi: 10.1103/PhysRevE.95.052104.
- Evans, S., Hudson-Smith, A. and Batty, M. (2011) '3-D GIS: Virtual London and beyond', *Cybergeo*. doi: 10.4000/cybergeo.2871.
- Gabey, A. M., Grimmond, C. S. B. and Capel-Timms, I. (2019) 'Anthropogenic heat flux: advisable spatial resolutions when input data are scarce', *Theoretical and Applied Climatology*. Theoretical and Applied Climatology, 135(1–2), pp. 791–807. doi: 10.1007/s00704-018-2367-y.
- Gastellu-Etchegorry, J. P. (2008) '3D modeling of satellite spectral images, radiation budget and energy budget of urban landscapes', *Meteorology and Atmospheric Physics*, 102(3–4), pp. 187–207. doi: 10.1007/s00703-008-0344-1.
- Gastellu-Etchegorry, J. P. *et al.* (2015) 'Discrete anisotropic radiative transfer (DART 5) for modeling airborne and satellite spectroradiometer and LIDAR acquisitions of natural and urban landscapes', *Remote Sensing*, 7(2), pp. 1667–1701. doi: 10.3390/rs70201667.

- Gastellu-Etchegorry, J. P. *et al.* (2017) ‘DART: Recent advances in remote sensing data modeling with atmosphere, polarization, and chlorophyll fluorescence’, *IEEE Journal of Selected Topics in Applied Earth Observations and Remote Sensing*, 10(6), pp. 2640–2649. doi: 10.1109/JSTARS.2017.2685528.
- Gastellu-Etchegorry, J. P., Grau, E. and Lauret, N. (2012) ‘DART: A 3D Model for Remote Sensing Images and Radiative Budget of Earth Surfaces’, in *Modeling and Simulation in Engineering*. InTech. doi: 10.5772/31315.
- Ghandehari, M., Emig, T. and Aghamohamadnia, M. (2018) ‘Surface temperatures in New York City: Geospatial data enables the accurate prediction of radiative heat transfer’, *Scientific Reports*. Springer US, 8(1), pp. 1–10. doi: 10.1038/s41598-018-19846-5.
- Ghent, D. *et al.* (2010) ‘Assimilation of land surface temperature into the land surface model JULES with an ensemble Kalman filter’, *Journal of Geophysical Research Atmospheres*, 115(19), pp. 1–16. doi: 10.1029/2010JD014392.
- Gong, F. Y. *et al.* (2018) ‘Mapping sky, tree, and building view factors of street canyons in a high-density urban environment’, *Building and Environment*. Elsevier, 134(December 2017), pp. 155–167. doi: 10.1016/j.buildenv.2018.02.042.
- Google (2019a) ‘Google Earth Pro’, *Google*. Google. Available at: [https://www.google.com/intl/en\\_uk/earth/desktop/](https://www.google.com/intl/en_uk/earth/desktop/).
- Google (2019b) *Google Maps API*. Available at: [maps.googleapis.com](https://maps.googleapis.com).
- Grau, E. and Gastellu-Etchegorry, J. P. (2013) ‘Radiative transfer modeling in the Earth-Atmosphere system with DART model’, *Remote Sensing of Environment*. Elsevier Inc., 139, pp. 149–170. doi: 10.1016/j.rse.2013.07.019.
- Grimmond, C. S. B. (2006) ‘Progress in measuring and observing the urban atmosphere’, *Theoretical and Applied Climatology*, 84(1–3), pp. 3–22. doi: 10.1007/s00704-005-0140-5.
- Grimmond, C. S. B. *et al.* (2010) ‘The International Urban Energy Balance Models Comparison Project: First Results from Phase 1’, *Journal of Applied Meteorology and Climatology*, 49(6), pp. 1268–1292. doi: 10.1175/2010JAMC2354.1.
- Gronemeier, T., Raasch, S. and Ng, E. (2017) ‘Effects of unstable stratification on ventilation in Hong Kong’, *Atmosphere*, 8(9), pp. 1–15. doi: 10.3390/atmos8090168.
- Hammerle, A. *et al.* (2017) ‘Implications of atmospheric conditions for analysis of surface temperature variability derived from landscape-scale thermography’, *International Journal of Biometeorology*. International Journal of Biometeorology, 61(4), pp. 575–588. doi: 10.1007/s00484-016-1234-8.
- Harman, I. N. and Belcher, S. E. (2006) ‘The surface energy balance and boundary layer over urban street canyons’, *Quarterly Journal of the Royal Meteorological Society*, 132(621), pp. 2749–2768. doi: 10.1256/qj.05.185.
- Harman, I. N., Best, M. J. and Belcher, S. E. (2004) ‘Radiative exchange in an urban street canyon’, *Boundary-Layer Meteorology*, 110(2), pp. 301–316. doi: 10.1023/A:1026029822517.
- Harshan, S. *et al.* (2018) ‘Evaluation of an urban land surface scheme over a tropical suburban neighborhood’, *Theoretical and Applied Climatology*. Theoretical and Applied Climatology, 133(3–4), pp. 867–886. doi: 10.1007/s00704-017-2221-7.
- Hartley, R. ~I. and Zisserman, A. (2004) *Multiple View Geometry in Computer Vision*. Second. Cambridge University Press.
- Heikkila, J. and Silven, O. (2002) ‘A four-step camera calibration procedure with implicit image correction’, in *Proceedings of IEEE Computer Society Conference on Computer Vision and Pattern Recognition*. IEEE Comput. Soc, pp. 1106–1112. doi: 10.1109/cvpr.1997.609468.
- Hénon, A. *et al.* (2012) ‘An urban neighborhood temperature and energy study from the CAPITOU experiment with the Solene model’, *Theoretical and Applied Climatology*, 110(1–2), pp.

197–208. doi: 10.1007/s00704-012-0616-z.

- Hogan, R. J. (2019) ‘An Exponential Model of Urban Geometry for Use in Radiative Transfer Applications’, *Boundary-Layer Meteorology*. Springer Netherlands, 170(3), pp. 357–372. doi: 10.1007/s10546-018-0409-8.
- Howard, L. (1833) *The Climate of London*. London: Harvey and Darton.
- Hu, L. *et al.* (2014) ‘How can we use MODIS land surface temperature to validate long-term urban model simulations?’, *Journal of Geophysical Research*, 119(6), pp. 3185–3201. doi: 10.1002/2013JD021101.
- Hu, L. *et al.* (2016) ‘A first satellite-based observational assessment of urban thermal anisotropy’, *Remote Sensing of Environment*. Elsevier Inc., 181, pp. 111–121. doi: 10.1016/j.rse.2016.03.043.
- Hu, L. and Wendel, J. (2019) ‘Analysis of urban surface morphologic effects on diurnal thermal directional anisotropy’, *ISPRS Journal of Photogrammetry and Remote Sensing*. Elsevier, 148(December 2018), pp. 1–12. doi: 10.1016/j.isprsjprs.2018.12.004.
- Huang, F. *et al.* (2016) ‘Temporal upscaling of surface urban heat island by incorporating an annual temperature cycle model: A tale of two cities’, *Remote Sensing of Environment*. Elsevier Inc., 186, pp. 1–12. doi: 10.1016/j.rse.2016.08.009.
- Jacovides, C. P., Steven, M. D. and Asimakopoulos, D. N. (2000) ‘Solar Spectral Irradiance under Clear Skies around a Major Metropolitan Area’, *Journal of Applied Meteorology*, 39(6), pp. 917–930. doi: 10.1175/1520-0450(2000)039<0917:SSIUCS>2.0.CO;2.
- Jeanjean, A. P. R. *et al.* (2017) ‘Air quality affected by trees in real street canyons: The case of Marylebone neighbourhood in central London’, *Urban Forestry & Urban Greening*. Elsevier GmbH., 22, pp. 41–53. doi: 10.1016/j.ufug.2017.01.009.
- Jiang, L. *et al.* (2018) ‘Remote estimation of complete urban surface temperature using only directional radiometric temperatures’, *Building and Environment*. Elsevier, 135(March), pp. 224–236. doi: 10.1016/j.buildenv.2018.03.005.
- Jiménez-Muñoz, J. C. and Sobrino, J. A. (2006) ‘Error sources on the land surface temperature retrieved from thermal infrared single channel remote sensing data’, *International Journal of Remote Sensing*, 27(5), pp. 999–1014. doi: 10.1080/01431160500075907.
- Johnson, G. T. and Watson, I. D. (1984) ‘The Determination of View-Factors in Urban Canyons’, *Journal of Climate and Applied Meteorology*, 23(2), pp. 329–335. doi: 10.1175/1520-0450(1984)023<0329:TDOVFI>2.0.CO;2.
- Jokar, J. *et al.* (2015) ‘An introduction to OpenStreetMap in GIScience : Experiences , Research , Applications’, *OpenStreetMap in GIScience Experiences, Research, and Applications*, (January).
- Kanda, M. *et al.* (2007) ‘Roughness lengths for momentum and heat derived from outdoor urban scale models’, *Journal of Applied Meteorology and Climatology*, 46(7), pp. 1067–1079. doi: 10.1175/JAM2500.1.
- Kandel, H., Melesse, A. and Whitman, D. (2016) ‘An analysis on the urban heat island effect using radiosonde profiles and Landsat imagery with ground meteorological data in South Florida’, *International Journal of Remote Sensing*. Taylor & Francis, 37(10), pp. 2313–2337. doi: 10.1080/01431161.2016.1176270.
- Kato, S. and Yamaguchi, Y. (2005) ‘Analysis of urban heat-island effect using ASTER and ETM+ Data: Separation of anthropogenic heat discharge and natural heat radiation from sensible heat flux’, *Remote Sensing of Environment*, 99(1–2), pp. 44–54. doi: 10.1016/j.rse.2005.04.026.
- Kato, S. and Yamaguchi, Y. (2007) ‘Estimation of storage heat flux in an urban area using ASTER data’, *Remote Sensing of Environment*, 110(1), pp. 1–17. doi: 10.1016/j.rse.2007.02.011.

- Kawai, T. *et al.* (2007) 'Validation of a numerical model for urban energy-exchange using outdoor scale-model measurements', *International Journal of Climatology*, 27(14), pp. 1931–1942. doi: 10.1002/joc.1624.
- Kazhdan, M. and Hoppe, H. (2013) 'Screened poisson surface reconstruction', *ACM Transactions on Graphics*, 32(3), pp. 1–13. doi: 10.1145/2487228.2487237.
- Kirsch, M. *et al.* (2018) 'Integration of Terrestrial and Drone-Borne Hyperspectral and Photogrammetric Sensing Methods for Exploration Mapping and Mining Monitoring', *Remote Sensing*, 10(9), p. 1366. doi: 10.3390/rs10091366.
- Kotthaus, S. *et al.* (2014) 'Derivation of an urban materials spectral library through emittance and reflectance spectroscopy', *ISPRS Journal of Photogrammetry and Remote Sensing*. International Society for Photogrammetry and Remote Sensing, Inc. (ISPRS), 94, pp. 194–212. doi: 10.1016/j.isprsjprs.2014.05.005.
- Kotthaus, S. and Grimmond, C. S. B. (2014) 'Energy exchange in a dense urban environment – Part I: Temporal variability of long-term observations in central London', *Urban Climate*. Elsevier B.V., 10(P2), pp. 261–280. doi: 10.1016/j.uclim.2013.10.002.
- Kotthaus, S. and Grimmond, C. S. B. (2018) 'Atmospheric boundary-layer characteristics from ceilometer measurements. Part 2: Application to London's urban boundary layer', *Quarterly Journal of the Royal Meteorological Society*, 144(714), pp. 1511–1524. doi: 10.1002/qj.3298.
- Krayenhoff, S. E. and Voogt, J. A. (2007) 'A microscale three-dimensional urban energy balance model for studying surface temperatures', *Boundary-Layer Meteorology*, 123(3), pp. 433–461. doi: 10.1007/s10546-006-9153-6.
- Krayenhoff, S. and Voogt, J. (2016) 'Daytime thermal anisotropy of urban neighbourhoods: Morphological causation', *Remote Sensing*, 8(2), pp. 1–22. doi: 10.3390/rs8020108.
- Kusaka, H. *et al.* (2001) 'A simple single-layer urban canopy model for atmospheric models: Comparison with multi-layer and slab models', *Boundary-Layer Meteorology*, 101(3), pp. 329–358. doi: 10.1023/A:1019207923078.
- Kuusik, A. (2017) 'Canopy Radiative Transfer Modeling', in *Comprehensive Remote Sensing*. Elsevier, pp. 9–22. doi: 10.1016/b978-0-12-409548-9.10534-2.
- Lagouarde, J. P. *et al.* (2004) 'Airborne experimental measurements of the angular variations in surface temperature over urban areas: Case study of Marseille (France)', *Remote Sensing of Environment*, 93(4), pp. 443–462. doi: 10.1016/j.rse.2003.12.011.
- Lagouarde, J. P. *et al.* (2010) 'Modelling daytime thermal infrared directional anisotropy over Toulouse city centre', *Remote Sensing of Environment*, 114(1), pp. 87–105. doi: 10.1016/j.rse.2009.08.012.
- Lagouarde, J. P. *et al.* (2014) 'Directional anisotropy of brightness surface temperature over vineyards: Case study over the Medoc Region (SW France)', *IEEE Geoscience and Remote Sensing Letters*, 11(2), pp. 574–578. doi: 10.1109/LGRS.2013.2282492.
- Lalic, B. and Mihailovic, D. T. (2004) 'An Empirical Relation Describing Leaf-Area Density inside the Forest for Environmental Modeling', *Journal of Applied Meteorology*, 43(4), pp. 641–645. doi: 10.1175/1520-0450(2004)043<0641:aerldd>2.0.co;2.
- Lee, J. *et al.* (2019) 'Ceilometer Monitoring of Boundary-Layer Height and Its Application in Evaluating the Dilution Effect on Air Pollution', *Boundary-Layer Meteorology*. Springer Netherlands, (0123456789). doi: 10.1007/s10546-019-00452-5.
- Lee, S. *et al.* (2018) 'Analyzing thermal characteristics of urban streets using a thermal imaging camera: A case study on commercial streets in Seoul, Korea', *Sustainability (Switzerland)*, 10(2), pp. 1–21. doi: 10.3390/su10020519.
- Leutner, B. and Horning, N. (2016) 'RStoolbox: Tools for Remote Sensing Data Analysis. R package

version 0.1.4.9000'. Available at: <https://github.com/bleutner/RStoolbox>.

- Li, D. and Bou-Zeid, E. (2014) 'Quality and sensitivity of high-resolution numerical simulation of urban heat islands', *Environmental Research Letters*. IOP Publishing, 9(5). doi: 10.1088/1748-9326/9/5/055001.
- Li, Z. L. *et al.* (2013) 'Land surface emissivity retrieval from satellite data', *International Journal of Remote Sensing*, 34(9–10), pp. 3084–3127. doi: 10.1080/01431161.2012.716540.
- Lindberg, F. *et al.* (2019) 'Exploiting satellite, meteorological and geo-data for urban net storage heat flux modelling.', *Theoretical and Applied Climatology*, Submitted.
- Lindberg, F. and Grimmond, C. S. B. (2011) 'Nature of vegetation and building morphology characteristics across a city: Influence on shadow patterns and mean radiant temperatures in London', *Urban Ecosystems*, 14(4), pp. 617–634. doi: 10.1007/s11252-011-0184-5.
- Loridan, T. *et al.* (2010) 'Trade-offs and responsiveness of the single-layer urban canopy parametrization in WRF: An offline evaluation using the MOSCEM optimization algorithm and field observations', *Quarterly Journal of the Royal Meteorological Society*, 136(649), pp. 997–1019. doi: 10.1002/qj.614.
- Masson, V. (2000) 'A physically-based scheme for the urban energy budget in atmospheric models', *Boundary-Layer Meteorology*, 94(3), pp. 357–397. doi: 10.1023/A:1002463829265.
- Meier, F. *et al.* (2011) 'Atmospheric correction of thermal-infrared imagery of the 3-D urban environment acquired in oblique viewing geometry', *Atmospheric Measurement Techniques*, 4(5), pp. 909–922. doi: 10.5194/amt-4-909-2011.
- Meier, F. and Scherer, D. (2012) 'Spatial and temporal variability of urban tree canopy temperature during summer 2010 in Berlin, Germany', *Theoretical and Applied Climatology*, 110(3), pp. 373–384. doi: 10.1007/s00704-012-0631-0.
- Meier, F., Scherer, D. and Richters, J. (2010a) 'Determination of persistence effects in spatio-temporal patterns of upward long-wave radiation flux density from an urban courtyard by means of Time-Sequential Thermography', *Remote Sensing of Environment*. Elsevier Inc., 114(1), pp. 21–34. doi: 10.1016/j.rse.2009.08.002.
- Meier, F., Scherer, D. and Richters, J. (2010b) 'Determination of persistence effects in spatio-temporal patterns of upward long-wave radiation flux density from an urban courtyard by means of Time-Sequential Thermography', *Remote Sensing of Environment*, 114(December 2015), pp. 21–34. doi: 10.1016/j.rse.2009.08.002.
- Meng, Q. *et al.* (2018) 'Characterizing spatial and temporal trends of surface urban heat island effect in an urban main built-up area: A 12-year case study in Beijing, China', *Remote Sensing of Environment*. Elsevier, 204(November 2016), pp. 826–837. doi: 10.1016/j.rse.2017.09.019.
- Meyn, S. K. and Oke, T. R. (2009) 'Heat fluxes through roofs and their relevance to estimates of urban heat storage', *Energy and Buildings*, 41(7), pp. 745–752. doi: 10.1016/j.enbuild.2009.02.005.
- Mitraka, Z. *et al.* (2012) 'Improving the estimation of urban surface emissivity based on sub-pixel classification of high resolution satellite imagery', *Remote Sensing of Environment*. Elsevier Inc., 117, pp. 125–134. doi: 10.1016/j.rse.2011.06.025.
- Moritz, S. and Bartz-Beielstein, T. (2017) 'imputeTS: Time Series Missing Value Imputation in R', *The R Journal*, 9(1), pp. 207–218. Available at: <https://journal.r-project.org/archive/2017/RJ-2017-009/index.html>.
- Morrison, W. *et al.* (2018) 'A novel method to obtain three-dimensional urban surface temperature from ground-based thermography', *Remote Sensing of Environment*. Elsevier, 215(May), pp. 268–283. doi: 10.1016/j.rse.2018.05.004.
- Nadeau, D. F. *et al.* (2009) 'Estimation of urban sensible heat flux using a dense wireless network of observations', *Environmental Fluid Mechanics*, 9(6), pp. 635–653. doi: 10.1007/s10652-009-

9150-7.

- Nakayoshi, M., Kanda, M. and de Dear, R. (2015) 'Globe Anemo-radiometer', *Boundary-Layer Meteorology*, 155(2), pp. 209–227. doi: 10.1007/s10546-014-0003-7.
- NERC-ARF (2016) *NERC Airborne Research Facility Data Analysis Node, Software Downloads*. Available at: <https://nerc-arf-dan.pml.ac.uk/trac/wiki/Downloads/software> (Accessed: 25 July 2017).
- NERC ARSF (2010) 'Data from the Photographic Camera, ATM AZ-16, Optech LIDAR and AISA Eagle and Hawk Instruments on-board the Dornier Do228-101 D-CALM Aircraft during Flight GB08/19 over London Area.' NERC. Available at: <https://catalogue.ceda.ac.uk/uuid/d0d41776042b3d81651af1dafd2f883f>.
- Norman, J. M. and Becker, F. (1995) 'Terminology in thermal infrared remote sensing of natural surfaces', *Agricultural and Forest Meteorology*, 77(3–4), pp. 153–166. doi: 10.1016/0168-1923(95)02259-Z.
- Nunez, M., Eliasson, I. and Lindgren, J. (2000) 'Spatial variation of incoming longwave radiation in Göteborg, Sweden', *Theoretical and Applied Climatology*, 67(3–4), pp. 181–192. doi: 10.1007/s007040070007.
- Offerle, B. *et al.* (2007) 'Surface heating in relation to air temperature, wind and turbulence in an urban street canyon', *Boundary-Layer Meteorology*, 122(2), pp. 273–292. doi: 10.1007/s10546-006-9099-8.
- Offerle, B., Grimmond, C. S. B. and Fortuniak, K. (2005) 'Heat storage and anthropogenic heat flux in relation to the energy balance of a central European city centre', *International Journal of Climatology*, 25(10), pp. 1405–1419. doi: 10.1002/joc.1198.
- Oke, T. . (1987) *Boundary Layer Climates*. Routledge, Taylor and Francis Group.
- Oke, T. R. (1981) 'Canyon geometry and the nocturnal urban heat island: Comparison of scale model and field observations', *Journal of Climatology*, 1(3), pp. 237–254. doi: 10.1002/joc.3370010304.
- Oke, T. R. (1982) 'The energetic basis of the urban heat island', *Quarterly Journal of the Royal Meteorological Society*, 108(455), pp. 1–24. doi: 10.1002/qj.49710845502.
- Oke, T. R. *et al.* (2017) *Urban Climates*. Cambridge: Cambridge University Press. doi: 10.1017/9781139016476.
- Oke, T. R. and Fuggle, R. F. (1972) 'Comparison of urban/rural counter and net radiation at night', *Boundary-Layer Meteorology*, 2(3), pp. 290–308. doi: 10.1007/BF02184771.
- Optris GmbH (2018) 'Optris PI Operator's Manual'. Germany. Available at: <https://www.optris.co.uk/thermal-imager-pi160>.
- Ordnance Survey (2018) 'OS MasterMap Greenspace Layer'. Ordnance Survey Limited. Available at: <https://www.ordnancesurvey.co.uk/business-and-government/products/os-mastermap-greenspace.html>.
- Peng, J. *et al.* (2018) 'Seasonal contrast of the dominant factors for spatial distribution of land surface temperature in urban areas', *Remote Sensing of Environment*. Elsevier, 215(April), pp. 255–267. doi: 10.1016/j.rse.2018.06.010.
- Peng, S. *et al.* (2012) 'Surface urban heat island across 419 global big cities', *Environmental Science and Technology*, 46(2), pp. 696–703. doi: 10.1021/es2030438.
- Pigeon, G. *et al.* (2008) 'Simulation of fall and winter surface energy balance over a dense urban area using the TEB scheme', *Meteorology and Atmospheric Physics*, 102(3–4), pp. 159–171. doi: 10.1007/s00703-008-0320-9.
- Pisek, J., Ryu, Y. and Alikas, K. (2011) 'Estimating leaf inclination and G-function from leveled digital camera photography in broadleaf canopies', *Trees - Structure and Function*, 25(5), pp. 919–924. doi: 10.1007/s00468-011-0566-6.

- Plowright, A. (2018) 'ForestTools: Analyzing Remotely Sensed Forest Data v.0.2'. Available at: <https://cran.r-project.org/package=ForestTools>.
- Porson, A. *et al.* (2010) 'Implementation of a new urban energy budget scheme in the MetUM. Part I: Description and idealized simulations', *Quarterly Journal of the Royal Meteorological Society*, 136(651), pp. 1514–1529. doi: 10.1002/qj.668.
- Qi, J. *et al.* (2019) 'LESS: Large-Scale remote sensing data and image simulation framework over heterogeneous 3D scenes', *Remote Sensing of Environment*. Elsevier, 221(March 2018), pp. 695–706. doi: 10.1016/j.rse.2018.11.036.
- R Core Team (2017) 'R: A Language and Environment for Statistical Computing'. Vienna, Austria. Available at: <https://www.r-project.org/>.
- Roberts, S. M. *et al.* (2006) 'Comparison of four methods to estimate urban heat storage', *Journal of Applied Meteorology and Climatology*, 45(12), pp. 1766–1781. doi: 10.1175/JAM2432.1.
- Rosenzweig, C. *et al.* (eds) (2018) *Climate Change and Cities: Second Assessment Report of the Urban Climate Change Research Network*. Cambridge University Press. doi: 10.1017/9781316563878.
- Rotach, M. W. *et al.* (2005) 'BUBBLE - An urban boundary layer meteorology project', *Theoretical and Applied Climatology*, 81(3–4), pp. 231–261. doi: 10.1007/s00704-004-0117-9.
- Roth, M. (2000) 'Review of atmospheric turbulence over cities', *Quarterly Journal of the Royal Meteorological Society*, 126(564), pp. 941–990. doi: 10.1256/smsqj.56408.
- Roth, M., Oke, T. R. and Emery, W. J. (1989) 'Satellite-derived urban heat islands from three coastal cities and the utilization of such data in urban climatology', *International Journal of Remote Sensing*, 10(11), pp. 1699–1720. doi: 10.1080/01431168908904002.
- Roussel, J.-R. and Auty, D. (2018) 'lidR: Airborne LiDAR Data Manipulation and Visualization for Forestry Applications'. Available at: <https://cran.r-project.org/package=lidR>.
- Santamouris, M. (2013) 'Using cool pavements as a mitigation strategy to fight urban heat island - A review of the actual developments', *Renewable and Sustainable Energy Reviews*. Elsevier, 26, pp. 224–240. doi: 10.1016/j.rser.2013.05.047.
- Schaepman-Strub, G. *et al.* (2006) 'Reflectance quantities in optical remote sensing-definitions and case studies', *Remote Sensing of Environment*, 103(1), pp. 27–42. doi: 10.1016/j.rse.2006.03.002.
- Snyder, W. C. and Wan, Z. (1998) 'BRDF models to predict spectral reflectance and emissivity in the thermal infrared', *IEEE Transactions on Geoscience and Remote Sensing*, 36(1), pp. 214–225. doi: 10.1109/36.655331.
- Snyder, W. C., Wan, Z. and Zhang, Y. (1997) '<Thermal Infrared bidirectional reflectance mea.pdf>', 109(July 1996), pp. 101–109.
- Sobrino, J. A. *et al.* (2011) 'Evaluation of the DART 3D model in the thermal domain using satellite/airborne imagery and ground-based measurements', *International Journal of Remote Sensing*, 32(22), pp. 7453–7477. doi: 10.1080/01431161.2010.524672.
- Sobrino, J. A., Coll, C. and Caselles, V. (1991) 'Atmospheric correction for land surface temperature using NOAA-11 AVHRR channels 4 and 5', *Remote Sensing of Environment*, 38(1), pp. 19–34. doi: 10.1016/0034-4257(91)90069-I.
- Sobrino, J. A. and Cuenca, J. (1999) 'Angular variation of thermal infrared emissivity for some natural surfaces from experimental measurements.', *Applied optics*, 38(18), pp. 3931–6. Available at: <http://www.ncbi.nlm.nih.gov/pubmed/18320001>.
- Soux, A., Voogt, J. A. and Oke, T. R. (2004) 'A model to calculate what a remote sensor "sees" of an urban surface', *Boundary-Layer Meteorology*, 111(1), pp. 109–132. doi: 10.1023/B:BOUN.0000010995.62115.46.
- Suckling, P. W. (1981) 'Nocturnal observations of incoming longwave radiation and the urban heat

- island for a small prairie city', *Archives for Meteorology, Geophysics, and Bioclimatology Series B*, 29(1–2), pp. 23–27. doi: 10.1007/BF02278187.
- Sugawara, H. and Takamura, T. (2006) 'Longwave radiation flux from an urban canopy: Evaluation via measurements of directional radiometric temperature', *Remote Sensing of Environment*, 104(2), pp. 226–237. doi: 10.1016/j.rse.2006.01.024.
- Sun, J. and Mahrt, L. (1995) 'Relationship of surface heat flux to microscale temperature variations: Application to BOREAS', *Boundary-Layer Meteorology*, 76(July), pp. 291–301. doi: 10.1007/BF00709355.
- Thorsson, S., Lindqvist, M. and Lindqvist, S. (2004) 'Thermal bioclimatic conditions and patterns of behaviour in an urban park in Göteborg, Sweden', *International Journal of Biometeorology*, 48(3), pp. 149–156. doi: 10.1007/s00484-003-0189-8.
- United Nations (2018) *World Urbanization Prospects: The 2018 Revision, Methodology. Working Paper No. ESA/P/WP.252*. New York. Available at: <https://population.un.org/wup/Publications/Files/WUP2018-Methodology.pdf>.
- Verseghy, D. L. and Munro, D. S. (1989) 'Sensitivity studies on the calculation of the radiation balance of urban surfaces: II. Longwave radiation', *Boundary-Layer Meteorology*, 48(1–2), pp. 1–18. doi: 10.1007/BF00121780.
- Vollmer, M. (2009) 'Newton's law of cooling revisited', *European Journal of Physics*, 30(5), pp. 1063–1084. doi: 10.1088/0143-0807/30/5/014.
- Vollmer, M. and Möllmann, K.-P. (2017) *Infrared Thermal Imaging*. Weinheim, Germany: Wiley-VCH Verlag GmbH & Co. KGaA. doi: 10.1002/9783527693306.
- Voogt, J. A. (2000) 'Image representations of complete urban surface temperatures', *Geocarto International*, 15(3), pp. 21–32. doi: 10.1080/10106040008542160.
- Voogt, J. A. (2008) 'Assessment of an Urban Sensor View Model for thermal anisotropy', *Remote Sensing of Environment*, 112(2), pp. 482–495. doi: 10.1016/j.rse.2007.05.013.
- Voogt, J. A. and Grimmond, C. S. B. (2000) 'Modeling Surface Sensible Heat Flux Using Surface Radiative Temperatures in a Simple Urban Area', *Journal of Applied Meteorology*, 39(10), pp. 1679–1699. doi: 10.1175/1520-0450-39.10.1679.
- Voogt, J. a. and Oke, T. R. (1997) 'Complete Urban Surface Temperatures', *Journal of Applied Meteorology*, 36(9), pp. 1117–1132. doi: 10.1175/1520-0450(1997)036<1117:CUST>2.0.CO;2.
- Voogt, J. A. and Oke, T. R. (1998a) 'Effects of urban surface geometry on remotely-sensed surface temperature', *International Journal of Remote Sensing*, 19(5), pp. 895–920. doi: 10.1080/014311698215784.
- Voogt, J. A. and Oke, T. R. (1998b) 'Effects of urban surface geometry on remotely-sensed surface temperature', *International Journal of Remote Sensing*, 19(5), pp. 895–920. doi: 10.1080/014311698215784.
- Voogt, J. A. and Oke, T. R. (2003) 'Thermal remote sensing of urban climates', *Remote Sensing of Environment*, 86(3), pp. 370–384. doi: 10.1016/S0034-4257(03)00079-8.
- Wan, Z. (1996) 'A generalized split-window algorithm for retrieving land-surface temperature from space', *IEEE Transactions on Geoscience and Remote Sensing*, 34(4), pp. 892–905. doi: 10.1109/36.508406.
- Wan, Z. (1997) 'A physics-based algorithm for retrieving land-surface emissivity and temperature from eos/modis data', *IEEE Transactions on Geoscience and Remote Sensing*, 35(4), pp. 980–996. doi: 10.1109/36.602541.
- Wan, Z. (2014) 'New refinements and validation of the collection-6 MODIS land-surface temperature/emissivity product', *Remote Sensing of Environment*, 140, pp. 36–45. doi: 10.1016/j.rse.2013.08.027.

- Wan, Z., Ng, D. and Dozier, J. (1994) 'Spectral emissivity measurements of land-surface materials and related radiative transfer simulations', *Advances in Space Research*, 14(3), pp. 91–94. doi: 10.1016/0273-1177(94)90197-X.
- Wang, D. *et al.* (2018) 'A Geometric Model to Simulate Urban Thermal Anisotropy for Simplified Neighborhoods', *IEEE Transactions on Geoscience and Remote Sensing*. IEEE, 56(8), pp. 4930–4944. doi: 10.1109/TGRS.2018.2842794.
- Wang, D., Chen, Y. and Zhan, W. (2018) 'A geometric model to simulate thermal anisotropy over a sparse urban surface (GUTA-sparse)', *Remote Sensing of Environment*. Elsevier, 209(19), pp. 263–274. doi: 10.1016/j.rse.2018.02.051.
- Wang, W., Liang, S. and Meyers, T. (2008) 'Validating MODIS land surface temperature products using long-term nighttime ground measurements', *Remote Sensing of Environment*, 112(3), pp. 623–635. doi: 10.1016/j.rse.2007.05.024.
- Wang, W. M., Li, Z. L. and Su, H. B. (2007) 'Comparison of leaf angle distribution functions: Effects on extinction coefficient and fraction of sunlit foliage', *Agricultural and Forest Meteorology*, 143(1–2), pp. 106–122. doi: 10.1016/j.agrformet.2006.12.003.
- Ward, H. C. (2017) 'Scintillometry in urban and complex environments: A review', *Measurement Science and Technology*. IOP Publishing, 28(6). doi: 10.1088/1361-6501/aa5e85.
- Weng, Q. (2012) 'Remote sensing of impervious surfaces in the urban areas: Requirements, methods, and trends', *Remote Sensing of Environment*. Elsevier Inc., 117, pp. 34–49. doi: 10.1016/j.rse.2011.02.030.
- Weng, Q. and Lu, D. (2008) 'A sub-pixel analysis of urbanization effect on land surface temperature and its interplay with impervious surface and vegetation coverage in Indianapolis, United States', *International Journal of Applied Earth Observation and Geoinformation*, 10(1), pp. 68–83. doi: 10.1016/j.jag.2007.05.002.
- Wu, S. *et al.* (2018) 'Characterization of Remote Sensing Albedo Over Sloped Surfaces Based on DART Simulations and In Situ Observations', *Journal of Geophysical Research: Atmospheres*, 123(16), pp. 8599–8622. doi: 10.1029/2018JD028283.
- Xu, W., Wooster, M. J. and Grimmond, C. S. B. (2008) 'Modelling of urban sensible heat flux at multiple spatial scales: A demonstration using airborne hyperspectral imagery of Shanghai and a temperature-emissivity separation approach', *Remote Sensing of Environment*, 112(9), pp. 3493–3510. doi: 10.1016/j.rse.2008.04.009.
- Yang, J. *et al.* (2015) 'Modeling the effective emissivity of the urban canopy using sky view factor', *ISPRS Journal of Photogrammetry and Remote Sensing*. International Society for Photogrammetry and Remote Sensing, Inc. (ISPRS), 105, pp. 211–219. doi: 10.1016/j.isprsjprs.2015.04.006.
- Yang, J. *et al.* (2016) 'Development of an improved urban emissivity model based on sky view factor for retrieving effective emissivity and surface temperature over urban areas', *ISPRS Journal of Photogrammetry and Remote Sensing*. International Society for Photogrammetry and Remote Sensing, Inc. (ISPRS), 122, pp. 30–40. doi: 10.1016/j.isprsjprs.2016.09.007.
- Yang, L. and Li, Y. (2009) 'City ventilation of Hong Kong at no-wind conditions', *Atmospheric Environment*. Elsevier Ltd, 43(19), pp. 3111–3121. doi: 10.1016/j.atmosenv.2009.02.062.
- Yin, T. *et al.* (2013) 'A new approach of direction discretization and oversampling for 3D anisotropic radiative transfer modeling', *Remote Sensing of Environment*. Elsevier Inc., 135, pp. 213–223. doi: 10.1016/j.rse.2013.03.030.
- Yin, T., Lauret, N. and Gastellu-Etchegorry, J. P. (2015) 'Simulating images of passive sensors with finite field of view by coupling 3-D radiative transfer model and sensor perspective projection', *Remote Sensing of Environment*. Elsevier Inc., 162, pp. 169–185. doi: 10.1016/j.rse.2015.02.020.
- Zeng, L. *et al.* (2018a) 'A fast approach for large-scale Sky View Factor estimation using street view

- images', *Building and Environment*. Elsevier, 135(December 2017), pp. 74–84. doi: 10.1016/j.buildenv.2018.03.009.
- Zeng, L. *et al.* (2018b) 'A fast approach for large-scale Sky View Factor estimation using street view images', *Building and Environment*. Elsevier, 135(December 2017), pp. 74–84. doi: 10.1016/j.buildenv.2018.03.009.
- Zhou, B. *et al.* (2016) 'Assessing seasonality in the surface urban heat island of London', *Journal of Applied Meteorology and Climatology*, 55(3), pp. 493–505. doi: 10.1175/JAMC-D-15-0041.1.